OPTICAL TECHNIQUES ILLUMINATE PHASE BEHAVIOR IN MODEL MEMBRANES

A Dissertation

Presented to the Faculty of the Graduate School

of Cornell University

in Partial Fulfillment of the Requirements for the Degree of

Doctor of Philosophy

by

Elaine Ruth Farkas

May 2010

OPTICAL TECHNIQUES ILLUMINATE PHASE BEHAVIOR IN MODEL MEMBRANES

Elaine Ruth Farkas, Ph.D.

Cornell University 2010

The lipid raft hypothesis, which describes active role of lipid heterogeneities in the organization and function of mammalian cell plasma membranes, has produced an enormous body of research since its inception in the late 1980's. Much of this research employs model systems, with the goal of elucidating the thermodynamics governing lateral heterogeneity in membrane lipids. This dissertation describes an optical approach for investigating the behavior of one model system, a ternary lipid system composed of dioleoylphosphatidylcholine (DOPC), N-stearoyl-sphingomyelin (SSM), and cholesterol. Measurements included miscibility transitions of the coexistence regions of this system and an all-optical method for determining the acyl chain order parameters in each phase and the tie directions of coexisting liquid-ordered (L_o) and liquid disordered (L_d) phases.

A variety of fluorescent probes were examined for their partitioning behavior in the different phases of the SM/DOPC/cholesterol system (Chapter 2). This resulted in the selection of PAH probes with similar partitioning to cholesterol for use in subsequent studies: for the imaging of temperature-dependent phase behavior (Chapter 3) and for the characterization of the lipid acyl chain order as a function of composition (Chapter 5).

The detailed phase behavior as a function of temperature and composition is mapped out and a quasi-ternary phase diagram is presented (Chapter 3). The phase diagram depicts the miscibility behavior of optically resolvable coexisting lipid phases as determined by fluorophore partitioning. Specific perturbations during sample

preparation and imaging that affect the observed lipid phase behavior are discussed in the general context of model membrane research. This is important because these perturbations affect the validity of analogies drawn between model and biological systems. During the course of this research, an apparatus for ultra-stable (mK) control of the sample temperature during imaging was developed and it is the first of its kind. The details of the hardware necessary for such fine temperature control are related in Chapter 4. Finally, a new technique that uses mass spectrometry in conjunction with membrane patch excision is discussed in Chapter 6. The results of these experiments are preliminary but promising as a method of determining the absolute compositions of each phase.

BIOGRAPHICAL SKETCH

Elaine Farkas was born in Grand Rapids, Michigan in 1980. She moved to Florida in 1984 with her mother, father, and two older sisters Michelle and Julie. Elaine became interested in science in high school when she was a student in Ms. Margaret Peek's AP chemistry and physics classes. She obtained her bachelor's degrees in physics and in chemistry from the University of Florida in 2002, where she worked as an undergraduate researcher in Professor Andrew Rinzler's lab on the purification of single walled carbon nanotubes by chromatography. Elaine matriculated into the field of Physics at Cornell University in 2002. She obtained a master's degree in 2006 while working on lipid model membrane research in Professor Watt W. Webb's lab; she continued this work for her doctoral research. Upon graduation, Elaine will be moving to the industrial sector to pursue a career in alternative energies.

In loving memory of Kent Edmund Farkas, D.V.M., 1946-2002 and for my mom,

Tamara D. Farkas

ACKNOWLEDGEMENTS

This work would not be possible without the help, knowledge, and *patience* of many people. First and foremost among them is Professor Watt Webb. Thank you for giving the opportunity and privilege of working in your research group; it has been a great honor. I would like to thank Professor Gerald Feigenson for all the helpful scientific discussions and professional advice throughout my tenure as a graduate student, and for letting me attend your group meetings. I would also like to thank current and former Webb group members: Professor Tobias Baumgart and Dr. Jonas Korlach for having the patience to work with me and show me the ropes in the Webb group; Professor Warren Zipfel and Dr. Becky Williams for helping me with my imaging equipment and many other practical matters of experiments; Dr. Dan Dombeck for the Labview routine; and Dr. Alex Kwan for various Matlab routines and the use of the patch-clamping apparatus.

This work would not have been possible without the unconditional support of my family, especially my mom; thank you for your strength. And thank you for not letting me watch television as a child. Julie and Michelle deserve many thanks as well for listening to me when I needed to be listened to. The completion of this thesis, however, I would like to dedicate to the love of my life, Andrew C. Smith: if I could express in words what you mean to me, I would be a very famous poet not a physicist!

TABLE OF CONTENTS

LIST OF TABLES

LIST OF FIGURES

LIST OF ABBREVIATIONS

AFM, atomic force microscopy

BSM, brain sphingomyelin

CARS, coherent anti-Stokes Raman spectroscopy

DI, deionized water

DLPC, dilaurylphosphatidylcholine

DMPC, dimyristoylphosphatidylcholine

DOPC, dioleoylphosphtidylcholine

DOPE, dioleoylphosphatidylethanolamine

DPPC, dipalmitoylphosphatidylethanolamine

DPPE, dipalmitoylphosphatidylcholine

DSC, differential scanning calorimetry

DSPC, distearoylphosphatidylcholine

DTT, dithiothreitol

EMCCD, electron-multiplying charge-coupled device

ESR, electron spin resonance

FCS, fluorescence correlation spectroscopy

FFA, free fatty acid

FOX, ferrous oxidation in xylenol orange

FRET, Forster resonance energy transfer

GPI, glycosyl phosphatidylinositol

GUV, giant unilamellar vesicle

HPLC, high performance liquid chromatography

ICCD, intensified charge coupled device

ITO, indium tin oxide

L_α, liquid crystalline (same as L_d)

L_β, gel (solid)

L_d, liquid disordered

LC, liquid chromatography

L_o, liquid ordered

LR-DPPE, lissamine-rhodamine dipalmitoylphosphatidylcholine

MA, malonaldehyde

MAS, magic angle spinning

MPE, multiphoton excitation

MRM, multiple reaction monitoring

MS, mass spectrometry

NA, numerical aperture

NBD, 7-nitrobenz-2-oxa-l,3-diazol-4-yl

NMR, nuclear magnetic resonance

NSOM, near field scanning optical microscopy

OSPC, 1-oleoyl-2- stearoylphosphatidylcholine

PAH, polycylclic aromatic hydrocarbon

PC, phosphatidylcholine

PE, phosphatidylethanolamine

PERY, N,N, bis-dimethylphenyl 2,4,6,8, perylenetetracarbonyl diamide

PMT, photomultiplier tube

SANS, small angle neutron scattering

SD, standard deviation

SM, sphingomyelin

SOPC, 1-stearoyl-2-oleoyl phosphatidylcholine

SS, steady state

SSM, stearoyl sphingomyelin

TBA, thiobarbituric acid

TLC, thin layer chromatography

TS, titanium sapphire (laser)

Ti-Sapph, titanium sapphire (laser)

WAXS, wide-angle x-ray scattering

COLLABORATORS AND CONTRIBUTORS

This work would not have been possible without contributions from a number of persons. Professor Watt Webb was the guiding force for the entire body of this research. Professor Tobias Baumgart and Professor Gerald Feigenson were designed the partitioning research described in Chapter 2 and helped guide the mapping of the ternary phase diagram described in Chapter 3. Professor Watt Webb contributed greatly to the design of the sensitive temperature control apparatus described in Chapter 4 and in the experiments of Chapter 3 that utilized this apparatus. The main idea described in Chapter 5, to use polarized light microscopy to deduce acyl chain order, was introduced to me by Professor Baumgart. The HPLC and mass spectrometry in the experiments described in Chapter 6 were executed by Dr. Sheng Zhang and Dr. Robert Sherwood of the Cornell Life Sciences Proteomics resource. Dr. Zhang also developed the separation protocols for the ternary lipid mixtures that were studied. The phosphate assay described in Chapter 7 comes from the Feigenson research group and was originally conceived by Kingsley and Feigenson (1979). Thalia Mills first showed the phosphate assay when she was a student in Professor Feigenson's group. Robin Smith, Vinisha Garg, and Nelson Morales of Professor Feigenson's group performed the thin layer chromatography I used to check for lipid breakdown in Chapter 3.The Labview code for obtaining annular intensity profiles was written by Dr. Dan Dombeck, and the Biorad image file reader by Dr. Alex Kwan.

CHAPTER ONE: INTRODUCTION AND REVIEW OF THE LITERATURE

1.1 INTRODUCTION

The plasma membrane of mammalian cells comprises mainly proteins, hydrophobic sterols, and amphiphilic lipids. The plasma membrane serves many purposes beyond demarcation of the cell and containment of the cell's organelles from the environment. These include acting as a sterol and signaling lipid reservoir (Singer and Nicholson 1972), sorting of proteins (Simons and van Meer 1988, Brown and Rose 1992, Brown and London 2000, Ahmed et al 1997, Dibble et al 1993, Florine and Feigenson 1987), cell signaling (Field et al 1995, Sheets et al 1999a, Thomas et al 1994, Harder and Kuhn 2000), and modulation of protein activity (Maloney et al 1996, Soubias et al 2008, Jensen and Mouritsen 2004). There has been an extraordinary amount of interest in the details surrounding the roles of lipids and sterols in the lateral organization and chemical functions of the membrane following experimental observations that indirectly inferred lateral heterogeneity in the lipid composition of plasma membranes (Carter and Hakomori 1981, Okada et al 1984, Simons and van Meer 1988). The heterogeneities, termed "lipid rafts," are thought to be made of mainly of a saturated lipid, such as sphingomyelin, and a sterol, such as cholesterol (Simons and Ikonen 1997, Brown and London 1997). Rafts are postulated to exist in a particular thermodynamic phase known as the liquid-ordered (L_o) phase which can only exist in the presence of sterols. There are, however, various physical definitions of rafts depending on the system observed and the measurement made. In order to understand how different measurements and conditions affect the native state of the membrane, for the goal of unifying the plurality of observations regarding rafts, it is crucial to understand the fundamental thermodynamics of lipid mixtures in bilayer membranes.

The focus of this dissertation is the use of optical methods to deduce

temperature-dependent phase behavior in a simple ternary mixture of lipids which produces an L_o phase: dioleoylphosphatidylcholine (DOPC), D-erythro-stearoyl sphingomyelin (SSM), and cholesterol. In this chapter, the basic thermodynamics of membrane phase behavior and raft literature are reviewed. In Chapter 2, fluorescent probe partitioning into lipid phases for the visualization of phase separation in model membranes is reported. In Chapter 3, the temperature-dependent phase behavior of the ternary lipid system is discussed. In Chapter 4, the detailed design and operation of the temperature-controlled microscopy apparatus is explained. Chapter 5 discusses polarized light microscopy experiments used to determine the chain order in the lipids. Chapter 6 relates preliminary experiments using mass spectrometry to find tie lines for the liquid-liquid phase coexistence region of the ternary system described in Chapter 3. Finally, Chapter 7 relates the details of experimental and data analysis protocols not discussed in the preceding chapters.

1.2 BACKGROUND

Lipids are polar molecules, with "water-loving" hydrophilic ends known as headgroups, and "oil-loving" hydrophobic ends which are commonly fatty acid, or acyl, chains (Figure 1.1). Lipids may have one or two chains per molecule. Lipids are differentiated from one another according to their headgroups and their chains. There are three main families of lipids which are depicted in Figure 1.2: the glycerophospholipids, the sphingolipids, and the sterols (Lodish et al 2004). Within each family, different lipids are divided into classes according to (in order of decreasing priority): their headgroups, their chain lengths, and the degree and location of unsaturation. The glycerophospholipids have a 3-carbon glycerol backbone (colored black in Figure 1.2). The hydroxyl groups at the C1 and C2 positions form ester bonds to the fatty acid (acyl) chains (blue), and the C3 position is bonded to a phosphate group (red). The phosphate group bonds to one of many types of molecules which

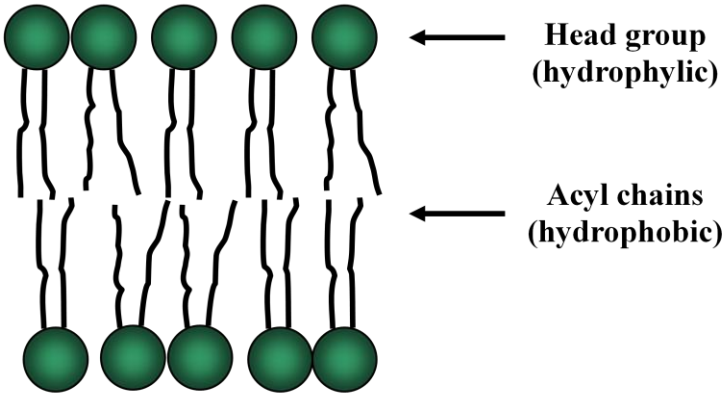

Figure 1.1 Bilayer structure. In aqueous solution, bilayers may spontaneously form. Polar lipid headgroups (green) orient toward the water, and non-polar hydrophobic fatty acid (acyl) chain orient to face one another.

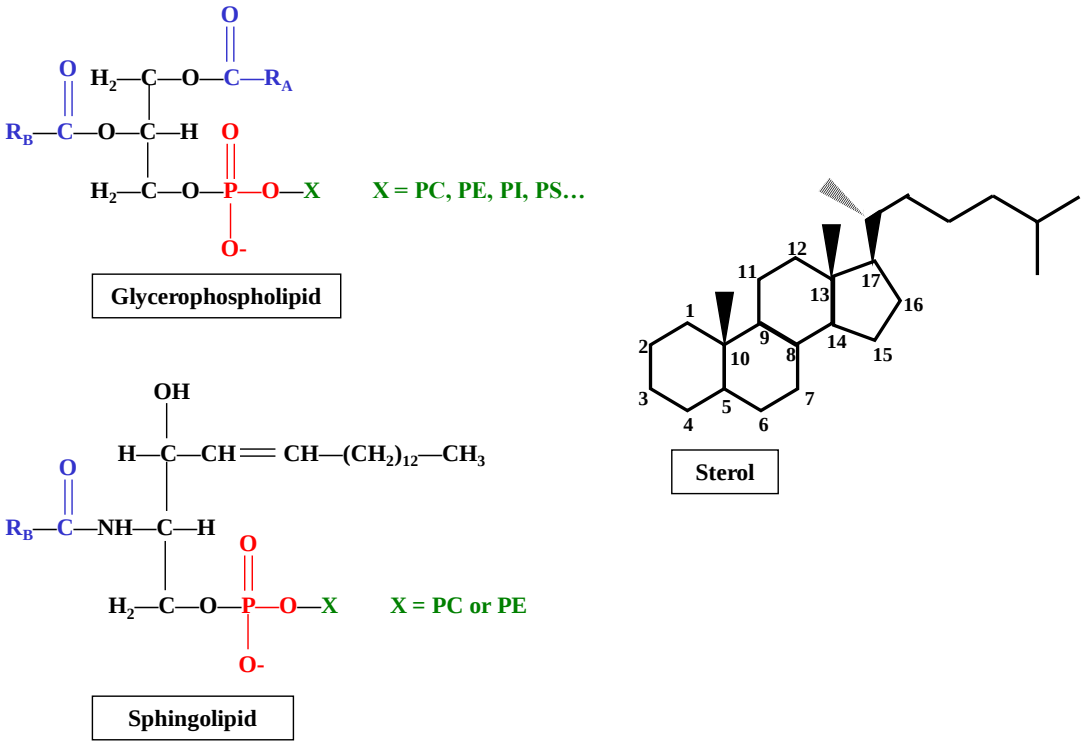

Figure 1.2 Lipid families. a. Glycerophospholipids. Black: blue fatty acid (acyl) chains, red: phosphate group, green: headgroup. b. Black: sphingosine, blue: acyl chain, red: phosphate, green: headgroup. c. Sterol ring structure. The IUPAC notation for numbering the carbons in the main rings is shown. Cholesterol has an additional OH group at carbon 3 and a double bond between 5 and 6.

define the headgroup (green). For example, a phosphatidylcholine (PC) lipid has the choline molecule bonded to the phosphate. The sphingolipids are derivatives of the lipid sphingosine (black, in Figure 1.2). Fatty acids (blue) may form an amide bond to the amino group to yield a ceramide, and like the glycerophospholipids, a phosphate group and an additional headgroup may bond to the C3 hydroxl group. Sphingomyelin (SM) is the most ubiquitous of the sphingolipids found in mammalian cells and possesses a phosphocholine headgroup like that of phosphatidylcholine. Sterols are generally less polar than lipids (in terms of molecular dipole magnitude). They comprise a planar hydrophobic structure made of four rings, known as a sterane, and a hydroxyl group (-OH) at the C3 position of this ring structure (Figure 1.2). They are distinguished from one another by additional functional groups at other carbons in the sterane ring. Among the sterols, cholesterol is the most ubiquitous in the plasma membrane, comprising roughly 30-40 mole % of the entire membrane (Lodish et al 2004, Takamori et al 2006).The polar moiety of a sterol is oriented in the membrane with the hydroxyl group facing the aqueous boundaries. The hydrophobic region is made of the planar ring structure.

The average composition of lipids in the plasma membranes of two different human cell types is shown in Table 1.1 (Lodish et al 2004). Not only are plasma membranes made of many different kinds of lipids, but the species found in each leaflet are typically very different; charged lipids, such as phosphatidylserine (PS), and phosphatidylethanolamine (PE) lipids are found in the inner leaflet, while neutral SMs and PCs are found in the outer leaflet (Lodish et al 2004, Wang and Silvius 2003, Edidin 2003). This asymmetry is dynamic and the lipid components are actively replenished by the cell. Cholesterol is found in both bilayers, though its distribution with respect to the leaflets is still a matter of debate (Edidin 2003, Mukherjee et al 1998).

Table 1.1 Average lipid composition in the plasma membranes of different cell types. Data are from Lodish et al 2004. The percentages are of the total lipids in the membrane, not the total in each leaflet.

Membrane	PC (mole %)	SM (mole %)	Cholesterol (mole %)	PE + PS (mole %)
Human erythrocyte plasma membrane	0.21	0.21	0.26	0.29
Human neuron myelin membrane	0.16	0.13	0.34	0.37
Leaflet:	outer	outer	both	inner

The other major components of the plasma membrane are proteins. The amount of protein in the plasma membrane depends on the type of cell and can vary from anywhere between 18 and 76 % by weight (Lodish et al 2004). Proteins interact with the membrane in three broad ways: they can physically span the membrane as integral or transmembrane proteins do via insertion of hydrophobic peptide segments into the membrane; they can be acylated such that they are anchored to the membrane by fatty acid chains attached to the protein; or they can interact with lipid headgroups or other membrane proteins direct binding or electrostatic interactions (peripheral membrane proteins). Proteins both modulate lipid order and are modulated by lipid order (Maloney et al 1996, Epand et al 2001, Fahsel et al 2002, Jensen and Mouritsen 2004), complicating the interpretation of the lipid raft hypothesis.

Particular attention should be paid to proteins that are cytoskeletal anchors. The cytoskeleton is a heterogeneous collection of organized structures in the cytoplasm of the cell. Each type of structure is made of a different kind of protein subunit. These structures maintain cell architecture, motility, and polarity. Most types of cytoskeletal polymers interact with the plasma membrane indirectly by binding to proteins which bind plasma membrane proteins. Recent evidence suggests that the 3-d structure created by these anchors may effectively create fences or corrals around

small populations of lipids, thus confining their lateral diffusion (Murase et al 2004, Kusumi et al 2005).

1.3 BIOLOGICAL CELL MEMBRANES AND RAFTS

One of the early organizational models of the plasma membrane was known as the fluid-mosaic model (Singer and Nicolson 1972), and it depicted plasma membrane lipids as relatively inert and laterally homogenous medium which only hosted the proteins and provided a substrate for protein-dominated processes (Figure 1.3). Although it was known that certain lipids, such as ceramide and PIP, played a crucial role in the chemistry of many signaling and metabolic processes at the time this model was developed, lipids were viewed as passive structural components with respect to membrane architecture and organization. Proteins were thought to be organized by the interactions with the actin filaments of the cytoskeleton and by protein-protein interactions.

Lateral inhomogeneities in the lipid composition of the plasma membrane were implicated in membrane organization by Simons and van Meer (1988) and Brown and Rose (1992), though it was not yet the formal "raft hypothesis." Evidence of the preferential colocalization of certain proteins with certain lipids in cell extracts (Carter and Hakomori 1981, Okada et al 1984, Simons and van Meer 1988, Brown and Rose 1992, Field et al 1995), and evidence of liquid-liquid immiscibility in model mixtures prepared from ternary lipid mixtures (Silvius et al 1996), led scientists to probe the lipid organization in the plasma membrane much closer.

It had been known for some time prior to these observations that the addition of cholesterol to lamellar lipid systems led to the appearance of the L_o phase, a term first used by Ipsen et al (1987). This led to an effective decoupling of the translational order from the acyl chain order in binary systems made up of a saturated lipid and a sterol (Estep et al 1978, Sankaram and Thompson 1990, Vist and Davis 1990). It was

also observed that lipid composition could affect protein function and partitioning (Dibble et al 1993, Florine and Feigenson 1987, Maloney et al 1996, Thomas et al 1994). In 1997, the collective findings in the plasma membranes of the biological field and in the model membranes of the physical chemistry field were integrated into the lipid raft view of cell plasma membranes (Ahmed et al 1997, Simons and Ikonen 1997). The raft hypothesis describes the plasma membrane not as a homogeneous, inert lipid sea, but as a sea with many small islands, or "rafts" that actively participate in protein function and organization (Figure 1.3, right). These rafts were postulated to be in the L_o phase because they contained mainly saturated lipids (such as sphingomyelins) and cholesterol, while the surrounding matrix in the plasma membrane resided in a less ordered L_d phase; recent studies have shown an opposite arrangement to be true in many cell types (Swamy et al 2006), with the L_o phase as the matrix or dominant phase. This does not negate a broad conclusion of the hypothesis that lateral inhomogeniety is important for cell function, however. Since the inception of the raft hypothesis, lateral inhomogeneities of lipid composition have been associated with a wide variety of cellular functions including signaling pathways (Sheets et al 1999a, Fridriksson et al 1999, Surviladze et al 2007, Wilson et al 2004) and protein sorting (Anderson and Jacobsen 2002, Pei and Chen 2003).

In the earlier studies of plasma membranes, several biochemical assays were used to infer the existence of rafts and it is important to note that this experimental evidence did not include imaging, at least not on native, unperturbed cells. Because the heterogeneities could not be observed through imaging of native and unperturbed cells, they are postulated to be smaller than the limit of optical resolution (<300nm). However, some of these early assays have certain caveats which warrant discussion. The first assay for raft detection was the exposure of the plasma membrane to non-ionic detergents such as Triton-X 100 (Carter et al 1981, Okada et al 1984, Ahmed et

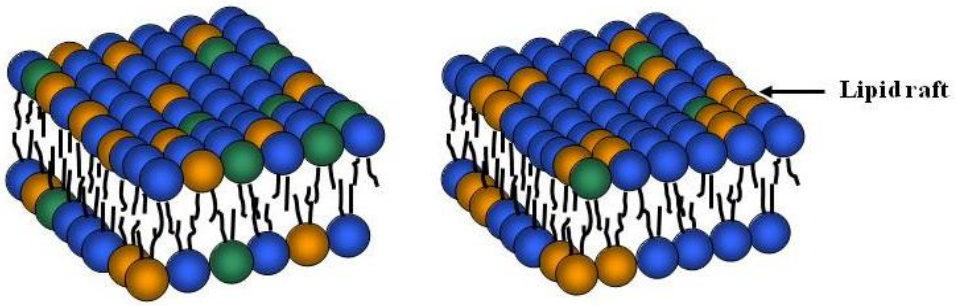

Figure 1.3 Membrane inhomogeneity. The fluid mosaic model (Singer and Nicholson 1972) on the left described the lipids of the plasma membrane as fluid and completely randomly mixed. Experiments later suggested the existence of small clusters of lipids and sterols, called "rafts," which were in a different fluid phase than the majority of the lipids, as depicted on the right. A lipid raft is shown as a cluster of "orange" and "green" lipids.

al 1997, Brown and Rose 1992, Brown and London 1997). The detergent solubilizes many proteins and lipids and thus breaks apart the membrane into small water-soluble chunks, in the same way regular household detergent does for dirt when one washes one's hands with soap. Certain proteins, such as GPI anchored proteins (Carter and Hakomori 1981, Okada et al 1984, Brown and Rose1992, Simons and van Meer 1988) were found to co-localize with saturated-chain sphingolipids and cholesterol in insoluble, or detergent-resistant membrane (DRM), fractions. Model membranes prepared from mixtures approximating these sphingolipid-cholesterol ratios were also found to be largely insoluble to non-ionic detergents (Schroeder, London and Brown 1994). Detergent resistance, however, should be subject to scrutiny for at least three reasons: the experiments are conducted at low temperatures (4ºC) where chain ordered phases may form via a miscibility transition even if they were not originally present at biologically relevant temperatures, ~37ºC (Baumgart et al 2007a, Magee et al 2005); the addition of small amounts of detergent below the concentrations required for complete disruption of the plasma membrane can induce phase separation in intact plasma membranes (Heerkoltz 2002, Arnulphi et al 2007); and the composition of the insoluble fractions isolated from cells can vary with both the type of detergent

(Surviladze et al 1998) and the concentration of a particular detergent (Arnulphi et al 2007).

Another biological assay for raft detection was cholesterol depletion, in which methyl-β-cyclodextrin (Sheets et al 1999b, Samsonov et al 2001, Hao et al 2001, Benninger et al 2005) was used to remove cholesterol from the plasma membranes of living cells; this can be reversible (Bacia et al 2004). Biological processes that changed in response to cholesterol depletion were concluded to be raft-mediated. However, the conclusions drawn from these experiments should be carefully scrutinized because cholesterol is used by cells for a variety of other functions (Lodish et al 2004), and the domain formation may be a result of some secondary process such as an alteration of actin organization or a change in the overall lateral pressure due to a change in the membrane area. Moreover, recent evidence suggests that cholesterol is not depleted exclusively from raft fractions (Mahammad and Parmryd 2008).

Despite the caveats to early methods of detecting lipid rafts, mounting evidence from a variety of experimental techniques continues to support the existence of lateral inhomogeneities in cell membranes (Varma and Mayor 1998, Fridriksson et al 1999, Harder and Kuhn 2000, Surviladze et al 2007, Hancock 2006) and close associations of "raft protein" functions with certain lipid environments in biological membranes (Eroglu et al 2003, Anderson and Jacobsen 2002). Of major concern is that there is no unambiguous definition of the physical parameters that comprise a raft in biological membranes. There are still many questions that warrant attention: exactly what lipids constitute a raft, how large are they, and which thermodynamic or kinetic parameters associated with small domains prevent the membranes from undergoing macroscopic (optically resolvable, >300nm) phase separation? Each measurement and interpretation thereof seems to yield a different answer. Some of these are summarized in Table 1.2. It should be noted that some of the experimental methods reported in

Table 1.2 with extremely high spatial resolution, like FRET, or extremely high temporal resolution, like ESR, may be sensitive to inhomogeneities that are not necessarily true thermodynamic phase separation, such as non-ideal mixing. A complete understanding of a system thus requires multiple temporal and spatial scales to be probed (Feigenson and Buboltz 2001).

The understanding of the basic thermodynamics of the lipid contributions to lateral inhomogeneities is essential for future studies on the more complicated biological membrane. Model membranes are extremely useful tools to isolate the thermodynamic contributions of lipids to the formation of inhomogeneities in much simpler systems. Model membranes containing ternary lipid mixtures have been observed to exhibit both macroscopic liquid-liquid phase separation (Dietrich et al 2001, Veatch and Keller 2002 and 2003) and sub-optical-resolution domain formation (Tokamsau et al 2003, Feigenson and Buboltz 2001, Burgos et al 2003). The overall compositions in model membranes are well defined, and one does not have to consider other possible effects of cell death, loss of bilayer compositional asymmetry, and other perturbations that may drive the system from equilibrium beyond the control of the researcher; of course, it may be these very things that end up defining rafts!

There are a variety of structures with which one can prepare model mixtures, including planar bilayers, multilamellar vesicles, and unilamellar vesicles. Giant vesicles perhaps present the most physical likeness to real cell membranes in the context that curvature-composition coupling effects are not ignored (Baumgart et al 2003, Lipowski 1992, Leibler and Andelman 1987, Kumar et al 1999, Seifert 1993). In this thesis, the giant unilamellar vesicle (GUV) is the structural model employed. A ternary lipid mixture containing an unsaturated lipid (DOPC), a saturated lipid (SSM), and cholesterol is used to mimic an average composition of the outer leaflet of the mammalian plasma membrane (Table 1.1).

Table 1.2 Inhomogeneity size depends on the measurement technique and on the system. The average time and space scales of different techniques are shown in the left columns and the sizes of inhomogeneities for biological and model membranes inferred from each technique in the right columns.

Method	Time scale	Spatial scale	Biological membranes	Model membranes
AFM	--	d>1nm	--	50-200nm[7]
CARS microscopy	$t>10^{0}$s	d>300nm	--	1-20μm[8]
Electron microscopy	--	d>1nm	20-100nm[1]	--
ESR	$t\sim10^{-9}$s	d>1nm	>2nm with L_o the majority phase[2]	1-10nm[9]
FCS (regular) FCS (scanning)	$t>10^{-6}$s $t>10^{-4}$s	d<300nm	>300nm[3]	<300nm[10] 1μm[11]
Fluorescence microscopy (scanning)	$t>10^{0}$s	d>300nm	1-10μm[4]	1-10μm[12]
Fluorescence anisotropy (time resolved)	$t\sim10^{-8}$s	d>300nm (microscopy)	--	1μm[13]
FRET	$t>10^{-7}$s	d<5nm	<5nm[5]	>0.6nm[14]
^{2}H-NMR ^{1}H-MAS NMR	$t<10^{-5}$s $t<10^{-4}$s	d>20nm d>100nm	--	20nm[15] 226nm[16]
Mass spectrometery (scanning)	--	d<100nm	--	100nm[17]
NSOM	--	d>30nm	70-600nm[6]	100-200nm[18]

[1]Wilson et al 2004, [2]Swamy et al 2006, [3]Bacia et al 2004, [4]Thompson et al 1994, [5]Sharma et al 2004, [6]Hwang et al 1998, [7]Yuan et al 2002, [8]Potoma and Xie 2003, [9]Sanakram and Thompson 1990a, [10]Korlach et al 2005, [11]Celli et al 2008, [12]Baumgart et al 2003, [13]Ariola et al 2006, [14]Feigenson and Buboltz 2001, [15]Vist and Davis 1990, [16]Polozov et al 2006, [17]Kraft et al 2006, and [18]Burgos et al 2003

1.4 LIPID PHASES

In aqueous solutions above the critical micelle concentration, lipids and lipid-sterol mixtures spontaneously organize according to the principle of "like-dissolves-like" with respect to their headgroups and acyl chain regions: either as micelles comprising one lipid layer, or as bilayers comprising two lipid layers (leaflets). The precise structural configuration, known as a lyotropic phase, depends on many factors including temperature, the intrinsic shape or curvature of the molecules, and the

concentration of the molecules in aqueous solution (Chaikin and Lubensky 2000, Silver 1985). The bilayer, depicted in Figure 1.1, is the most important lyotropic phase in biology because it is the configuration of membranes and vesicles. Bilayers contain two leaflets arranged with the acyl chain regions of each leaflet facing each other and the headgroups facing the aqueous solution on either side of the cell.

In addition to the lyotropic phases, lipids also have thermotropic phases. These are populations of ordered and disordered lipids that exist within the same lyotropic structure (the bilayer), exactly the L_d, L_o, and gel phases mentioned earlier. These phases, as well as a tilted gel phase are depicted in Figure 1.4. Order parameters that distinguish these phases from one another are depicted in Figure 1.5. They include chain orientational (or just chain order, S), chain conformational order, positional order or packing density $\rho(\boldsymbol{r})$, and the lipid director tilt, as depicted in Figure 1.5. Both orientational and positional orders are long-range and are found in gel phase bilayers. Long-range positional order is lost in fluid-phase bilayers, but long-range orientational order is retained. Chain conformational order is high in gel and L_o phases, but not L_d phases. Both the conformational and the chain orientational order can be segmental and refer to only one C-C (or C-H) bond in an acyl chain, or they can be spatially averaged over all bonds and refer to the whole acyl chain; the choice is dependent on the spatial and temporal resolution of the experimental method used to measure them.

These four order parameters are interrelated and the selection, with respect to a theoretical description of data, is dependent on the phases present and the type of order to which a measurement is sensitive. For example, packing density and orientational order are coupled in gel phases (Jahnig 1979 and 1981a), as are the orientational and conformational order. Orientation and conformation are linearly related in both liquid disordered phases (Kodati and LaFluer 1993) and in ordered phases when the model includes a finite number of chain conformations (Tuchenhagen et al 1994). However,

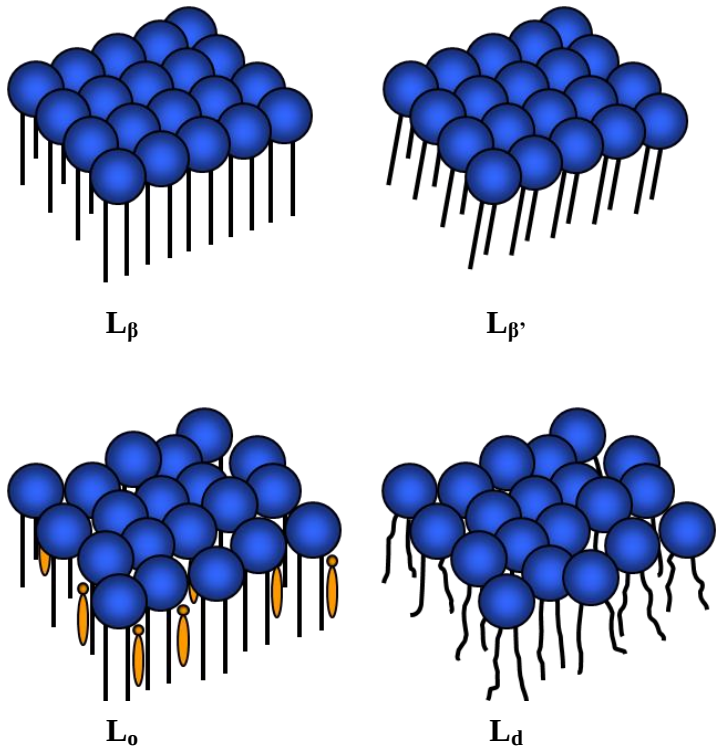

Figure 1.4. Lipid phases. Clockwise from upper left: Untilted gel (L_β), tilted gel ($L_{\beta'}$), liquid crystalline (L_α) or liquid-disordered (L_d), and liquid-ordered (L_o). The orange molecules depicted in the L_o phase are sterols.

the relations between order parameters are not always simple and may be model dependent (Ipsen et al 1990, Jahnig 1981a and 1981b), so each parameter is treated individually in this dissertation.

The chain orientational order parameter is one of the most ubiquitous measuresof lipid order because it is one to which many experimental techniques, such as NMR, x-ray diffraction, IR spectroscopy, and fluorescence anisotropy, are sensitive (Jahnig 1979, 1981a, 1981b, Albrecht et al 1978, Pastor et al 1991, Nagle and Wilkinson 1978, Tuchtenhagen et al 1994). The most microscopic definition acyl chain orientational order is that of the segmental order parameter of each C-C (or C-H bond) in the acyl chain, which can be deduced from NMR experiments (Seelig and Seelig 1974, Stockton and Smith 1976). The *i*th C-C segment in an acyl chain has a local axis (the C-C bond) which makes an angle, θ_i, with respect to the membrane

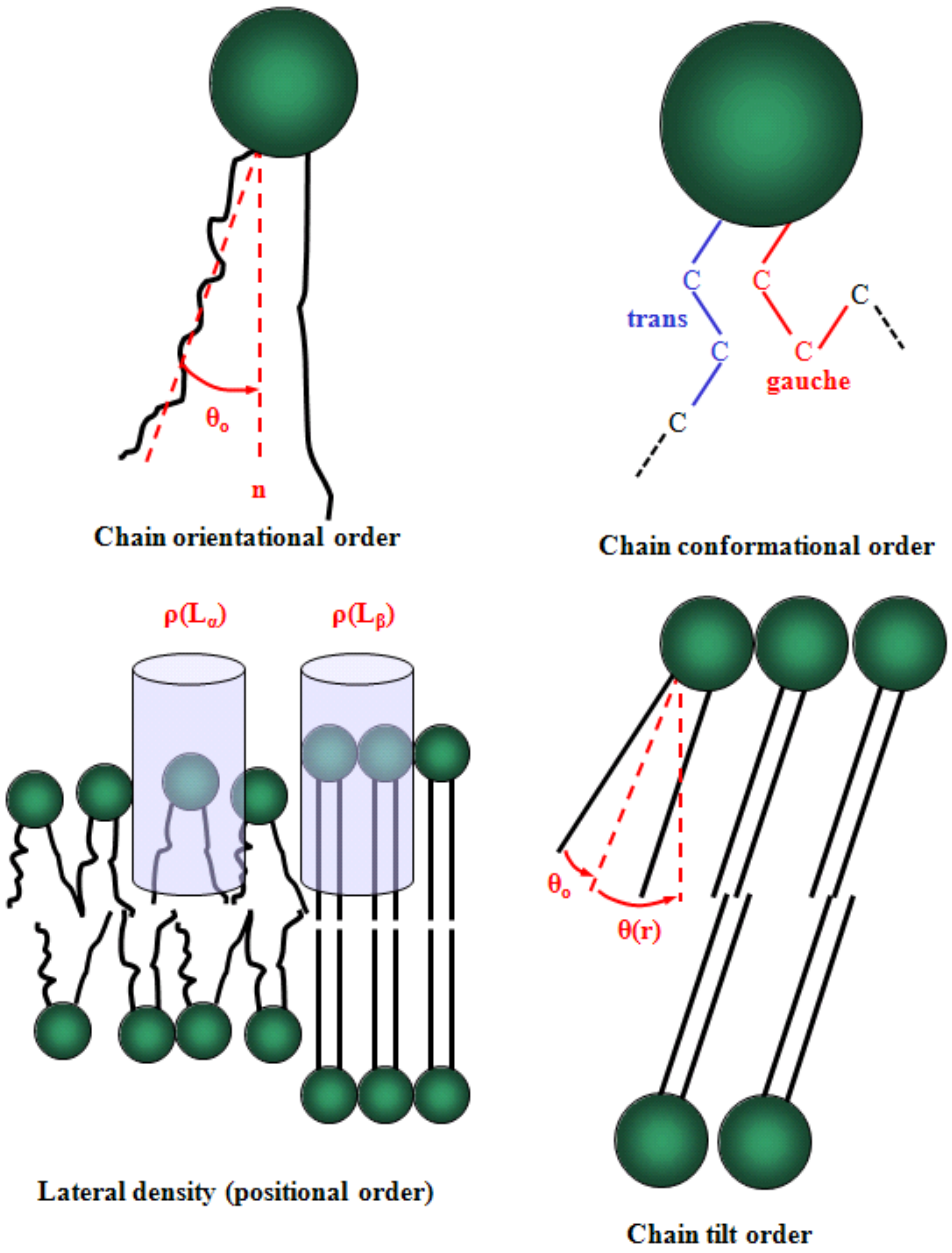

Figure 1.5 Common order parameters. Clockwise from upper left: acyl chain orientational order (molecular), acyl chain conformational order (local), tilt order, and positional order.

normal and has its own order parameter, S_i. This order parameter is defined as the second moment (Legendre polynomial) of the angle the *i*th C-C bond makes with respect to the lipid director, *n* (Maier and Saupe 1958). The lipid director is generally parallel to the membrane normal except in the cases of tilted phases discussed below.

The order parameter of the *i*th C-C segment is then defined as (Jahnig 1979):

1.1) $$S_i = \frac{1}{2} < 3\cos^2\theta_i - 1 >$$

where the brackets denote an ensemble average over all accessible chain orientations. In ^{2}H-NMR experiments, the order parameter is actually deduced from measurement of the order of the C-H bond, where hydrogen is replaced by deuterium. It is thus known as S_{CD}. S_{CDi} is related to *Si* by a simple relation, $S_i = -2S_{CDi}$ (Seelig and Niederberger 1974). The average chain order parameter for an entire lipid, <*S*>, also known as the molecular order parameter S_{mol}, is denoted:

1.2) $$< S > = S_{mol} = \frac{1}{M}\sum_{i=1}^{i=M} S_i$$

where *M* is the number of CH_2 groups (i.e., chain length). <*S*> depicts the (average) angle the entire chain makes relative to the lipid director. These whole-chain values can be measured by ESR (Rectenwald and McConnell 1981), fluorescence lifetime anisotropy (Lentz et al 1976, Knutson et al 1986), and x-ray diffraction (Mills et al 2008). The whole chain orientational order parameter is depicted in the upper left panel of Figure 1.5. For the remainder of this dissertation, *S* will be used to denote the whole chain order parameter, because that is what is measured by polarized fluorescence experiments described in Chapter 5 of this dissertation.

Conformational order is defined as the ratio of *trans*-to-*gauche* isomers of the C-C bonds with a chain. It is often described as an internal order to the orientational order. For a given chain orientation, the chain internal energy is made up of rotational isomers about each C-C bond (Jahnig 1979, Ipsen et al 1987, Pink and Carroll 1978, Nagle 1973). The chain is fully extended (ordered) when all the C-C bonds are in a *trans* configuration (Seelig and Seelig 1974). When this is the case, a series of vectors $\boldsymbol{b}_i$ connecting the midpoints of *M* consecutive C-C bonds form a straight line (Jahnig

1979). One can see qualitatively from Figure 1.5, where *trans* bonds (blue) and *gauche* bonds (red) are depicted, that a gauche bond adds a "kink" to the acyl chain that shortens the effective length of the chain. The chain cannot pack as regularly as it would in an all-*trans* configuration and thus *gauche* bonds lead to greater average disorder in the chain as a whole. Unsaturated double bonds have this effect as well. In fluid phases, a linear relationship between molecular orientational order and conformational order is observed (Kodati and LaFleur 1993). In ordered phases, *S* can be related to the number of kinked gauche bonds; the relation is operational in that it is derived based on the assumption of a finite number of preferred conformational states (Tuchenhagen et al 1994, Peterson and Chan 1977):

1.3) $$< S > = \frac{<S_{CD}>}{S_\gamma} \text{ where } S_\gamma = \frac{n_{Gauche}}{2n_{CH_2}} - \frac{1}{2}$$

This relation recovers the relation S=-2S_{CD} when the number of gauche bonds (n_{Gauche}) is zero.

The positional order refers to the positions of lipid molecules on a lattice. It is described by the lateral packing density $\rho(\boldsymbol{r})$, the lateral concentration of lipid molecules per area perpendicular to the bilayer normal. This is depicted in the lower left panel of Figure 1.5. The ordered phase has elongated and tightly packed chains; thus, there are more molecules per area in the shaded sample area than in the disordered phase, which is thinner due to chain kinks and which has less tightly packed chains. Though $\rho(\boldsymbol{r})$ may be viewed as a separate order parameter, it is in reality proportional to *S* in bilayer phases, though in a complicated manner (Jahnig 1981b, Ipsen et al 1990). This makes intuitive sense given the experimental observations that lipids with more ordered acyl chains reside with their chains in an elongated conformation parallel to the bilayer normal and thus take up less area in the perpendicular direction (Figure 1.5). Because elongated lipids take up less lateral area,

they are able to pack closer together (Lis et al 1982).

The collective tilt of the molecules, if present, is described by (Sackmann 1995):

1.4) $$T(\vec{r}) = \theta(\vec{r}) - \theta_o$$

where $\theta(r)$ is the angle of the lipid director tilt relative to the bilayer normal in the gel phase and θ_o is the averaged chain orientational angle with respect to the lipid director. This is depicted in Figure 1.5. The tilt, like chain conformation, is viewed as an internal order to the chain orientation order or to the positional order. In bilayer systems, only molecules in ordered gel phases, $L_{\beta'}$ or $P_{\beta'}$, (Wack and Webb 1989) or hexatic phases (Nagano et al 1995, Nelson and Peliti 1987) have been observed to have intrinsic tilt. This is due to the packing constraints on tilted molecules. If the chains become more liquid-like or disordered, they will not be able to pack together. In bilayer systems containing proteins, tilt is an important parameter in describing the disordering effects of the protein (Jahnig 1981a, Silver 1985).

In addition to the four parameters, other order parameters have been used in theoretical free energy descriptions of lipids and lipid mixtures. These include bilayer thickness (Ipsen et al 1990, Komura et al 2004, Yuan et al 2002), area per lipid, concentrations of different lipids and sterols (Huang and Feigenson 1999, Taniguchi et al 1996), and partition coefficients of probe molecules such as fluorescent dyes (Loura et al 2001) or spin labels (Chiang et al 2005, Smith and Freed 2009). Concentrations and partition coefficients are particularly useful for immiscible lipid mixtures.

1.4a GEL AND L_d PHASES

Positional and acyl chain (including conformation) order are the fundamental parameters in determining phase behavior of a particular lipid at a given temperature (Nagle 1973 and 1980). The thermotropic phases encountered in pure lipids (as

opposed to lipid-lipid and lipid-sterol mixtures) are the liquid crystalline (L_α or L_d) phase and the gel (solid or L_β) phase. Qualitatively, the two are distinguished from one another by both the degree of conformational freedom of the acyl chains and the lateral mobility of the lipids within a leaflet. These phases are depicted in the upper images of Figure 1.4.

In the gel phase, the acyl chains pack tightly and regularly. The chains are extended and in an all-trans conformation (Seelig and Seelig 1974), and the positions of the molecules are described by a triangular lattice with correlation lengths of about 290nm (Sun et al 1994). The lateral diffusion constant, *D*, of lipids in the gel phase is approximately 10^{-11} to 10^{-10}cm^2/s at 25°C (Fahey and Webb 1978, Almeida et al 1993, Bacia et al 2005). Gel phase structure has been studied extensively by x-ray diffraction (Sun et al 1994, Shipley et al 1974, Wack and Webb 1989), and NMR (Seelig and Seelig 1974). For a given lipid, there may be more than one gel phase reflecting different degrees of order. For example, gel phases may have a net tilt of the molecular axes ($L_{\beta'}$ phase) with respect to the normal of the bilayer in addition to chain order. In all gel phases, chain-conformational order is present.

Fluid phases, as the name suggests, lack positional order. The L_d lamellar phase is characterized by both high lateral mobility ($D \sim 10^{-8}$cm^2/s at 25°C) (Korlach et al 1999 and 2005, Fahey and Webb 1978, Bacia et al 2004) and high number of hydrocarbon chain conformations. The high number of acyl chain conformations available translates into smaller values of *S* and larger molecular areas. The area/molecule for lipids in the L_d phase is roughly 1.2 to 1.4 time larger than that in the gel phase at a given temperature: for DPPC, roughly 0.7nm^2 in the L_d phase versus 0.5nm^2 in the gel phase at 25°C (Sun et al 1994); for SSM, ~0.6nm^2 in the L_d phase versus 0.5nm^2 in the gel phase at 25°C (Shipley et al 1974). Due to the conformational disorder of the acyl chains, bilayers in the L_d phase are thinner than in the gel phase

(Lis et al 1982).

A hexatic phase is an intermediate between the gel and L_d phases in which short-ranged hexagonal bond orientation order, or tilt order, is retained but the long-range translational order is broken. In other words, the lipids are tilted and elongated and retain nearest neighbor hexagonal packing, but long-range placement on a triangular lattice is not present (Nelson and Peliti 1987). Lipids with polymorphic gel phases such as DMPC and DPPC may exhibit hexatic states, though experimental studies on this phase in lipids, in comparison to other amphiphilic molecules, are relatively scarce (Nagano et al 1995).

1.4b L_o PHASES

A different kind of phase forms when a sterol is added to a lipid sample. This phase is known as the "liquid-ordered," or L_o, phase (Ipsen et al 1987). The L_o phase is thought to be of biological relevance and that is often correlated to DRMs and rafts in biological membranes, though the correlation between model and biological systems has been disputed recently (Kaiser et al 2009). An L_o phase forms when cholesterol (or other sterol) is added to a gel phase lipid bilayer at mole fractions roughly greater than 10 mole %, though the exact amount depends on the system composition (Ahmed et al 1997, Ipsen et al 1987, Vist and Davis 1990, Sanakram and Thompson 1990a, Snyder and Freire 1980). The addition of cholesterol is thought to decouple the packing and conformational order in the gel state and in the gel -to- L_d (chain-melting) phase transition (Ipsen et al 1987, Galley et al 1976). Below the main chain-melting transition temperature, or for saturated lipids in a gel phase, it disrupts lateral packing (Galley et al 1976, Estep et al 1978), because it cannot intercalate into the lattice regularly. Above the main chain-melting transition, or for unsaturated lipids in the L_d phase, it forms van der Waals interactions with the acyl chains and imposes an all-trans conformational order. Consequently, the orientational order increases

(Yeagle 1985, Stockton and Smith 1976, Reinl et al 1992), leading to a decrease in the effective molecular area; this is known as the cholesterol condensing effect. The L_o phase retains the lateral fluidity and lack of long-range positional order of the L_d phase (D~10^{-9} cm^2/s at 25°C) (Almeida 1992, Kuo and Wade 1979), but the lipid chains are elongated and conformationally ordered in an all-trans state (Galley et al 1976, Vist and Davis 1990).

It is important to note the difference between binary systems of sterols and saturated or gel-phase lipids and binary systems of sterols and unsaturated, L_d-phase, lipids. Phase diagrams for binary cholesterol-saturated chain lipid systems often show evidence of phase separation between gel and liquid ordered phases, though this is always below optical resolution and is quite controversial, as discussed in section 1.5c (Rectenwald and McConnell 1981, Vist and Davis 1990, Bloom and Thewalt 1995). Phase separation between the L_o and L_d phases may also occur for some of these lipids above T_{CM} with sterol addition, notably for sphingomyelins (SM) and long chain saturated lipids like DPPC (Guo et al 2002, Vist and Davis 1990, Sanakram and Thompson 1990a, Collado et al 2005). The persistence of orientational and conformational order in these systems above the chain melting transition may be due to hydrogen bonding between SM and cholesterol (Mitchell and Wynne-Jones 1953, Kaiser et al 2009), or to inhomogeneity stabilization due to the formation of condensed complexes (McConnell 2005 and 2009). However, it may be that it is not true phase separation but could be attributed to slow lipid diffusion in comparison to the timescale of the measurement (Synder and Freire 1980).

In contrast, the induction of an L_o-like phase with the addition of sterols to L_d-phase lipids with *unsaturated* chains, such as DOPC does *not* result in any evidence of L_o-L_d phase separation for lipids where both chains contain an unsaturated bond (Pan et al 2008, Mills et al 2008, Warachawski and Devaux 2005). Instead, sterol addition

results in a gradual increase in chain order *S* to that of an L_o-like phase (Warachawski and Devaux 2005, Mitchell and Litman 1998). These observations support those found in binary DOPC-cholesterol and binary SSM-cholesterol systems studied here using an optical imaging technique. The results are described in Chapter 5 of this dissertation.

1.5 LIPID PHASE TRANSITIONS

In addition to a description of the phases and order parameters, it is important to illustrate immiscibility behavior for different lipid mixtures because the careful study of immiscibility is one of the focal points of this dissertation (Chapter 3). Lipid phase transitions can generally be separated into two categories: ordered-fluid (or ordered-disordered) and fluid-fluid. These transitions can be induced by changing the temperature, the area per molecule, or the external pressure. The chain melting transition of one-component bilayers and the miscibility transitions of lipid mixtures without sterols are examples of ordered-fluid transitions. In these transitions, both the positional order and the chain orientational order change. Fluid-fluid transitions are miscibility transitions that are only found in sterol lipid mixtures where two fluid phases, L_o and L_d, coexist. In simple terms, ordered-fluid transitions appear to have a non-conserved order parameter (chain conformational order) while fluid-fluid transitions have a conserved order parameter (lipid model fraction).

1.5a ORDERED-FLUID PHASE TRANSITIONS: CHAIN MELTING IN ONE-COMPONENT MODEL SYSTEMS

In the gel state, lipid molecules are organized on a triangular lattice and their chains are generally in an all-*trans* configuration. At the chain melting temperature, T_{CM}, the long-range positional order is lost and the acyl chains become conformationally disordered. Some degree of orientational order is retained if the lipids remain in a bilayer configuration. As a consequence of the chain disorder, the

bilayer thickness decreases and the lateral area per lipid increases (Sun et al 1994, Shipley et al 1974, Lis et al 1982). The nature of the chain melting transition is first order and shows a latent heat, though it has sometimes been described as having both first order and second order characteristics depending on the property measured to infer phase behavior: there is latent heat in DSC measurements, and the changes in specific heat, density, and chain order are abrupt on the time scales sampled in experiments, which indicate a first order transition; compressibility and ultrasonic velocity and absorption are anomalously broad and thus indicate of a second order transition (Mitaku et al 1983). This seeming inconsistency has been ascribed to steric hindrance, which makes the first order transition less sharp but couples the orientational and positional order (Jahnig 1979). The constraint of bilayer geometry couples the packing and acyl chain order, making the transition a cooperative one (Nagle 1973 and 1980). The L_d-gel transition in a one-component system has been modeled extensively using both lattice models (Nagle 1973, Doniach 1978) and Landau expansions (Lee et al 1977, Mitaku et al 1983). In general, the salient features of the transition require only a three-state model (Nagle 1980, 1973) in which each C-C bond in the acyl chain can have a *trans*, *gauche*, or neutral configuration. The order of the transition may change as a function of external field variables such as pressure (Nagle 1973, Albrecht et al 1978).

The chain melting transition temperature of a particular lipid depends on the chain length via van der Waals interactions (Berde et al 1983, Nagle and Wilkinson 1978), on the headgroup type via charge and steric constraints (Tuchtenhagen et al 1994, Hung et al 2000), and on the chain unsaturation (Berde 1983). Lipids with long unsaturated chains such as sphingomyelin and DPPC tend to form gel phases at room temperature, and these lipids have higher chain melting temperatures for the gel-to-L_d melting transition. In fact, it has been shown experimentally that the enthalpy change,

ΔH_{CM}, and the entropy change, ΔS_{CM}, increase with each additional CH_2 group as 4.5kJ/mol and 12 J/mol*K, respectively, and thus $T_{CM} = \Delta H_{CM}/\Delta S_{CM}$ increases monotonically with chain length (Berde et al 1983, Nagle and Wilkinson 1978). This shows that the main chain melting transition is determined by the cohesive van der Waals forces between chains, which are in turn influenced by the packing properties of the gel phases (Nagle 1973). The size, charge, and structure of the head-group influence the packing properties and thus chain melting temperature as well (Berde et al 1983). For example, the degree of hydration, dependent on the size and mobility of the headgroup, influences the conformers available to the glycerol backbone of a lipid. At a given temperature, PC is more hydrated than PE because PE groups engage in extensive hydrogen bonding (Tuchtenhagen et al 1994). The headgroup contribution to the chain melting transition properties becomes less important as the chain gets longer. Nagle showed in 1973 that when the melting temperatures of various PCs are plotted and then extrapolated to infinite chain length, the melting temperature approached that of polyethylene, 138°C. The amount of unsaturation in the hydrocarbon chains also influences packing properties and order. Lipids with unsaturated chains tend to form L_d phases and have a lower chain melting temperatures, since the double bond(s) prevents tight packing into a gel state and the formation of van der Waals interactions.

1.5b ORDERED-FLUID PHASE TRANSITIONS: IMMISCIBILITY OF L_d - GEL IN BINARY MODEL SYSTEMS WITHOUT STEROLS

When there is a mismatch of properties at an interface, a tension develops: a line tension for 2-d systems and a surface tension for 3-d systems. Phase separation occurs to reduce the size of the interface and the extent of the mismatch. In binary lipid mixtures without any sterols, the lipids can separate into a liquid (L_d) and a gel phase in a temperature range between the main chain-melting transition temperatures of the pure lipids. As described in section 1.4, the T_{CM} of a pure lipid is influenced by

a variety of structures in the lipid: headgroup, chain length, and chain saturation. Thus, when two lipids are mixed together, different behaviors are observed depending on the difference in the chain lengths, chain saturation, and head-groups. These differences can be roughly equated with the difference in T_{CM}'s of the lipids.

There had been extensive experimental studies including NMR (Shimshick and McConnell 1973), neutron scattering (Knoll et al 1981 and 1983), fluorescence microscopy (Bagatolli and Gratton 1999), DSC (Mabrey and Sturdevandt 1976), and fluorescence anisotropy (Lentz et al 1976, Lentz et al 1981, de Almeida et al 2002), to characterize the phase behavior and diagrams in binary lipid mixtures. Theoretical descriptions use the same type of physical reasoning described above for unary L_d-gel transitions and are applied to mixtures with the concentration difference of the two components in a phase as the order parameter.

If the lipids are of similar length (within two CH_2 groups of each other), but differ in chain saturation or headgroup, the phase diagram exhibits a lens-shaped L_d-gel coexistence region like that shown in Figure 1.6a[1], as is the case for DPPE-DPPC mixtures (Shimshick and McConnell 1973) and DOPC-DPPC mixtures (Lentz et al 1976). If two lipids have the *same* headgroup but the chains differ appreciably in length, namely by more than two CH_2 groups, a similar lens-shaped immiscibility region develops (Shimshick and McConnel 1973, Lentz et al 1976). The lens-shaped phase diagrams of such mixtures can be described theoretically by regular solution theory (Cheng 1980, Lee 1977).

If the chain mismatch is very large or if there is an appreciable structural difference among the solid phases such as one lipid being tilted and the other untilted, a solid-solid miscibility gap can appear below the L_d-gel coexistence region. This gap

[1] Figure 1.6a is taken from Shimshick, E. J. and H.M. McConnell (1973) Lateral phase separation in phospholipid membranes, *Biochemistry*, **12**, 2351-2360 and reprinted with permission. Copyright 1973 American Chemical Society.

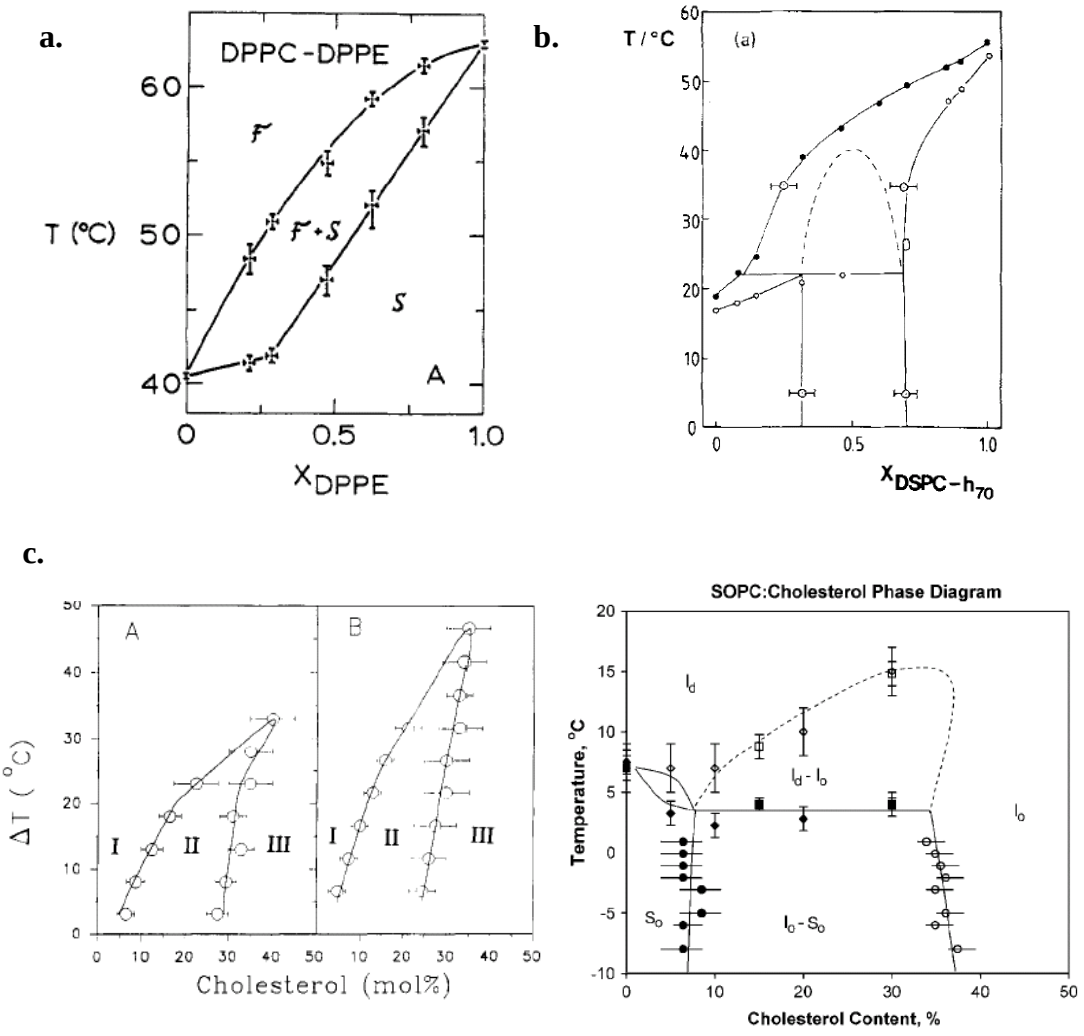

Figure 1.6 Binary phase diagrams. In each figure, the vertical axis refers to temperature except the left panel of (c), where it refers to the difference between the measurement temperature and T_{CM}. a) Lens shaped coexistence for structurally similar lipids DPPE and DPPC determined using EPR (Shimshick and McConnell 1973). The horizontal axis is mole fraction DPPE. b) Peritectic behavior for lipids with very dissimilar structures, DSPC and DMPC, determined using SANS (Knoll et al 1983). The horizontal axis is mole fraction DSPC. c) Possible eutectic behavior in lipid-sterol systems. Left: Liquid-liquid phase coexistence (II) between L_d (I) and L_o (III) phases for DPPC (left) and BSM (right) determined using ESR (Sankaram and Thompson 1990a). Right: SOPC-cholesterol diagram showing eutectic behavior determined using ^{1}H MAS NMR (Polozov and Gawrisch 2006). The latter diagrams are controversial, because the evidence of phase separation depends on the measurement. For both panel of (c), the horizontal axis is mole fraction cholesterol.

may intersect the L_d-gel regions, creating a solid-solid miscibility gap within the liquid-solid coexistence region, and leading to peritectic behavior (Figure 1.6b[2]). Peritectic behavior has been observed in several binary lipid mixtures (Knoll et al 1983), whereas eutectic behavior (Figure 1.6c[3,4]) is generally thought to be observed in binary lipid-cholesterol mixtures (see section 1.5c).

1.5c FLUID-FLUID PHASE TRANSITIONS: IMMISCIBILITY OF L_o-L_d IN BINARY SYSTEMS CONTAINING CHOLESTEROL

Long before the raft hypothesis, experimentalists were intrigued by the effects of sterols on lipid membranes. These effects include the cholesterol-condensing effect (Stockton and Smith 1976) by which cholesterol straightens an acyl chain and increases orientational and conformational order of lipids in the L_d phase (Pan et al 2008, Mills et al 2008, Warchawski et al 2005); evidence of liquid-liquid immiscibility in sterol-saturated chain lipid systems (Sankaram and Thompson 1990a, Reinl et al 1992); a broadening of the temperature range, and eventual disappearance, of the gel-L_d transition as monitored by DSC (Yeagle 1985); and an increase in the diffusion coefficient for gel-phase lipids, making them more fluid-like (Kuo and Wade 1979) as well as a decrease in the diffusion coefficient of L_d phase lipids, making them more gel-like (Almeida et al 1992). These observations have led to a variety of theoretical models and explanations for the interactions of sterols and lipids.

Vist and Davis (1990) were the first to outline the controversial phase diagram containing eutectic behavior. Their diagram for DPPC and cholesterol is similar to the

---

[2] Figure 1.6b is taken from Knoll, W. et al (1983) Critical demixing in fluid bilayers of phospholipid mixtures: a neutron diffraction study, *Journal of Chemical Physics*, **79**, 3439-3442 and reprinted with permission. Copyright 1983 American Institute of Physics.

[3] Figure 1.6c (left) is taken from Sankaram, M. B. and T. E. Thompson (1990) Interaction of cholesterol with various glycerophospholipids and sphingomyelin, *Biochemistry*, **29**, 10670-10675 and reprinted with permission. Copyright 1990 American Chemical Society.

[4] Figure 1.6c (right) is taken from Polozov, I. V. and K. Gawrisch (2006) Characterization of the liquid-ordered state by photon MAS NMR, *Biophysical Journal*, **90**, 2051-2061 and reprinted with permission. Copyright 2006 The Biophysical Society published by Elsevier Inc.

one shown in the right panel of Figure 1.6c and was very different from earlier diagrams (Estep et al 1980, Lentz et al 1980, Rectenwald and McConnell 1981). Below the main chain-melting temperature of DPPC, ^{2}H-NMR showed the unambiguous coexistence of the gel phase with a liquid phase between 5 and 25 mole % cholesterol; this appears as two separate spectra, one for each phase. Above the main chain melting temperature of DPPC, however, the NMR spectra were unresolved. ESR spectra from a different research group, though, showed separate L_o and L_d signals above the T_{CM} of DPPC. The discrepancy was attributed to lipid exchange at time scales equal to or slower than the inverse NMR frequency difference (~10μs) and thus put the upper limit of the domain sizes at <100nm (Huang et al 1993, Bloom and Thewalt 1995). However, the presence of phase separation inferred from these relatively fast time-scale methods must be interpreted with caution due to their potential susceptibility to non-equilibrium motions and to the effects of membrane curvature and domain coupling in multilamellar vesicles on the lipid diffusion used to calculate the exchange rate (Faraudo 2002, Yoshigaki 2007). It has been shown in theory that lateral diffusion rates on a curved surface in the presence of obstacles like lipid domains can be suppressed or enhanced depending on the size and arrangement of the obstacles (Holyst et al 1999).

The behavior of lipids and sterols has been interpreted theoretically as the effective decoupling of the translation order from the acyl chain conformational order (Ipsen et al 1987 and 1989). For any given lipid below its main chain transition temperature, cholesterol cannot fit as tightly into the quasi two-dimensional lattice; thus, the packing, or translational, order is disrupted. Evidence for this includes, but is not limited to, an increase in the lateral diffusion coefficient of the gel phase with cholesterol content (Kuo and Wade 1979), and a decrease in the gel tilt angle with increasing cholesterol content (McIntosh 1978). The conformational order of the acyl

chains persists as cholesterol interacts with the chains to impose steric constraints on movement; at a certain interval of cholesterol concentration, roughly 10 to 30 mole % for DPPC and SM systems (Sanakram and Thompson 1990a and 1990b), the L_o phase coexists with the gel phase. These steric constraints persist above the main chain melting temperature (Galley et al 1976, Wang and Silvius 2003, McConnell and Radhakrishnan 2007 and 2008), where the L_o phase coexists with the L_d phase.

Several theories have been developed to explain these observations and to delineate a driving force for the preferential association of cholesterol with saturated acyl chains. Three of the most prevalent theories are discussed in the appendix (7.6).

1.6 IMMISCIBILITY IN MODEL MEMBRANE SYSTEMS: TERNARY SYSTEMS CONTAINING CHOLESTEROL

Optically resolvable liquid-liquid coexistence was first observed in ternary mixtures by Silvius et al (1996) and by Deitrich et al (2001) in liposomes and in supported bilayers using fluorescence microscopy. Samsonov et al (2001) were the first to observe temperature-dependent miscibility transitions, and noted that the transitions were correlated with the T_{CM} of the saturated lipid. Korlach et al (1999), Buboltz and Feigenson (2001), Crane and Tamm (2004), and Almeida et al (1993) have studied liquid-solid and liquid-liquid coexistence in ternary systems resulting in constant-temperature phase diagrams. Veatch and Keller (2002, 2003, and 2005) later systematically investigated the temperature dependence of the miscibility transitions in liquid-liquid coexistence regions of various ternary systems and published the phase diagrams for L_o-L_d coexistence. These papers have been followed by numerous studies, because the ternary mixture is the simplest mixture that may be biologically relevant in the sense that the plasma membrane is roughly 1/3 unsaturated lipid, 1/3 cholesterol, and 1/3 saturated lipid (see Table 1.1).

1.7 CONCLUSIONS

The reasons underlying the lack of macroscopic phase separation in native biological membranes (Varma et al 1998, Yuan et al 2002, and Hwang et al 1998 for example) continues to be a topic of considerable disagreement (Hancock 2006, Veatch et al 2009). In both model and real membrane studies, several mechanisms for the formation of sub-optical resolution inhomogeneities (in addition to macroscopic domains) have been proposed. These include thermodynamic explanations such as critical fluctuations (Jin et al 2002, Raudino 1998, Honerkamp-Smith et al 2008) and non-critical non-ideal mixing (Cheng1980, Cantu et al 1997, Huang et al 1993, Feigenson and Buboltz 2001). There are also dynamic or kinetic explanations (Laggner 1993, de Almeida et al 2002) such as mesoscale texturing due to competition between surface (or line) tension and curvature (Leibler and Andelman 1987, Seul and Andelman 1995, Kumar et al 1999, Seiffert 1993); entropically driven nanodomain stabilization due to slow coarsening (Frolov et al 2006); the prevention of coarsening due to cytoskeletal corrals (Murase et al 2004, Kusumi et al 2005); and the formation of microemulsions (Levitas et al 2006) due to the stabilization of small domains by biological surfactants such as asymmetric lipids (Brewster et al 2009, Yethiraj and Weisshaar 2007). Depending on the lipid mixture and the external conditions, *all* of these contributions may be present!

This lack of consensus can be partially attributed to the fact that different measurements and theories give different values for the intrinsic size of rafts in both model and biological membrane systems, as demonstrated by the data collected for Table 1.2. Even for well defined model systems, investigations with multiple techniques lead to discrepancies in the basic interpretations of phase behavior. For example, some studies show that model membrane vesicles near the miscibility critical point are well described by a 2-d Ising model (Honerkamp-Smith et al 2008), while

others show that a 3-d model is more appropriate (Halstenberg et al 2003, Jahnig 1981a).

This underscores the continued requirement for very careful measurements in both model and biological systems. To this end, the research described in this dissertation explores a single ternary mixture, SM/DOPC/cholesterol, with a variety of optical techniques. Careful attention is paid to the influence of temperature, compositional, and kinetic artifacts that may alter the observed phase behavior of the system in unforeseen ways. The end result of this research was a temperature-dependent quasi-ternary phase diagram (Chapter 3). A very meticulous method to control the sample temperature while performing optical microscopy (Chapter 4) was developed to obtain this phase diagram; this is one of the first systems to allow milli-Kelvin temperature control near room temperature on an optical microscope. The phase diagram and observed phase behavior are subtly different from those already in the literature, and this can give rise to very different interpretations and conclusions, especially with regard to biological systems. For example, an L_d-gel coexistence region at 22°C was observed, which has not been reported in the literature for ternary systems containing a sphingolipid. It can only be observed with very slow temperature changes during sample preparation. Also, the location and behavior at the upper miscibility, or critical, point are markedly different in a qualitative sense from that described in the literature (Honerkamp-Smith et al 2008), albeit for a different ternary system. One major difference is the critical region (temperature range over which critical behavior is observed) described in this dissertation appears much less broad than that described in Honerkamp-Smith et al (2008). Finally, the directions of the tie lines (Chapter 5 and Chapter 6) in the L_o-L_d coexistence region at 22°C are different from the two published ternary diagrams containing sphingomyelin (Veatch and Keller 2005, Smith and Freed 2009).

CHAPTER TWO: MEMBRANE PROBES*

2.1 INTRODUCTION

This chapter describes the systematic characterization of commercially available membrane dyes, focusing on potential probes for the liquid ordered (L_o) phase. These dyes have been characterized with respect to their partitioning behavior in different coexistence regions for the ternary lipid mixture BSM/DOPC/cholesterol. Both one- and two-photon fluorescence microscopy imaging were used. Fluorescent lipid analogs with saturated and with unsaturated acyl chains labeled at the headgroup with a dye molecule were found to partition strongly into the L_d phase. In contrast, polycyclic aromatic hydrocarbons (PAHs) with a flat ring system were found to partition equally or preferentially into liquid-ordered (L_o) phases. A more complete study can be found in Baumgart et al 2007b, which includes 26 fluorescent probes.

It is important to identify fluorescent probes that prefer the L_o phase, because this phase is thought to make up lipid rafts in biological membranes (Dietrich et al 2001). Investigations into the properties of L_o phases are therefore essential for understanding their roles in biological membranes. In this chapter, L_o phase probes are identified and the molecular features responsible for their partitioning are suggested. Two different compositions of a single ternary lipid system were examined.

2.2 MATERIALS AND METHODS

Porcine brain sphingomyelin (BSM) and dioleoylphosphatidylcholine (DOPC) were purchased from Avanti Polar Lipids, Inc. (Alabaster, AL) and used without purification after phospholipid purity was confirmed by thin-layer chromatography as described in the appendix, Chapter 7 of this dissertation. Phospholipid stock solutions

---

* Reprinted with permission from: Baumgart, T, G. Hunt, E. R. Farkas, W. W. Webb, and G. W. Feigenson (2007) Fluorescence probe partitioning between Lo/Ld phases in lipid membranes, *Biochimica et Biophysica Acta,* **1768**, 2182-2194. Copyright 2007 Elsevier.

were prepared in chloroform and quantified by means of a phosphate assay (Kingsley and Feigenson 1979) which is described in the appendix (7.1). Cholesterol was obtained from Nu Chek Prep (Elysian, MN) or Avanti Polar Lipids, and a stock solution was prepared in chloroform.

The fluorescent probes N-(Lissamine Rhodamine B sulfonyl) dioleoyl phosphatidylethanolamine (LR-DOPE), 1,2-dipalmitoyl-sn-glycero-3-phosphoethanolamine-N-(Lissamine Rhodamine B Sulfonyl) (LR-DPPE), were purchased from Avanti Polar Lipids, Inc (Alabaster, AL). Naphtho[2,3a]pyrene, perylene, rubicene, and N,N, bis-dimethylphenyl 2,4,6,8, perylenetetracarbonyl diamide (PERY) were purchased from Sigma-Aldrich Corp. (St. Louis, MO). Terrylene and periflanthene were purchased from Chiron AS Chemicals (Trondheim, Norway).

The membrane model used was the GUV. GUV's were prepared according the electroswelling method of Angelova (1986 and 1992). Chloroform solutions were deposited onto indium tin oxide (ITO) slides (Delta Technologies, Ltd., Stillwater, MN). Deposition and electroswelling occurred at a temperature of 65^{o}C to ensure vesicle formation from homogenous bilayer membranes; this temperature is far above the highest chain melting transition of any lipid in this mixture. For electroswelling, GUV's were prepared using an alternating electric field applied for two hours in a 100mM sucrose solution (Mathivet et al 1996). The sucrose solution was heated before application to the ITO slides. GUV's were slowly cooled at approximately 1-2^{o}C/h to 25^{o}C. They were subsequently deposited onto #1 glass coverslips and enclosed by a clean glass slide containing a ring of silicone high-vacuum grease as a surrounding seal and spacer. A more in-depth discussion of electroswelling and its caveats can be found in Chapter 3 of this dissertation.

The vesicle compositions in molar ratio of BSM/DOPC/cholesterol, for

vesicles with liquid phase coexistence, was 0.27/0.50/0.23 (composition A) or 0.58/0.19/0.23 (composition B). The probes perylene, naphthopyrene, rubicene, periflanthene, and terrylene were added at concentrations of 0.5 mole %. The remaining fluorescent probes were added at a concentration of 0.1 mole %.

GUV's were imaged with either confocal microscopy using a Leica TCS SP2 spectral confocal system (Leica Microsystems Inc, Bannockburn, IL) or by two-photon excitation microscopy using a homebuilt multiphoton laser scanning microscope (W.R. Zipfel, Cornell University) based on a Bio-Rad 1024 scanhead (Bio-Rad, Richmond, CA), using a two-photon excitation wavelength of λ = 750 nm. In the case of confocal one-photon excitation microscopy, the following wavelengths were used for excitation: 458 nm (naphthopyrene), 488 nm (rubicene and PERY), and 568 nm (Lissamine rhodamine). Membrane phase assignment was checked by double labeling vesicles with the probe of interest and another probe of known partitioning behavior (LR-DOPE).

Angular emission patterns were determined by imaging non-phase separated vesicles containing *binary* lipid mixtures using linearly polarized light, and extracting the angular intensity profiles from the obtained fluorescence micrographs by means of a tracing algorithm. Each angular profile consisted of averaged measurements of ten different vesicles. All imaging was performed at room temperature, 25°C.

2.3 PARTITIONING RESULTS

In order to identify molecular factors governing probe partitioning, we examined dye distributions between two coexisting liquid phases, a liquid ordered (L_o) and a liquid disordered (L_d) phase, in vesicles made of a ternary lipid mixture. All vesicles had molar ratios of BSM /DOPC/cholesterol equal to 0.27/0.50/0.23 (A) or 0.58/0.19/0.23 (B). According to published phase diagrams of ternary lipid mixtures (Veatch and Keller 2005, Veatch and Keller 2003, Smith and Freed 2009), the

composition of our vesicles leads to segregation into a DOPC-rich majority L_d phase, and a SM- rich L_o minority phase at the composition 0.27/0.50/0.23 (A), and DOPC-rich minority L_d phase and SM-rich majority L_o phase at 0.58/0.19/0.23 (B). A rendering of the phase diagram at 25°C is depicted below in Figure 2.1[5]. These compositions were chosen in order to investigate the effect of phase composition on partitioning behavior; both samples contain the same amount of cholesterol, but differ in the relative amounts of saturated and unsaturated lipids. Since these compositions are not believed to lie along a tie line, it is expected that the L_o phase for one will a have a much different composition than the L_o phase of the other. The directions of the tie lines found in Veatch et al 2004 and Smith and Freed 2009 imply that the L_o phase of composition A will be more enriched in cholesterol than the L_o phase of composition B.

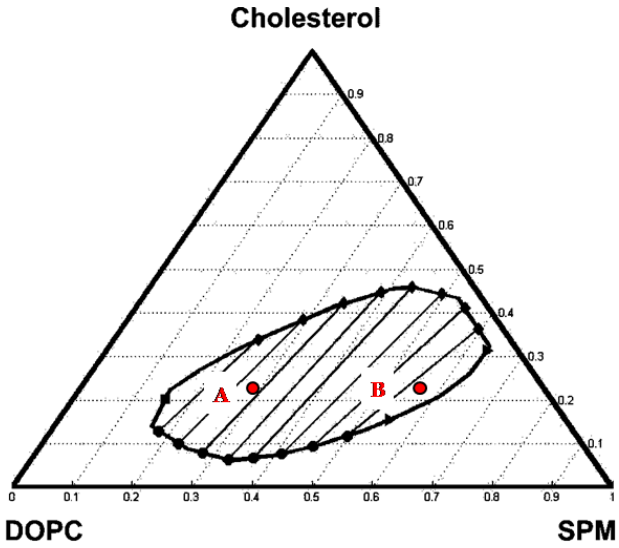

Figure 2.1. BSM /DOPC/cholesterol phase diagram. The diagram is adapted from Smith and Freed (2009). The points A and B were added to show the relative locations of the two compositions used in this research with respect to the tie lines determined by Smith and Freed (2009). Tie lines were determined by ESR. "SPM" stands for (brain) sphingomyelin.

[5] Figure 2.1 is adapted from Smith, A. K. and J. Freed (2009) *Journal of Physical Chemistry B*, **113**, 3957-3971, reprinted with permission. Copyright 2009 American Chemical Society.

The assignment of phases to L_o or L_d in GUV's imaged by fluorescence microscopy was accomplished by determining the following membrane phase features: (a) area fraction, (b) phase continuity (connectivity), and (c) the partitioning of fluorophores with known partitioning behavior. Phase assignment was verified using the fluorophore LR-DOPE, which had previously been found to partition strongly out of L_o phases coexisting with L_d phases (Samsonov et al 2001). For all dyes studied, vesicles were double labeled with the dye and LR-DOPE. The exception was terrylene, because its fluorescence emission was too similar to that of lissamine-rhodamine to facilitate the distinction of phases.

Figure 2.2 shows the molecular structures of the fluorophores that were examined in this study. The dyes may be categorized as follows: (a) phospholipids with unsaturated acyl chains and a headgroup label (LR-DOPE); (b) phospholipids with saturated acyl chains and a headgroup label (LR-DPPE); (c) fluorescent polycyclic aromatic hydrocarbons (naphthopyrene, rubicene, perylene, terrylene, periflanthene, and "PERY"); (d) the fluorescent hydrophobic membrane marker DPH. Table 2.1 summarizes the partitioning behavior of the fluorescent membrane probes used in this study. In this table, the partitioning of fluorophores is divided into three categories: L_o phase preference, L_d phase preference, and equal partitioning into either L_o or L_d phases. In principle, fluorescence microscopy allows the quantification of fluorophore partitioning in terms of partition coefficients. However, a quantitative approach is challenging beyond the usual problems of background subtraction and shading corrections over the image; it requires meticulous correction for effects such as concentration- dependent self-quenching, the influence of each membrane phase on fluorescence intensity due to fluorophore environmental sensitivity, and selective excitation due to phase-dependent confinement of fluorophore orientations (see below). Thus, only the qualitative partitioning behavior of the probe is reported here.

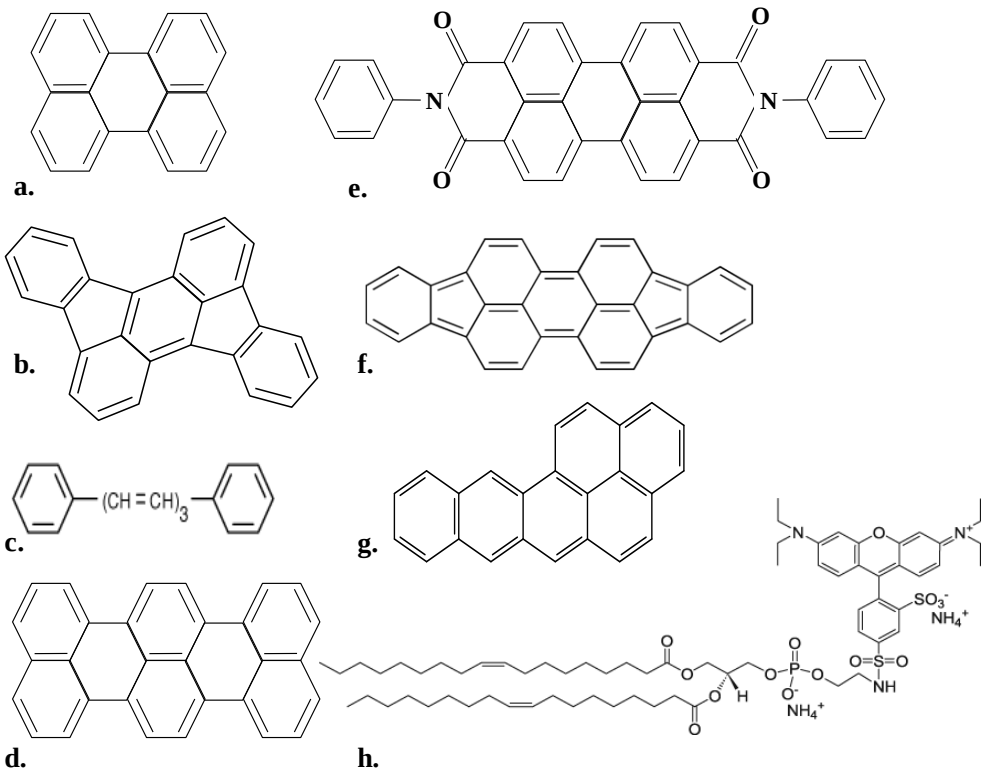

Figure 2.2. Fluorescent membrane probes. a. perylene, b. rubincene, c. diphenylhexatriene (DPH), d. terrylene, e. N,N, bis-dimethylphenyl 2,4,6,8, perylene tetracarbonyl diamide (PERY), f. perflianthene, g. naphtho[2,3a]pyrene, and h. Lissamine - rhodamine-dioleoyl phosphatidyl-choline (LR-DOPE).

Figure 2.3 depicts the partitioning of all the dyes in composition A and Figure 2.4 depicts the partitioning in composition B. Each dye produced two images, since the vesicles were double-labeled: one for the dye fluorescence and one for the fluorescence of LR-DOPE. The color of the border in each pair of images indicates the color of the emission channel; the right hand panels depict the red emission channels used to detect the LR-DOPE fluorescence and the left panels are the blue or green emission channels used to detect the fluorescence of all the other dyes studied. The exceptions were terrylene and periflanthene, in which vesicles labeled with these dyes were not double-labeled with LR-DOPE. In Figures 2.3a and 2.4a, a white arrow points to the L_d phase labeled by LR-DOPE.

Table 2.1. Partitioning behavior of the fluorescent membrane probes. Composition A: BSM/DOPC/cholesterol = 0.27/0.50/0.23, composition B: BSM/DOPC/cholesterol = 0.58/0.19/0.23. The dashes for periflanthene in composition A indicate that no data was taken.

Fluorophore	Composition A	Composition B
perylene	Equal L_o and L_d	Equal L_o and L_d
rubicene	L_d	Equal L_o and L_d
naphthopyrene	L_o	L_o
terrylene	L_o	L_o
PERY	L_d	L_d
DPH	Equal L_o and L_d	L_d
periflanthene	--	Equal L_o and L_d
LR-DOPE	L_d	L_d
LR-DPPE	L_d	L_d

As expected, the head-group labeled fluorescent membrane marker, LR-DOPE, which contains an unsaturated bond on each acyl chain, was observed to partition strongly out of the L_o phase and into the L_d phase. The intensity did not depend on the composition of the L_d phase from compositions A to B, at least not from a qualitative standpoint. Representative examples are found in the right hand panel of each pair of images in Figures 2.3 and 2.4. In every case, brightly labeled L_d domains are found, whereas in the L_o phase matrix, hardly any fluorescence could be detected. L_d phases of the mixtures used in the present study are enriched in DOPC relative to the coexisting L_o phases.

Since L_o phases are enriched in long-chain saturated lipids, the present study examined the partitioning behavior of a long and saturated chain, head group labeled membrane dye derived from DPPE, LR-DPPE. Using planar supported membranes of

the SM/POPC/cholesterol system with composition 0.25/0.5/0.25, Dietrich et al (2001) observed that the fluorophore NBD-DPPE partitioned with modest preference into the L_o phase, while the fluorophore Texas-red-DPPE strongly preferred the L_d phase. Similar partitioning behavior of Texas-red-DPPE was also found by Veatch et al (2003) in GUV's of a range of different compositions. In accordance with these findings, it was observed that LR-DPPE strongly preferred the L_d phase in the BSM/DOPC/cholesterol system. The difference between the NBD-DPPE and the LR-DPPE partitioning behavior is likely due to the difference in the size of the fluorophores: because lissamine-rhodamine is much bulkier than NBD, it disrupts the lateral packing in the headgroup region of an ordered phase to a greater extent.

The partitioning behaviors of the fluorescent PAHs are depicted in Figures 2.3 and 2.4. In both figures, the white arrows point to the L_d phase demarcated by LR-DOPE. PAH behavior is of interest, because some show sufficient quantum yield, photo-stability and wavelength characteristics to make them suitable for fluorescence microscopy. This investigation was focused on polycyclic aromatic hydrocarbons that were not attached to lipid analogs (Koivusalo et al 2004) in order to find probes with an L_o phase preference since it was thought that these dyes would mimic the packing properties of cholesterol, given their flat, disk-shaped molecular structure. Cholesterol is expected to enrich in L_o phases relative to coexisting L_d phases, according to the tie line directions (Figure 2.1) in lipid systems similar to the ones examined in this study (Veatch et al 2004, Smith and Freed 2009).

Perylene is highly photostable and has been used as a fluorescent membrane dye for spectroscopic studies (Lakowicz et al 1980, Chong et al 1985, Zandvoort et al 1997) as well as in fluorescence microscopy of coexisting liquid phases in model membranes, where it was found to preferentially partition into L_o phases in ternary lipid mixtures containing egg sphingomyelin, DOPC, and cholesterol (Baumgart et al

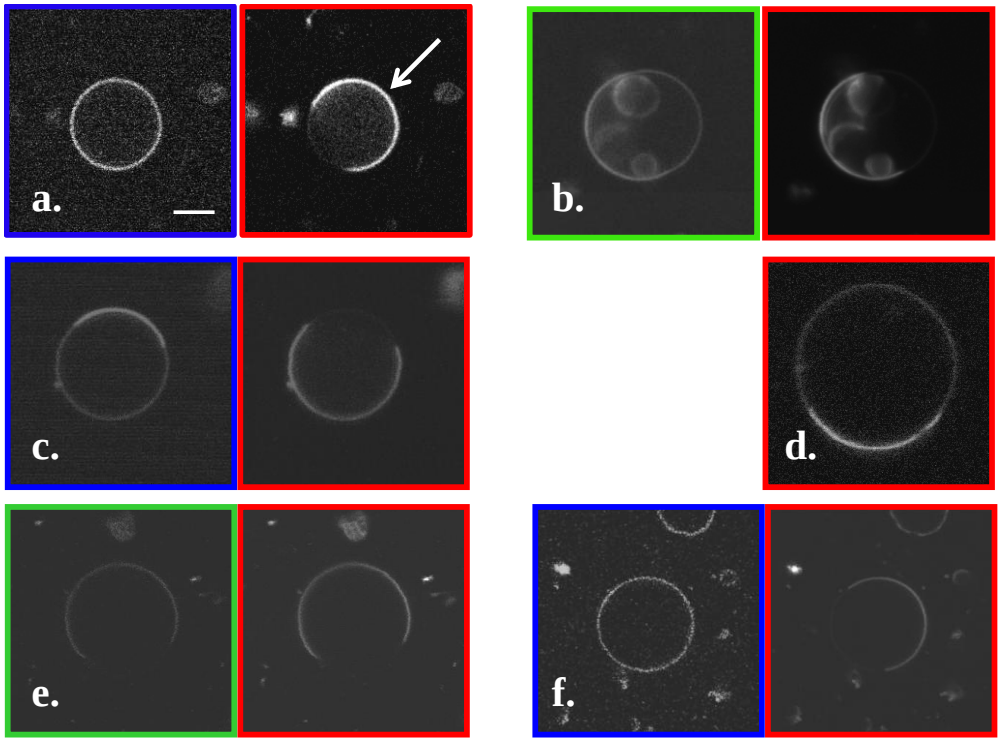

Figure 2.3 Fluorophores in composition A (BSM/DOPC/cholesterol = 0.27/0.50/0.23). The white arrow points to the L_d phase, as labeled with LR-DOPE. Left panels: green or blue fluorophore emission channel. Right panels: orange or red fluorophore emission channel. For a-f, where two images are shown, the vesicle was double labeled with LR-DOPE and the right panel corresponds to LR-DOPE fluorescence. a. perylene, b. rubicene, c. napthopyrene, d. terrylene, e. PERY, and f. DPH. Scale bar is approximately 10 µm.

2003). In the present study, however, perylene partitions equally in ternary mixtures containing BSM, as depicted in Figures 2.3a and 2.4a. The discrepancy may be due to the differences in the distribution of predominant chain lengths for the sphingomyelin mixtures: egg SM is predominantly (~85 %) C-16 SM, while porcine BSM is roughly 50 % C18 SM, 30% C24 SM, and 20% other chain lengths (Filipov et al 2006, Estep et al 1979). Because BSM has a greater distribution of chain lengths, it may not pack as tightly as egg SM in ordered phases, and will thus have more conformational disorder in the acyl chains. In fact, the chain order parameters determined using polarized light microscopy as described in Chapter 5 of this dissertation show that this

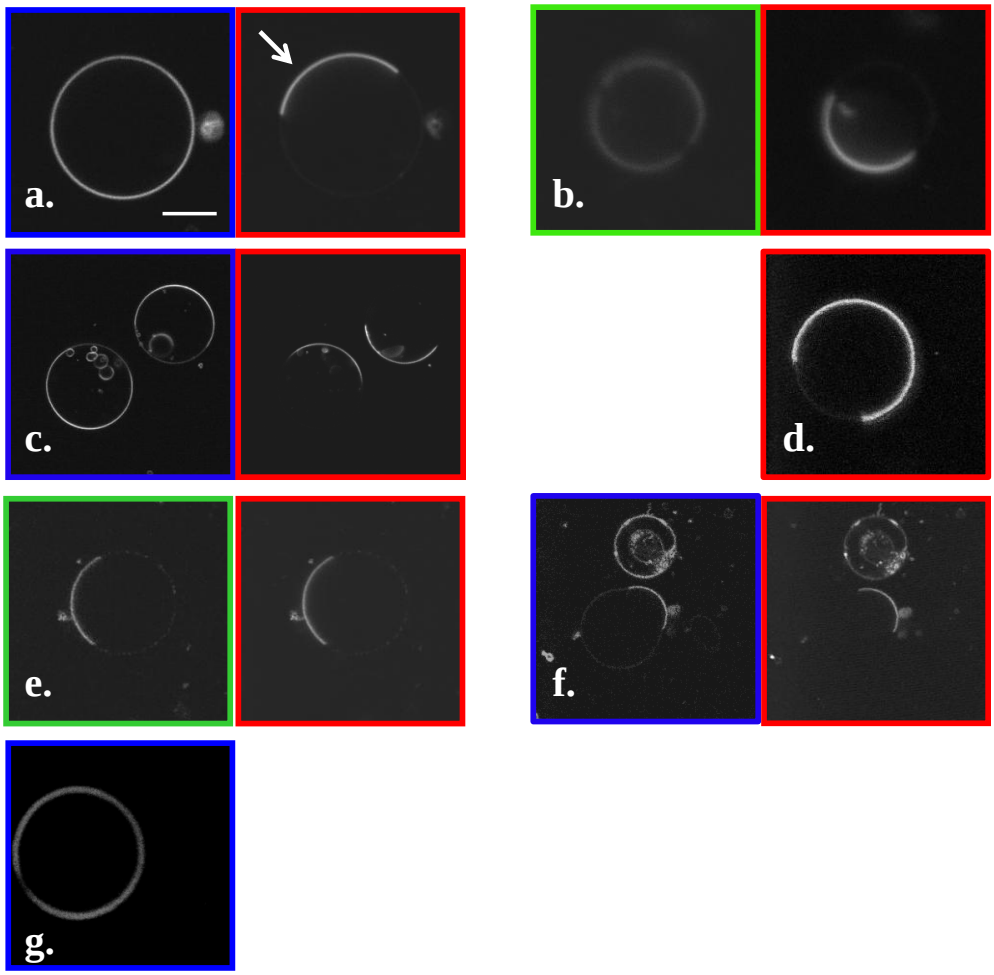

Figure 2.4 Fluorophores in composition B (BSM/DOPC/cholesterol = 0.58/0.19/0.23). The white arrow points to the L_d phase, as labeled with LR-DOPE. Left panels: green or blue fluorophore emission channel. Right panels: orange or red fluorophore emission channel. For a-f, where two images are shown, the vesicle was double labeled with LR-DOPE and the right panel corresponds to LR-DOPE fluorescence. a. perylene, b. rubicene, c. napthopyrene, d. terrylene, e. PERY, f. DPH, and g. periflanthene. Scale bar is approximately 10 µm.

is the case: BSM was *less* ordered than pure C18 SM (SSM) for both pure SM vesicles and in vesicles containing 50 mole percent SM and 50 mole percent cholesterol. It may also be that some of the components of BSM partition more readily into the L_d phase than the components of egg SM, making this phase more ordered than an L_d phase in a ternary mixture prepared with egg SM. This would also make the L_o and L_d

phases of ternary BSM mixtures more similar to each other and explain that lack of strong partition preference.

Rubicene, like perylene, is PAH with high photostability and can be used for microscopy imaging. Rubicene showed equal L_o-L_d partitioning behavior similar to perylene for composition B (Figure 2.4b), but it weakly favored the L_d phase in composition A (Figure 2.3b). This may be due to the differences in cholesterol content of the two L_o phases. The L_o phase of composition A is more enriched in cholesterol than composition B according to the tie lines for this system (Smith and Freed 2009, Chapter 5). Thus, the L_o phase of composition A is expected to be more ordered; since rubicene is less planar than PAHs of stronger partitioning behavior, it will not pack as well in this more ordered phase. Periflanthene behaved similarly to rubicene and perylene and did not display any phase preference in composition B (Figure 2.4g). No data were taken for periflanthene in composition A as it readily photobleached.

Naphtho[2,3a]pyrene and terrylene showed stronger partitioning into L_o phases in the BSM ternary system, as depicted in Figures 2.3c and 2.4c (naphthopyrene) and Figures 2.3d and 2.4 d (terrylene). Although it seems counterintuitive that a larger PAH would be able to intercalate an ordered phase better than a smaller one, the preference for the L_o phase of terrylene and napthopyrene versus perylene may be due to the fact that their larger size and their planar geometry allows them to overcome steric repulsion by making more van der Waal's bonds with the acyl chains. Large but less planar molecules such as rubicene and periflanthene do not show strong partitioning. In addition, the smaller size of perylene may allow it to position itself between leaflets, with its long axis perpendicular to the membrane normal instead of parallel to it (Zandvoort et al 1997).

The bi-substituted perylene derivative PERY was observed to strongly prefer the L_d phase for both composition A (Figure 2.3e) and B (Figure2.4e). The bis-

dimethylphenyl groups of this fluorophore are known to be able to rotate around the C-N bond (Rademacher et al 1982). This molecular feature, as well as the polar additions to the perylene backbone, makes PERY much different from the other PAHs in this study. The strong partitioning of PERY into the L_d phases supports the finding that PAH dyes partition into the L_o phase only when the hydrophobic, rigid ring system does not obstruct lipid chain packing.

The last probe examined in this study is DPH. DPH has been used extensively in the past to analyze chain ordering in lipid model membranes (Knutson et al 1986, Lentz 1993, Lakowicz et al 1992) as well as cellular membranes (Gidwani et al 2001). In a DPPC system, the partition coefficients between cholesterol- and DPPC-rich Lo phases and pure DPPC above the main phase transition temperature (L_d) have been described as being close to unity (Gidwani et al 2001, Lentz et al 1980). However, in the present ternary mixture this is only true of composition A (Figure 2.3f). In composition B, DPH favors the L_d phase (Figure 2.4f). DPH may prefer to partition out of L_o phases because it lacks the rigid ring structure of the PAH dyes and cannot pack as efficiently. Differences between this and the DPPC studies may be due to the sphingomyelin.

2.4 PAH ORIENTATION IN MEMBRANES

Fluorescent probe positions and orientations within the membrane are important properties that can be used to infer quantities such as the acyl chain order (Lipari and Szabo 1980, Kinosita et al 1977) and the degree of hydration (Bagatolli and Gratton 1999, Kaiser et al 2009) to quantify lipid phase behavior. In this section, probe orientations were studied in order to elucidate why certain planar hydrophobic PAHs partition preferentially into L_o phases. Probe orientations were determined with respect to the membrane normal direction by using polarized excitation fluorescence microscopy. Optically homogenous vesicles of gel, L_d, and L_o phase state were

illuminated with linearly polarized light and imaged in the equatorial planes. Figure 2.5 compares the intensity patterns of perylene, naphthopyrene, terrylene, PERY, and DPH in gel phase vesicles (pure BSM, left column), L_o phase vesicles (BSM:cholesterol = 1:1, middle column), and L_d phase vesicles (pure DOPC, right column). Rubicene and periflanthene were not studied with respect to their orientations in the membrane. The direction of the polarization of the excitation light is depicted by the double headed green arrow in Figure 2.5. For perylene and napthopyrene, two images are shown for each of the three phases. The left panel in each pair of images depicts the fluorescence of the probe LR-DOPE, so the emission pattern could be used as reference.

The angular emission patterns for probes excited with linearly polarized light can be used to infer average probe orientations within the membrane if the directions of the absorption or emission dipoles are known relative to the probe geometry (Axelrod 1979, Florine-Casteel 1990, Bagatolli and Gratton 2000). For perylene, terrylene, naphthopyrene, PERY, DPH, and lissamine-rhodamine, the directions of absorption and emission dipole moments point roughly along the longest axis of the dye molecules (Sepiol et al 1997, Axelrod 1979, Chong et al 1985). The orientation of the headgroup label lissamine-rhodamine has previously been shown to be parallel to the membrane tangent (Bagatolli and Gratton 2000), which allows it to serve as a reference for the orientations of the other dyes. Given the excitation light polarization direction relative to the membrane equator (Figure 2.5), the emission pattern of LR-DOPE is depicted in left panels of the image pairs in Figure 2.4 as expected and in accordance with Bagatolli and Gratton (2000): photoselection rules dictate that the smaller the angle between the absorption dipole and the excitation light polarization, the higher the probability of excitation. This is the famous cosine-squared relation between intensity and the polarization angle and is observed experimentally in

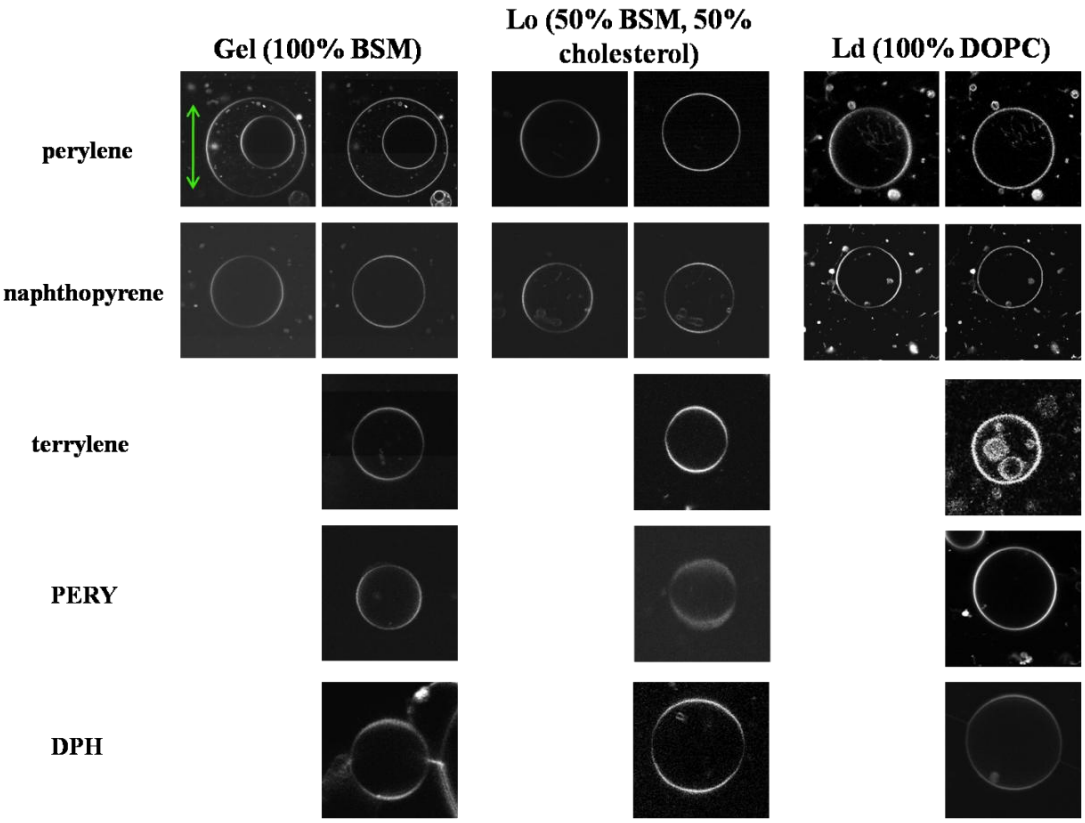

Figure 2.5. Fluorescence emission patterns of different PAH probes membranes of different compositions. The arrow depicts the polarization direction of the 750nm excitation light relative to the membrane equator; this the same for all images depicted here. For perylene and naphhthopyrene, the left hand panel depicts the fluorescence of LR-DOPE, and the right hand panel depicts the fluorescence of the PAH.

imaging as bright regions on the two poles of the vesicle where the dipoles roughly align parallel to the excitation light.

It should be noted that in two-photon excitation, one does not actually have an absorption *dipole*, but rather a three-dimensional *tensor*. Without a proper selection of the excitation wavelength (transition symmetry), the relationship between the probe geometry and the direction of maximal absorption is much more complicated than a simple cosine-squared. For rod-like molecules such as DPH, it may be as simple as a cosine^4 for the appropriate wavelength (symmetry transition), but for molecules of other quantum mechanical group symmetries such as the D_{2h} molecule perylene and

terrylene, the relationship is often more complicated. This is explored in detail in Chapter 5 of this dissertation. Here we rely on the fact that the emission is still described by a dipole because it is a single photon event, and that dipole is *roughly* parallel to the long axis of each dye studied.

Perylene, naphthopyrene, and terrylene showed approximately uniform angular emission patterns for L_d phase vesicles consisting of DOPC membranes. This indicates random orientations of emission dipole moments of these PAHs in L_d phase membranes (right most set of panels in Figure 2.5). This makes sense intuitively since the acyl chain region in this phase is very disordered; therefore, it does not inhibit the probes from tumbling and rotating into different orientations. Both DPH and PERY were more polarized in the L_d phase, with DPH aligning parallel to the membrane normal and PERY aligning parallel to the tangent to the membrane. PERY is likely situated between the two leaflets of the bilayer membrane in the L_d phase.

In contrast to these findings, we observed an angular emission pattern in L_o phase vesicles that was rotated by 90° compared to the LR-DOPE pattern for all PAHs as well as DPH (middle set of panels in Figure 2.5). This indicates that in the L_o phase, PAH excitation dipole moments are oriented preferentially along the membrane normal. This suggests that the PAHs intercalate into L_o phase membranes in a way similar to cholesterol, by association of the long axis of the flat molecular surface with the saturated lipid chains. This property is what one desires in a fluorescent probe for chain order, and this property is exploited in Chapter 5 of this dissertation in order to quantify acyl chain order. Note that these angular emission patterns depicted in Figure 2.5 imply that PERY changes orientations from the L_d phase the L_o phase. The angular emission patterns in gel phase vesicles (pure BSM) are similar to those for the L_o phase vesicles for all dyes except for PERY, which appears to have the same orientation as in the L_d phase. Notice that the difference between the intensity

maximum and minimum appears slightly weaker in the gel phase than in the L_o phase for each dye.

The normalized fluorescence intensity traces versus angle around the membrane perimeter are depicted in Figure 2.6. These were obtained from microscopy images equivalent to those shown in Figure 2.5. The relative intensity differences between the intensity maxima and minima of angular emission patterns (Figure 2.6) are related to the width of a probe′s orientational probability distribution (Florine-Casteel 1990). Larger dyes like terrylene experience a stronger confinement in lipid membranes compared to smaller PAHs like perylene. This is quantified in Chapter 5 of this dissertation. In fact, Figure 2.6 depicts a direct correlation between molecular size and the difference between the maximum and minimum of the angular intensity profiles in the L_o and gel phases: perylene has the shallowest profile, followed by naphthopyrene, and then terrylene.

2.5 DISCUSSION

The study examined the partitioning behavior between coexisting L_o and L_d phases of fluorophores suitable for fluorescence microscopy imaging. It was found that headgroup-labeled fluorophores partition out of the L_o and into the L_d phase. The partitioning of LR- DOPE and LR-DPPE probes indicates that the phase preference of these fluorophores is dominated by the fluorescent label and not by the lipid backbone. Large PAHs such as terrylene and naphthopyrene were found to have preference for L_o phases, while the smaller PAH perylene did not. Less planar PAH's such as rubicene and periflanthene showed little preference, probably due to their inability to pack tightly with the acyl chains. The PAHs with strongest L_o partitioning consist of a planar ring system. It is known that the cholesterol-lipid interaction leads to an effective elongation of the acyl chains of the lipids by increasing the fraction of *trans*-configurations in the chain (Yeagle 1985, Vist and Davis 1990, Sankaram and

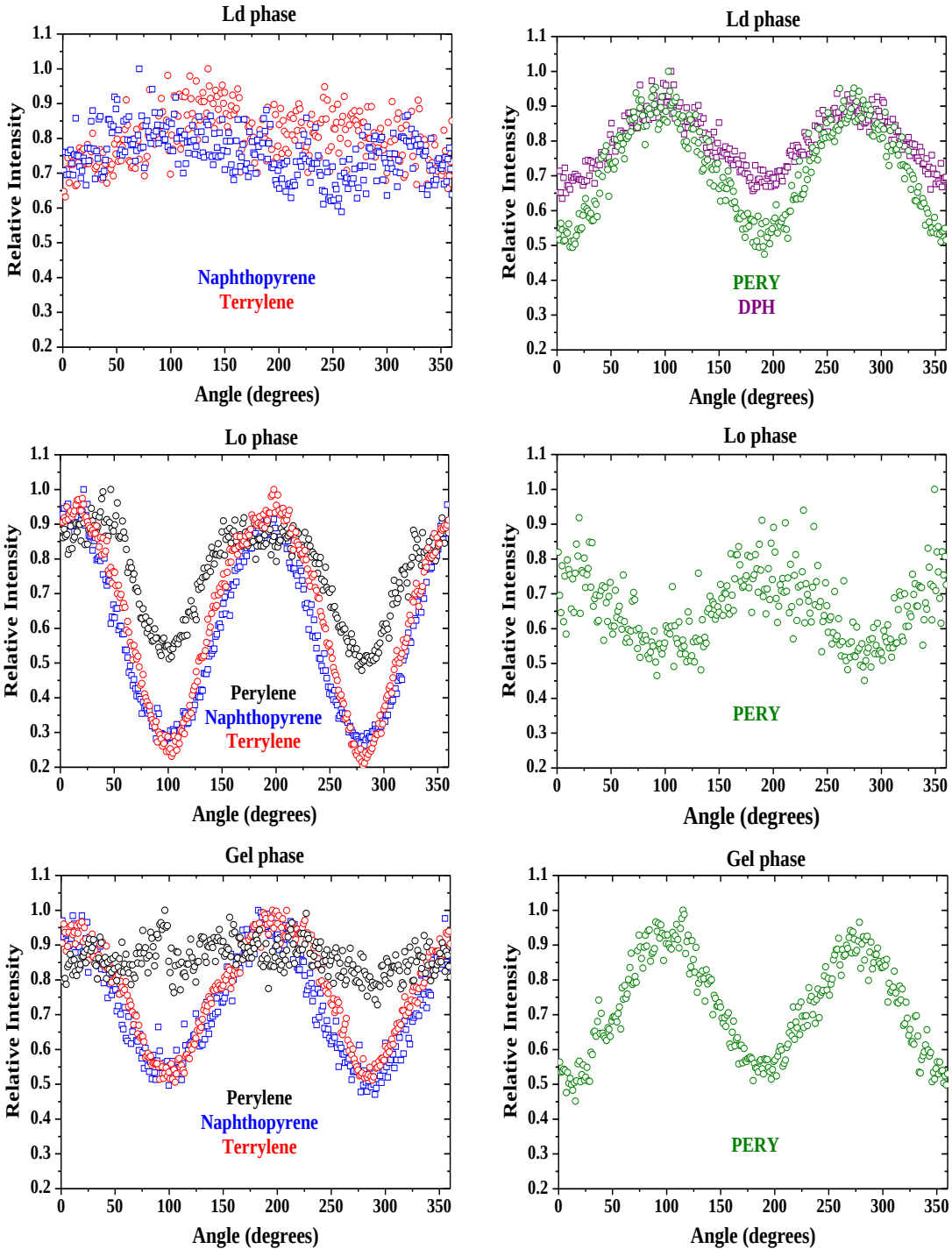

Figure 2.6 Relative fluorescence intensity versus angle around the perimeter of an equatorial GUV section. Each set of data is the average of at least 10 GUV's, but error bars are omitted for the sake of clarity. The color coding is as follows: black: perylene, blue: naphthopyrene, red: terrylene, green: PERY, and purple: DPH. λ_{EX} = 750nm.

Thompson 1990b) and that cholesterol preferentially associates with saturated chain sphingo- and phospholipids with high main phase transition temperature (Sanakram and Thompson 1990a). Thus, the partitioning behavior of the L_o preferring PAHs suggests that they do indeed roughly model the behavior of cholesterol. While the relatively high photostability of naphthopyrene, perylene, rubicene and terrylene makes each of them suitable for studying the properties of L_o phases by fluorescence methods, the more consistent and strong partitioning behavior of naphthopyrene and terrylene renders them perhaps the most suitable.

In principle, it should be possible to obtain quantitative results for probe partitioning by comparing fluorescence intensities of fluorophores in coexisting phases. Partitioning coefficients could be determined for probes in ternary lipid mixtures if phase coexistence is optically resolvable. Fluorescence microscopy imaging is advantageous in that sense over spectroscopic cuvette measurements of probe partitioning. Spectroscopic techniques can yield quantitative measurements of partitioning coefficients in binary, but not in ternary mixtures, unless the phase diagram tie lines are known or other assumptions of partitioning are made.

Using two-photon fluorescence microscopy with polarized excitation light, it was observed that PAHs tend to align their excitation dipole moment along the membrane normal in L_o phase membranes, but not in L_d phase membranes. A recent NMR study (Hoff et al 2005) examined the orientation of pyrene in lipid bilayer membranes. Pyrene is a PAH similar in structure to the ones used in this study, but smaller. In L_d phase POPC membranes, the long axis of the molecule was found to align parallel to the membrane normal within a range of ±30° (Hoff et al 2005). The difference may also be explained by the qualitative nature of this study: when the intensity versus angle data are actually fit to a model of probe motion, the result is consistent with a small degree of order. This is demonstrated in Chapter 5 of this

dissertation. The conclusion in Hoff et al 2005 is in agreement with our results for L_o phase membrane, though. For perylene, the angular intensity profile shows an interesting feature: the flattening of the peak intensity profile compared to naphthopyrene and terrylene. It appears as if there are actually two poorly resolved peaks (Figure 2.6). This phenomenon could indicate two distinct orientational populations of the fluorophore in the membrane (Florine-Casteel 1990): one parallel to the membrane normal and one perpendicular to it. Two populations have been suggested previously for perylene (Zandvoort et al 1997).

2.6 CONCLUSIONS

A variety of fluorescent probes for lipid membranes have been characterized for their partitioning between L_o and L_d phases, with an emphasis on finding L_o phase probes. In general, headgroup labeled lipid analogs partitioned strongly into L_d phases; PAHs partitioned into L_o phases or showed equal phase partitioning; and probe partitioning was found to depend on both the characteristics of the fluorophore (i.e. size and molecular structure of polycyclic intercalating probes) and on the lipid composition and phase. That membrane fluorophore partitioning depends on the mixing ratio of the host lipids may be useful for quantitative studies on composition-dependent properties.

CHAPTER THREE: TEMPERATURE DEPENDENT PHASE BEHAVIOR IN GUV's[*]

3.1 INTRODUCTION

This chapter describes the temperature dependent phase behavior of the ternary mixture dioleoylphosphatidylcholine (DOPC), N-stearoyl-sphingomyelin (SSM), and cholesterol in GUV's. Both quasi-adiabatic and kinetic properties were examined using fluorescence microscopy. A ternary phase diagram was constructed on the basis of miscibility transitions observed using microscopy.

Unilamellar liposomes composed of ternary mixtures of lipids and cholesterol are the simplest systems in which to study temperature dependent phase behavior that still possess most of the physical and chemical characteristics of the outer plasma membrane when compared to other model membrane systems such as monolayers, supported bilayers, and multi-lamellar vesicles (Samsonov et al 2001, Veatch and Keller 2002 and 2003, Baumgart et al 2003 and 2005). The mixture of DOPC, SSM, and cholesterol was chosen to emphasize the extremes of immiscibility behavior as the lipids are very different structurally, though DOPC does not occur naturally in biological membranes: DOPC has two unsaturated bonds (one on each acyl chain) and a T_{CM} of –20°C (Clayden et al 1999), and SSM is fully saturated with a T_{CM} of 45°C (Maulik et al 1991) to 52.8°C (Shipley et al 1974, Barenholz et al 1976). The extreme difference in packing properties of the two lipids produces rich, optically resolvable physical behaviors in agreement with the arguments and observations outlined in Chapter 1 of this dissertation and previous studies of ternary systems (for example Veatch and Keller 2002 and 2003, Smith and Freed 2009). SSM was chosen over other sphingomyelins because it is a very abundant sphingomyelin found in the outer

[*] Portions of the material in this chapter will be submitted to Biochimca et Biophysica Acta by Morales-Penningston, J. Wu, E. R. Farkas, S. L. Goh, T. M. Konyakhina, W. W. Webb, and G. W. Feigenson and to Biophysical Journal by Farkas, E. R. and W. W. Webb.

plasma membranes of many cell types and in natural mixtures like brain sphingomyelin (Estep et al 1979).

3.2 MATERIALS AND METHODS

Giant vesicles were prepared from DOPC, SSM, and cholesterol (Avanti Polar Lipids, Inc., Alabaster, AL). The structures of the lipids are shown in Figure 3.1. The lipids were stored at –20°C and used without further purification. For dry lipids, stock solutions were prepared for each lipid by dissolving the lipid in chloroform. Otherwise, chloroform solutions were purchased directly. The overall concentrations of the stock solutions were determined using the phosphate assay techniques of the Feigenson lab (Kingsley and Feigenson 1979); the phosphate assay procedure described on the Avanti website was found to be highly unreliable due to the amount of liquid leftover after the washing step. The full protocol for the procedure is given in the appendix (Chapter 7) of this dissertation.

To construct a phase diagram, chloroform solutions containing the average compositions of a particular point on a ternary diagram were prepared by mixing the appropriate volumes of the stock solutions to obtain the lipid molar ratio at that point. Fluorescent dyes with phase-preferential partitioning (see Chapter 2) were added to these mixtures at 0.1 mole percent or less (0.05 mole percent or less for each dye). The head group labeled fluorescent dye N-Lissamine-Rhodamine-DPPE (LR-DPPE, Avanti Polar Lipids, Inc.) or, in a few cases, the water-soluble headgroup binding dye di-4-ANEPP-DHQ (Molecular Probes, Eugene, OR) were used to label the L_d phase, and the polycyclic aromatic hydrocarbons naphthopyrene or perylene (Sigma-Aldrich Corp., St. Louis, MO), or di-4-ANEPP-DHQ were used to label the L_o and gel phases. The structures of the dyes are shown in Figure 3.2.

3.2a ELECTROSWELLING: OLD PROCEDURE

Prior to the discovery of lipid breakdown induced by indium tin oxide (ITO)

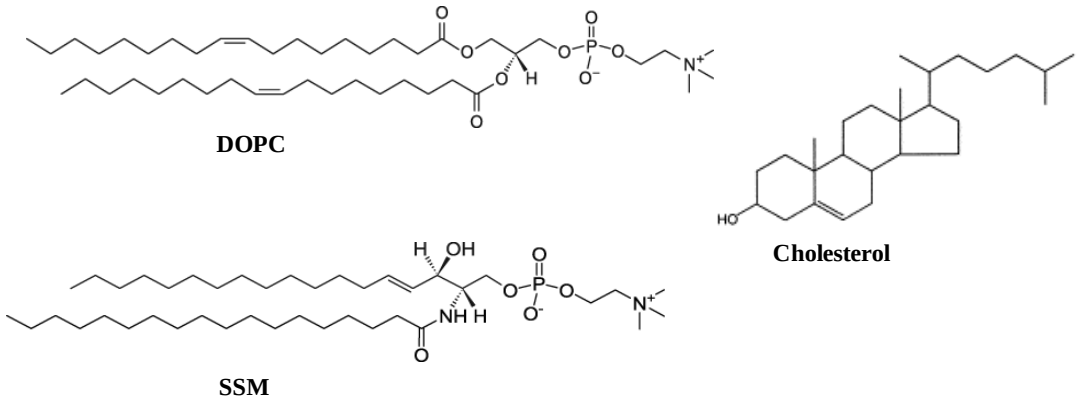

Figure 3.1 Lipids used in this study. Dioleoylphosphatidylcholine (DOPC), cholesterol, and N-stearoyl sphingomyelin (SSM).

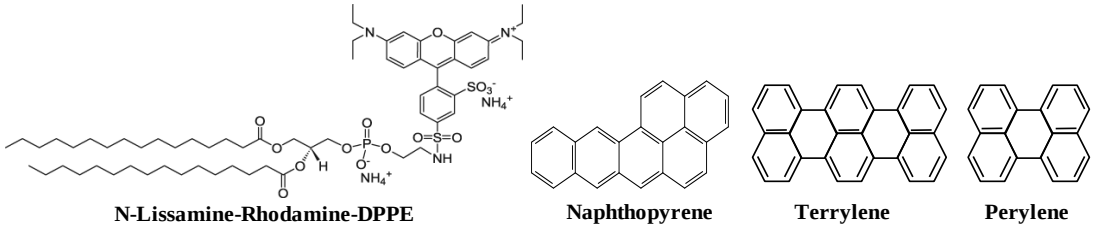

Figure 3.2 Fluorophores used in this study. Left to right: LR-DPPE (L_d phase), naptho[2,3-a]pyrene, terrylene, and perylene (L_o and gel phases).

and oxygen (Ayuyan and Cohen 2006), vesicles were prepared following the method of Angelova et al (1992) and Angelova and Dimitrov (1986). The final phase diagram was constructed using the modified electroswelling method found in Ayuyan and Cohen (2006). There are four main steps to conventional electroswelling, regarless of the electrode material: lipid film deposition onto the electrode, sovent evacuation from the lipid film, lipid film rehydration, and the application of an electric field to the hydrated lipid film. Briefly, ~100μL of the chloroform solutions containing dye and lipids at molar ratios of a particular point on the phase triangle are uniformly spread onto each conductive face of two identical ITO slides (4-8 ohm, Delta Technologies Ltd., Stillwater, MN). The slides were held at an elevated temperature of 60-65°C,

above the maximal observed main chain T_{CM} of SSM, 52.8°C to prevent phase separation upon deposition. It was observed that depositing films onto ITO at temperatures lower than 50°C led to more highly disperse distribution of area fractions of the two phases for given sample composition. The lipid-coated ITO slides were then placed in a vacuum chamber for no less than 3 hours and no more than 24 hours to evaporate any remaining chloroform. It is very important to get rid of any remaining chloroform, because chloroform is known to effect membrane fluidity and organization (Turkyilmaz et al 2009).

After the vacuum treatment, giant vesicles were produced by electroswelling (Angelova et al 1992 and 1986). The two lipid-coated conductive sides were placed to face each other, separated by a nitrile o-ring. The volume contained in the o-ring is filled with 100mM sucrose solution at 65-70°C prepared with Milli-Q (18.2 Mega ohms) water such that no air bubbles were present. This arrangement effectively forms a capacitor and is depicted in Figure 3.3. It is important that water used contain no transition metals, especially iron; iron has been known for many decades to act as a catalyst in lipid peroxidation at unsaturated bonds (Mozuraityte et al 2008). The capacitors were held at 65°C inside a custom-machined aluminum-block inserted into a dry temperature bath (Fisher Scientific, Pittsburg, PA). A sinusoidal AC electric

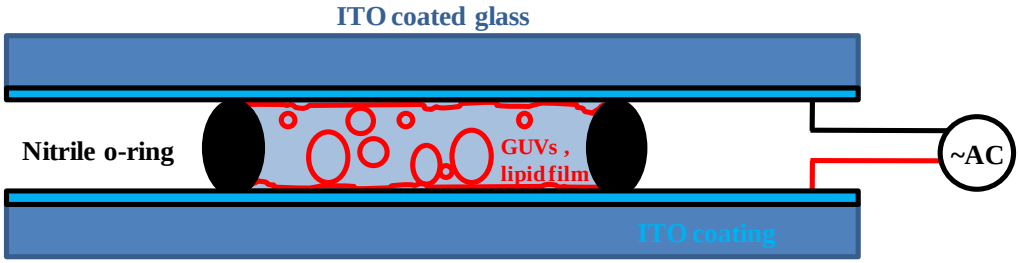

Figure 3.3 ITO electroswelling configuration. The conductive faces of two ITO slides (blue) are coated with a lipid film (red) which is dried down in a vacuum chamber. The film is then rehydrated in 100mM sucrose and electroswelled with AC voltage. The arrangement effectively forms a capacitor.

field (1.8Vpp, 5Hz) was applied across the two slides using a function generator. Vesicles form spontaneously after the addition of aqueous solution to lipid films, but it is believed by some that the alternating field causes them move, collide, and coalesce with one another to form "giant" (25-60μm diameter) vesicles (Angelova et al 1992, Mathivet et al 1996, Dimitrov and Angelova 1987); this is not clearly established, though. This hypothesis was qualitatively supported by observations in this study. A special chamber, depicted in Figure 3.4, was mounted over the inverted microscope such that the optical axis was parallel to the ITO surfaces and perpendicular to the direction of the applied field. Two ITO slides were adhered to a # 1.5 coverslip by the application of adhesive- backed silicone spacers and additional caulk around the silicone spacers. Warmed sucrose was injected through a small hole (dashed line in

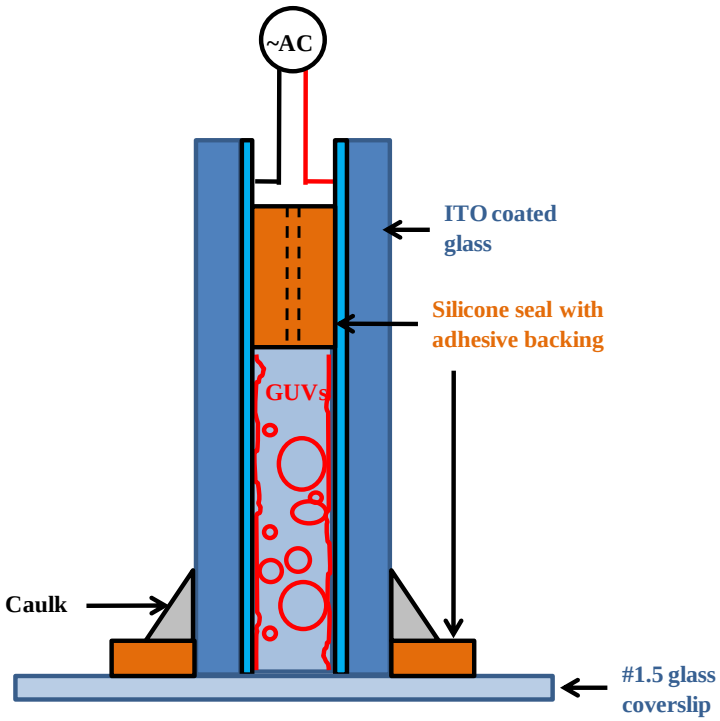

Figure 3.4 ITO electroswelling configuration for imaging. The hydrated lpid film for GUV preparation is viewed from below, through the #1.5 coverslip, using real time, widefield imaging. This allows one to observe how GUV's form and to collect data on the amplitude and frequency dependence of the GUV yields.

Figure 3.4) in the inner silicone spacer separating the two ITO slides. Vesicle formation was observed using widefield fluorescence imaging with an EMCCD camera (Andor Technology, South Windsor, CT).

The electroswelling of vesicles requires approximately 2 hours. The samples were then slowly cooled for roughly 30 hours to room temperature (22ºC). Slow cooling is necessary to avoid kinetic effects such as the super-cooling of a sample (Frolov et al 2006, de Ameida et al 2002, Laggner 1993). When a sample is quenched, or cooled instantaneously, phase separation may be artifactually hindered or trapped (Frolov et al 2006) in a metastable state. In the case of supercooling, this may lead one to misinterpret what should be a phase-separated region for a homogeneous one in the equilibrium phase diagram. To demonstrate this, vesicles of several compositions previously shown to display L_o-L_d coexistence were quenched to 22ºC in 2-3 hours and compared to vesicles of the same overall lipid molar ratios that were slowly cooled. In most cases, the quenched vesicles were either not phase separated at all, or displayed much greater dispersion in the area fractions of the two phases from vesicle to vesicle than the corresponding slowly cooled samples. For gel-L_d coexistence, the effect is even more pronounced. In fact, most researches using ternary GUV's containing a sphingolipid do not report any gel-L_d coextistence along the binary unsaturated lipid-sphinogolipid (no cholesterol) edge of the phase diagram. This is disussed further in section 3.3d of this chapter.

3.2b DISCUSSION OF CONTAMINANTS

There are three major types of chemical reactions that can alter the lipid composition and introduce impurities with respect to the GUV preparation and microscopy procedures: lipid hydrolysis in aqueous solution (Grit et al 1993); lipid peroxidation and oxidation (Geoffroy et al 2000,Tejero et al 2007, Fukuzawa et al 2006); and photo-induced chemical reactions that may include oxidation and

peroxidation (Ayuyan and Cohen 2006, Zhao et al 2007) and free-radical crosslinking.The products of each type of reaction are known to alter the membrane fluidity and phase behavior (Ayuyan and Cohen 2006, Zhao et al 2007, van Ginkel and Sevanian 1994, Busch et al 1998, Bruckner et al 2001, Mills and Needham 2005).The presence of these impurities will thus lead to misinterpretations of the phase behavior.

This is especially important near a miscibility critical point. Depending on the mobility of the impurity with respect to the relaxation time of a composition fluctuation, impurities may simply broaden the critical region by introducing multiple critical points, or they may actually renormalize the critical exponents (Voronel 1976, Anisimov 1975 and 1991). Impurities that reach equilibrium with the system within the measurement sampling time generally lead to a disappearance of the divergence of the thermodynamic quantity under study as well as an apparent shift in the critical temperature. This is depicted in Figure 3.5a[6] for the heat capacity of ethane to which various amounts of an n-heptane impurity were introduced. In such cases, the critical exponents describing these transitions must be renormalized. Impurities that do not reach equilibrium during the measurement time are known as frozen impurities, and lead to a broadening of the observed critical region. This is depicted in Figure 3.5b[7] for the heat capacity of air (Anisimov 1991).

Lipid hydrolysis

Lysolipids and free fatty acids (FFA) are the products of hydrolysis reactions that "split" a lipid at the glycerol backbone. They form in aqueous solution and thus

[6] Figure 3.5a is taken from Anisimov, M. A., E. E. Gorodetskii, and N. G. Shmakov (1973) Experimental verification of the isomorphism hypothesis of critical phenomena, *Soviet Physics JETP*, **36**, 1143-1150 and reproduced with permission. Copyright 1973 American Institute of Physics.
[7] Figure 3.5b is taken from Chashkin, Y. R., V. G. Gorbunova, and A. V. Voronel (1966) Influence of impurities on singularity of thermodynamic potential at liquid-vapor critical point, *Soviet Physics JETP*, **22**, 304-306, and reproduced with permission. Copyright 1966 American Institute of Physics.

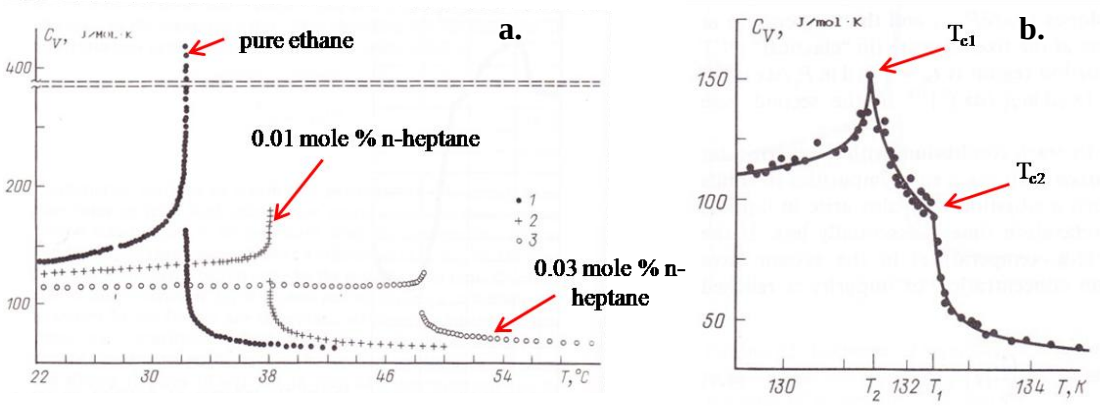

Figure 3.5 The effects of impurities. a) The effect of mobile (equilibrium) impurities on the heat capacity C_v of ethane: the left most curve is for pure ethane, the middle curve for 0.01 mole fraction n-heptane, and the rightmost curve for 0.03 mole fraction n-heptane. The location of the critical temperature appears to shift (Anisimov et al 1973 in Anisimov 1991). b) The effect of an immobile impurity on the heat capacity C_v of air near the critical temperature. Immobile, or "frozen-in", impurities lead to a broadening of the critical region (Chashkin et al 1966 in Anisimov 1991).

seem unavoidable in many methods used for GUV preparation, even under anaerobic conditions (Grit et al 1993). Lysolipids alter membrane fluidity due to their conical shape which allows them to stabilize regions of high curvature that may otherwise be energetically unfavorable in the membrane, such as pores (Mills and Needham 2005, Fuller and Rand 2001) and small domains (Maloney et al 1996). Far from a critical point or phase transition, the temperature dependence of lipid hydrolysis in a buffered solution is described by the Arhennius equation (Grit et al 1993). Thus, the lowest possible elevated temperature should be used in the rehydration step of GUV preparation. The reaction kinetics are pseudo-first order and are not dependent on cholesterol content (Grit et al 1993), but are highly dependent on the pH. The latter point is important with respect to the electrode material and applied voltage, as discussed in the next section, because electrode and/or water decomposition can alter the pH of the hydrating medium for the lipid films. Lysolpids and FFAs can be detected using TLC, provided there is enough material. In summary, the effect can be lessened by working at lowest allowable temperature and at neautral pH.

Photo-reactions

Another source of impurities are the reactions of the lipids or the lipid dyes mediated by exposure to light. Many of these reactions involve the production and subsequent reaction of singlet oxygen ($^1O_2$), though they may also be radical mediated (Stratton and Leibler 1997). In the former case, singlet oxygen is commonly produced by a sensitizing agent, often the fluorophore in microscopy and spectroscopy studies. Singlet oxygen is also implicated in many mechanisms of dye photobleaching (Burke et al 1996, Christ et al 2001).The hydroxyl radical is a common species associated with lipid degradation. It can be produced from water in the absence of oxygen by photochemistry in the presence of a sensitizing agent (fluorophore or another aromatic additive), by Fenton chemistry in the presence of iron or copper (Tejero et al 2005), or even by reactions of water with a glass surface (Narayanasamy and Kubicki 2005). The latter three are likely more important with respect to the electroswelling procedure than with imaging and will be discussed in section 3.2c.

There are a variety of products that can form from photo-induced reactions, including cross-linked lipids, cross linked dyes, lipid oxides, lipid hydroperoxides, and lipid malonaldehydes (MA), the product of lipid hydroperoxide breakdown. These impurities are important in a generic, or system-independent, sense with respect to critical exponents as discussed earlier and in Chapter 4 of this dissertation (Anisimov 1991). Impurities can also affect the observed phase behavior away from a critical point. For example, it has been shown that hydroperoxides reduce the interfacial tension in micellar solutions (Nuchi et al 2002), promote macroscopic phase separation in GUV's (Ayuyan and Cohen 2006), and result in aggregates of impurities in GUV's (Busch et al 1998). Hydroperoxides may also lead to an increase in the observed chain orientational order *S* (van Ginkle and Sevanian 1994) or a decrease in it (Drobnies et al 1999), depending on the specific products formed. Independent of

impurities, singlet oxygen-mediated reactions of the dyes lead to photobleaching (Burke et al 1996, Christ et al 2001), which obviously disrupts imaging experiments. This is especially important for experiments where fluorescence intensity is used to impart partitioning data and phase assignements.

Depending on the products of the reaction, there are several detection methods available. Lipid peroxides and hydroperoxides can be detected with TLC (Lasch et al 1998) or spectrophotometrically with the ferrous oxidation in xylenol orange (FOX) assay (Wolff 1994, Fukuzawa et al 2006, Ayuyan and Cohen 2006). The FOX is selective for hydroperoxides only. Fukuzawa et al (2006) recently extended the FOX analysis to distinguish the amount of product in two different phases in lipid bilayer membranes. MAs are spectrophotometrically detected with the thiobarbituric acid conjugation (TBA) assay. However, this assay is not specific for MA; it detects hydroperoxides as well (Wolff 1994). Cross-linked lipids and lipid-dye adducts can be detected with TLC.

To lessen the effects of $^1O_2$ mediated reactions, one can prepare the samples in anaerobic conditions and seal the samples used for imaging under argon or nitrogen, as the GUV's in the modified preparation procedure of this study were. Additionally, one can use an oxygen scavenging system (Sacconi et al 2006) or add an antioxidant to the aqueous solution such as DTT (Esposito et al 2007). A hydrophobic antioxidant such as tocopherol is not recommended for studies on phase behavior since these too may act as an impurity. Perhaps the best O_2 scavenger is the mitochondrial membrane (Bloom and Webb 1984). A useful system for future experiments where the membrane preparations must be exposed to atmosphere and thus O_2 may be to have the aqueous GUV sample surrounded by mitochondrial membrane suspension. The GUV's would be separated from the mitochondrial membrane fractions by a barrier permeable only to water and electrolytes. This would be most useful for experiments where direct

mechanical manipulation of the vesicles is desired such as pipette aspiration (Esposito et al 2007) or the patch excision experiments described in Chapter 6 of this dissertation. Because lipid oxidation and peroxidation can be radical mediated or singlet oxygen mediated (Stratton and Leibler 1997), O_2-independent pathways must not be neglected. All solutions should be purified so that no transitions metals, especially iron and copper, are present. A chelator such as EDTA may be added as well.

In these experiments, it was observed that 2-photon illumination eliminated or greatly slowed two particular types of photo-effects. These effects were incurred upon exposure to intense light from an arc lamp, in the presence of fluorophores and oxygen. The first effect involved irreversible shape changes. When flaccid, phase separated vesicles were exposed to light during wide-field illumination, they tended to become more tense and adopt a spherical shape, as depicted in Figure 3.6. This effect occurred in vesicles containing intercalating PAH probes (perylene or naphthopyrene, at 405nm excitation) as well as in vesicles containing only a headgroup-labeled probe (LR-DPPE, at 568nm excitation). A similar phenomenon has been reported in Bruckner et al (2001) for intercalating probes and was attributed there to a transient change in the bending elasticity caused by the formation of excimers of the pyrene dye they used as a label. However, in the present case, the sphericalization was irreversible on a much longer time scale (hours) than observed in Bruckner et al (2001) (minutes), and thus could be indicative of chemical changes (Esposito et al 2007); these experiments should be revisted using mass spectrometery or other methods to screen the illuminated material for products of a chemical reaction.

The second type of photo-effect involved changes in the observed miscibility transition temperatures, and was especially prevalent in vesicles that had undergone sphericalization. When a vesicle was imaged using wide-field microscopy and

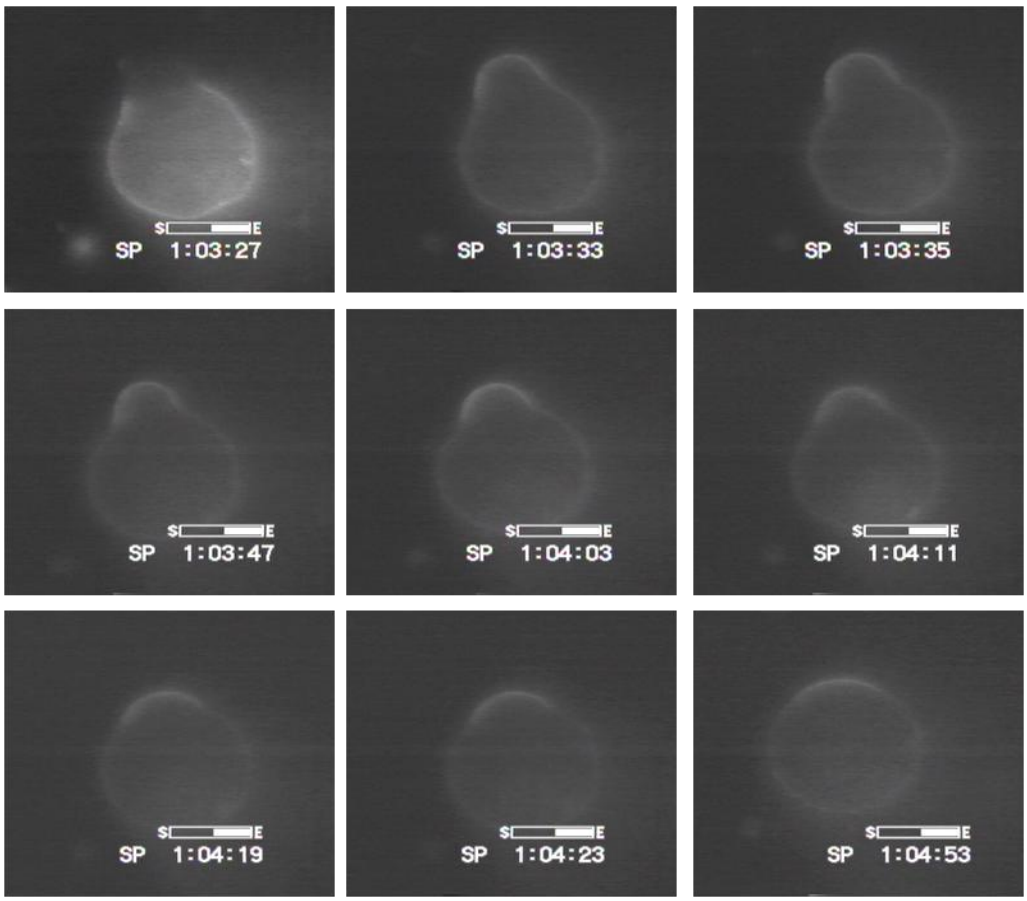

Figure 3.6 Shape changes induced by one-photon illumination. The upper left panel depicts a flaccid GUV under 568nm illumination (LR-DPPE fluorescence). All other panels depict 405nm illumination and the corresponding fluorescence of perylene. After one minute and twenty seconds of intense 405nm illumination, the vesicle changes shape and becomes more rigid. This sort of transformation was also associated with an increase in the observed miscibility transition temperature, T_M.

subjected to successive heating and cooling cycles, the observed miscibility temperature appeared to increase with time. This maybe due to light-induced L_o-like domain formation, similar to that reported in Zhao et al (2007). This was not the case with two-photon illumination, though, even with similar exposure times. Samples were checked for light-induced domain formation by the method described in 3.2d.

3.2c MODIFIED ELECTROSWELLING PROCEDURE

The wrong choice of voltage or electrode material can lead to both lipid

hydrolysis and to oxidation reactions, even under anaerobic conditions. The kinetics of lipid hydrolysis in lamellar lipid systems are strongly dependent on pH, with the lowest rate near neutral, pH=7 (Grit et al 1993). This is one of the reasons why the electrode material and the applied voltage in the electroswelling procedure are so important: the wrong material or wrong voltage will hydrolyze water, releasing H+ and OH- into the solution and facilitating the degradation of the lipids by hydrolysis. In addition to hydrolysis, electrode decomposition can result in lipid peroxidation (Ayuyan and Cohen). Ayuyan and Cohen (2006) found ITO to be inherently unstable at the voltages normally applied in electroswelling (1.4 to 2 Vpp). The products of hydrolysis reactions can be detected by TLC. The modified electroswelling procedure lessened the amount of lysolipid but did not completely eliminate it, which is to be expected given the relative spontaneity of the reaction water (Grit et al 1993).

Alternatively, OH- ions may form radicals that oxidize the lipids, adding additional impurities (Tejero et al 2007). The amount of oxidation and peroxidation can be lessened by modifying the electroswelling procedure to either include a buffer, which has only been recently reported (Pott et al 2008), or to modify the electrode material to something non-reactive and electroswell under anaerobic conditions (Ayuyan and Cohen 2006).

In the modified electroswelling procedure, ~90 µL of the chloroform solutions of dye and lipids are uniformly spread onto each face of two identical titanium plates (McMaster-Carr, Sante Fe Springs, CA) coated in oxide (TiO_2), under a dry nitrogen stream. Titanium was chosen due to its less reactive properties in solution compared to the ITO slides; Ayuyan and Cohen (2006) found that ITO led to the formation of lipid peroxides even in the absence of applied voltage or dissolved oxygen. The slides were separated by a Teflon spacer and the aqueous chamber was sealed by o-rings as depicted in Figure 3.7. All steps subsequent to the solvent vacuuming, such as the

addition of warm sucrose solution and electroswelling, were carried out in a nitrogen glovebox (Electrotech Systems, Glenside, PA). The components of the glovebox are depicted in Figure 3.8. Oxygen content was monitored using a Clark electrode (Diamond General Development Corp., Ann Arbor, MI) calibrated in sterile 0.9% (w/v) NaCl solution.The sucrose solution was sparged with dry nitrogen for 20 minutes prior to use. A glass frit was used for bubbling instead of stainless steel to prevent any iron from entering the solution, because iron is known to catalyze the oxidation of lipids at unsaturated elements (Mozuraityte et al 2008). Electroswelling took place using 8 to 10 Hz AC voltage at 1.2 Vpp. The lower voltage was deemed necessary to avoid hydrolysis of water and dissolution of titanium ions. According to the Pourbaix diagram of titanium metal (Wulfsberg 2000), at higher voltages titanium metal becomes solubilized and can transfer electrons, which results in chemical reactions with the lipids. Known passivating layers include TiO_2, Nb_2O_5, and ZrO_2.

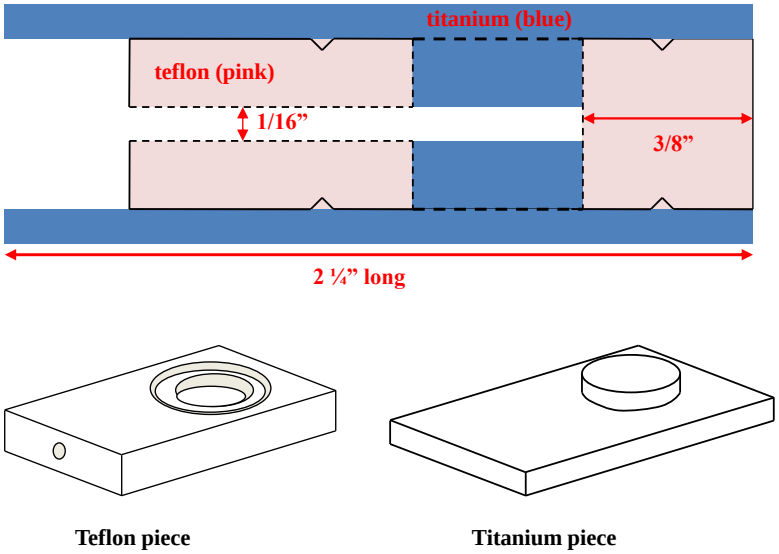

Figure 3.7 Titanium plate electroswelling configuration. Above: a side view of the titanium plate electrodes (blue) and the corresponding Teflon spacer (pink). The bore hole is included so that sucrose solution can be added to the assembly via syringe. Bottom left: Teflon spacer. Note the grove for the o-ring. Bottom right: titanium plate geometry. Lipid films are deposited on the raised portion. Two titanium pieces per Teflon piece are used in the final assembly.

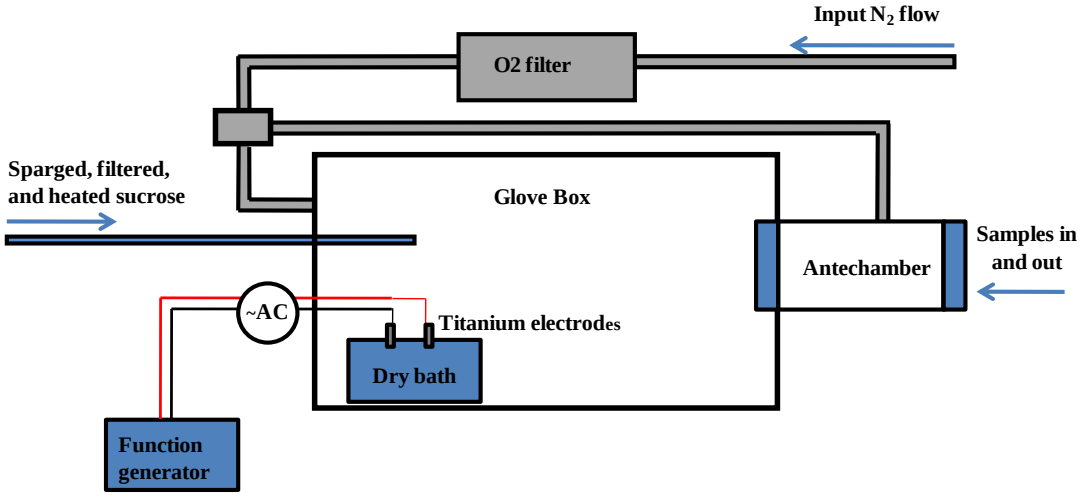

Figure 3.8 Glovebox diagram. The major components and basic set-up of the anaerobic chamber used to prepare GUV's are depicted. The sample enters through the antechamber (right) to minimize O_2 introduction into the main chamber. Sparged and heated sucrose solution enters via tubing through a custom bored hole in the glove box plexiglass, and the leads to the function generator used in electroswelling also enter through a custom bored hole. GUV samples for imaging are made in the glovebox to ensure that minimal O_2 is dissolved in the solutions and thus minimize singlet oxygen reactions upon illumination.

It was observed that the L_o-L_d boundary of the DOPC/SSM/cholesterol phase diagram shifted depending on the preparation procedure. For samples with SSM >30 percent, the procedure appeared to amke little difference, but for high-DOPC, low-SSM samples, the phase boundary effectively shrunk by shifting toward the right (higher SSM) for the samples prepared in anaerobic conditions on titanium versus those prepared in the presence of O_2 on ITO. Thus, electroswelling in the presence of O_2 with ITO as the electrode effectively leads to a falsely high percentage of L_o phase at low-SSM points, consistent with the results found in Ayuyan and Cohen (2006) and Zhao et al (2007). This is depicted in Figure 3.9. However, from these results, it is still not clear whether the ITO or O_2-mediated reactions are responsible. For samples that did not appear to have preparation-dependent area fraction or morphology, no detectable difference in T_M was observed in GUV's at a given composition prepared

by each method. There was qualitatively more lysolipid product in samples prepared on ITO in an oxygen-saturated environment than with those prepared on titanium as indicated by TLC.

It is important to note that impurities at concentrations undetectable by TLC, imaging, and the reproducibility of miscibility transitions may still be extremely important in the vicinity of a critical point. Compositional impurities may lead to a falsely large broadening of the critical region or a shift in its location depending on whether or not the impurity reaches equilibrium with its surroundings. Details can be found in Chapter 4 of this dissertation.

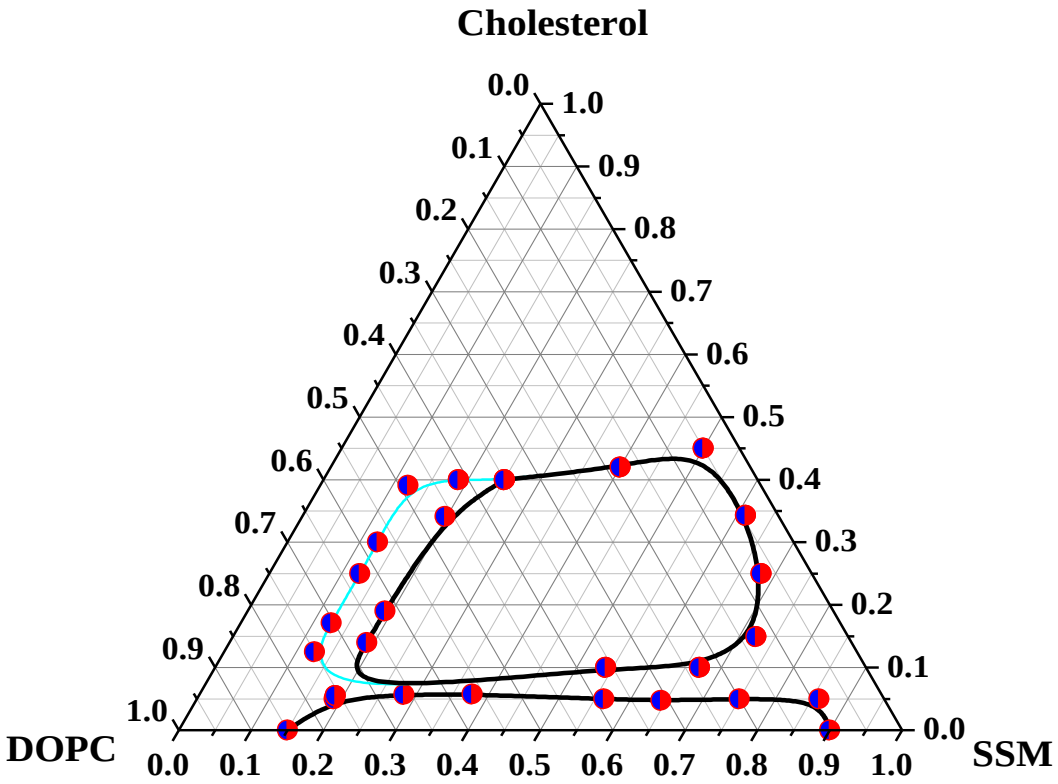

Figure 3.9 L_o-L_d phase boundary shift at 22°C. The coexistence region for samples prepared using ITO as the electrodes are denoted by the blue line, which encloses a larger miscibility gap than that of the sample prepared in anaerobic conditions on titanium. The L_d-gel coexistence depicted in the diagram refers only to sample prepared under anaerobic conditions on titanium.

3.2d IMAGING

The samples were imaged using both wide field and two-photon fluorescence microscopies, with each method using the same inverted Zeiss Axiovert 135 microscope. The two-photon apparatus is depicted in Figure 3.10. Equilibrium studies, such as observing the area fractions of different phases on GUV's at different temperatures during very slow heating and cooling cycles, were implememted using two-photon microscopy. Kinetic, or time-dependent, studies such as observing phase evolution following a temperature quench, were implemented using wide-field microscopy. Kinetic studies are the subject of section 3.3d of this chapter, but wide-field imaging was otherwise avoided because of the possibility of more rapid photo-reactions described in section 3.2b. The main reason why kinetic studies must employ wide field imaging is speed: the piezo scanners in the commercial scanbox (Biorad MRC 600) used for two-photon imaging are too slow to capture image sequences in real time at a high frame rates.

When wide field imaging was necessary, LR-DPPE was visualized by illumination with the 568nm line selected from a mercury arc lamp, and fluorescent emission collected between 580-620nm. Perylene and naphthopyrene were illuminated at 405nm and fluorescence collected at 460-495nm. Images were collected using an ICCD camera (Stanford Photonics) and processed using EPIX XCAP software, or with an EMCCD (Andor Technologies) and processed with Andor IQ software. For two-photon imaging, an excitation wavelength of 780nm was used to illuminate both probes simultaneously, and images were collected using a BioRad MRC 600 scanning system (Bio-Rad, Richmond, CA) operating in the non-descanned mode with external GaAsP PMT's (Hamamatsu**,** Middlesex, NJ).

The details of the temperature-control set-up and operation are discussed in Chapter 4 of this dissertation. For temperature-controlled imaging, the samples were

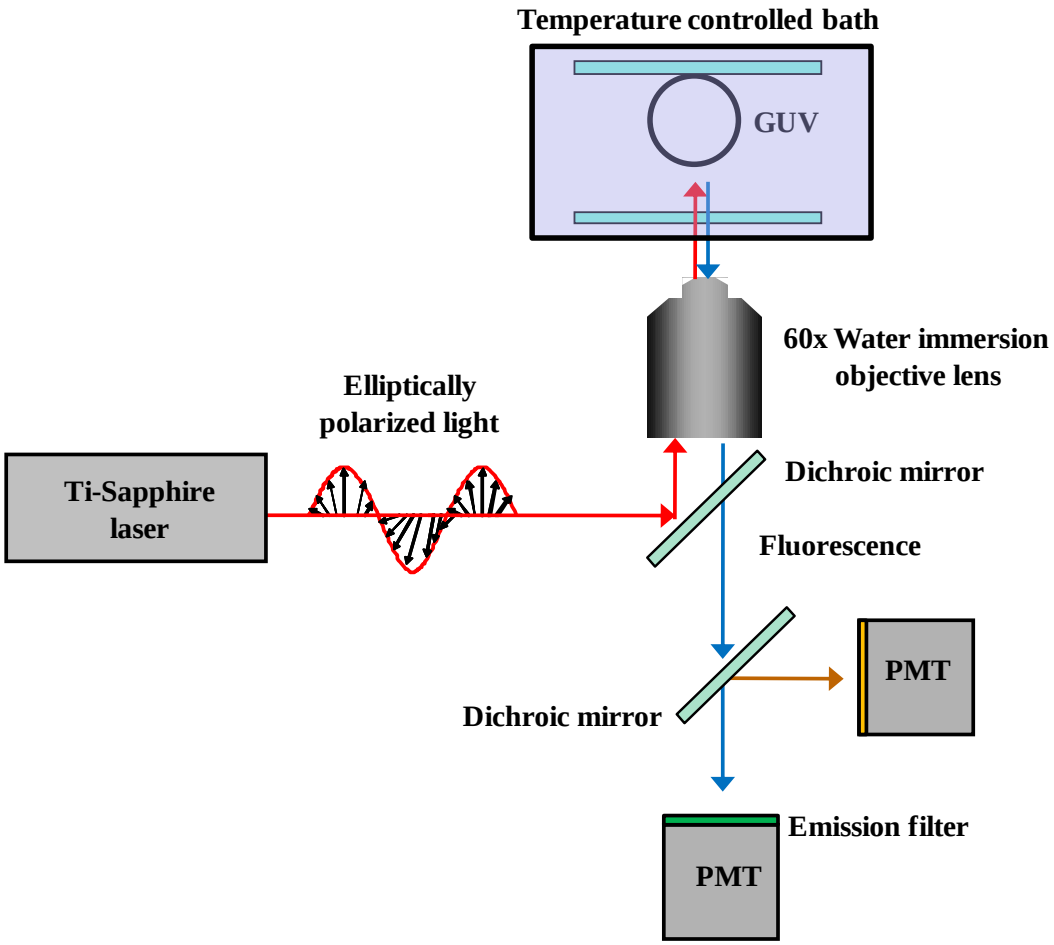

Figure 3.10 Temperature-controlled two-photon microscopy apparatus. GUV's are illuminated by 780nm light and fluorescence is collected in the epi-direction by non-descanned PMTs. Mirrors mounted on piezo-scanners inside a scanbox (not shown, Biorad MRC 600) raster scan the excitation light across the sample. Resulting fluorescence is collected by PMTs external to the scanbox and this light does not pass back to the scan mirrors ("non-descanned"). Details of the temperature chambers can be found in Chapter 4 of this dissertation.

prepared by adding 6µL - 8 µL of the GUV solution (100mM sucrose) to an area (~0.9cm diameter) on a # 1.0 round coverslip surrounded by Fomblin VAC-3 perfluorinated vacuum grease (Ausimont, Bollate, Italy). Another # 1.0 round coverslip was placed on top and pressed down until no air bubbles were visible; the sides of the sample were then sealed with water-proof enamel. Unless otherwise noted, 2µL - 3µL of DI water was added to create an osmotic pressure that would swell the

GUV's to a spherical shape. This helps to prevent 3-d deformation and domain budding of the GUV's that may lead one to misinterpret the phase behavior; it has its own caveats, though, such as the ordering effects of both the sugar on the headgroup and the outward pressure on the acyl chain order.

Miscibility transition determination

All imaging used to determine miscibility transitions was done using the two-photon apparatus. To determine the miscibility transition temperature for a given composition on the phase diagram, vesicles were initially heated and cooled at 0.25°C/minute using the slowest automated ramp rates of the external heaters. The initial heating and cooling cycle was performed at this rate to determine an approximate range for the miscibility temperature. After this was determined, the samples were heated and cooled at a rate no faster than 0.01°C/minute using the manual operation of the external bath or heater. Samples were heated and cooled at least twice. The set of temperatures from the faster heating and cooling scans were not used to compute the average miscibility transition temperatures. For each composition point, at least two separate vesicle preparations were used, prepared from two different sets of lipid stock solutions, and at least three vesicles per preparation were observed.

To check for irregularities due to photo-induced reactions of the dyes or the lipids (Zhao et al 2007), a few composition points well within a roughly determined L_o-L_d coexistence region at 22ºC were chosen from those where miscibility transitions had already been determined . These samples were heated to temperatures just above the miscibility transition temperatures (by 1-2ºC), but without any prior imaging or exposure to light other than the initial exposure required to set the objective height such that the sample was in focus. These samples were imaged in two-photon mode. In almost all cases, the samples were homogeneous above the reported miscibility transition temperatures, suggesting that the original phase separation was likely not

light-induced, or at least that any light induced phase separation did not significantly alter the miscibility behavior. The methods is not fool-proof, though, if the "control" miscibility temperature was falsely high to begin with due to light-induced effects.

Area fractions

L_o area fractions were determined using the method described in the appendix of this dissertation (Chapter 7). In this method, equatorial slices of GUV's with only two domains are used. This method is only accurate if the plane separating the two phases is parallel to the optical axis and if there are only two liquid domains. This method does not work for L_d-gel coexistence or for L_o-L_d coexistence with more than two phase domains.

3.3 RESULTS AND DISCUSSION

3.3a PHASE DIAGRAM

The temperature-dependent, quasi-ternary phase diagram is depicted in Figure 3.11a. The samples used to prepare this diagram were all made under anaerobic conditions. Sample points displaying two-phase coexistence are colored blue (L_o-L_d) and red (L_d-gel); sample points appearing optically homogeneous are black; and sample points displaying certain behaviors indicative of three-phase coexistence are green. These behaviors are delineated in the next section. The colored contours indicate the miscibility transition temperatures of the compositions inside the miscibility gaps (solid lines). The phase boundaries at 22°C are where the colored region ends. The L_o-L_d coexistence region extends very close to the SSM-cholesterol binary axis. Temperature measurements were not recorded in the region of < 5 mole % DOPC because the L_d domains consistently bulged outward and budded off of the parent vesicles, even with osmotic swelling of the GUV's. Thus, the right (high SSM) side of the miscibility gap for L_o-L_d coexistence at 22°C depicted in Figure 3.11a is not very accurate. The three-phase region is denoted by the triangle circumscribed by

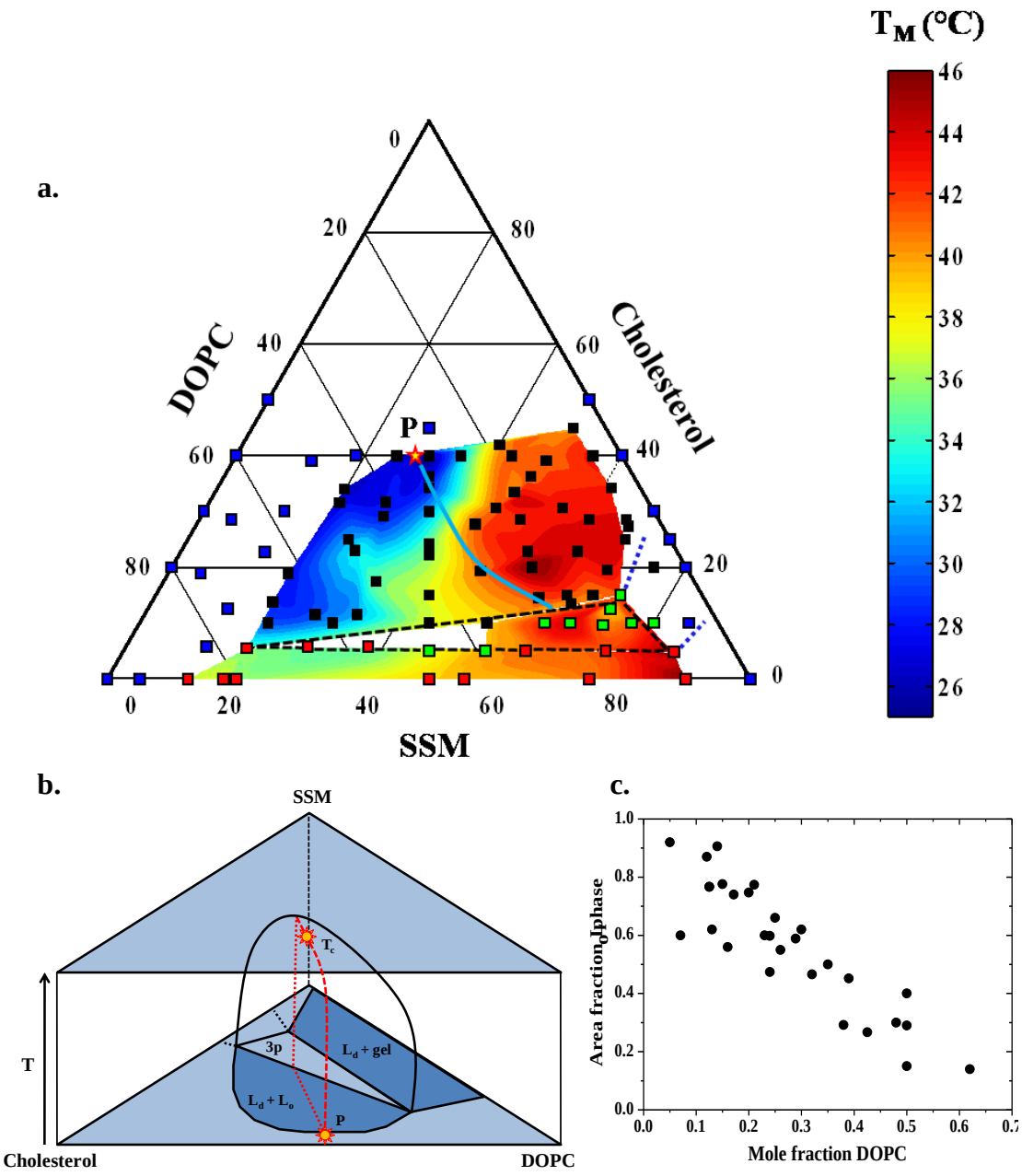

Figure 3.11 Temperature-dependent ternary diagram for cholesterol/ SSM/DOPC. a) Ternary diagram. Color denotes miscibility transition temperatures as indicated by the scale to the right, and the coexistence boundaries for the colored regions are for 22°C. Blue points refer to one-phase samples at 22°C, black points to L_o-L_d coexistence at 22°C, red points to gel-L_d coexistence at 22°C, and green points to 3-phase samples at 22°C, as observed using two-photon microscopy. "*P*" and the red star denote the plait point. b) A schematic of the L_o-L_d coexistence region with the line of critical points (red) extending from the plait point at 22°C to the upper critical point T_c. c) Area fraction L_o phase versus mole fraction DOPC for L_o-L_d region.

the black dashed line. The dashed blue lines indicate the two-phase region of L_o-gel coexistence that theoretically must be present (Kim and Fisher 2002) but was not directly or unambiguously observed using optical microscopy. Note that this region does not have to touch the binary cholesterol-SSM axis as drawn; in theory, it could instead form a closed loop without touching a binary axis, like the L_o-L_d coexistence region at 22°C. The extensions of the coexistence regions appear to obey Schreinemaker's rules. Figure 3.11b depicts a 3-d view of the L_o-L**d** coexistence region, with temperature as the third axis. Note that in theis figure, the composition axes are rotated with respect to Figure 3.11a. The area fraction of the L_o phase decreased linearly with DOPC mole fraction, but did not seem correlated with the other two components (Figure 3.11c).

The solid light blue line in Figure 3.11a corresponds to the approximate location of the 50/50 L_o-L_d area fraction line at 22°C: to the left (higher DOPC) of this line, the majority (or continuous) phase was the L_d phase, and to the right of the line the majority phase was the L_o phase. The location of the L_o-L_d plait point, *P*, at 22°C corresponds roughly to the composition cholesterol/SSM/DOPC = 0.40/0.28/0.32 and is denoted by the red star in Figure 3.11a. It should be noted that a plait point in this context refers to a critical point with respect to composition at some fixed temperature lower than that of the consolute, or upper critical, point temperature. The compositions identified as plait points at different temperatures exhibited violent fluctuations of the phase boundary, indicating a minimal line tension in comparison to the other compositions. The phases also exhibited much weaker dye preferences, suggesting that the partition coefficients were very similar, as expected for a critical point (Widom 1967). These observations are depicted in Figure 3.12.The plait point is just one point in a line of critical points in which this sort of behavior was observed, as depicted in Figure 3.11b by the red dashed line on the outside of the coexistence

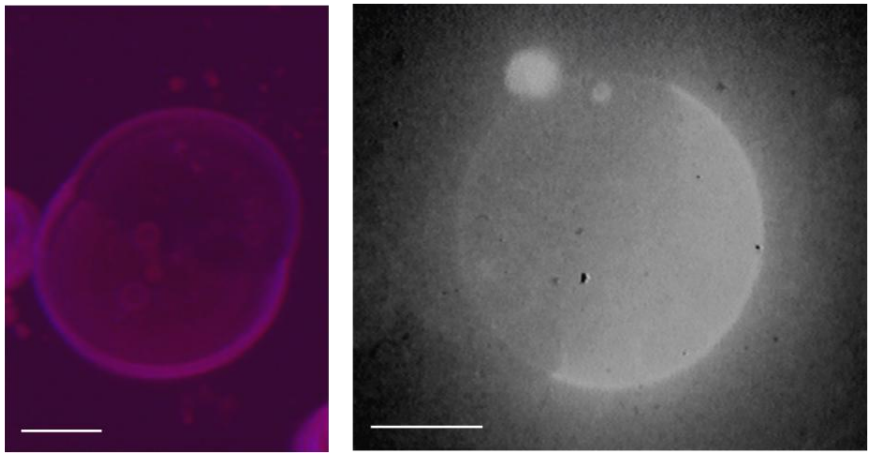

Figure 3.12 Plait point identification. Left: cholesterol/SSM/DOPC = 0.20/0.38/0.42 at *T* = 36°C. Right: cholesterol/SSM/DOPC = 0.40/0.28/0.32 at *T* = 22°C. The left image was produced using two-photon imaging with naphthopyrene and LR-DPPE fluorescence excited at 780nm. The right image is a wide field image and depicts LR-DPPE excited by the 568nm line of a mercury arc lamp. These critical points displayed similar partitioning of the dyes and fluctuations of the interface. Scale bars are 10μm.

surface. The composition with the highest upper miscibility transition temperature was determined to be the critical point of this system, and occurred at composition cholesterol/ SSM/DOPC = 0.20/ 0.56/0.24. The critical temperature was 46.0 ± 1.5°C.

3.3 b PHASES

L_o – L_d and L_d-gel coexistence

The typical domain topology and phase coexistence of the phases observed in this system are shown in Figure 3.13. Blue false color corresponds to naphthopyrene fluorescence, and thus the ordered phases (L_o and gel), and red false color corresponds to LR-DPPE fluorescence and thus the disordered phase (L_d) unless otherwise noted. For L_o-L_d coexistence, GUV's typically separated completely into two large domains after the thirty hour cooling period. Dark stringy domains that exclude both labels were demarcated as gel phase. In the literature, L_o and gel domains are typically distinguished from one another by their morphologies and behavior (Korlach et al 1999): the gel phases have elongated and rigid domains, while the fluid L_o domains

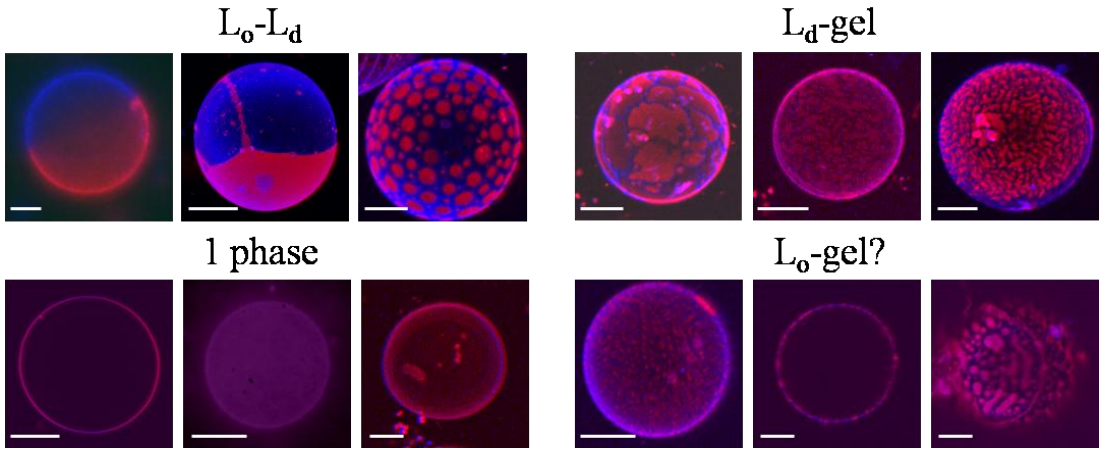

Figure 3.13 Typical morphology of two-phase and homogeneous vesicles. Compositions in cholesterol/SSM/DOPC, top (left to right): 0.32/0.20/0.48, 0.28/0.43/0.29, 0.20/0.56/0.24, 0.05/0.56/0.39, 0.00/0.50/0.50, 0.05/0.62/0.33; bottom (left to right): 0.30/0.12/0.58, 0.45/0.275/0.275, 0.10/0.85/0.05, 0.20/0.75/0.05, 0.25/0.68/0.07, and 0.25/0.68/0.07 up close. Excitation: 780nm, red: LR-DPPE (L_d phase), blue: naphthopyrene (L_o and gel phases). Scale bars are approximately 10μm.

are round and deformable. Fluid domains generally deform and merge upon collision with each other while gel domains do not. However, at certain compositions with a high SSM content, approximately >40 mole %, and low cholesterol content, between 5 and 10 mole %, naphthopyrene also labeled what appeared to be a gel phase morphologically; this phase could be a very viscous L_o phase as well. This behavior typically occurred in what was designated the three-phase coexistence region, which is discussed in more detail below.

For some compositions at high SSM content (>60 mole %) in the L_o-L_d coexistence region, a persistent hexagonal structure was observed (Figure 3.14). The minority phase domains usually coalesced such that two large liquid domains appeared after a few hours or days, upon heating, or upon additional osmotic swelling. These compositions always lie near the 50/50 area fraction line on the phase diagram (Figure 3.11, blue line) or in what was designated to be the three-phase region (green markers in Figure 3.11).

Three-phase coexistence

The three-phase region in Figure 3.11a was indirectly inferred for *most* of the samples contained within it; only three compositions definitively displayed three different phases simultaneously present on a particular GUV and these are depicted in Figure 3.15. With the microscopy apparatus employed in this research, three phase coexistence is observed as three different colors or three different intensities. In this sense it may be difficult to definitively assign a third fluorescence signature to a separate phase without a third dye with partitioning preference for that phase; one could argue that such a phaseis actually a wetting layer for a very viscous phase or some other non-equilibrium structure. Vesicles with compositions inside the three phase region more often displayed three different morphologies, but with only two coexisting on any given vesicle: either gel and L_d or L_o and L_d. This is depicted in Figure 3.16: some vesicles were homogeneous, some had elongated gel domains coexisting with L_d, and some had round deformable domains. At least three preparations from three different sets of stock solutions were used to verify these findings.

Another indication of a three-phase region was the observation of two different phase transitions; this is described in detail in section 3.3b. This behavior is akin to the vanishing of two menisci in a three phase fluid system at two different tempertures,

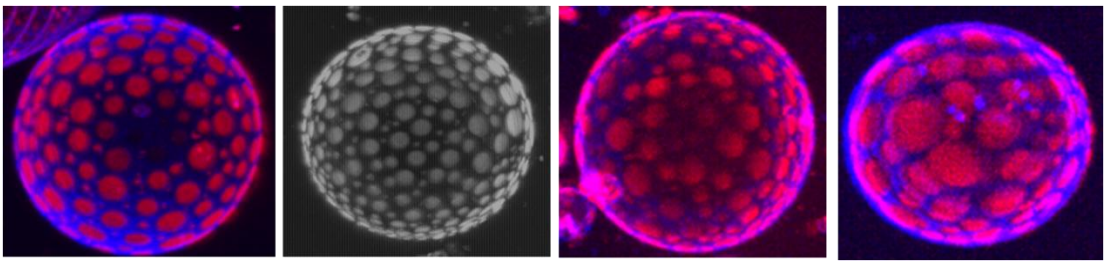

Figure 3.14 Samples with hexagonal packing. Compositions in cholesterol/ SSM/DOPC (left to right): 0.20/0.56/0.24, 0.15/0.64/0.21, 0.10/0.67/0.23, and 0.14/0.65/0.21. All of the samples lie near the 50/50 area fraction line depicted in Figure 3.11a.

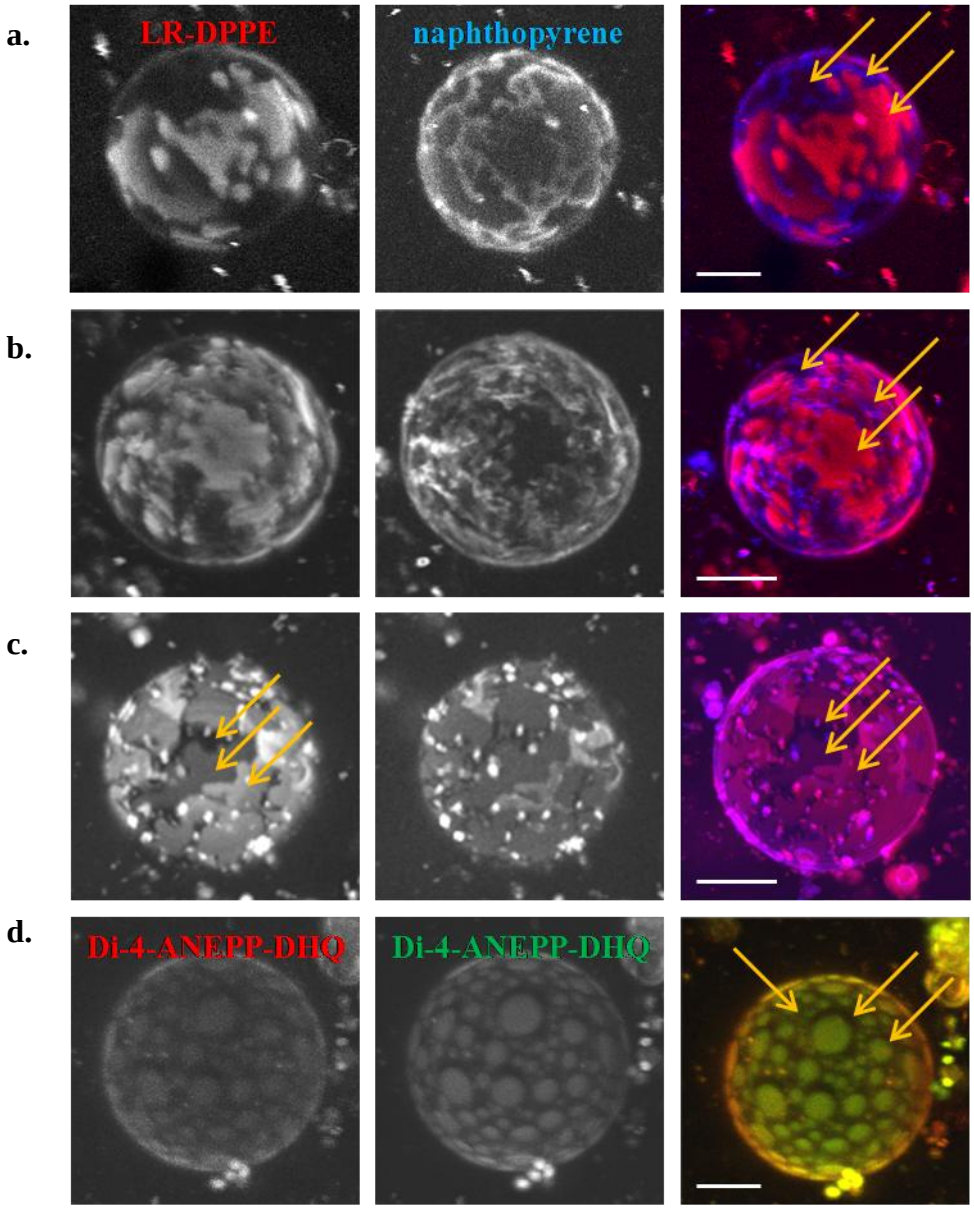

Figure 3.15 Three-phase coexistence: three-phase coexistence on the same vesicle. Cholesterol/SSM/DOPC = (a) to (b) 0.05/0.475/0.475 for all three; (c) 0.05/0.56/0.39; and (d) 0.10/0.80/0.10. All vesicles show three different intensities or colors, indicative of three phases. Vesicles with blue and red false coloring are labeled with LR-DPPE (left panel) and naphthopyrene (right panel) both excited by 780nm light. The arrows in the upper right composite image composed of fluorescence from the two channels point to the three different phases. The vesicle in the lower series (e) showing green fluorescence was labeled with di-4-ANEPP-DHQ (488nm excitation, 1-photon excitation). Di-4-ANEPP-DHQ emits at different wavelengths depending on the cholesterol content and hydration of a phase (Jin et al 2005). Scale bars are 15μm.

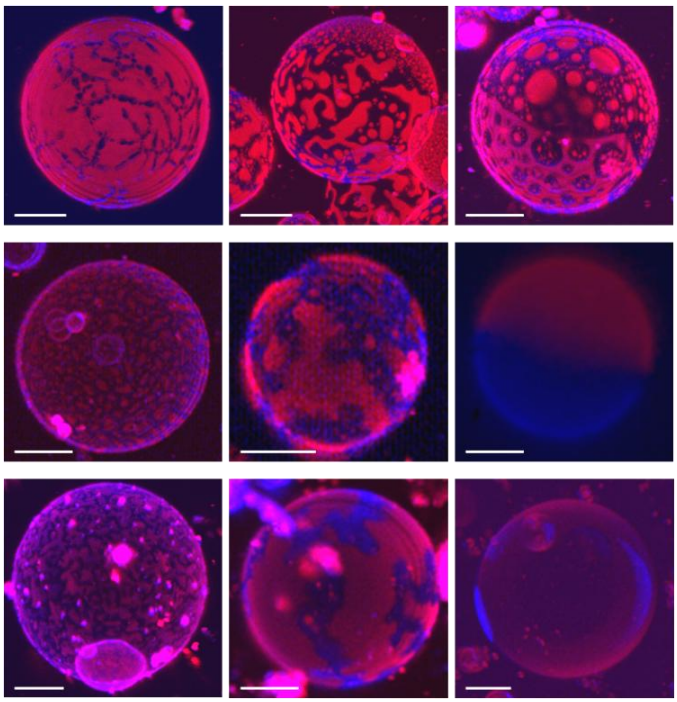

Figure 3.16 Three-phase coexistence: three-phase coexistence in the same sample. Top and middle rows: cholesterol/SSM/DOPC = 0.10/0.63/0.27 (all three), bottom row: cholesterol/SSM/DOPC = 0.05/0.475/0.475 (all three). For all three rows, the left and middle images depict gel (or very viscous L_o) coexistence with L_d, and the right image depicts normal L_o-L_d coexistence. All vesicles are labeled with LR-DPPE and naphthopyrene and imaged using two-photon excitation at 780nm. Scale bars are 12μm.

something quite common unless one actually reaches a tricritical point (Hankey 1974, Griffiths and Widom 1973). The latter scenario is unlikely in the closed vesicle system for reasons discussed in the next section (3.3b). Discrepancies with published phase diagrams for SM/DOPC/cholesterol systems (Veatch and Keller 2005, Smith and Freed 2009) in the extent of the of the three phase region or in the lower bound of the L_o-L_d coexistence region at 22°C depicted in Figure 3.11a may due to the presenc of fluorescent probes, the fact that optical microscopy cannot distinguish nanodomains less than roughly 300nm in size (Feigenson and Buboltz 2001), and/or the fact that the published results were obtained from different techniques using model systems that included multilamellar vesicles (MLV's) or small unilamellar vesicles (SUV's) which may not produce exactly the same phase behavior as GUV's.

If compositions along the binary SM-cholesterol axis produce domains in the gel-L_o coexistence region, these regions have been shown to be below the resolution of optical microscopy (<300nm) by methods including NMR and ESR. The polarization data in Chapter 5 of this dissertation may support sub-resolution phase separation on the binary SM-cholesterol axis: an isothermal plot of chain order parameter versus cholesterol content yields a peaked feature which may correspond to two coexisting populations with the same order parameter.

3.3b MISCIBILITY TRANSITIONS

The phase diagram in Figure 3.11 was produced by observing temperature- and composition-dependent miscibility transitions. The experimental deviations in transition temperatures for a given average composition ranged from 0.8°C to 5°C; a higher degree of variation in the observed T_M's for a given composition was observed with increasing SSM content and with decreasing cholesterol content and was thus especially prevalent in vesicles containing a gel phase. These variations may be due to slight differences in the vesicle compositions within a given sample, to thermal gradients in the sample chamber, or to kinetic effects. The latter are especially important in vesicles where the phases have a markedly different viscosity.

Examples of the behavior observed during a miscibility transition between L_o and L_d domains are depicted in Figure 3.17. For samples to the left of the 50/50 area fraction line (Figure 3.11, blue line), the majority phase was the L_d phase (red) and the area fraction of the L_d phase gradually increased as the temperature was raised. For samples to the right of this line, the majority phase was the L_o phase (blue) and fraction of the L_d phase gradually decreased as the temperature was raised.

The gradual decrease in the area fraction of one of the two phases as observed was not observed for the plait points or the upper miscibility critical point of the L_o-L_d coexistence region once a 50/50 area fraction was obtained. At this point, the area

fraction remained roughly constant at 50/50 and the phases appeared to blur together as the transition temperature was approached from below. Occasionally during a cooling cycle, morphology similar to that expected in spinodal decomposition for an Ising-like system was observed (Honerkamp-Smith et al 2008, Veatch et al 2007). An example of this is depicted in the rightmost panel of the middle series of images in Figure 3.17. This did not occur frequently within samples at this composition, though. More often, small round domains appeared and grew by accretion and then collision with other domains. An example of a L_d-gel transition is shown in Figure 3.18. In general, the hysteresis for L_d-gel transitions was much larger than for L_o-L_d transitions, usually falling around 3-5°C.

Overall, the transition temperatures increased with increasing SSM content for both L_o-L_d and L_d-gel coexistence regions (left to right in Figure 3.11). Transition

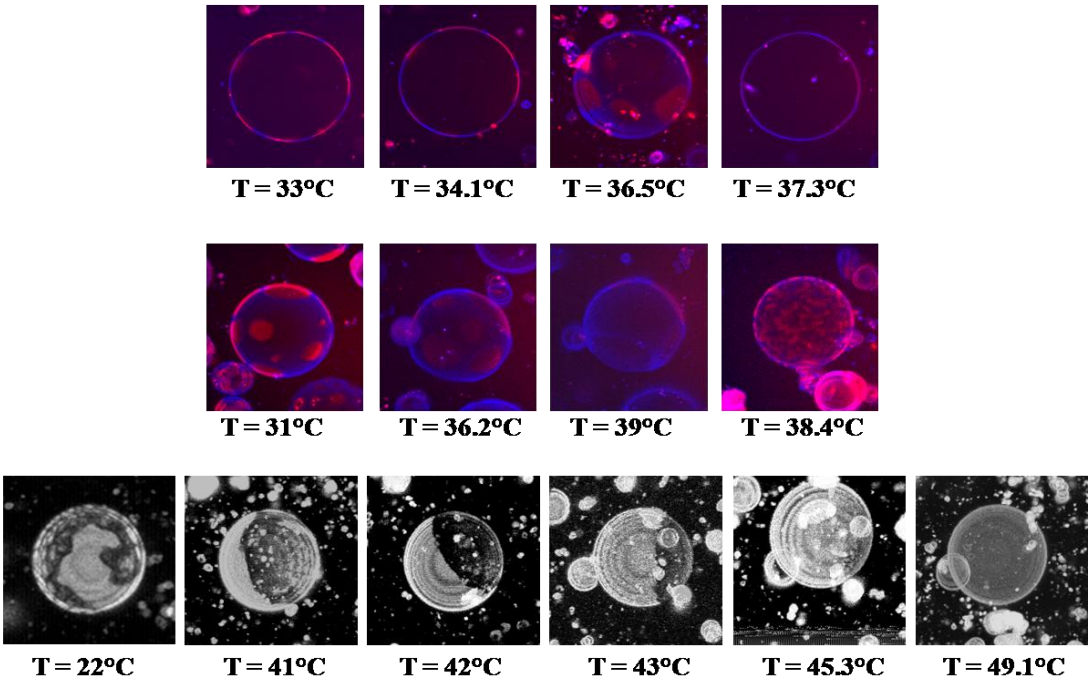

Figure 3.17 Miscibility transitions for L_o-L_d coexistence. Cholesterol/ SSM/DOPC: top row, 0.125/0.72/0.155; middle row, 0.10/0.67/0.23; bottom row, 0.15/0.64/0.21. The top and middle images were taken using naphthopyrene and LR-DPPE labels, while only LR-DPPE was used in the bottom series of images. Excitation wavelength: 780nm.

temperatures increased slightly with the area fraction of L_o phase. The miscibility transition temperatures at constant ratios of two of the components versus the amount of the third component are depicted in Figure 3.19. These "profile" sections give a cross-section view of the coexistence surface parallel to the temperature axis.

A transition in the tentative three-phase region is depicted in Figure 3.20. Some very interesting phase behavior was observed in this region: some samples appeared to exhibit both a lower miscibility transition and an upper miscibility transition (Figure 3.20). These samples would appear either homogeneous or grainy at 22°C, with very finely dispersed amounts of phases. As the temperature was increased, L_o-L_d coexistence appeared to occur, followed by a miscibility transition between these phases. The upper miscibility transition was reversible to with +/- 5°C, but the lower transition to a homogeneous state was not, at least not on the timescale of hours. Thus, the lower transition may not be a true miscibility transition, but rather a transition from a metastable state. This could occur, for example, via composition-curvature coupling for domains below optical resolution (<300nm); the sample would

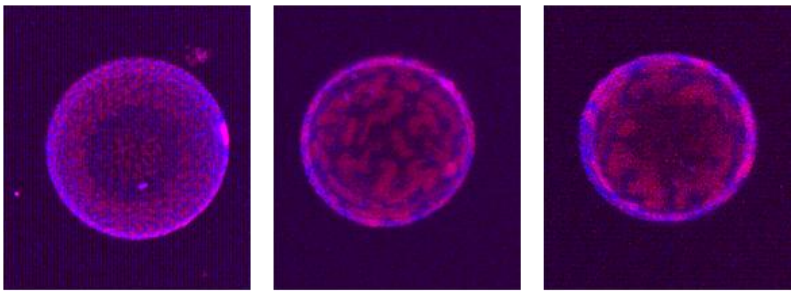

22ºC **25.7ºC** **34ºC**

Figure 3.18 Miscibility transition for gel-L_d coexistence. Cholesterol/ SSM/DOPC = 0.05/0.675/0.325. Napthopyrene (blue) labels the gel phase and LR-DPPE (red) labels the L_d phase. Notice how the blue stripes thicken as temperature is raised. Nearer to the T_M (39°C for this sample), these stripes begin to thin and gradually disappear. For other compositions, the stripes simply thin and disappear. Excitation wavelength: 780nm.

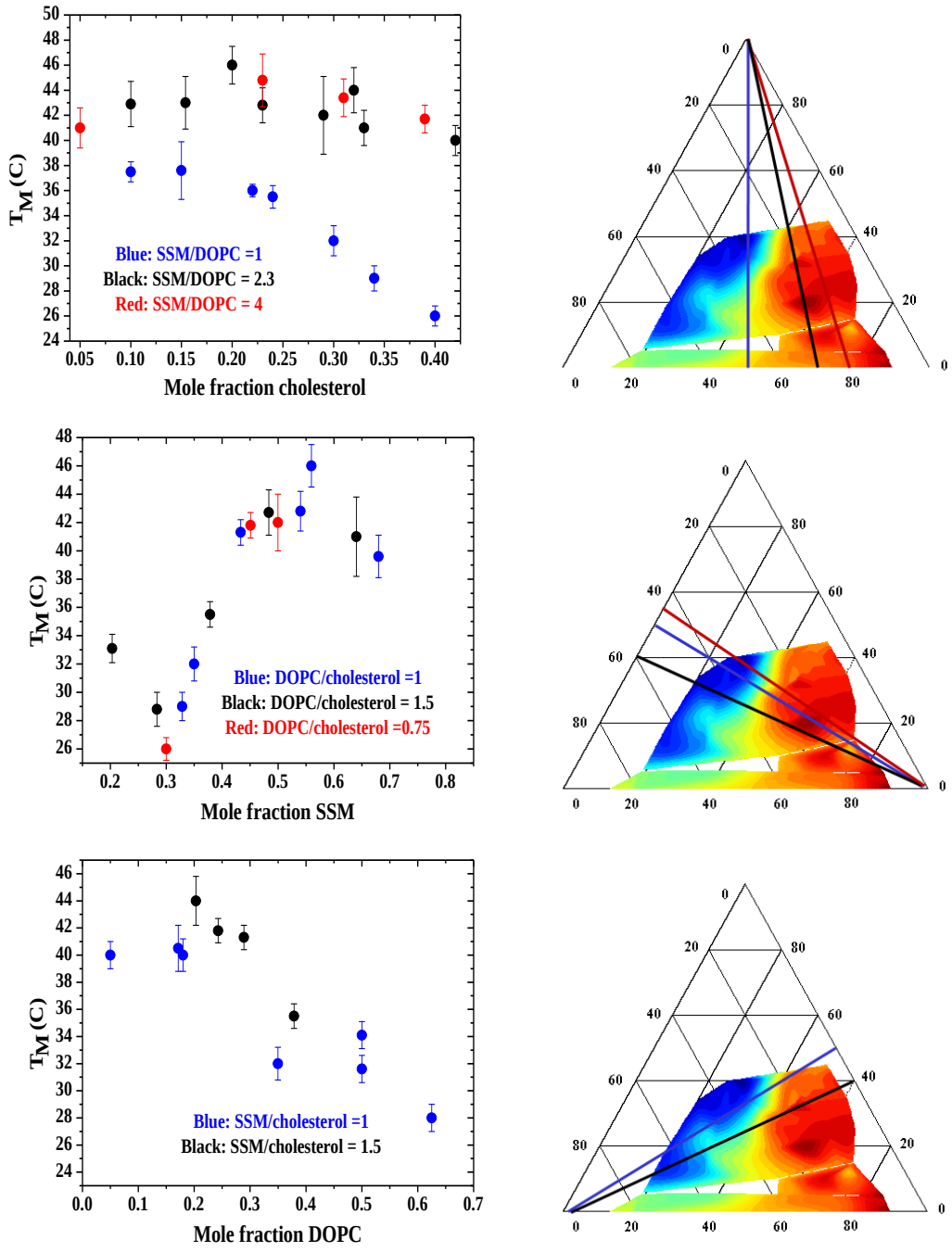

Figure 3.19 Miscibility transition temperatures for constant ratios of two components versus the mole fraction of third component. Top row: T_M versus mole fraction cholesterol at SSM:DOPC = 1 (blue), 2.3 (black) and 4 (red). Middle row: T_M versus mole fraction SSM at DOPC:cholesterol = 1 (blue), 1.5 (black) and 0.75 (red). Bottom row: T_M versus mole fraction DOPC for SSM:cholesterol = 1 (blue) and 1.5 (black).

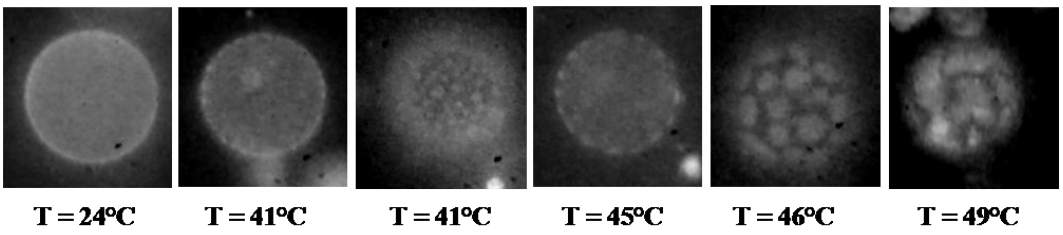

Figure 3.20 Miscibility transition near or in the three-phase region. cholesterol/SSM/DOPC = 0.15/0.72/0.13. The sample appears to have a lower miscibility point in the first heating cycle, but only the upper miscibility transition was reversible.

appear homogeneous under the microscope while actually being composed of small, hexagonally arranged domains (Leibler and Andelman 1987). This could also be the result of a chemical reaction; though the samples were prepared in the absence of oxygen, light could interact with other molecules such as the fluorophore to produce free radicals.

Samples displaying the viscous gel- or L_o-like phase (Figure 3.16, middle column) also appeared to have two distinct phase transitions upon raising the temperature: the first was morphological or structural and appeared to involve "melting" of this gel-like phase to a true liquid phase (L_o) during which the domains became rounded and appeared less viscous. This phase remained distinct from the liquid phase which favored LR-DPPE partitioning. This was followed by the miscibility transition between the two phases and occurred in a manner similar to that for "normal" L_o-L_d coexistence. However, the transition back to the elongated gel-like state upon cooling the sample did not occur (on the time scale of hours) and only the upper miscibility transition was reversible. It is unclear if and how this sort of behavior may be connected to that described above in the samples with apparent lower miscibility gaps, but the seeming lack of reversibility for the lower-temperature morphological transition in both could be indicative of hydrodynamic effects due to a large viscosity difference between the phases of this region. These transitions could

also be "true" phase transitions involving a gel and thus have much slower phase separation dynamics. However, transitions involving only L_d and gel phases in the L_d-gel coexistence region were observed to be reversible. Further analysis might involve measurements more sensitive to phase separation dynamics such as ESR and FCS, and the application of theories like those developed by Fialkowski and Holyst (2002), Taniguchi (1996), or Dorgan and Yan (1998) for morphological transitions in complex systems. Seifert (1993) has developed a theory for curvature *induced* phase separation which predicts phase separation upon heating due to the coupling of out-of-plane curvature in the shape fluctuations of two-component vesicles, which may also apply here.

The samples with three phases present, but only two coexisting per vesicle, displayed one upper miscibility transition per vesicle (except for those with the viscous gel-like phase coexisting with an L_d phase, the transitions for which were described in the preceding paragraph). This was a strong piece of evidence used to demarcate the three-phase region in Figure 3.11: it is akin to the non-simultaneous vanishing of two different menisci in a three-phase liquid system. The vanishing of the two menisci is unlikely to occur at the same temperature, a tricritical point, unless the appropriate pressure is reached (Hankey et al 1974, Griffiths and Widom 1973, Albrecht et al 1978). This is unlikely in a vesicle system because the lateral pressure $\pi(T)$, automatically adjusts with temperature (Sackmann 1995) and is nearly impossible to control in a closed vesicle system. The change as a function of temperature is given by the expression:

3.1) $$\pi(T) = \pi(T_o) - \kappa\alpha_{//}[T - T_o]$$

where κ is the lateral compressibility modulus and $\alpha_{//}$ is the lateral expansion coefficient (Sackmann 1995).

The cumulative data for transition temperatures in the three-phase region are compiled in Table 3.1. It should be noted that in Figure 3.11, the transitions denoted by color in the three-phase region refer to the highest observed T_M, that for L_o-L_d miscibility. It should be reiterated that the observed lower miscibility transitions may be due to kinetic effects.

3.3d KINETICS

Thus far, the research description has mainly been concerned with quasi-equilibrium measurements. In this section, a few preliminary experiments on the kinetic aspects of phase behavior are discussed. The importance of kinetic, or non-eqilibrium, effects has already been illustrated in the previous section by the observation of gel-L_d coexistence when GUVs are slowly cooled. The data presented in section 3.3 of this Chapter show a large gel-L_d coexistence region along the binary SSM-DOPC axis of the phase diagram which is observed from SSM:DOPC = 0.16:0.84 to 0.90:0.10 at 22°C. Though it has been observed before in a ternary system containing sphingolipid, it is not surprising: it has been shown both experimentally (de Almeida et al 2002) and theoretically (Jorgensen and Mouritsen 1995) that very slow cooling is necessary for gel-L_d equilibrium, typically on the scale of hours to days, depending on the lipid mixture. When the GUVs are rapidly cooled (quenched), the samples appear homogenous likely because they are trapped by kinetic barriers in a metastable state.

Kinetic properties can provide an important complement to equilibrium (quasi-adiabatic) studies of phase behavior: for example, the morphology of phase separation and the time-dependent domain growth can vary as functions of system dimensionality, of whether the order parameter is conserved or not, and on hydrodynamics (whether the surface tension competes with viscous or inertial forces, for example). Thus, kinetic information could be used to help distinguish between

Table 3.1 Data for transitions in the three-phase region. Stars in the first column refer to lower miscibility transitions, and unmarked numbers to the temperatures at which elongated domains appeared to become round and liquid-like. None of the transition temperatures recorded in this table refer to vesicles displaying macroscopic three-phase coexistence; all were for samples where only two intensity profiles were distinguished using two-photon fluorescence microscopy.

Cholesterol/SSM/DOPC	Gel-L_d	L_o-L_d
0.10/0.63/0.27	39.6 ± 2.0°C	42.9 ± 1.8°C
0.15/0.72/0.13	--	43.0 ± 5.0°C
0.10/0.72/0.18	35.2 ± 3.2°C	40.0 ± 2.4°C
0.10/0.76/0.14	--	40.6 ± 3.9°C
0.05/0.56/0.39	36.5 ± 2.5°C	38.0 ± 3.0°C

appropriate models for a complex system like the phase separated bilayer.The most direct kinetic experiments to perform are the observations of the phase evolution in non-equilibrium conditions; in this study, temperature quenches and osmolarity changes were used to perturb the system.

The morphology of separating liquid phases during a temperature quench can be compared to different theories to examine different models for membrane phase behavior (Mecke and Sofonea 1997, Taniguchi 1996, Dorgan and Yan 1998, Fialkowski and Holyst 2002). For some phase morphologies, a structure factor and critical exponent β can be determined (Tanaka 1984, Honerkamp-Smith et al 2008, Goncalves et al 1997). For round liquid domains, measurement of domain radius or total domain perimeters versus time and quench depth can be used to examine models of the phase separation process in terms of dimensionality and the influence of hydrodynamics (Siggia 1979, Laradji et al 1994, Haas and Torkelson 1995, Ernst et al 1992, Vladimirova et al 1999, Wu et al 1995). Exploring different stages of phase separation is important because phase morphology alone may be misleading: for instance, binary liquids at the critical composition and undergoing spinodal decomposition have been theoretically shown to do so without the classic bicontinuous

structure if the Peclet number is high enough (Vladimirova et al 1999).

For quench experiments, a special sample bath coupled to two thermostatted water lines was used and is described in detail in Chapter 4. The quench was relatively instantaneous, as depicted in the left panel of Figure 3.21. For each of four compositions, the temperature was quenched from 41-43°C to 20°C in roughly 45s. The radii of domains (in units of pixels) as functions of time (in seconds) were then recorded and are depicted in the right panel of Figure 3.21.The variation reflected in

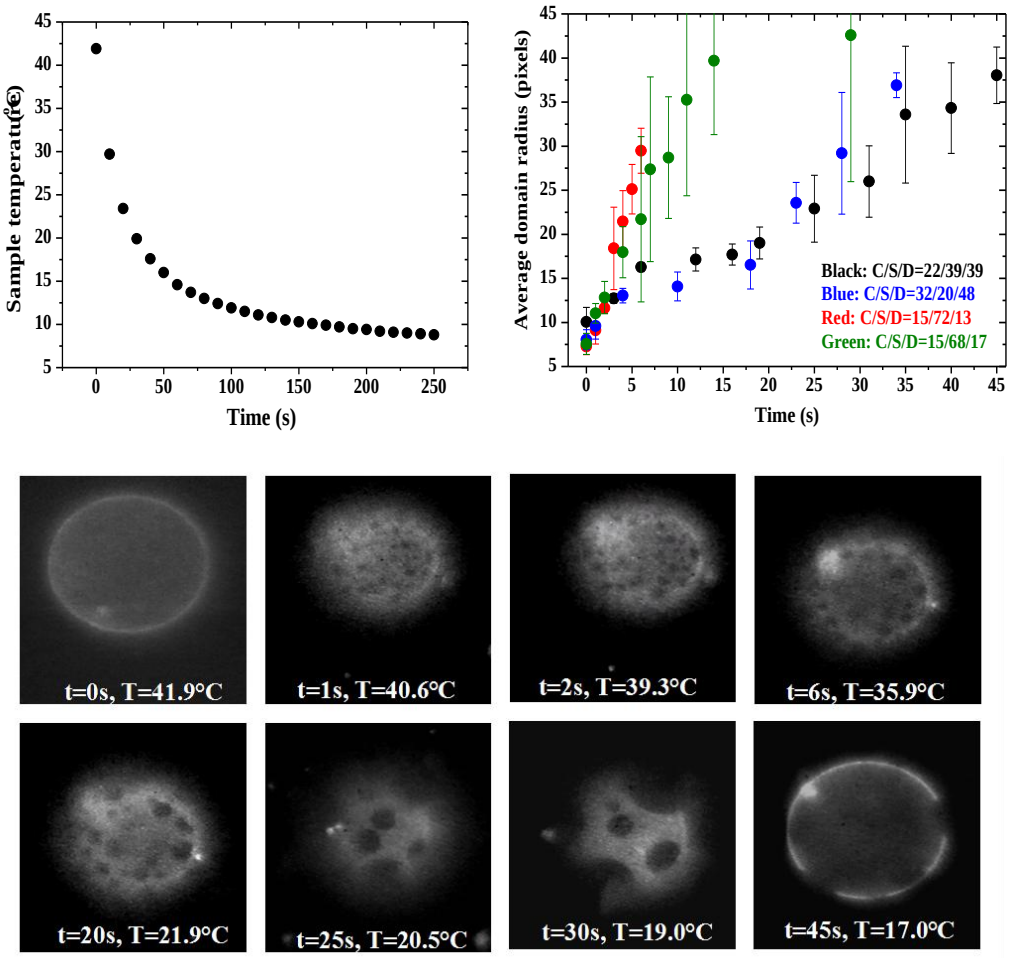

Figure 3.21 Quench data. Upper left: an example of the temperature (°C) reading near the sample versus time (s) for a quench experiment. Upper right: average domain radius (pixels) versus time (s) for four different compositions quenched below the L_o-L_d miscibility gap. Bottom panel: visual data for domain growth time and temperature dependence for composition cholesterol/SSM/DOPC = 0.32/0.20/0.48.

the error bars was due to variations of the domain radii at a given time. An example of domain growth with time for a quenched sample is depicted in the lower panel of Figure 3.21 for composition cholesterol/SSM/DOPC = 0.32/0.20/0.48.

It is obvious from Figure 3.21 that there are at least two different regimes of domain growth kinetics with respect to composition: the red and green curves, for cholesterol/SSM/DOPC = 0.15/0.72/0.13 and 0.15/0.68/0.17, respectively, comprise the "fast" regime, and the black and blue curves, for 0.22/0.39/0.39 and 0.32/0.20/0.48, respectively, comprise a "slow" regime. These data can be fitted according to known domain growth laws for which $R(t) \sim t^n$ (where R is the domain radius). The growth exponent n depends on the dimensionality of the system, and is characteristic of both different composition regimes, such as near critical or off critical (Haas and Torkelson 1995), and of different hydrodynamic regimes such as diffusive (early), viscous, or inertial (late) (Siggia 1979, Goncalves 1997). When these data were plotted on a log-log plot and fit to a linear equation, the result was that the fast regime samples had an exponent of 0.96 +/- 0.26 and the slow regime samples, for t >10s, had an exponent of 0.64 +/- 0.06. Interpretations of quench results are seldom straightforward, though: the exponent near 1 for the "fast" samples may be indicative of an off-critical composition in the viscous regime of a 2-d sample (Hass and Torkelson 1995), or it may be indicative of a critical composition in the viscous regime of a 3-d sample with a conserved order parameter (Goncalves et al 1997). Given the proximity to the composition with the highest observed upper miscibility transition temperature in the current ternary system, the latter may be the correct interpretation.

An obvious drawback to the quench experiments described here is that wide-field imaging is used in order for a fast time series to be collected. This may lead to photo-induced effects as described earlier. Another is that the quench, while, fast is

obviously not instantaneous; this can affect the validity of comparison to theories for domain growth in which a quench is normally assumed to be instantaneous.

Osmotic swelling

For a few samples, the phase morphology as a function of osmolarity was explored. This is important regarding the effects of composition-curvature coupling (Leibler and Andelman 1987, Baumgart et al 2003, Lipowski 1992, Seifert 1993, Kumar et al 1999); flaccid vesicles with excess free area can escape into the third dimension and become kinetically trapped. The phase morphology and temperature and pressure dependences of such samples may help elucidate the mechanism(s) responsible for such patterning (Leibler and Andelman 1987, Seul and Andelman 2005), and this information may be applicable to more complex mixtures such as those found in real cell plasma membranes. For example, a hexagonal arrangement of domains can occur due to coupling between curvature and composition of domains near a critical miscibility point in a 3-d system with Ising-like symmetry (Seul and Andelman 2005), or it can be due to the coupling of curvature to disclinations far away from a critical point in a 2-d system with XY-like symmetry (Korolev and Nelson 2008). Each theory has its own prediction for behavior and for the separation distances of the metastable hexagonal state. A simple way to perturb these states is by changing the temperature or the pressure. Since it is known that osmotic pressure affects phase behavior by decreasing the lateral area per lipid and increasing the acyl chain order, these order parameters could be studies as a function of pressure or temperature to select an appropriate theory.

In this dissertation, such elegant experiments were not performed; it was merely demonstrated that a change in the osmotic pressure could result in dramatic changes in morphology, as shown in Figure 3.22 for composition cholesterol/SSM/DOPC = 0.20/0.56/0.24. The two left panels in this figure depict flaccid vesicles in

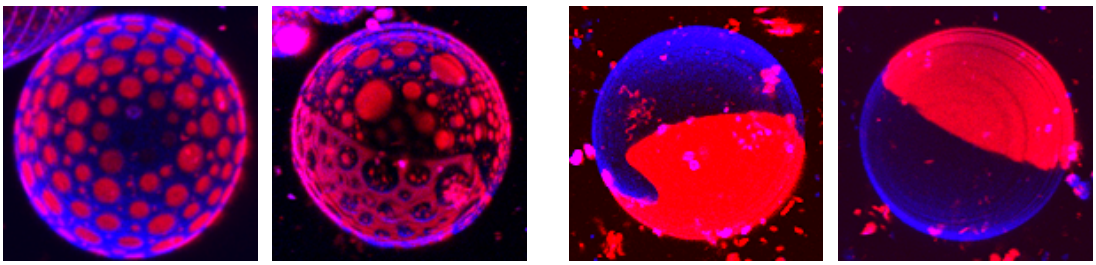

Non-osmotically swollen **Osmotically swollen**

Figure 3.22 Osmotic swelling. Cholesterol/SSM/DOPC = 0.20/0.56/0.24. The two left panels depict flaccid vesicles in 100mM sucrose. The two right panels depict vesicles swollen osmotically by adding 2μL DI to 9μL of the 100mM sucrose GUV suspension. All vesicles were labeled with LR-DPPE (red, L_d phase) and napthopyrene (blue, L_o phase). Excitation wavelength: 780nm.

100mM sucrose. The two right panels depict vesicles from the same preparation, but 2 hours after 2μL of deionized water was added to 9μL of GUV solution in 100mM sucrose.

Observations near the three-phase region taken together with the osmotic experiments suggest that curvature plays a very important role in the observed phase behavior. This may account for discrepancies in the dimensionality of the vesicle systems reported in the literature. Some authors observed purely 2-d Ising-like behavior (Honerkamp-Smith et al 2008), while the observations of others are better described by a 3-d model (Halstenberg et al 2003).

3.4 CONCLUSIONS

The temperature-dependent phase behavior of the quasi-ternary mixture SSM/DOPC/cholesterol in unilamellar vesicles has been determined using optical microscopy. The phase diagram depicted in this chapter was obtained using very careful composition and temperature control. Miscibility transitions were observed using two-photon laser scanning fluorescence microscopy, and kinetic phenomena were observed using wide field fluorescence microscopy. The importance of impurities, preparation and imaging conditions, and non-eqilibrium phenomena on the

observed phase behavior and conclusions about biological membranesdrawn from these observations cannot be overstated: the electrode and oxygen dependence of the shift in the L_o-L_d coexistence region at 22°C, the appearance of a gel-L_d coexistence region where few others have seen it in similar ternary systems, and the dependence on osmolar strength of the L_o-L_d morphology all demonstrate this principle. Despite the fact that the phase diagram depicted in this chapter was obtained using very careful composition and temperature control, it is only representative of lipid phase behavior under the conditions in which the samples were observed. Further studies on model membranes prepared in solutions of high osmolar strength (Pott et al 2008) that more closely resemble the cellular environment, for example, should be performed for more accurate comparisons to biological membranes.

CHAPTER 4: TEMPERTURE CONTROL ON THE MICROPSCOPE*

4.1 INTRODUCTION

The components and operation of a custom built, temperature-controlled chamber suitable for water immersion fluorescence microscopy are described in this chapter. The apparatus is designed to be a self-contained unit that is easily portable to and from the microscope, rather than a permanent fixture which may narrow the accessibility of the microscope. The apparatus is well below the cost of comparable commercially available environmental control chambers for microscopy, and offers a higher temperature resolution and stability than some of the cheaper commercially available ones. The system is applicable especially to biological specimens and measurements of temperature-dependent parameters in the vicinity of critical points, where high temperature resolution and stability are necessary.

As the field of biophysics expands, characterization of the fundamental physical properties of biological materials becomes more important. For some properties, temperature dependence of physical parameters is very important for biological application. This is well illustrated by studies on the physical properties of the plasma membrane in both model and biological lipid bilayer systems. It has long been hypothesized that the cell membrane may exploit features of critical phenomena, the singular behavior or divergence of physical parameters near the critical temperature T_c (or the critical pressure P_c or chemical potential μ_c) due to fluctuations of observables called order parameters. Studies on both biological and model membranes have examined critical behaviors for insight into biological membrane functions (Jin et al 1999, Celli et al 2008, Sackmann 1995, Mitaku et al 1983, Ruggiero and Hudson 1989, Halstenberg et al 2003, Heinrich et al 2008). Critical fluctuations in lipid composition have been linked to enzyme function (Raudino 1998,

* The material in this chapter will be submitted to Nature Methods by Farkas, E. R. and W. W. Webb.

Girard et al 2005) and to an anomalous increase in ion permeability (Doniach 1978). The singular behavior of the diffusion coefficient has been linked to protein mobility (Jin et al 1999) and environmental sensitivity (Tserkovnyak and Nelson 2006, Haataja 2009, Prost et al 1998). It has been hypothesized that long range protein-protein interactions may be due to the increase of the spatial scale of concentrations fluctuations (Sackmann 1995, Celli et al 2008). Critical mixing has been investigated theoretically with respect to the protein:lipid stoichiometry in membranes (Zhang et al 1993, Jahnig 1981a and 1981b). More recently, it has been proposed that critical fluctuations in the concentration of different lipids in both model (Honerkamp-Smith et al 2008) and plasma membranes (Veatch et al 2007) are in fact the lipid rafts responsible for protein sorting, modulation of protein activity, and membrane architecture. In summary, evidence suggests that biological membranes tune their compositions to be near a miscibility critical point to exploit the divergent properties for biological functions. Even if ternary model membranes turn out to be less biologically relevant than once thought (Kaiser et al 2009), they are still useful models for low dimensional physics near critical points. In this chapter, the temperature controlled chamber used in temperature dependent microscopy is described. It was designed with the imaging of fluorescently labeled vesicles specifically in mind, though it may easily be adapted for other systems.

4.2 BACKGROUND

To observe critical phenomena is to observe a singularity or anomaly of a physical property, defined by a thermodynamic derivative, due to fluctuations of another quantity, the order parameter, which differentiates one phase from another. Order parameters are derived from thermodynamic densities. The anomaly occurs as a function of an external field variable such as T, P, or chemical potential (μ), which define the proximity to the critical point, T_c, P_c, or μ_c. Anomalies are due to the

divergence in the spatial range of the correlations of the order parameter. Anomalies commonly associated with, and observed in, liquid solutions near the critical temperature include the infinite increase in the heat capacity (C_v), the infinite increase in the thermal compressibility, the infinite increase in thermal conductivity, the decay of surface (or line) tension to zero, the increase in the spatial extent of density or concentration fluctuations (opalescence), and the slowing down of mutual diffusion in binary mixtures as the diffusion coefficient, D, approaches zero (Anisimov 1991). The anomalies of these quantities are mathematically expressed as functions of the proximity to the critical point in terms of the reduced external variable such as the reduced temperature $t = (T-T_c)/T_c$. The expressions grow or decay algebraically with specific exponents, known as the critical exponents (Fisher 1967, Widom 1964). The observation of phase transitions, especially in the vicinity of a critical point, requires stable and accurate temperature determination for reasons that will be elucidated in this section.

The critical point location with respect to pressure, temperature, and chemical potential, is dependent on the property being measured by virtue of the limitations of the experimental apparatus and the physical state of the system (Anisimov 1975, Voronel 1976). Different physical properties of the same system have different critical exponents, with the result that some properties and systems are more susceptible to contamination by certain perturbations in the experiment than others. For example, it was demonstrated experimentally that the critical temperature for xenon differed depending on whether the thermal relaxation time or the heat capacity at constant volume was measured (Edwards et al 1968 in Anisimov 1975). The wrong choice of T_c, in this case as the temperature of maximum C_v, led to an erroneous calculation of the critical exponent because the measurement of C_v was much more susceptible to perturbations due to gravity than, for example, a measurement of the thermal

relaxation time (Anisimov 1975).

With respect to temperature control, there are two types of perturbations to the physical state of the system that may influence the observed critical behavior: stationary and nonstationary temperature gradients (Anisimov 1975, Voronel 1976). Stationary instabilities are those that do not change within the characteristic relaxation time of a perturbation to the system, τ_o. Nonstationary gradients are those that vary within a time τ_o. The value of τ_o for a binary system of simple liquids is (Anisimov 1975 and 1991):

4.1) $$\tau_o = \frac{l^2}{D_o}|t|^{\nu}$$

where l is the typical length of a concentration (or density) inhomogeneity, D_o is the diffusion coefficient far from the critical region, and t is the reduced temperature. The value of l depends on whether one is above ($T>T_c$) or below ($T<T_c$) the critical temperature: above T_c, l is on the order of the coherence length (correlation length) and below T_c, l is on the order of the smallest sample dimension. In Table 4.1, different values of τ_o for different values of l in both the 2-d and 3-d Ising models are given. The calculation uses equation 4.1with T_c~300K and D_o~10^{-9} cm^2/s, as found in the liquid ordered phase unilamellar lipid vesicles (Honerkamp-Smith et al 2008, Mitaku et al 1983, Almeida et al 1992). Note that this is only applicable near the critical point and this critical point applies to the miscibility transition. There are also nematic director and acyl chain conformational fluctuations which occur on different time scales (McConnell and Radhakrishnan 2007 and 2008, McConnell 2009, Jahnig 1981b).

Stationary temperature gradients are spatial gradients due to inhomogeneous heating or inhomogeneous heat dissipation. They lead to concentration (Chashkin et al 1966 and Blagoi et al 1970 in Anisimov 1975) or density gradients (Voronel 1976)

Table 4.1 Calculated impurity relaxation times. The relaxation times for impurities in a simple binary fluid determined using equation 4.1. The value of T_c is from Honerkamp-Smith et al (2008) and the value of D from Almeida et al (1992). The times are calculated for different length scales l and proximities t to the critical point for 2-d and 3-d Ising models.

Reduced temperature	τ_o (l = 20μm)	τ_o (l = 1μm)	τ_o (l = 50nm)
2-d: t=0.0167 (± 5.0°C)	6,900 hours	17 hours	2.6 minutes
3-d: t=0.0167 (± 5.0°C)	1,800 hours	4.4 hours	0.66 minutes
2-d: t=0.0033 (± 1.0°C)	33,333 hours	83.3 hours	12.5 minutes
3-d: t=0.0033 (± 1.0°C)	5,000 hours	12.4 hours	1.9 minutes
2-d: t=0.0003 (± 0.1°C)	333,333 hours	833 hours	2.1 hours
3-d: t=0.0003 (± 0.1°C)	23,111 hours	57.8 hours	8.7 minutes

within the sample because different points in the sample are at different temperatures. Concentration or density gradients induced by stationary temperature gradients have the same effect as frozen-in compositional impurities (Anisimov 1975), namely the rounding off to a finite value of a theoretically divergent parameter. There is a broadening or smearing out of the regime of the onset of that anomaly when plotted versus temperature, pressure, or composition. Thus, one may infer a falsely broad critical region if this type of perturbation is present, though the actual T_c (or P_c or μ_c) will not appear to be shifted to a new value.

Nonstationary temperature perturbations describe those temperature changes which occur more quickly than the sample's characteristic relaxation time. These lead to non-equilibrium conditions in experiments and increase the random error. According to Anisimov (1975 and 1991), a measurement is considered to be in equilibrium if the rate of temperature change with time satisfies:

4.2) $$\frac{dT}{d\tau} \ll T_c \frac{|t|}{\tau_o}$$

Nonstationary perturbations lead to shift in the observed T_c and thus could lead to improper determination of critical exponents if not properly accounted for with renormalized exponents; the example referred to earlier for the discrepancy between

the maximum equilibration time of xenon and the maximum heat capacity of xenon illustrates this (Edwards et al 1968). The influence of nonstationary gradients are strongly dependent on the property being measured, with some being more susceptible than others to perturbations in experimental conditions. Nonstationary gradients may be caused by inappropriate sample temperature control such as improper insulation leading to temperature fluctuations or improper PID coefficients in the control loop. This is especially important near the critical temperature where the relaxation time becomes very large (critical slowing down). Temperature jumps are, however, a required step in temperature dependent measurements: one must heat and cool the sample to observe phase transitions! The maximum rates of temperature change required to preserve equilibrium for various inhomogeneity scales l and reduced temperatures t calculated from equation 4.2 are given in table 4.2 for a binary system of simple liquids, for $T<T_c$. The values of T_c and D for L_o-phase membranes are used once again. One can see that larger l requires much slower heating, which is not surprising. Also, 2-d systems require slower rates of temperature change than their 3-d counterparts for the same model and the rate drastically decreases the nearer the approach to the critical temperature.

In addition to dependence on the temperature stability and spatial homogeneity, the experiment to determine a critical exponent is also directly dependent on the *accuracy* of the thermometer: Anisimov (1975) points out that in order to come within $t\sim10^{-2}$ degrees of the critical temperature, one must first have determined this temperature with an accuracy of $t\sim10^{-3}$. It should be noted that this type of accuracy refers to the deviation from the true temperature, and is thus represented by the calibration of the thermometer. It does not refer to the scale of the thermometer (resolution). Another type of accuracy refers to the interchangeability of different thermometers of the same kind and is generally reported by the manufacturer

Table 4.2 Appropriate rates of temperature change ($T<T_c$). The highest rates that still maintain equilibrium are calculated from equation 4.2 assuming simple binary fluids. τ is the relaxation time of a concentration impurity induced by the temperature gradient. The rates are calculated for different length scales l and proximities t to the critical point for 2-d and 3-d Ising models.

Reduced temperature	$dT/d\tau$ (l=20μm)	$dT/d\tau$ (l=1μm)	$dT/d\tau$ (l=50nm)
2-d: t=0.0167 (± 5.0°C)	1.3×10^{-5} °K/min	5.0×10^{-3} °K/min	2.0 °K/min
3-d: t=0.0167 (± 5.0°C)	5.0×10^{-5} °K/min	2.0×10^{-2} °K/min	7.0 °K/min
2-d: t=0.0033 (± 1.0°C)	5.0×10^{-7} °K/min	2.0×10^{-4} °K/min	8.0×10^{-2} °K/min
3-d: t=0.0033 (± 1.0°C)	3.0×10^{-6} °K/min	1.0×10^{-3} °K/min	5.0×10^{-1} °K/min
2-d: t=0.0003 (± 0.1°C)	5.0×10^{-9} °K/min	2.0×10^{-6} °K/min	8.0×10^{-4} °K/min
3-d: t=0.0003 (± 0.1°C)	7.0×10^{-8} °K/min	3.0×10^{-5} °K/min	1.0×10^{-2} °K/min

as a tolerance band for the thermometer. The accuracies of different types of thermometers are discussed in the next section.

With respect to nonstationary temperature gradients, the location T_c of a singular point is more accurately determined by the temperature of maximum relaxation time than by a peak anomaly in a physical parameter (Voronel 1976, Jahnig 1981a). Thus, it is useful to measure non-equilibrium (or kinetic) parameters. Fisher (1967) puts these into two categories: macroscopic and microscopic. Measurements of macroscopic parameters such as transport coefficients (the viscosity, thermal conductivity, and diffusion coefficient) can be useful provided the universality class of the dynamics is known, but measurements of microscopic molecular relaxation times are better. Techniques sensitive to microscopic times and spatial scales include ultrasonic attenuation and inelastic light or neutron scattering (Fisher 1967). In a sense, this is equivalent to saying it is more accurate to study the motion of the critical meniscus rather than where the meniscus vanishes to determine the location of a point (Anisimov 1975).

4.3 ELEMENTS OF DESIGN

A temperature control apparatus can be divided into four main elements: the

thermometer, the heater(s), the sample chamber, and the control unit. The thermometer measures the temperature of the chamber and sample, the heater supplies heat to the chamber and sample, and the sample chamber insulates the sample from heat loss. For the most stable control, the thermometer communicates with the heater via the controller so the desired temperature, the set-point, is achieved within a desired resolution using a feedback mechanism. For precise control, the reading is usually incorporated into a feedback loop with proportional, integral, and derivative gains (PID) that control the output current or voltage to the heater. Both the thermometer and the heater are usually located within the sample chamber housing. It may or may not be feasible to directly measure the temperature of the sample; in the membrane experiments to which the apparatus was applied, this was not feasible as the actual sample is sealed between two glass coverslips and submerged in a water bath.

Thermometer

There is a variety of temperature measurement devices commercially available. The four most commonly encountered types are thermistors, resistance temperature devices (RTD's), thermocouples, and diodes. The choice depends on a variety of factors including speed of the measurement, stability, cost, linearity of the response, and ruggedness and adaptability of the probe material. The properties are summarized in Table 4.3 below. The data were taken partly from Alan Tong's review of temperature sensors (2001), from Kamat and Naik (2002), and from compiled data available on the websites of five large sensor manufacturers: Omega Inc. (Stamford, CT), Minco (Minneapolis, MN), Wika Instrument Corp. (Deer Park, TX), Lakeshore (Westerville, OH), and Cryogenic Control Systems, Inc (or CryoCon, Rancho Santa Fe, CA).

As stated in the previous section, one of the most important sensor parameters for the measurement of critical exponents is the sensor's accuracy: due to long sample

Table 4.3 Sensor characteristics. Some representative characteristics for commercially available, non-custom temperature probes. Dashed lines indicate that no data was available or found. The response times refer to response time in air at the temperature indicated. Compensation refers to any special wiring arrangement or reference measurement necessary for the stated accuracy in the table. It should be noted that these values are very general and that many companies offer very specific custom probes with more desirable properties than those listed in this table.

	RTD	Thermistor	Thermocouple	Diode
Accuracy	0.01-0.1°C (at 25°C)	0.1-1.0°C (at 25°C)	0.5-5.0°C (at 25°C)	0.05°C (at 227°C)
Response time	Slow	Medium	Fast	Medium
Stability	Highest (0.1°C/year)	Medium	Low	Medium
Noise	Moderate	Low	High	Moderate
Self heating?	Yes	Yes	No	Yes
Other compensation?	4-wire	No	Cold junction	No
Typical range	-250-650°C (Pt)	-100-300°C	-200-400°C (Type T)	-273-227°C (Si)
Submersible?	Yes (wire-wound)	--	Yes (insulated)	--
Cost	High	Low	Low	Moderate

equilibration times near the critical temperature, the thermal time constant τ_{RT} of the sensor is not as important, provided it is faster than the sample equilibration time. For kinetic measurements in which the sample is "instantaneously" quenched, the thermal time constant is very important, though. The thermal time constant is usually defined as the time it takes the sensor to reach ~63% for its full response height when a step-function temperature change is applied. It may be quantified in terms of the physical properties of the probe via:

4.3) $$\tau_{RT} = \frac{\rho V C_p}{h A_S}$$

where V is the volume, C_p is the specific heat (at constant pressure), ρ is the density of the material, h is the heat transfer coefficient, and A_S is the surface area. This equation

obviously must be modified in order to describe realistic probes which are often made of multiple materials; it is simply used here to illustrate that the sensor dimensions and material properties are important even within a class of sensors. It does not account for differences based on probe environments, either. For example, both RTDs and thermocouples can have significantly faster effective response times when immersed in liquids than in gases.

Thermistors and RTD's employ the property of temperature-dependent resistance changes. Thermistors are typically made of a metal oxide with a negative temperature coefficient, meaning that the resistance decreases with temperature. RTD's are typically made of a pure metal or alloy which has a positive temperature coefficient, meaning the resistance increases with temperature. The most common metals and alloys used are platinum, nickel, copper, and nickel-iron alloy. For certain cryogenic applications where magnetic fields may produce errors, ruthenium oxide RTD's are employed. Both thermistors and RTD's are subject to self heating since they are both resistors and require an excitation current. This is where the cost can become very high, as very specialized control units are required to output small excitation currents and measure the corresponding small voltages to determine the temperature. The RTD typically has a very small resistance (100 ohms at 0°C), and because of this the resistance of the leads can cause significant errors in the temperature measurement. RTD's should be used in a four-wire configuration to negate the effects of lead resistance: two wires are used for the excitation current and two wires for the voltage measurement. Lead resistance does not affect thermistors because they typically have very large resistances. Thermistors may thus be more desirable in remote sensing if accuracy and tolerance are not of primary importance. A well calibrated RTD used in a 4-wire configuration will in general have the best overall accuracy and stability, though. Thermistors are typically not interchangeable

with one another, as the more accurate RTD's are.

A thermocouple device is composed of two different pure metals or alloys. The junction of two different metals creates a voltage that is dependent on the type of metals and on the temperature; this is known as the Seebeck effect. A thermocouple thus does not require an external excitation current. Common metal combinations for near room temperature (22°C) applications are type K, chromel (nickel-chromium)-alumel (nickel-manganese-aluminum-silicon) and type T, copper-constantan (copper-nickel alloy). These are the best near 22°C because their response curves are more linear in this region compared to other thermocouples. There are two main drawbacks to thermocouples: the small change in voltage with temperature and the voltages produced at junctions in the circuit. The change in voltage per degree temperature is typically very small (on the order of μV/°C at 25°C) so high gains must be applied, making the apparatus much more susceptible to pick-up noise and noise amplification. Moreover, when a thermocouple is connected to a measuring device, the connection creates a second voltage which must be compensated for to retain accuracy. The modern equivalent of a "cold junction" must be used; this often consists of an RTD or a thermistor to monitor the temperature of the internal circuit or the connection. Thermocouples have the advantage of having a fast response time and can be made very small and submersible in liquids, as with the typeT thermocouples sold by PhysiTemp (Clifton, NJ).

Diodes are semiconductor devices that can be used as thermometers because the forward-biased voltage drop across the diode decreases as a function of increasing temperature if a constant current is applied. For a typical silicon diode, this change is about 2mV/°C. Materials typically used in commercially available diode thermometers are silicon and GaAs (gallium-arsenide). Like RTD's, diodes can have very high accuracies and very small tolerance bands.

For application to the microscopy chamber described in section 4.4 of this chapter, the RTD is preferred for measurements of critical parameters. For kinetic experiments, however, a thermocouple was necessary to measure the extremely fast quenches. However, a film RTD (in contrast to the wire-wound variety employed in this research) could have been used as well, if there were any commercially available that were submersible in water.

Heater and controller

The heater is responsible for changing the temperature of the sample. There is an extremely wide variety of commercially available heaters differentiated from one another by the mechanism of heat generation (resistance versus Peltier), on their composite materials (conductor versus semiconductor), and on their geometries (thin films versus coils); this study will not attempt to describe them all. Only those that may be applicable to precision temperature control for water- and oil-immersion based optical microscopy or that are used in commercial apparatuses for temperature-controlled microscopy are addressed. By far the most commonly encountered type of commercially available heater in any field is the resistance heater, which exploits the fact that current passing through a resistor generates heat. The dissipated power follows the famous relation $P = I^2R$. Resistance heaters commonly employed in biological applications include indium tin oxide (ITO) coated glass heaters (Bioptechs, Butler, PA), flexible film resistance heaters such as those found in commercially available objective lens heaters (Minco or Bioptechs), and immersion resistance heaters (Watlow, St. Louis, MO). Each has its advantages: the ITO heaters allow one to heat the sample and simultaneously image *through* the heater because the ITO glass is approximately 80% transmissive in the visible range (Delta Technologies Ltd., Stillwater, MN). The flexible or foil heaters (Minco, Minneapolis, MN) allow one to adhere heaters to curved or arbitrarily shaped geometries as are often encountered in

the home-built apparatuses of academic research. Immersion heaters, as their name conveys, are immersible in liquids, making them useful where an immense thermal bath is required to maintain stability of temperature, as in the present application. While it is true that many ITO heaters can also contact water without shorting, they often have a limited temperature range since they cannot handle very large currents.

Another commercially encountered heater in the biological sciences is the Peltier device. A Peltier device consists of P- and N-doped semiconductor layers sandwiched between two ceramic plates. When a DC voltage is applied across the layers, electrons migrate, absorbing thermal energy from the "cold" side and depositing thermal energy on the "hot" side of the device. The device can thus heat or cool depending on the direction of the applied voltage (or current). Peltier devices have been used successfully in the past for temperature controlled microscopy (Nail et al 1994, Chabala et al 1985) for stabilities of +/- 0.1°C.

One of the most important properties in heater selection is the maximum voltage or current rating, because this is a crucial to the heater compatibility with the temperature controller if the two must be purchased from separate sources. A cryogenic temperature controller with extremely stable outputs may not supply a large rugged resistive heater with enough current to heat the sample. Conversely, a small delicate heater may get damaged if a rugged temperature controller (current source) or too high of a current is used. The sample chamber geometry and materials are also important factors for heater selection. In the present case, for example, submersible heating elements were required because the sample is submerged in a water bath. The heating element had to be small enough to fit inside of a petri dish and allow motion of the microscope stage in all three directions.

The heater power supply, usually part of the temperature controller, is a constant voltage or constant current device. Thus, the intrinsic stability of the system,

assuming all elements are properly insulated and mounted, is determined by the stability of the output of the controller. This can be challenging for applications that require very small changes in temperature, as small amounts of current are difficult to produce in a stable manner. Because the controller is also the thermometer in most cases where PID control is required, it is important to check the stability and compatibility of its probe inputs and output. Both of these reasons led to the selection of a controller more often used in cryogenic superconducting experiments for the apparatus described in the next section (4.4).

Sample chamber

The sample chamber design depends intimately on the system and the type of measurement desired. In general, it should insulate the sample from the environment to maintain adiabaticity for measurements of equilibrium parameters, and it should be able to be heated uniformly in the vicinity of the sample to avoid temperature gradients and convection of the bath (and the sample, if it is fluid). A constant temperature bath should surround the sample, especially if the heater cannot be placed directly on the sample.

An additional consideration from the material standpoint is the ruggedness of materials for a sample chamber: these should obviously be selected to withstand repeated heating and cooling cycles. In the prototypes of the sample chamber described here, a polycarbonate petri dish was used to house the water and the sample holder. This was replaced by a less brittle and better insulating PTFE dish, because temperature quench experiments often caused the polycarbonate dishes to crack.

Temperature control seems especially difficult in an imaging environment due to the need to accommodate the imaging equipment. Light microscopy generally requires the user to be able to directly access and manipulate the sample, unlike many cryogenic applications. An appropriate sample chamber should thus be small enough

to accommodate the commercial microscope with minimal effort and without compromise of microscope stage movement. Though this can be easily accomplished with the appropriate choice of materials, the need for a more "open" system obviously lends itself to heat loss and loss of thermal stabilization.

Heat dissipation through different elements in the sample chamber, and even the probe, is an important factor that must be dealt with in the experimental design. This is especially true in imaging systems, where the metal-cased objective lens can act as a heat sink. Moreover, imaging of biological materials often requires water or oil immersion lenses in which the immersion medium directly contacts the sample. Many of the sample containers used in biological imaging dissipate heat fairly efficiently: glass coverslips and thin polycarbonate plastic Petri dishes. This can be dealt with by insulation of the entire chamber and thermal compensation such as an objective heater (Bioptechs, Butler, PA).

4.4 MATERIALS AND METHODS

Two version of the sample bath were developed, one for measurement of equilibrium properties observed by 2-photon imaging, and one for the measurement of kinetic phenomena (quenches) observed in real time by wide field illumination. A diagram of the basic elements of the sample bath is depicted in Figure 4.1.The difference between the two types of baths was the type of heater used in the bulk bath medium: thermostatted copper tubing (bath type 1) or an immersion coil (bath type 2). The need for each is discussed below.

The sample chamber consisted of a cylindrical Teflon (PTFE) cup with approximately 1/8" thick walls. The cup was filled with water for the sample bath medium. A hole was bored through the bottom of the cup through which a portion of the objective lens (UPLAN APO 60x, Olympus) was inserted. A nitrile o-ring was situated between the Teflon and the lens to prevent leakage of the bath material

(water). A small groove was cut into the sidewall of the bore hole in the Teflon cup to accommodate compression of the o-ring without slippage. When all elements (heaters, sample holder, and thermometers) were assembled inside the chamber for imaging, the top portion was sealed from the atmosphere with flexible foam to prevent heat loss and water evaporation.

Water was chosen as the bath medium for the obvious reason that it is the lens immersion material. This is fortunate because its high specific heat makes it excellent thermal bath material: the more water surrounding the sample, the more difficult it is energetically to change the temperature, thus guarding against fluctuations and gradients. The bath accommodates roughly 100mL water. A similar design could also be used with lens immersion oil. The sample is placed into the bath by an external sample holder that is screwed onto the microscope stage, as depicted in Figure 4.2. The portion of the sample holder directly in contact with the sample is made of copper. The copper piece is tapped such that a threaded Teflon rod is screwed into it. The Teflon rod acts as a thermal isolator and attaches to an additional element that is screwed onto the microscope stage (Figure 4.2).

Temperature control was implemented by at least two independent PID loops. The first loop was used to heat the bulk of the water in the bath, and the second loop was used to maintain a stable temperature at the copper sample holder. In the first loop, heating was accomplished either by a coiled cable immersion heater (Watlow, St. Louis, MO) for equilibrium measurements or by a copper tubing thermostatted externally by a recirculating water bath (NESLAB RTE 221 microprocessor, Thermo Fisher Scientific, Waltham, MA) for quench measurements. In the former, a 1/8" OD cable immersion heater was coiled to fit tightly within the PTFE cup. A "dead" element was included at the portion of the heater that stuck up and out of the top of the cup; this prevented heat loss and ensured that only the hot portion of the heater was

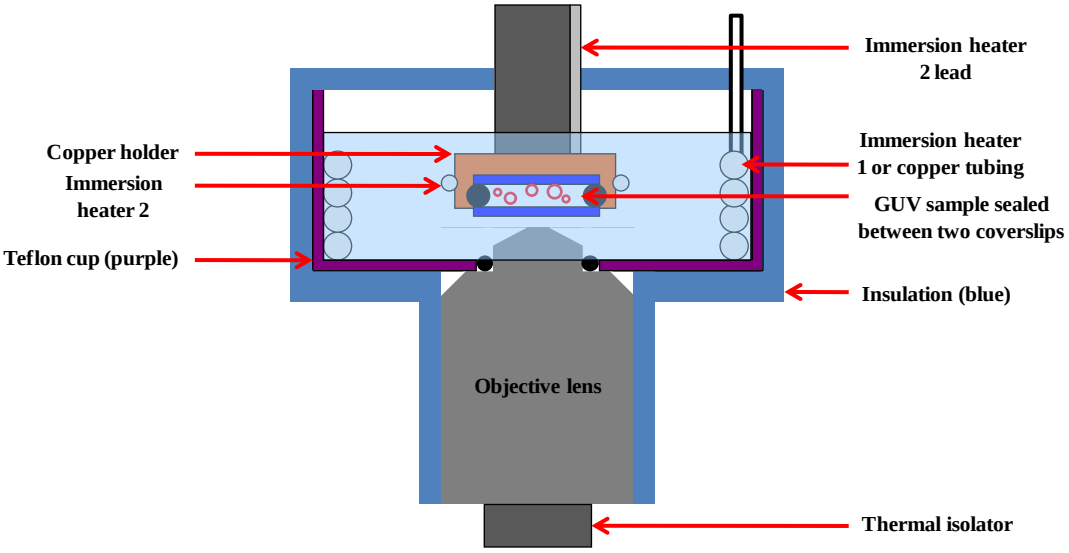

Figure 4.1 Sample chamber. A cross-sectional view of the sample chamber is depicted. The sample consists of an aqueous suspension of GUV's (red circle) sandwiched between two round glass coverslips (dark blue) separated by vacuum grease and sealed so there is no material exchange with the sample bath water. Two controlled heating elements are pictured: a large element (heater 1) heats the bulk of the bath water while a smaller element mounted to the copper sample holder maintains the holder and sample at a steady temperature.

submerged. In the latter type of heating process for the first control loop, thermostatted water was pumped through 1/8" ID copper tubing in a closed line. This copper tubing was tightly coiled and placed inside the PTFE sample chamber to heat the water of the bath. The copper tubing only spanned the height of the Teflon cup; the input and return to the recirculating bath were made of plastic tubing wrapped in thermally-insulating foam. This version of the bath could also cool and quickly quench the sample bath when two identical recirculating baths were used with two different set-point temperatures (see Chapter 3 of this dissertation). The plastic feed lines into the copper tubing had 3-valve stopcocks such that that switching between two baths at different temperatures was facilitated. Cooling below room temperature was facilitated by the addition of antifreeze to the recirculated water in one of the baths.

The heater in the second control loop consisted of one small coiled cable

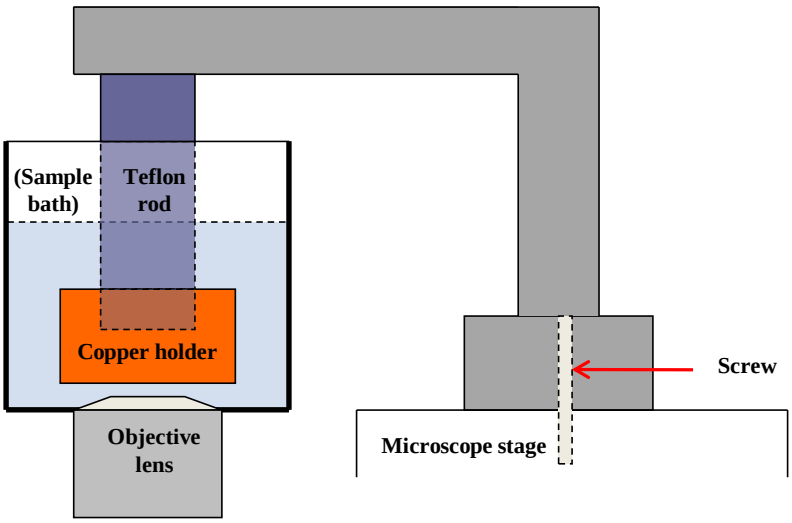

Figure 4.2 Sample chamber configuration in the lab. The sample chamber is mounted like a normal objective lens on an inverted microscope. It is filled with water. The sample holder is connected to the microscope stage through a custom aluminum lever arm (grey) that is screwed onto the stage. The Teflon thermal isolator between the copper sample holder and the aluminum arm is bolted onto the arm.

immersion heater (Watlow, St. Louis, MO) mounted directly to the sample holder such that it wrapped around the circumference of the copper piece. An additional heater that fit around the objective lens composed of a flexible "thermofoil" circuit (HK5244R43, Minco, Minneapolis, MN) was used, though this is only necessary at higher temperatures (>45°C). For all loops except that used for the recirculating water, a CryoCon model 32B (Rancho Santa Fe, CA) was used for the temperature controller. This model has very stable current outputs over 3 decades so that a wide range of temperatures can be accessed for the appropriate heaters and sample chamber design.

Temperature was monitored with one calibrated platinum RTD (100 ohm, 1/10 DIN, Alltemp Sensors, Deer Park, TX) per loop, except when quenches were preformed. For quenches, the temperature at the copper holder was monitored using a polyurethane insulated t-type thermocouple (IT-24P, Physitemp, Clifton, NJ) connected to a separate device from the heater controller (a BAT-10 thermometer from Physitemp). In both cases, the probe was mounted directly to the sample holder.

The recirculating water bath had its own PID controls independent of the CryoCon controller as well its own platinum RTD.

4.5 RESULTS AND DISCUSSION

Temperature versus time plots for fixed locations in the sample chamber are depicted in Figure 4.3 for four different set-point temperatures. These were obtained using the "type 2" bath with two cable immersion heaters. One can see that for a fixed probe location in the sample bath, the temperature is very stable for various set-point temperatures ranging from 25°C to 45°C on the time scale of hours: the overall standard deviation of fluctuations in the measured temperature is on the order of mill-degrees. The sample bath was also designed to minimize convection and spatial temperature gradients and to maximize the temporal temperature stability at the sample. Spatial temperature gradients are observed by measuring the temperature at two or more locations within the sample or sample chamber. This can be done using two probes simultaneously (provided they are interchangeable), or with the same probe at different locations. In these experiments, the latter option was used.

To check gradients in the plane of the sample, the RTD was placed at locations 1 cm apart on either side of the sample chamber, at a constant depth in the water. The temperature was recorded at 5s intervals by the CryoCon model 32B controller and the corresponding software. Two recordings were made at each location. The geometry and resultant recordings at a set point of 32°C are depicted in Figure 4.4a. The average gradient was $1x10^{-6}$°C/μm, or roughly 0.00025°C across a distance of 225μm; this length is the width of the field of view at a zoom equal to 1 for the 2-photon microscopy apparatus used in these experiments. To check for gradients in the vertical (optical axis) direction, the probe was placed at locations 3 cm apart in the sample bath. The results are depicted in Figure 4.4. The graphs are an average value for two measurements at each position; error bars are omitted for clarity due to the density of

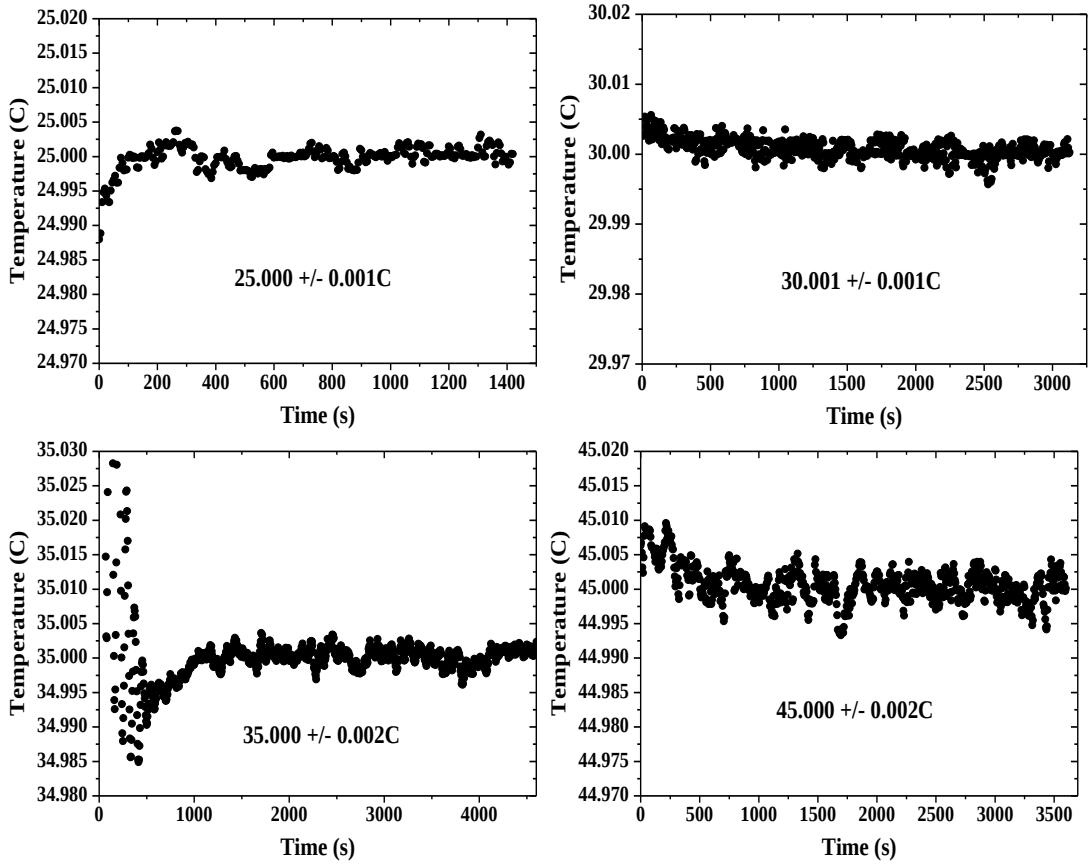

Figure 4.3 Temporal stability of the temperature for a fixed location in the sample bath. The sample temperature at a fixed location is stable to within milli-Kelvins of the set-point temperature for periods of hours. The temperatures displayed in the insets are the recorded temperatures; the set point temperatures were: (top row, left to right) 25°C and 30°C, (bottom row left to right) 35°C and 45°C.

sample points. Here, the gradient is more dramatic: 8.1×10^{-6} °C/μm. For a sample roughly 150 μm thick (the area between the two glass coverslips where the vesicles reside), this translates into a vertical gradient of 0.001°C over the entire chamber thickness.

Improvements for future designs

Using a Peltier device to heat the sample bath water may be more desirable than using resistance heaters due to the ability to cool the sample in a controlled manner as well as heat it. For equilibrium studies using the present system with the

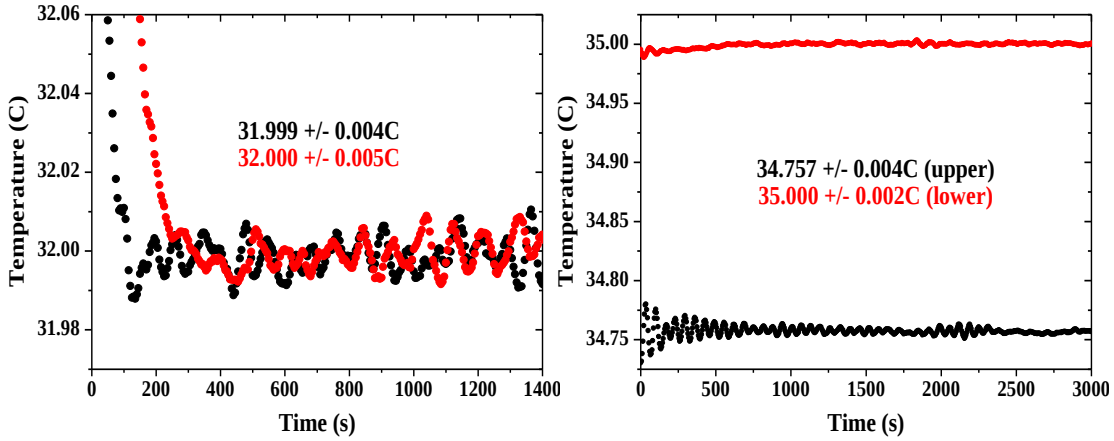

Figure 4.4 Spatial temperature gradients. Each red or black curve is an average of two measurements. The red and black colors refer to the two different locations. Left: measurement of the temperature versus time at positions 1cm apart, at a constant depth in the sample chamber (set point 32°C). Right: measurement of the temperature at different depths in the sample chamber, 3cm apart.

"type 2" bath, cooling was achieved simply by setting the set point temperature to a lower value and allowing the very slow equilibration with the surroundings. Setting the set point to a lower value does not remove heat from the system. However, there were no Peltier arrays that interfaced easily with both the geometry of the sample chamber and the output of the temperature controller. An improved design would have a cylindrically arranged array of Peltier devices encased and sealed within a waterproof cylinder. The cylinder should be made of a lightweight conductor of heat such as aluminum. This cylinder would replace the PTFE sample cup in the current system so that the immersion coils or thermostatted copper tubing would be unnecessary.

The ability to reach higher temperatures may be desired by some researchers as well. The main parameter preventing this is the lack of water immersion objective lenses with high temperature capabilities. Most water immersion objective lenses can only be used up to about 55°C.

4.6 CONCLUSIONS

This chapter described a temperature-controlled sample bath suitable for optical microscopy. This design, capable of milli-Kelvin stability in both space and time, is one of the most stable and accurate when compared with similar commercial and custom built designs described in the literature. The justifications for this level of temperature control were delineated in the first part of the chapter. In summary, quantitative analysis of critical phenomena in the form of critical exponents require this level of resolution; and elimination of spatial temperature gradients is required for the observation of non-critical miscibility transitions if one desires quasi-equilibrium conditions (Chapter 3 of this dissertation).

CHAPTER FIVE: POLARIZATION MICROSCOPY*

5.1 INTRODUCTION

Fluorescence polarization techniques have contributed significantly to the understanding of the organization and dynamics in lipid membranes; these techniques include fluorescence anisotropy decay (Lakowicz et al 1992, Lentz et al 1976), linear dichroism (Benninger et al 2005), and fluorescence microscopy with linearly polarized excitation light (Axelrod 1979, Florine-Casteel 1990, Yan and Mariott 2003, Haluska et al 2008, Corry et al 2006, Oreopoulos and Yip 2009).

When a fluorophore resides in an oriented environment such as a bilayer membrane, that environment places geometrical constraints on the rotational motions of the probe. Depolarization, or anisotropy decay, of emitted fluorescence reflects the extent of this constraint. This decay is a time dependent process. Time-resolved anisotropy decay measurements in lipid bilayer membranes have shown that it is the static molecular packing, not the dynamic rotational rate(s) of the probe, that give the dominant contributions to the steady state anisotropy and polarization (van Blitterswik 1981), provided that the rotational correlation time is much shorter than the probe fluorescence lifetime (Heyn 1979). The steady-state anisotropy, r_{SS}, can then be expressed in terms of two quantities: r_∞, the static component, and r_r, the dynamic rotational component. r_∞ is the dominant term and is proportional to the square of the lipid chain order parameter, or "first moment", S^2 (Heyn 1979, van Blitterswik et al 1981, Hare 1983, Silver 1985). Steady-state values are thus relatively good measures of the molecular order in the environment, as van Blitterswik et al showed in 1981: membranes with the same r_{SS} have roughly the same r_∞.

Anisotropies are typically measured in cuvette experiments via a fluorimeter or

* The material in this chapter will be submitted to Biochimica et Biophysica Acta by Farkas, E. R. and W. W. Webb.

spectrometer. However, fluorescence microscopy can also exploit the properties of oriented hosts to determine the degree of order surrounding a fluorophore. This can be done for steady-state (Florine-Casteel 1990, Axelrod 1989, Haluska et al 2008) or time resolved (Ariola et al 2006, de Almeida et al 2007) imaging. Microscopy has the advantage of letting the experimenter "preview" the sample by imaging it. When the absorption and emission dipoles of a fluorophore are known relative to the molecular geometry, then the fluorescence emission pattern in an oriented sample illuminated with linearly polarized light can be used to deduce the degree of order surrounding the probe. In this chapter, a method for determining acyl chain order parameters in binary and ternary lipid mixtures is presented and the results are discussed.

5.2 BACKGROUND

The thermodynamic behavior of lipid mixtures in membranes has become the subject of intense study over the past few decades. This is especially true of the interactions of cholesterol with the acyl chains of various kinds of lipids. The interest in this particular aspect of phase behavior is due to the hypothesis that lateral heterogeneities, referred to as lipid rafts, in eukaryotic cell membranes play important biological roles (Simmons and van Meer 1988) such as protein sorting (Brown and Rose 1992) and cell signaling (Simmons and Ikonen 1997). Lateral heterogeneity implies that there may be phase separation within the lipid mixtures in cell membranes. These rafts are postulated to be in a liquid-ordered (L_o) phase which only occurs in the presence of a sterol.

Thermodynamic phases are represented by physical quantities known as order parameters, which differ in one phase to the next and thus distinguish the phases. There are a variety of order parameters one might ascribe to different lipid mixtures, and the choice generally depends on the type of experiment used to measure them. Here, we study the average lipid acyl chain order as inferred from steady-state

polarization imaging of fluorescent probes which intercalate the acyl chain region of the membrane, because it is this particular order parameter that is most often used to distinguish the L_o (raft) phase from others.

Our experiments employ model membranes, giant unilamellar vesicles (GUV's), since real cell membranes are complex and contain a multitude of different kinds of lipids and sterols, which may complicate the interpretation of phase behavior with respect to composition. The simplest lipid mixture that exhibits the liquid-liquid phase separation found in cell membranes is a ternary mixture composed of a sterol, a saturated lipid, and an unsaturated lipid (Dietrich et al 2001, Samsonov et al 2001, Veatch and Keller 2002 and 2003, Baumgart et al 2003). In GUV's with certain ternary mixtures, the phase separation occurs on an optically resolvable scale, making the phase behavior of these systems amenable to optical microscopy whereas native cell membranes are not. Model membranes have thus been an invaluable system to define controls on the various thermodynamic parameters that may modulate membrane behavior in real cells.

The purpose of this investigation was to systematically obtain chain order parameter measurements as a function of composition for binary and ternary lipid and cholesterol mixtures. The broader goal of the determination of the chain order parameters for the ternary dioleoyl-phosphatidylcholine (DOPC) -stearoyl sphingomyelin (SSM)-cholesterol system (depicted in Chapter 3 of this dissertation) as functions of both composition and temperature was to deduce the tie lines within the 2-phase liquid-liquid coexistence regions of this system. In the experiments described here, a relative measure of the time- and space-averaged acyl chain order parameter for binary SSM-cholesterol and DOPC-cholesterol mixtures as well as ternary L_o and L_d phases containing SSM, DOPC, and cholesterol were determined. This was accomplished using polarized two-photon optical microscopy. The term

"relative measure" is used for two reasons: the experimental technique relies on conventional imaging, so the data are both time- and space-averaged (an absolute value for the acyl chain order parameter cannot be determined and S is purely operational); and the treatment of the data to extract an order parameter by this method is dependent on the theoretical model used to describe the acyl chain, or probe, motion within the membrane. The latter is not a problem if the same model is applicable in different phases, because relative trends in changes of the order parameter with respect to composition and temperature suffice to define phase boundaries and tie lines.

Although there have been many previous studies using optical methods to probe chain order (Axelrod 1979, Jahnig 1979, Van Blitterswik et al 1981, Hare 1983, Florine-Casteel 1990, Lakowicz et al 1992, Chen and van der Meer 1993, Blackman et al 1996, Dale et al 1999, Salamon and Tollin 2001, Benninger et al 2005, Ariola et al 2006), this investigation is one of the first that systematically addresses a ternary system with a completed phase diagram in both composition and temperature space; this has only recently been explored (Halsuka et al 2008). Moreover, because the miscibility and chain melting transitions can be observed directly and simultaneously with imaging methods, our technique is useful in determining the extent of the coupling between chain order and miscibility.

It is important to reiterate that our study uses an imaging-only method. In other methods used for obtaining order parameters, determining tie lines, and observing phase behavior with respect to a ternary phase diagram such as ESR (Chiang et al 2005, Freed and Smith 2009), NMR (Veatch et al 2004, Polozov and Gawrisch 2006), FRET (Buboltz and Feigenson 2001), and WAXS (Mills et al 2008)), there are caveats related to the non-imaging nature of the experimental set-up. First, one cannot directly observe the sample to determine whether or not it is representative, in the sense that a statistical majority of the vesicles show similar phase behavior, phase area fractions,

etc. Second, some non-imaging methods require sample geometries different from the unilamellar bilayer vesicle geometry which mimics the biological membrane: multi-lamellar vesicles are required for NMR experiments (Veatch et al 2004, Polozov and Gawrisch 2006), planar bilayers for WAXS (Mills et al 2008), and small unilamellar vesicles (SUV's) for ESR experiments (Chiang et al 2005, Freed and Smith 2009). With respect to the latter concern, it is not always well defined how order parameters obtained in these geometries map onto those in corresponding in composition to GUV systems. It has been known for decades that these geometries place additional constraints on the thermodynamic behavior including dependence on the vesicle radii of curvature for SUV's (Lentz et al 1981), substrate-induced domain formation in planar supported bilayers (Rinia et al 2001), or domain or bilayer couplings in multilamellar vesicles (Heimburg 1998, Gandhavadi et al 2002).

PAH dyes are employed due to their structural similarity to cholesterol (Figure 5.1). They have been shown to reside in a similar position and orientation within the bilayer as cholesterol, partition into different phases with similar preference as cholesterol, and experience steric hindrance to rotational motion in the acyl chain environment similar to cholesterol (Baumgart et al 2007b, Chong et al 1985). In the first set of experiments, optically homogeneous GUV's made up ofof binary mixtures of a lipid and cholesterol are employed. In the second set of experiments, ternary lipid mixtures are employed. The relative chain order parameter is obtained from two-photon images of equatorial sections of GUV's in a method that is the two-photon equivalent to that described by Axelrod (1979) and Florine-Casteel (1990). The data from the experiments on binary mixtures was used to extrapolate chain order behavior in phase separated GUV's made from the ternary lipid mixture.

Imaging is a steady-state method and requires little sophistication in the equipment. The trade-off versus time-resolved experiments lies in the analysis; this

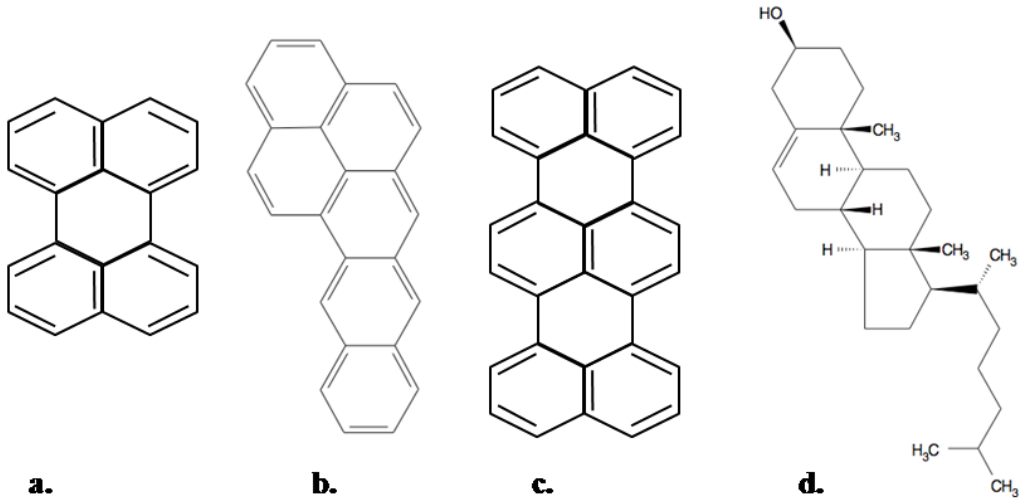

Figure 5.1. PAH dyes and cholesterol. a) perylene, b) naphtha[2,3a]pyrene, c) terrylene, and d) cholesterol. The three PAH dyes have a similar planar structure to cholesterol and thus are expected to intercalate into the membrane in a similar fashion, making them potential probes for the effects of cholesterol on lipid acyl chain order.

will be described in detail in section 5.3. Time resolved measurements and imaging to determine acyl chain order parameters have the advantage of being potentially model-independent (Dale et al 1999), have more literature and references available for the data analysis, and can measure dynamic properties (Lakowicz et al 1992, Ariola et al 2006, Davenport and Targowski 1996, de Almeida et al 2007).

5.3 THEORY

A hydrophobic dye molecule within the interior of a lipid bilayer is confined from free rotation by the acyl chains. If one considers only the slow rocking motion of the probe away from the membrane normal, the magnitude of this constraint reflects the ordering of the acyl chains and is represented geometrically as a reduced volume for probe rotational diffusion (Kinosita et al 1977). However, this "slow" motion must be faster than the fluorescence lifetime for the analysis described here to be valid (Heyn 1979). Fluorescence polarization and anisotropy are two properties which reflect confined diffusion and thus the acyl chain order. For example, one would

expect an L_d phase to provide greater freedom for the dye to wobble than an L_o phase; the L_d phase would thus have a larger reduced volume than the L_o phase.

The first polarization microscopy studies of dye orientation and lipid order in bilayer membranes were conducted by Axelrod (1979). A vesicle is illuminated with linearly polarized light through the objective, and fluorescence is collected in the epi-direction and passes through an analyzer, which can be oriented parallel or perpendicular to the excitation direction. If a polarizing beam splitter cube is used, both polarizations may be collected simultaneously.

To quantify how steady state polarized fluorescence depends on lipid order and membrane surface location, one must first define the coordinate systems of the fluorophore in the membrane frame and in the laboratory frame from which the membrane is visualized. A depiction of these coordinate systems is given in Figure 5.2. The subscripts *m* and *l* in Figure 5.2 refer to the membrane and lab coordinate systems, respectively. Figure 5.2a shows the membrane coordinate system exclusively. The coordinate $X_{3,m}$ is normal to the membrane surface and the coordinates $X_{2,m}$ and $X_{1,m}$ are tangent to the membrane surface. The black and red arrows represent the long axis of the dye molecule at times t=0 when it absorbs photons, and at time t, when it emits a photon, respectively. The long axis is, on average, parallel to the membrane surface normal denoted by the $X_{3,m}$ axis, but diffuses in a confined volume. The precise shape of this volume is model dependent and an example is denoted in Figure 5.2c by the dashed cone for the wobble-on-a-cone model. Figures 5.2b and 5.2c depict the relationship between the membrane coordinates and the lab coordinates for an arbitrary position on GUV (5.2b) and for an equatorial section of the GUV (5.2c), with the $X_{1,l}$ denoting the optical axis of the system. Thus, $X_{2,l}$ and $X_{3,l}$ define the focal plane of the microscope. In these experiments, the electric field vector of the excitation light is parallel to $X_{3,l}$. For an equatorial section of a GUV, the azimuthal

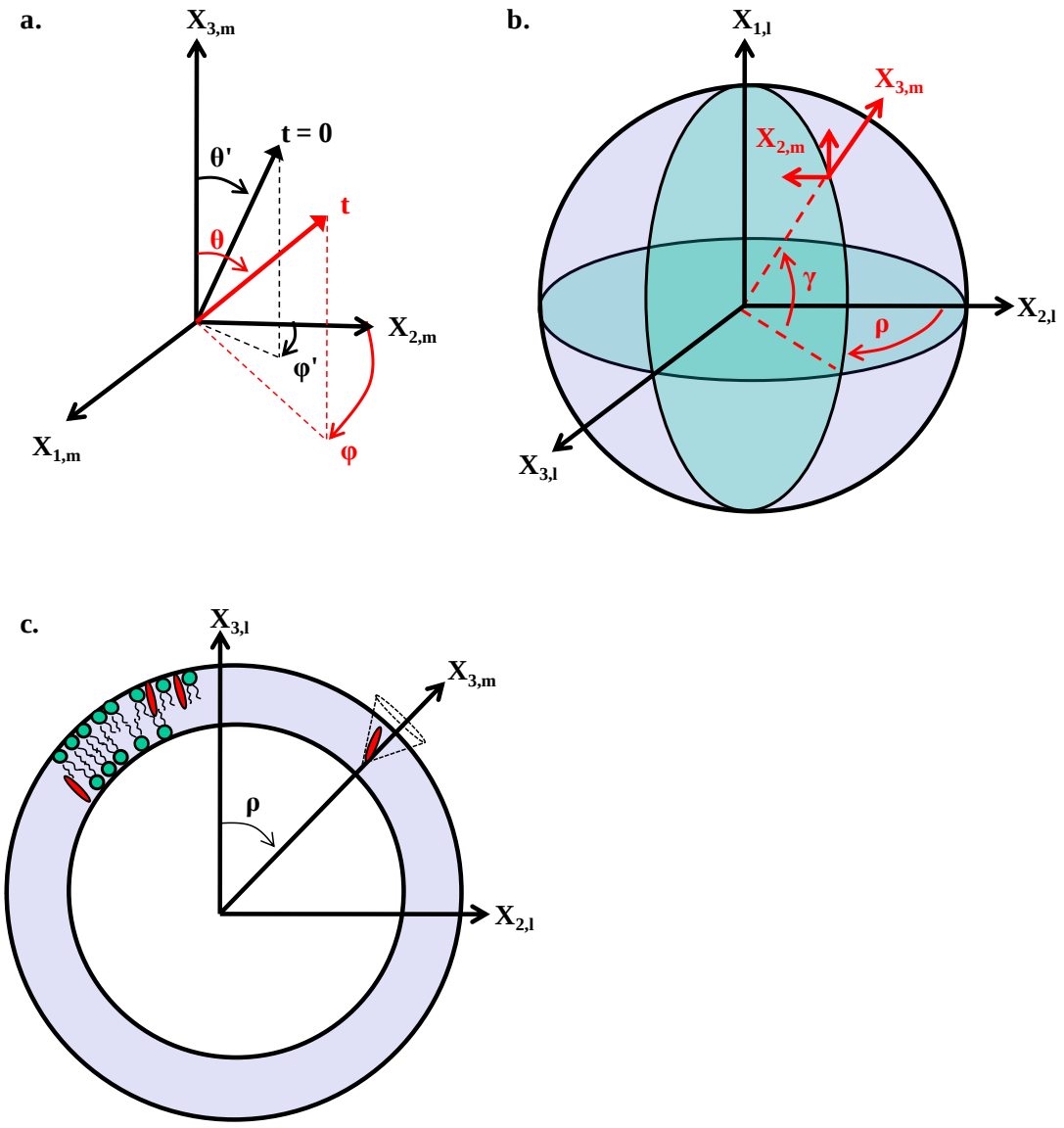

Figure 5.2 Coordinate systems. a) The membrane coordinate system. Primed and unprimed coordinates refer to times *t*=0 (photon absorption dipole, black arrow and corresponding black text) and *t*=*t* (photon emission dipole, red arrow and corresponding red text), respectively. Note that for two-photon microscopy, the absorption probability is actually depicted by a tensor, not a dipole, as explained in text. b) The laboratory coordinate system, and c) the laboratory coordinate system with respect to an equatorial section of a vesicle, as one would use to analyze equatorial GUV images. In (c), the lipids are blue and the fluorophores are red. It is assumed that the optical section is negligibly thin such that *γ*=0, which is reasonable in two-photon microscopy. The dashed line surrounding the fluorophore in (c) depicts the wobble-on-a-cone confined volume.

angle γ defines the optical thickness of the slice; for simplification, we set this to zero for 2-photon images. The data for intensity versus angle refer to the angle ρ as shown in 5c. Transformation between the two systems is given in the appendix of Axelrod's paper (1979). The components of a unit absorption dipole in the lab frame are described by:

5.1) $$x_{1,l} = \cos\gamma\sin\theta'\sin\varphi' + \sin\gamma\cos\theta'$$

$$x_{2,l} = \cos\rho\sin\theta'\cos\varphi' - \sin\rho\sin\gamma\sin\theta'\sin\varphi' + \sin\rho\cos\gamma\cos\theta'$$

$$x_{3,l} = -\sin\rho\sin\theta'\cos\varphi' - \cos\rho\sin\gamma\sin\theta'\sin\varphi' + \cos\rho\cos\gamma\cos\theta'$$

where $x_{3,l}$ describes the component of the unit dipole parallel to $X_{3,l}$, the direction of the excitation light polarization, for a given position ρ on the membrane. The primed coordinates denote absorption, but the expression for one-photon absorption is the same for emission coordinates relative to the lab frame, with different numerical values of the angles φ and θ.

For simplification, one-photon absorption is outlined first and then the arguments are extended to the two-photon case. Most researchers familiar with polarized fluorescence experiments are familiar with the one-photon process, in which a dipole oriented at (θ',φ') in the membrane frame (see Figure 5.2) at time t=0 absorbs a photon, undergoes rotational diffusion, and emits a photon at a later time, t. Note that this model assumes that the fluorescence lifetime of the dye is much larger than the mean rotational diffusion time, so that the dye rotates to a new position (θ, φ) in time t before emitting a photon. This is reasonable for the dyes used in this study. If the absorption dipole lies along the longest axis of the molecule, and that axis is, on average, parallel to the membrane normal, the probability of absorption in the *membrane* frame, $p(\theta',\varphi')$, is proportional to the projection of the excitation light

polarization onto absorption dipole, or to $\cos^2(\theta')$ in the membrane frame (= $|\boldsymbol{x}_{3,l}|^2$ in the lab frame). Similarly, the probability of emission in the membrane frame is proportional to $\cos^2(\theta)$.

Two-photon absorption is more complicated, because it involves the projection of the excitation light polarization onto a three-dimensional tensor rather than a two-dimensional dipole. For a two-photon absorption process, it is necessary to replace the absorption probability $\boldsymbol{x}_{3,l}^2$ with $|\boldsymbol{X}_{3,l'} \cdot Q \cdot \boldsymbol{X}_{3,l}|$, where Q is the two-photon absorption tensor. The tensor describing a transition from state 'i' to excited state 'f' is given by (Pauls et al 1998):

$$5.2) \qquad Q_{\sigma,\mu} = \sum_n \left[\frac{\sigma \cdot \langle i|\vec{r}|n\rangle\langle n|\vec{r}|f\rangle \cdot \mu}{\nu_n - \nu_\sigma + i\Gamma_n} + \frac{\mu \cdot \langle i|\vec{r}|n\rangle\langle n|\vec{r}|f\rangle \cdot \sigma}{\nu_n - \nu_\mu + i\Gamma_n}\right]$$

where σ and μ are the polarizations of the absorbed photons, $\boldsymbol{r}$ is the electronic dipole vector, υ_n is the transition frequency of the virtual state n, and Γ_n is the homogeneous line-width of the virtual state n.

This probability is, in general, much more complicated than a simple $\cos^4(\theta')$ dependence (Haluska et al 2008, Chen and Van der Meer 1993), which would be obtained by squaring the one-photon absorption probability, unless the probe is rod-like (Kinosita 1977, Callis 1993, Haluska et al 2008). For planar molecules, the dominant transition moments are in the plane of the molecule and the tensor can thus be treated as an effectively two-dimensional matrix (Callis 1993, McClain 1971, Pauls et al 1998). For molecules of D_{2h} symmetry such as perylene and terrylene, the off diagonal elements of the tensor (S_{xy} and S_{yx}) vanish for transitions between symmetric states, and the values of the polarized fluorescence and anisotropies are larger; thus, these transitions are more sensitive indicators of molecular orientation and it is important to select those wavelengths which induce symmetric transitions (Pauls et al 1998, McClain 1971). For planar D_{2h} molecules such as perylene and terrylene, this

dependence is approximately $\cos^2(\theta')\sin^2(\theta')\cos^2(\beta)$ in the membrane frame for certain excitation wavelengths and transition symmetries, where β is the angle between the molecular plane and that perpendicular to the excitation polarization (Chen and Van der Meer, 1993, Peticolas et al 1965). For simplicity, we apply this probability to naphthopyrene as well, despite its C_2 symmetry. A more accurate analysis for planar fluorophores of other symmetries can be found in Opanasyuk et al (2009). It is assumed here that the angle between absorption and emission directions is zero, which is reasonable (Sepiol et al 1997, Zannoni et al 1983). The emission probability is proportional to $\cos^2(\theta)$ for all dyes considered.

In the membrane interior, rotational diffusion of the dye is hindered by the lipid acyl chains. This diffusion can be described with the same formalism commonly applied to Brownian lateral diffusion using the Smoluchowski or Fokker-Plank equation. For this particular geometry, the constrained motion is described by the cylindrical Smoluchowski equation (Kinosita 1977, Florine-Casteel 1990, Wang and Pecora 1980, Lipari and Szabo 1980):

5.3) $$\frac{df(\theta',\varphi',0|\theta,\varphi,t)}{dt} = \nabla \cdot [D_R \vec{\nabla} f(\theta',\varphi',0|\theta,\varphi,t) + \frac{k_B T}{D_R} f(\theta',\varphi',0|\theta,\varphi,t) \vec{\nabla} V(\theta',\varphi')]$$

subject to the initial condition:

5.4) $$f(\theta',\varphi',0|\theta,\varphi,t) = \delta(\cos\theta - \cos\theta')\delta(\varphi - \varphi')$$

where f is the probability distribution function that a probe with orientation (θ',φ') at time t=0 will have orientation (θ, φ) at time t when it emits a photon, D_R is a rotational diffusion constant, and $V(\theta, \varphi)$ is the model-dependent potential felt by the probe. This function f accounts for the distribution of molecular orientations in the sample due to rotational motions of each dipole during the excited-state fluorescent lifetime.

Mathematically, the model-dependence of this description enters via the potential. For bilayer membranes at equilibrium, it is reasonable to assume cylindrical symmetry such that $V(\theta, \varphi) = V(\theta)$ only.

The time-dependent solution f of equation 5.2 is a Green's function. For time-averaged measurements such as images, the steady state solution for f, f_S, is given by (Kinosita et al 1977):

5.5) $$f_S = Ce^{-V(\theta)/k_BT}$$

where C is the normalization constant that depends on the model being used. In these experiments, two widely used models for the constraint imposed by lipid acyl chains are compared: the wobble-on-a-cone-model, and the Gaussian model (Kinosita et al 1977 and 1982, Jahnig 1979, Haluska et al 2008).

In the cone model, the dye is free to wobble within a conical space where the axis of the cone is parallel to the director of the lipid molecules as shown in Figure 5.2c. For lipids that are not tilted with respect to the membrane normal, this axis is parallel to the membrane normal. Lipid tilt is not expected for the liquid phases of the three lipids used here, or for the gel phase SSM mixtures (Maulik and Shipley 1996, Shipley et al 1974). For angles less than some maximum angle θ_{MAX}, the potential is a finite constant and for angles greater than θ_{MAX}, it is infinite:

5.6) $$V_{Cone} = \begin{cases} 0, & \theta \leq \theta_{MAX} \\ \infty, & \theta > \theta_{MAX} \end{cases}$$

The smaller the value of θ_{MAX}, the more constrained the dye is and thus the more ordered the acyl chains. The order parameter extracted from this model is (Lipari and Szabo 1980, Kinosita et al 1977, Florine-Casteel 1990):

5.7) $$S_{Cone} = \frac{1}{2}\cos\theta_{MAX}(1 + \cos\theta_{MAX})$$

The time-dependent cone model can become quite cumbersome analytically when one imposes the reflecting boundary condition on a cyclindrical Green's function expanded as Legendre polynomials (Wang and Pecora 1980, Florine-Casteel 1990). The equations can be solved numerically by invoking relationships between the derivatives of Legendre polynomials with respect to order (Pal 1919, Wang and Pecora 1980, Haines 1985). Fortunately, in imaging one can employ the fact that $f(t\rightarrow\infty) = f_S$. In the case of the cone model, this reduces to (Kinosita 1977):

5.8) $$f_{S,Cone} = \frac{1}{2\pi(1-\cos\theta_{MAX})} = C_{Cone}$$

In the Gaussian model, the potential is given by (Kinosita et al 1982):

5.9) $$V_{Gaussian} \propto \frac{q^2 cos^2\theta}{2} \approx \frac{q^2}{2}(1 - \frac{\theta^2}{2} + \ ...)$$

and the order parameter is given by:

5.10) $$S_{Gaussian} = \frac{1}{2} < 3\cos^2\theta - 1 > = \frac{\int_0^{\pi} \frac{1}{2}(3\cos^2\theta-1)e^{q^2(1-\theta^2/2)/2k_BT}\sin\theta d\theta}{\int_0^{\pi} e^{q^2(1-\theta^2/2)/2k_BT}\sin\theta d\theta}$$

Following the method of Axelrod (1979) and Florine-Casteel (1990), the steady-state distribution, F_S, of fluorophores over a spherical membrane surface as a function of angular position on the membrane is:

5.11) $$F_S \propto \iint p\,(\theta', \varphi') f(\theta', \varphi') \sin\theta' d\theta' d\varphi'$$

where the limits of integration on φ' are 0 to 2π, the limits of integration on θ' are either 0 to θ_{MAX} (cone model) or 0 to 2π (Gaussian model), and $p(\theta',\varphi')$ is the absorption probability. $p(\theta',\varphi')$ is equal to $\cos^2(\theta')\sin^2(\theta')\cos^2(\beta)$ in membrane coordinates (Figure 5.2) which is $|x_{3,l}|^2(\theta',\varphi',\rho)\,(1-|x_{3,l}|^2(\theta',\varphi',\rho))\cos^2(\beta)$ in terms of the Cartesian components of the unit dipole in the lab coordinate system. If we assume

that the molecule rotates around the long axis faster than it wobbles or that all orientations of the molecular plane are equally probable, then integration over β from 0 to 2π simply yields an additional multiplicative factor of π.

The total fluorescence intensity, I, collected at an arbitrary analyzer orientation Ψ with respect to the excitation light polarization, where $\Psi = 0$ for the parallel component and $\Psi = \pi/2$ for the perpendicular component of fluorescence emission, is given by (Florine-Casteel 1990):

$$5.12) \quad I(\theta,\varphi,\rho) = \iint F_S\,[K_a x_1^2(\theta,\varphi,\rho) + (K_b\cos^2\Psi + K_c\sin^2\Psi)x_2^2(\theta,\varphi,\rho) + (K_b\sin^2\Psi + K_c\cos^2\Psi)x_3^2(\theta,\varphi,\rho) + 2(K_b - K_c)\sin\Psi\cos\Psi x_2(\theta,\varphi,\rho)x_3(\theta,\varphi,\rho)]\sin\theta\, d\theta\, d\varphi$$

where x_i are now the components of the emission dipole (unprimed coordinates) in the lab frame. The constants K_a, K_b, and K_c are the factors that account for the mixing of polarizations of the emitted fluorescence due to a high numerical aperture (*NA*) objective as determined by Axelrod (1979):

$$5.13) \quad K_a = \frac{(2 - 3\cos\alpha + \cos^3\alpha)}{6(1 - \cos\alpha)}$$

$$K_b = \frac{(1 - 3\cos\alpha + 3\cos^2\alpha - \cos^3\alpha)}{24(1 - \cos\alpha)}$$

$$K_c = \frac{(5 - 3\cos\alpha - \cos^2\alpha - \cos^3\alpha)}{8(1 - \cos\alpha)}$$

where $NA = R\sin\alpha$ and R is the refractive index of the lens immersion medium (1.33 for the 60x water immersion lens used in these experiments). Equation 5.12 can be modified to include the additional variables of the fraction of fluorophores that may be aligned parallel to the membrane surface, and the net tilt angle of the cone axis due to

a net tilt of the lipid director (Florine-Casteel 1990).

5.4 MATERIALS AND METHODS

Optical apparatus

A diagram of the experimental apparatus is shown in Figure 5.3. Equatorial images of GUV's were obtained by illuminating GUV's with ~200fs pulsed light at 780nm and 80MHz from a Titanium-Sapphire laser (Tsunami, Spectra Physics, Mountain View, CA). Non-descanned images were collected using Hamamtsu (Middlesex, NJ) gallium arsenide phosphate (GaSP) photomultiplier tubes (PMT's) interfaced to a Biorad MRC 600 scanbox. Excitation light was converted from elliptically polarized light to linearly polarized light using a Berek's compensator (New Focus, San Jose, CA). Illumination powers were kept as low as possible to prevent photo-bleaching and photo-damage of the samples. Fluorescence emissions and images were separated into parallel and perpendicular polarizations, with respect to the polarization of the excitation light, using a polarizing beam splitter cube (Thorlabs, Newton, NJ). For naphthopyrene and perylene labelled samples, a 490nm short pass emission filter (Chroma Technologies, Rockingham, VT) was used in front of each PMT, and for terrylene and LR-DPPE, a 600nm long pass emission filter (Chroma Technologies) was used.

To compensate for the depolarizing effects of optics through the scanbox on the excitation light, a polarizing film on a rotatable mount was placed atop the stage with the objective lens removed. A power meter was placed on top of the film and the film polarization axis was set to correspond to the $X_{3,l}$ direction in the image plane. The Berek's compensator was then adjusted to achieve maximum intensity for the desired polarization direction in the image plane.To account for depolarizing effects of the emission pathway, which may impart a false value for the tilt of gel phases, pure DOPC vesicles labeled with LR-DPPE were imaged and the orientation of the beam-

splitting cube was adjusted to give maximum intensity in the direction perpendicular to $X_{3,l}$; these vesicles will display a polarization pattern perpendicular to that of the PAH dyes since the fluorophore rests on the head-group region parallel to the membrane normal (see Chapter 2 of this dissertation and Baumgart et al 2007b). For this fluorophore, the choice of lipid phase is irrelevant because of the exterior location of the fluorophore: it is not affected by chain order/disorder.

Sample preparation

DOPC, cholesterol, SSM, and LR-DPPE were purchased from Avanti Polar Lipids (Alabaster, AL) and used without further purification. Plant derived cholesterol

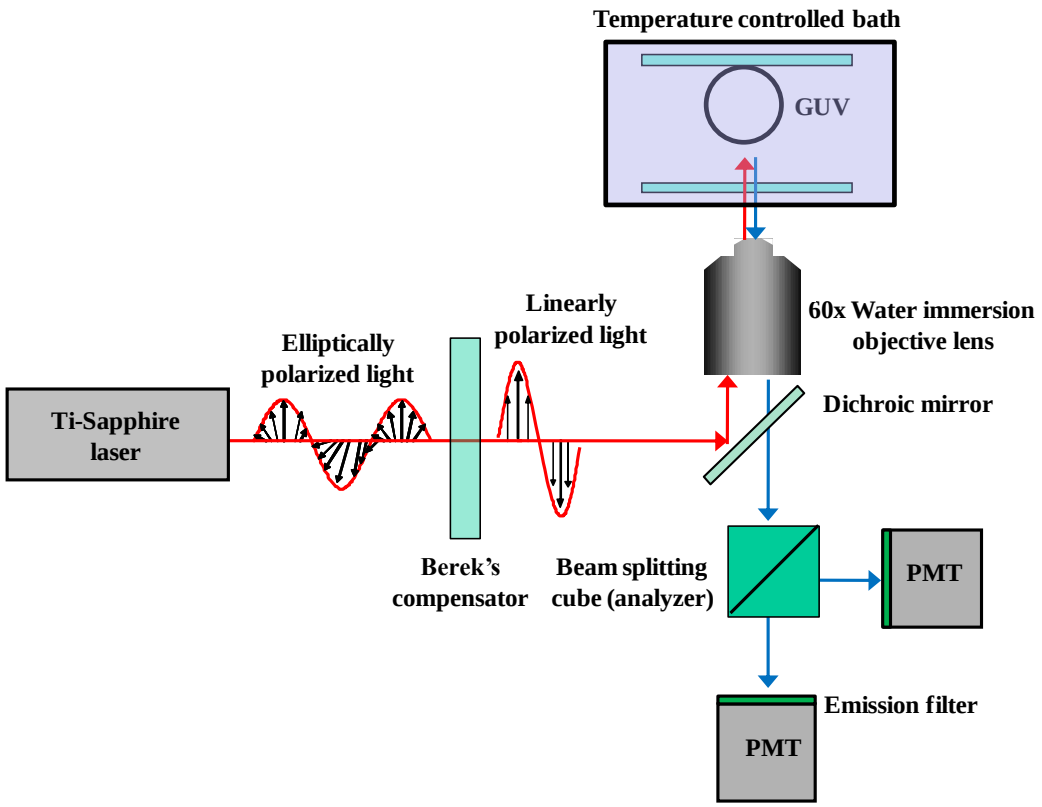

Figure 5.3 Experimental apparatus. 780nm light (red) is linearly polarized by the Berek's compensator. Fluorophores within an equatorial section of the GUV are excited. The emitted fluorescence (blue) is separated into parallel and perpendicular components using a beam-splitting cube. For phase-separated GUV's, additional band-pass emission filters are placed in front of the PMT detectors.

and BSM were purchased from Avanti as well. Naphthopyrene and perylene were purchased from Sigma-Aldrich (St. Louis, MO) and terrylene was purchased from Chiron (Trondheim, Norway). DOPC and LR-DPPE were purchased in chloroform, while SSM, naphthopyrene, terrylene, and cholesterol were purchased in powder form and dissolved in HPLC-grade chloroform (Mallinkroft Baker, Phillipsburg, NJ). The concentrations of lipid-chloroform stock solutions were determined by the organic phosphate analysis method described by Kingsley and Feigenson (1979).

GUV's were prepared by a modified version (Ayuyan and Cohen 2006) of the electroswelling procedure described by Angelova et al (1986 and 1992). Briefly, titanium-oxide coated titanium plates were used in place of ITO-coated slides. Lipid mixtures containing dyes at a ratio of at most 1:500 dye:lipid in chloroform were deposited onto the titanium plates under a nitrogen stream. The slides were then placed in vacuum for at least 4 hours to evaporate any remaining solvent. Slides were transferred to a nitrogen glove box where the remaining steps of the typical electroswelling procedure were carried out. GUV's were produced in 100mM sucrose prepared with filtered water; solutions were sparged with nitrogen gas for at least 20 minutes prior to use in electroswelling to remove any dissolved oxygen. An AC voltage of 1.25 V (Vpp) at 8 Hz was applied across the plates for 1.5-2 hours. Vesicles were then slowly cooled to room temperature under nitrogen atmosphere. Aliquots were put into sealed "sandwiches" consisting of a glass slide and a cover glass separated by Fomblin high vacuum grease and sealed by clear nail polish. GUV's in all aliquots were osmotically swelled by the additional of sparged, deionized water unless otherwise indicated.

Data

Each GUV of each composition point produced two images: one of the fluorescence emission parallel to the direction of excitation light polarization, and one

perpendicular to it (Figure 5.4a). Traces of relative intensity versus angle (ρ) around the perimeter of an equatorial section of a GUV are depicted in Figure 5.4b. These were obtained from GUV images (Figure 5.4a) using a custom Labview routine described in the appendix (National Instruments, Austin, TX) which extracts the raw intensity between two concentric regions of interest containing the image of the membrane. For each image, the average background intensity was subtracted from the intensity versus ρ data. On average, background intensities were no more than 20% of the maximum signal intensity. The data were then normalized by the maximum intensity value such that each result for a particular composition had a maximum of 1, and then the normalized data were averaged. Traces were obtained for at least 10 separate GUV's per composition point, and the sample deviations are depicted as error bars in Figure 5.4b. Intensity in the perpendicular direction is corrected by multiplication of intensity value by a quantity known as the *g*-factor (Chen and Bowman 1965, Dix and Verkman 1990).The data were then fit to steady-state solutions (equation 5.12) of the Smoluchowski equation using two different models of probe rotational diffusion in the membrane interior.

5.5 RESULTS AND DISCUSSION

5.5a BINARY SAMPLES

The samples used in this study are depicted on the phase diagram for the DOPC/SSM/Cholesterol GUV system in Figure 5.5. DOPC/cholesterol samples are denoted as red points on the left axis of the diagram, and SSM/cholesterol samples as blue points on the right axis of the diagram. The blue-and-red points represent ternary samples. The L_o-L_d coexistence region is depicted for reference as blue and red markers in the middle. This diagram was determined using temperature-controlled optical microscopy of GUV's (Chapters 3 and 4 of this dissertation).

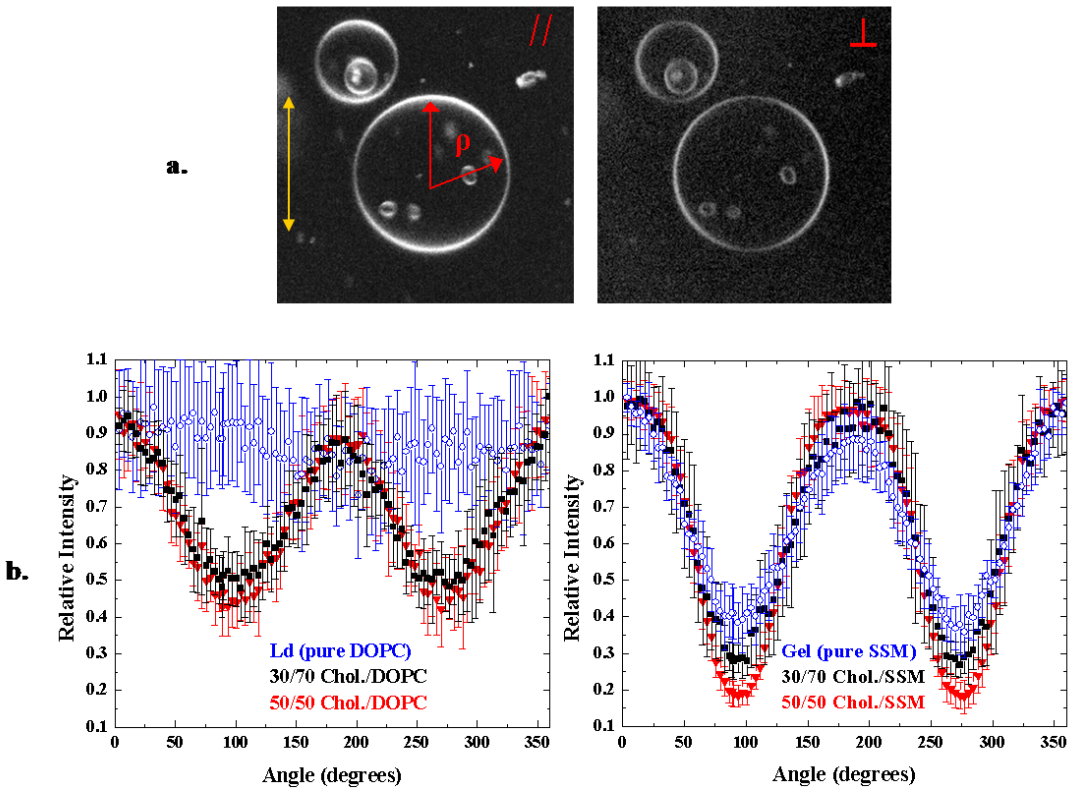

Figure 5.4 Angular intensity of GUV slices. a) The parallel (left) and perpendicular (right) components of terrylene fluorescence are shown in a SSM sample containing 30% cholesterol. The yellow arrow on the left indicates the polarization direction of the excitation light with respect to the image orientation. Excitation: 780nm. The data are collected as intensity versus angle, ρ. For each composition, at least 10 such images were used to obtain an appropriate sample size. b) The numerical data (intensity vs. ρ) for terrylene in DOPC (left) and SSM (right) samples with varying amounts of cholesterol. In both cases, the blue curve is 0% cholesterol, the black curve is 30%, and the red curve is 50% cholesterol.

Fits with different models

A summary of the data is given in Table 5.1. Terrylene was sensitive to a higher degree of order than napthopyrene and perylene, which is expected because larger molecules experience less freedom of motion; this is reflected in both the intensity versus angle data for all three PAH dyes in pure SSM (Figure 5.6) and from the corresponding order parameters (Table 5.1).

When the normalized intensity versus angle (ρ) data are fit to equation 5.12,

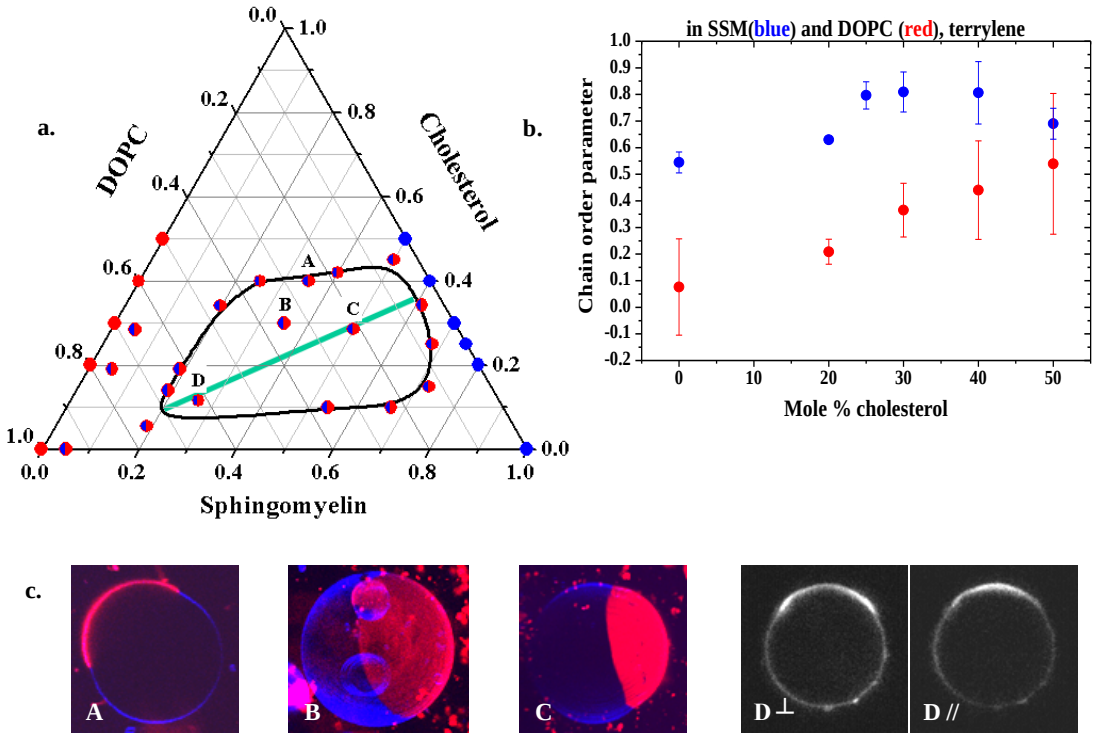

Figure 5.5. Phase diagram. a) The ternary diagram for the SSM/DOPC/cholesterol system at 22°C. L_o-L_d phase coexistence region (blue and red points) was determined by temperature-controlled 2-photon microscopy. Binary SSM samples containing cholesterol are depicted as blue points on the rightmost axis, and binary DOPC samples containing cholesterol as red points on the left axis. Ternary samples are depicted as blue and red points; those that display L_o-L_d coexistence are marked A-D. The tie line determined from polarization imaging is depicted as a blue line between samples C and D. b) The chain order parameters as functions of cholesterol content obtained with the Gaussian model for binary samples are shown. The points correspond to those on the binary axes of the phase diagram in (a). c) Images of the ternary samples A-D. A, B, and C are shown labelled with naphthopyrene and LR-DPPE (780nm excitation), though polarization data was obtained with terrylene labeling. Blue (naphthopyrene) corresponds to L_o and red (LR-DPPE) corresponds to L_d. Sample D is shown labelled with only terrylene; the bright region corresponds to the L_o phase, into which terrylene preferentially partitions (780nm excitation).

the Gaussian model for $f(\theta,\varphi)$ gave the best fit for both dyes in both the DOPC and SSM binary samples as well as the ternary samples, with respect to the residuals of the fits. This is demonstrated in Figure 5.7 which depicts a SSM sample containing 40

Table 5.1. Binary sample data. Average molecular acyl chain order parameters were determined using steady state imaging for different dyes with different models as a function of cholesterol content. It is obvious from the numerical values that terrylene is the most sensitive to changes in composition. The cholesterol ('chol.') content is mole % of the total lipid.

Sample	Chol.	Terrylene		Naphthopyrene		Perylene	
		Cone	Gaussian	Cone	Gaussian	Cone	Gaussian
SSM-chol. (L_o)	0	0.85 ± 0.02	0.54 ± 0.04	0.84 ± 0.04	0.33 ± 0.43	0.84 ± 0.01	0.49 ± 0.01
	20	0.86 ± 0.01	0.63 ± 0.01	0.84 ± 0.04	0.43 ± 0.36	--	--
	25	0.91 ± 0.04	0.80 ± 0.05	--	--	--	--
	30	0.90 ± 0.03	0.81 ± 0.08	0.84 ± 0.04	0.47 ± 0.23	--	--
	40	0.93 ± 0.07	0.81 ± 0.12	0.84 ± 0.04	0.43 ± 0.29	--	--
	50	0.86 ± 0.02	0.69 ± 0.06	0.85 ± 0.02	0.42 ± 0.07	--	--
DOPC-chol. (L_d)	0	0.36 ± 0.01	0.08 ± 0.18	0.79 ± 0.03	0.08 ± 0.09	--	--
	20	0.68 ± 0.09	0.21 ± 0.05	--	--	--	--
	30	0.80 ± 0.05	0.37 ± 0.10	0.84 ± 0.01	0.24 ± 0.04	0.80 ± 0.11	0.40 ± 0.34
	40	0.83 ± 0.03	0.44 ± 0.19	0.83 ± 0.03	--	--	--
	50	0.84 ± 0.03	0.54 ± 0.26	0.84 ± 0.03	0.39 ± 0.08	--	--

mole % cholesterol. The graphs show the averaged intensity versus angle data for the parallel component of terrylene fluorescence. Here one can easily see that the black line (Gaussian model) fits the data slightly better than the red line (cone model). This is in accordance with previous observations concerning the accuracy of models of chain order (Jahnig 1979, Kinosita et al 1982) for binary samples where a Gaussian model was also tested and fit the data better. However, this conflicts with recent data concerning ternary samples (Haluska et al 2008). The discrepancy is likely due to the

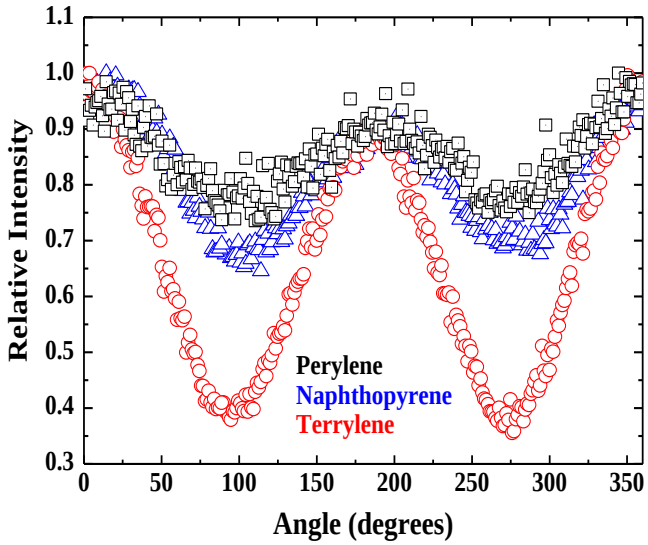

Figure 5.6 Three PAH dyes in SSM. The graph depicts the relative fluorescence intensity of the parallel component of fluorescence versus angle around the membrane perimeter for three PAH dyes, terrylene (red), naphthopyrene (blue), and perylene (black). The difference between the value of relative intensity for the maximum and minimum increases as a function of molecular size with terrylene having the largest, followed by naphthopyrene, and then perylene.

differences in probe geometries: in Haluska et al (2008), DPH and headgroup-labeled lipids were used.

Both models show the same qualitative trends in the chain order parameter as a function of cholesterol, as depicted in Figure 5.8, but terrylene is much more sensitive: there is a much larger change in the computed order parameter with cholesterol content for terrylene, in accordance with the data in Table 5.1 and Figure 5.6. For both DOPC and SSM, the order parameters determined using the Gaussian model appear lower than those determined using the cone model, most likely due to the different definitions of the chain order. This is inconsequential for the ultimate goal of determining tie lines so long as the same model is used for all compositions and temperatures (or that an appropriate relation between models is established). It should be noted that the use of probes that model cholesterol must influence membrane fluidity; we have not taken the probe concentrations into account in the overall

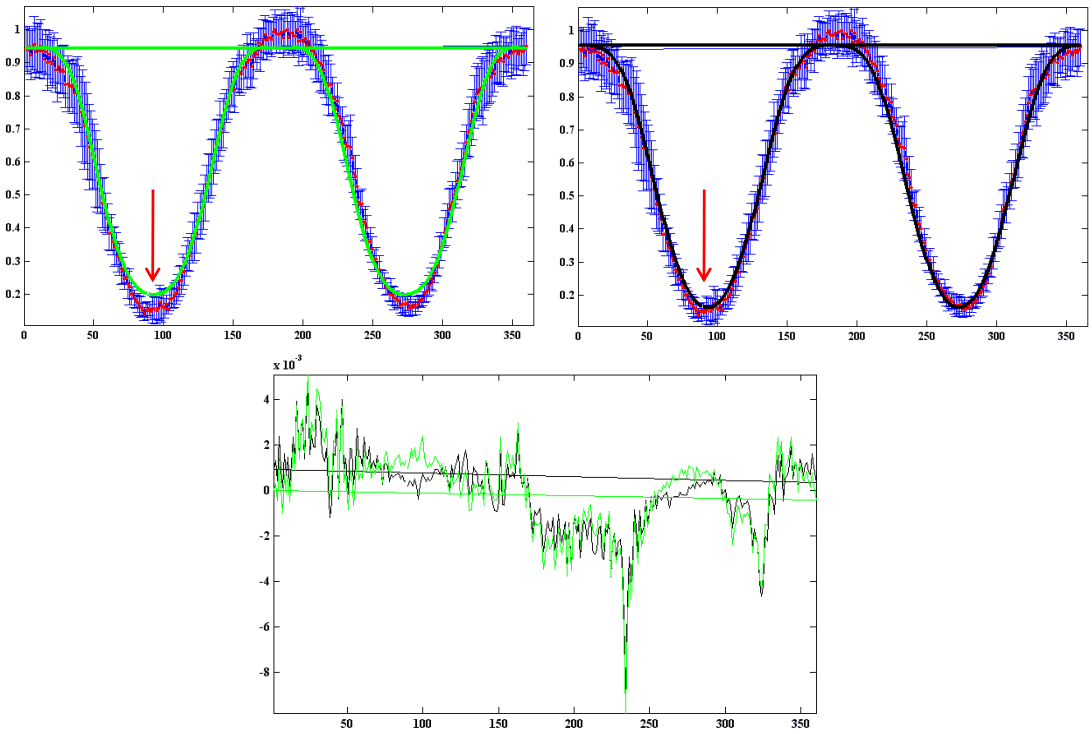

Figure 5.7 Fits and corresponding residuals. The Gaussian model (black line) and the cone model (green line) are compared for the same data from the parallel component of terrylene in a SSM sample containing 40 mole % cholesterol. Notice that the Gaussian model fits the data slightly better (red arrows) and has slightly lower residuals. The x-axis in each of the three graphs represents the angle around the membrane (in degrees) and the y-axis represents the relative fluorescence intensity. Data are depicted as red dots and the error bars are blue. The y-axis of the lower graph represents the residual value between the fitted and measured data.

cholesterol concentrations. Thus, the data are not absolute measures of chain order but rather are relative measures, as stated earlier.

It is interesting to note the appearance of a bump in the order parameter versus cholesterol content for the SSM-cholesterol data (Figure 5.8 left) with the dye terrylene. This may represent phase separation. Macroscopic phase separation in sphingomyelin systems has never been observed with microscopy, but has been postulated to exist from ESR and NMR data (Guo et al 2002, Collado et al 2005, Sanakram and Thompson 1990b). Moreover, the cholesterol mole fractions where this occurs, between 20% and 30%, are in accordance with those found in Sanakram and

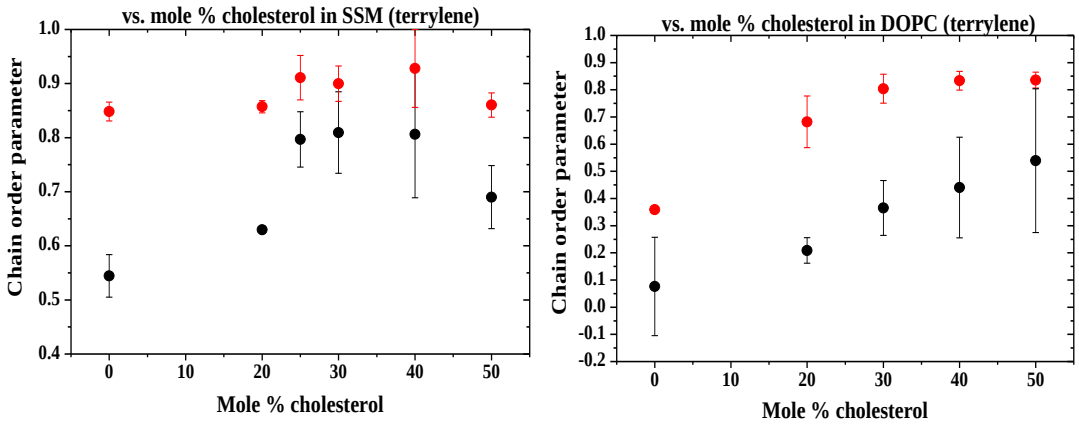

Figure 5.8 Cone and Gaussian for terrylene in binary DOPC- and SSM-cholesterol GUV's. The Gaussian model is depicted by black markers and the cone model is depicted in red markers. Chain order parameter data for SSM-cholesterol samples are shown in the left graph, and data for DOPC-cholesterol samples are shown in the right graph.

Thompson (1990b).

The order parameter versus cholesterol content graphs for DOPC show trends in accordance to those observed in fluid-phase lipid-cholesterol systems investigated by other groups using x-ray diffraction (Mills et al 2008), imaging (Haluska et al 2008), and NMR (Warachawski et al 2005), though the absolute magnitude of the order parameters are different in each case.

Two other types of samples were examined: one set with different cholesterols and one set with different SMs. The cholesterols used in the first set were 98% pure cholesterol from ovine wool and 99% pure cholesterol from plant sources (both from Avanti). Binary samples of 30 and 50 mole % cholesterol with DOPC and a sample with 50 mole % cholesterol and SSM were prepared using terrylene as the fluorophore. Data was taken from at least 8 vesicles for each sample and the results obtained by fitting to the Gaussian model are displayed in Table 5.2. For all three samples, GUV's prepared with the less pure cholesterol had slightly lower order parameters, though it could be argued that the difference is not statistically relevant.

Table 5.2 Comparison of different cholesterols and SMs. The average molecular chain order parameters for GUV's made with different cholesterols and SMs are tabulated. In all cases, the dye used was terrylene and the angular emission patterns were fit using the Gaussian model.

	Sample composition	Permutation	Average chain order parameter (terrylene)
Cholesterol comparison	30% cholesterol, 70% DOPC	Plant (99% pure)	0.37±0.10
		Wool (98% pure)	0.24±0.03
	50% cholesterol, 50% DOPC	Plant (99% pure)	0.54±0.26
		Wool (98% pure)	0.52±0.24
	50% cholesterol, 50% SSM	Plant (99% pure)	0.69±0.06
		Wool (98% pure)	0.66±0.08
SM comparison	100% SM	SSM	0.54±0.04
		BSM	0.39±0.03
	50% cholesterol, 50% SM	SSM	0.69±0.06
		BSM	0.41±0.03

However, that was not the case for vesicles in which SMs were compared. Samples containing pure SM and 50 mole % (99% pure) plant cholesterol with SM were prepared with terrylene and 8 vesicles were used for each sample. The results, in Table 5.2, show a dramatic difference: in all cases, BSM had significantly lower order parameters. This may actually come as a surprise since porcine BSM contains many long chain saturated SMs (Filipov et al 2006) which could be expected to form van der Waals bonds with neighboring lipids. However, hydrophobic mismatch and interdigitation may lead to a disruption in orderly packing in this case.

5.5bTERNARY SAMPLES

The results of the experiments on binary GUV's described in section 5.4a are very encouraging. If changes in the probe environment in the L_d and L_o phase with cholesterol concentration can be measured, then the approximate locations of tie lines can be found in phase separated vesicles because the L_o and L_d phases across a tie have the same compositions and thus would be expected to have the same order parameters. The imaging technique is limited to vesicles for which the area fractions of both phases cover an angular distance, ρ, of at least 90°, which ensures that both a

maximum and a minimum of the intensity profile can be recorded.

First, a set of controls was prepared in order to check that the order parameter versus composition followed similar trends in ternary vesicles as binary vesicles. This was only possible with L_d phases on the left, or low SSM, side of the phase diagram in Figure 5.5, however, because phase separation at as little as 5 mole % DOPC was observed for the high SSM (right) side of the diagram. This phase separation is depicted in Figure 5.9 for the compositions SSM/DOPC/cholesterol = 0.61/0.05/0.34 (left) and 0.75/0.05/0.20 (right).

The same strategy for observing *S* as a function of cholesterol as described for binary samples in section 5.4a was applied to ternary samples. Three ternary samples were prepared with cholesterol:DOPC ratios of 0:100, 20:80, and 30:70. SSM was added to each such that every sample contained 5% SSM. The sample compositions were thus cholesterol/SSM/DOPC = 0.00/0.05/0.95, 0.19/0.05/0.76, and0.285/0.05/0.665. The locations of these samples on the ternary diagram are shown in Figure 5.5. None of these samples showed macroscopic phase separation. All three

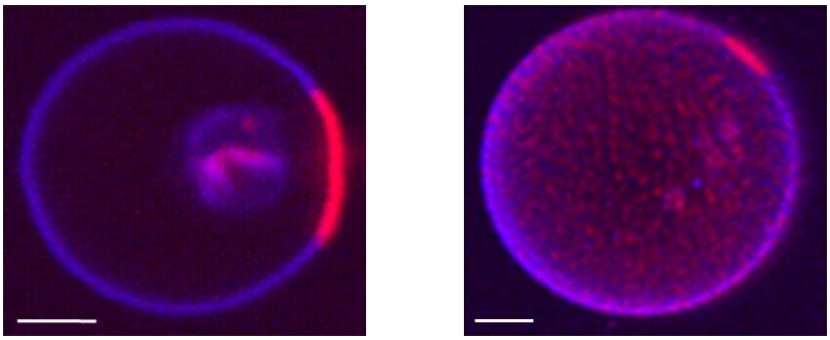

Figure 5.9 Phase separated samples at 5 mole % DOPC. Investigations of trends in the order parameter versus composition for optically homogenous ternary samples of a high SSM, L_o-like phase was not possible due to phase separation very near the SSM-cholesterol axis of the ternary phase diagram (Figure 5.5). The vesicles pictured here were labeled with naphthopyrene (blue) and LR-DPPE (red) excited at 780nm. The compositions were SSM/DOPC/cholesterol = 0.61/0.05/0.34 (left) and 0.75/0.05/0.20 (right). Scale bars are 5μm.

samples were prepared with the dye terrylene added at 0.1 mole %, and the data was fit using the Gaussian model. The ternary data are depicted in Table 5.3.

Chain order parameters were determined in the same manner as those for the binary samples using the Gaussian model. Plotting the chain order parameter versus cholesterol:DOPC ratio (Figure 5.10) indicated a slightly greater degree of chain order in the sample containing the fully saturated lipid at 5 mole percent versus the binary samples.

Next, the order parameters for four phase-separated ternary samples (depicted in Figure 5.5) were determined. Samples were labeled with terrylene at 0.1 mole percent. Compositions analyzed were cholesterol/SSM/DOPC = 0.4/0.35/0.25 (A), 0.30/0.35/0.35 (B), 0.29/0.50/0.21 (C), and 0.12/0.26/0.62 (D). The data are depicted in Table 5.3. It was observed that both the L_o phases and the L_d phases of samples C and D had the same average order parameters. Thus, these compositions likely lie along a tie line. The direction of this tie is consistent with those determined by ESR (Smith and Freed 2009) and by NMR (Veatch et al 2004). The slope is shallow, but is not parallel to the base of the ternary diagram, indicating the cholesterol does not partition equally into the two phases: cholesterol favors the L_o phase. This is also

Table 5.3 Ternary sample acyl chain order parameter data. The average chain order parameters for ternary GUV's determined using terrylene fluorescence and fitting to the Gaussian model are displayed. Samples A-D were phase separated, while the other three were optically homogeneous.

Cholesterol/SSM/DOPC	L_d phase OP (terrylene)	L_o phase OP (terrylene)
0/5/95	0.14±0.07	--
19/5/76	0.26±0.05	--
28.5/5/66.5	0.41±0.12	--
12/26/62 (D)	0.20±0.21	0.69±0.08
29/50/21 (C)	0.21±0.08	0.69±0.07
30/35/35 (B)	--	0.84±0.08
40/35/25(A)	--	0.78±0.04

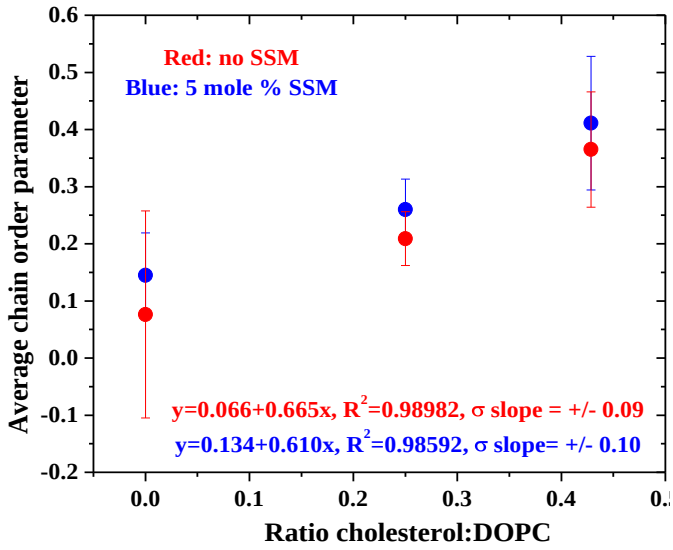

Figure 5.10 Order parameter versus DOPC:cholesterol ratio for ternary samples containing a fixed amount of SSM (5 mole %). Average molecular acyl chain order parameters were determined at each composition using at least eight different vesicles and fitting the angular intensity data to the Gaussian model.

consistent with recent mass spectrometry data on planar bilayers composed of POPC, SM, and cholesterol, where it was observed that cholesterol partitioned more favorably into the phase with a higher percentage of the saturated lipid (McQuaw et al 2007). If one neglects the variation in composition from vesicle to vesicle and uses only the inherent error in the measurement of the concentrations of the lipid and cholesterol stock solutions, the data is still consistent with a non-horizontal tie-line. The estimated error in composition is less than 2% for the lipids, as determined by the phosphorous assay (Kingsley and Feigenson 1979) and no greater than 5% for cholesterol based on the calibration of the Hamilton syringes used to prepare stock solutions. Moreover, whole-vesicles extracted from similar preparations were analyzed by mass spectrometry, as described in Chapter 6 of this dissertation, and were found to agree with the expected molar ratios of each lipid and cholesterol to within 2%. Rough estimates of the tie line direction were also deduced using mass spectrometry and were found to be consistent with this slope.

5.6 CONCLUSIONS

The results of this study indicate that one can obtain useful measures of the relative chain order parameters in lipid bilayers by all-optical means. Possible evidence of phase separation along the SSM-cholesterol binary system was observed (Figure 5.8). Terrylene was superior in sensitivity to membrane order versus the smaller PAH dyes napthopyrene and perylene.

This kind of data can be used to investigate phase separated GUV's within the L_o-L_d coexistence region. It can and should be use to find definitive boundaries of the three-phase region of the ternary cholesterol/SSM/DOPC system (Chapter 3): within a three phase triangle on a ternary diagram, each of the phases have the same composition anywhere within the triangle at constant temperature, but the phases are present in different amounts.

Phase behavior should be studied with respect to temperature dependence as well as composition in future research. Recent literature suggests that there may be uncoupling between the miscibility transition (order parameter) and the acyl chain conformational order parameter (McConnell and Radhakrishnan 2007 and 2008). If the miscibility and the chain order are uncoupled, or least not coupled in any predetermined manner, it makes sense to consider each order parameter separately in order to deduce the correlation. These references show that even above the highest miscibility transition temperature for a ternary lipid mixture (DOPC/DPPC/ cholesterol), there exists a fraction of chain ordered phase in matrix otherwise homogeneous with respect to the composition parameter. It may be that ternary mixtures that exhibit an L_o phase require at least two order parameters (Neilson et al1996, Zhong et al 1998, Watanabe and Usui 1985) for a valid theoretical treatment or they may be better described by a decorated Ising model instead of a traditional Ising model (McConnell 2009, Wu 1973).

It should be noted that in conventional fluorescence imaging, one loses detailed information about the nature of different kinds of rotations that time dependent methods can measure (Lakowicz et al 1992, Ariola et al 2006, van Blitterswik et al, Hare 1983). Fluorescence lifetimes have been shown to change as a function of composition and are more sensitive to environmental changes. Time-resolved measurements also allow one to probe the dynamics, which become important when considers the process of phase separation and critical phenomena.

In an alternative method to the one outlined here, one could calculate the steady state anisotropies from the parallel and perpendicular images and extract a chain order parameter using the relations as outlined by Van Blitterswik et al (1981).

CHAPTER 6: MASS SPECTROMETRY

6.1 INTRODUCTION

Mass spectrometry has been used successfully to profile lipid species in complex biological samples (Wenk et al 2003, Gu et al 1997, Sandhoff et al 1999). Recent experimental evidence obtained using this technique supports the raft hypothesis when detergent-resistant (Fridriksson et al 1999, Ivanova et al 2001) or antibody selective lipid domains (Surviladze et al 2007) are analyzed using mass spectrometry. It has more recently been applied to models of the plasma membrane (Kraft et al 2006, McQuaw et al 2007) to answer fundamental questions regarding cholesterol partitioning into phases and domain distribution. Mass spectrometry can also be used to investigate the products of chemical reactions such as oxidized lipids (Spickett and Dever 2005); these impurities are important perturbations on observed phase behavior in model membrane systems (Ayuyan and Cohen 2006, Zhao et al 2007).

The main goal of this project was to determine the tie lines for the ternary DOPC/SSM/cholesterol system by analyzing portions of excised GUV domains using mass spectrometry, as depicted schematically in Figure 6.1. Patches of domains were excised using techniques drawn from the patch-clamping field in neurobiology (Opsahl and Webb 1994, Larmer et al 1997). Ultimately, this goal was not resoundingly successful, though approximate tie line directions at 22°C were obtained. This will be explained in the discussion section and the sample preparation techniques responsible for this failure should be revised so that this promising hybrid of techniques can be used in the future.

This experiment was intended to complement the all-optical technique of finding tie lines described in Chapter 5 of this dissertation. In an absolute sense, the optical technique is model dependent, and the assumptions contained in that model

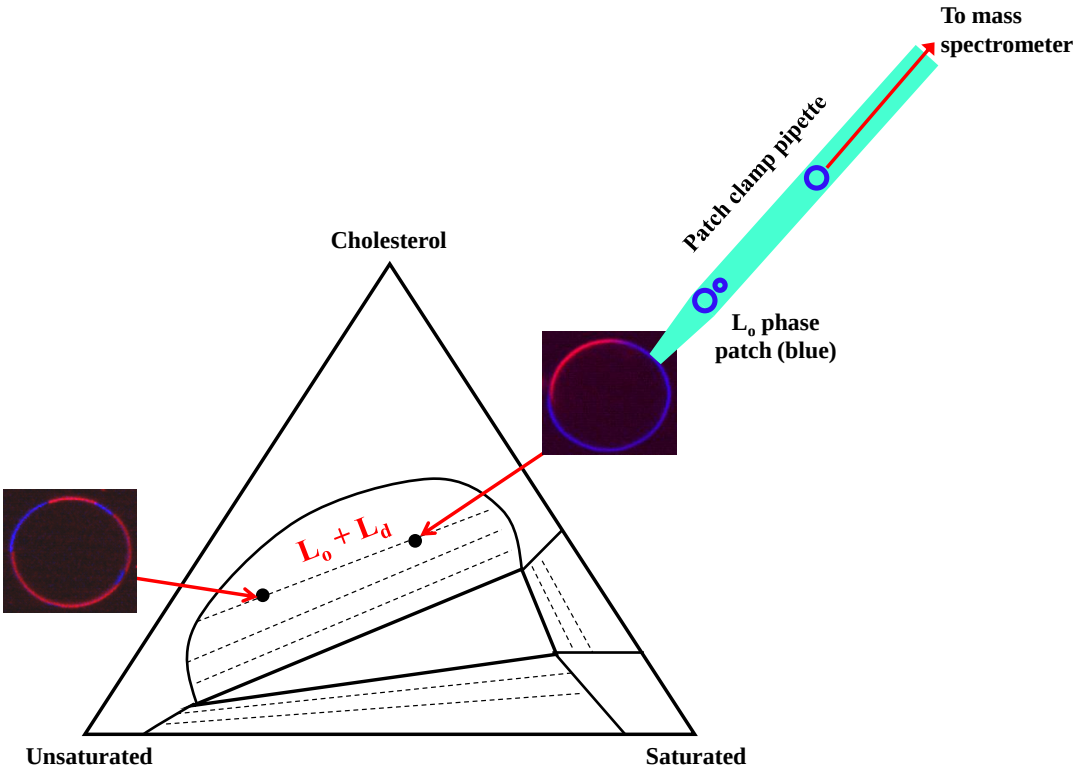

Figure 6.1 Experimental method. Two different overall compositions produce two different kinds of GUV's. If these compositions lie along a tie line as depicted here, the composition of the L_o (blue) and L_d (red) phases, in terms of molar ratios of the three components will be the same for both sets of GUV's. Only the relative proportions (area fraction) of the two phases will change across the tie line. Because mass spectrometry is sensitive to the relative abundance of the components of mixtures, it can be used to determine the tie lines. Pieces of each phase for GUV's with different overall compositions are collected with a patch clamp micropipette and then analyzed by mass spectrometry; GUV's with the same relative molar proportions of the three components lie along a tie line.

dependence may lead to ambiguities in the interpretation of the data. With a mass spectrometry based approach, there are no theoretical assumptions except that the composition excised is representative of the bulk phase being probed. In other model membrane analyses using mass spectrometry (Kraft et al 2006, McQuaw et al 2007), only planar bilayers are used and these have certain caveats with respect to substrate interference (Rinia et al 2001). The experiments described here involve GUV samples

prepared from the ternary mixture of DOPC/SSM/cholesterol. It is important to sample from GUV's for tie line determination since other methods require different sample geometries. Previous mass spectrometry on model membranes (McQuaw et al 2007, Kraft et al 2006) require planar bilayers; even in the absence of substrate-induced effects in planar bilayer, it is well know that curvature plays an important role in lipid sorting (Baumgart et al 2003) and morphology (Leibler and Andleman 1987). Thus, our sampling method preserves this important parameter.

6.2 MATERIALS AND METHODS

Samples

DOPC, SSM, and cholesterol were used to prepare GUV's. Oleoyl-stearoyl PC (OSPC) was used as an internal standard for DOPC; D-7 deuterated cholesterol was used as an internal standard for cholesterol; and N-heptadecanoyl SM (C-17 SM) was used as an internal standard for SSM. DOPC, SSM, cholesterol, D-7 cholesterol, and OSPC were purchased from Avanti Polar Lipids (Alabaster, AL) and used without further purification. C-17 SM was purchased from Matreya (Pleasant Gap, PA). Ternary GUV samples were prepared from chloroform-lipid solutions as described in Chapter 3. The anaerobic electroformation method on titanium electrodes was used. GUV's were not osmotically swelled, because it was easier to adhere the patch pipette to flaccid vesicles. The fluorescent dyes LR-DPPE and naphtho[2,3a]pyrene were added at 0.1 mole % each to aid in visualization and phase assignment. The concentrations of all phospholipid stock solutions were checked with the microphosphorous assay (Kingsley and Feigenson 1979) as described in the appendix.

Pipettes

Micropipettes were prepared from 1.5mm OD borosilicate glass capillary tubes containing microfilament using either an automated P-2000 Sutter Instruments laser puller (Novato, CA) or a Narishige PC-10 (East Meadow, NY) manual puller. Tips

were pulled to approximately 1-5um ID (~ 10MΩ). The necessary pressure to engage a patch was determined by measuring the change in resistance of the micropipette before and after patch adherence; this is a standard measurement in patch clamping. Recordings were obtained using an Axopatch 200B amplifier (Axon Instruments, Foster City, CA). An example of a recording is depicted in Figure 6.3 for a vesicle made of composition cholesterol/SSM/DOPC = 0.4/0.3/0.3 and labeled with terrylene at 0.1 mole %.

Visualization

GUV's were dispensed into Maytek wells with # 1.0 or # 1.5 glass bottoms and imaged using both wide field fluorescence microscopy and transmitted light microscopy on a Zeiss Axiovert 135 microscope. Fluorescence was used to focus the field of view and, check for sample irregularities, and select GUV's for excision. Then, the apparatus was switched to transmitted light mode in order to view and orient the pipette tip. During excision, both modes were used: a slight amount of transmitted light was permitted during fluorescence imaging such that the outline of the pipette and the GUV fluorescence could be simultaneously observed. An example of the image is depicted in Figure 6.2. Excitation was kept at minimum power to prevent oxidation because samples were collected in open atmosphere.

Patch excision

The imaging apparatus is exactly the same as that depicted in Chapter 3 with a micro-positioning device mounted onto the microscope stage. The pipette position was controlled by a Luigs and Neumann micro-positioning device (SM5, Ratingen, Germany). Pipettes were pulled on their day of use. They were then filled with a 100mM sucrose solution by first applying suction to the pipette with the tip immersed in the sucrose solution and then back-filling the remaining pipette volume with a small diameter syringe attachment (MicroFil, World Precision Instruments, Sarasota, FL)

that fits inside the untapered portion of the pipette. Pressure was applied to the loaded pipette using a home built system calibrated with a micropressure gauge (World Precision Instruments, Sarasota, FL). Positive pressure (~5 mmHg) was applied to the pipette as it was lowered into the GUV chamber to prevent vesicles from being sucked up. Patches of domains were excised by applying negative pressure (suction) after touching the pipette tip to the outside of a GUV. Once the GUV was adhered, the membrane patch was visible inside the pipette body as shown in Figure 6.2. To dislodge the GUV, the pipette tip was quickly moved in the vertical direction away from the objective lens (along the optical axis), though this is not the most reliable method and may have contributed to sampling errors. The objective lens was then refocused onto the pipette to make sure that the patches remained adhered to the inner wall, though this was not always visible.

Once the patches were excised, the pipette was transferred to a glass vial containing methanol and cleaned by the alternating application of positive and negative pressure to wash off the contents adhering to the pipette walls. Only one patch was excised per pipette, making the sample collection process extremely time-consuming. The amount of lipid in each patch was estimated assuming a 5μm pipette,

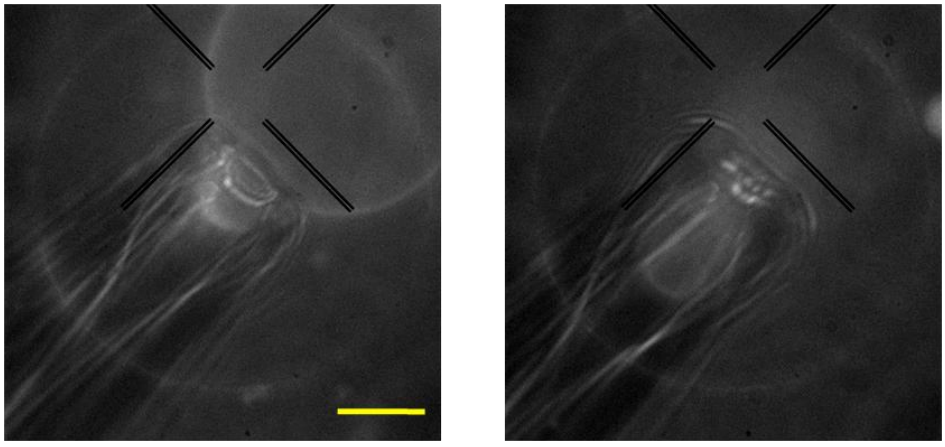

Figure 6.2 A vesicle before (left) and after (right) patch excision. The vesicle was in the L_d phase and was labeled with LR-DPPE. The vesicle composition was cholesterol/SSM/DOPC = 0.38/0.13/0.49. Scale bar: 10μm. *T* = 22° C.

0.4nm^2 area per lipid, and 700 g/mole per lipid. Assuming a circular patch of diameter 5µm is excised, these conditions yield approximately 2pg lipid per patch as a lower limit, not counting sample loss or cholesterol. However, the actual amount is likely higher because the patch was often significantly larger than the radius of the pipette (Figure 6.2). For each trial, 5 to 10 patches were collected.

As a control, whole vesicles were also extracted, using a pipette with a larger inner diameter (~10µm). These were used to check for discrepancies in the excision process and in the mass spectrometry protocols. When whole vesicles samples are analyzed, the molar ratios for the original point on the ternary diagram should be recovered. If this is not the case, then there may be a systematic error with either the pipette extraction process or the sample preparation protocol for the HPLC and mass

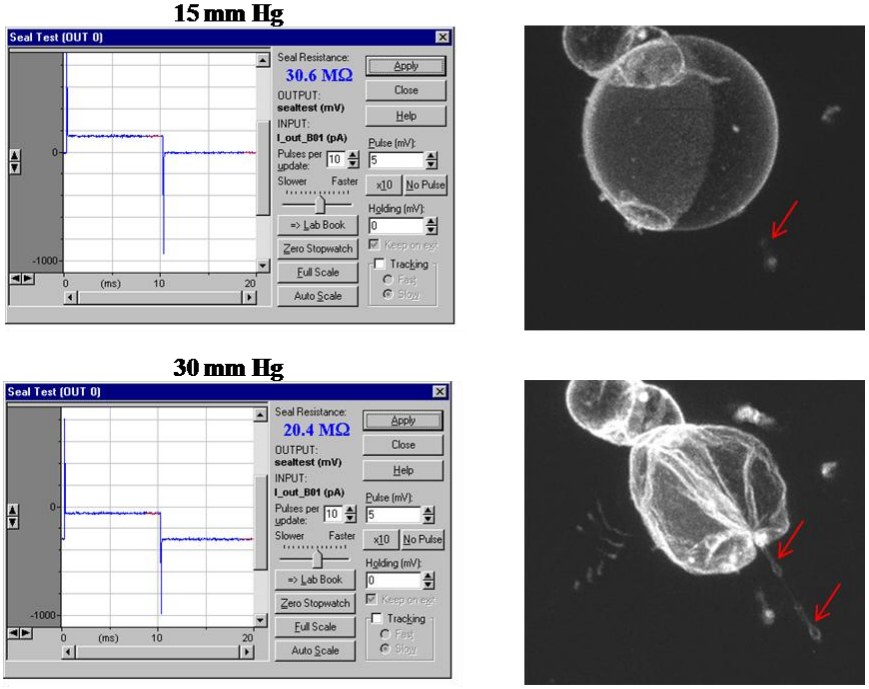

Figure 6.3 Patch clamp recording of a vesicle labeled with terrylene. The red arrows denote the patch inside the pipette. At 15mmHg applied pressure, the resistance is 30.6 mega-Ohms (upper left). At a higher pressure (30 mm Hg), the seal is broken, multiple pieces of membrane get sucked into the pipette (lower right), and the resistance falls to 20.4 mega-Ohms. Excitation wavelength: 750nm, buffer: 0.4% saline with 50mM sucrose, 40x water immersion objective.

spectrometry procedures. If the ratio is recovered for whole vesicles, but the combined L_o and L_d results for excised patches fall along a line the does not contain the original point on the ternary diagram, then the error can likely be traced to the excision and extraction processes, not the HPLC or mass spectrometry.

HPLC-MS-MS

For LC/MS/MS, the sample containing a mixture of substances is first separated by HPLC. The individual components are then injected into the mass spectrometer for quantitative analysis. The methanol solutions containing whole vesicle or excised patch samples were dried down and reconstituted with a 90% methanol-5mM ammonium acetate mixture (solvent or buffer 'A') prior to injection into the HPLC. A recovery yield test was performed on the internal standard lipids to estimate the amount of sample lost during drying and reconstitution. Methanol stock solutions of D-7 cholesterol, C-17 SM, and OSPC were mixed to make a ternary test solution with final concentrations of 100pg/µL D-7 cholesterol, 5pg/µL C-17 SM, and 10pg/µL OSPC. 100 µL of this solution was added to each of the four tubes. Two tubes were used to test the losses during the drying, and the other two to test the direct loss in the HPLC/MS/MS analysis. The percent recovery is the combined recovery yield of both processes. This was 76.1% for D-7 cholesterol, 82.4% for C-17 SM, and 85.2% for OSPC.

Optimal HPLC parameters were determined by Dr. Sheng Zheng (Cornell University). First, methanol stock solutions of each individual lipid at known concentrations, as determined by the phosphorous assay, were used to obtain mass spectra of each lipid, a standard curve for each lipid, and to estimate the detection limits of each lipid. The lipid and cholesterol stocks were prepared in anhydrous methanol, dried down by speed vacuum, and reconstituted to concentrations of 10ng/µL in buffer A. This was first done without internal standards using isochratic

elution in an LC Packings UltimatePlus capillary HPLC system equipped with a Switchos valve switching unit and a Famous autosampler (Dionex, Sunnyvale, CA). A 20μL sample loop was used and 10μL was injected. A mixture containing 100pg/μL cholesterol, 4pg/μL DOPC, and 4pg/μL SSM was prepared from the methanol stock solutions to test the sensitivity of LC/MS/MS for a ternary mixture in isochratic HPLC elution, and a mixture containing 50pg/μL cholesterol, 1pg/μL DOPC, and 2pg/μL SSM was used to test the sensitivity of LC/MS/MS for a ternary mixture in gradient HPLC elution.

For isochratic studies, the buffer (mobile phase) was 90% methanol-5mM ammonium acetate (buffer A). For gradient elution, solvent A was 90% methanol-5mM ammonium acetate, and solvent B was 99% methanol-5mM ammonium acetate. The samples were vacuum dried and reconstituted in solvent A for gradient elution. The gradient used was 0-2-10-13-14-25 minute = 20-20-100-100-20-20 % solvent B. The flow rates were 45μL/minute for isochratic studies and 50μL/minute for the gradient studies. The column was a C-4 Vydac reverse phase micro-column (1 mm ID x 150 mm) for both isocratic and gradient elution. Gradient elution resulted in much better separation of the three components in the controlled ternary mixtures, as depicted in Figure 6.4. Gradient HPLC was subsequently used on the whole vesicle and excised patch samples.

The mass spectrometer employed was a hybrid triple quadrupole-linear ion trap mass spectrometer, 4000 Q Trap from ABI/MDS Sciex (Framingham, MA) equipped with a Turbo ion source. Molecular ions were produced by electrospray ionization (ESI), in which the ionizing agent is an intense electrical field. In these experiments, a multiple reaction monitoring (MRM) technique was used because it is by far the most sensitive technique for mixtures.

MRM requires a triple quadrupole detector. In MRM, a product ion scan and a

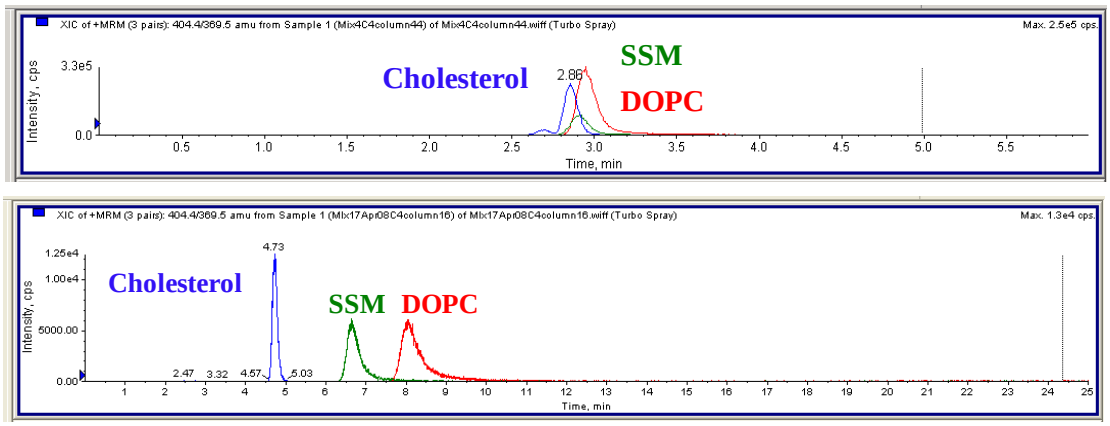

Figure 6.4 Gradient versus isochratic HPLC elution. Upper panel: isochratic elution in 90% methanol 5mM ammonium acetate (solvent A) of a control mixture of 100pg/µL cholesterol, 4pg/µL SSM, and 4pg/µL DOPC prepared in the same solvent. Lower: gradient elution with a control ternary mixture of 50pg/µL cholesterol, 2pg/µL SSM, and 1pg/µL DOPC prepared in solvent A. With isochratic elution, the peaks of the individual lipids are not well separated.

precursor ion scan are essentially combined. In a product ion scan, quadrupole 1 (Q1) selects a constant m/z ratio, and fragments produced in Q2 are scanned in Q3 to produce the typical product ion, or MS/MS, scan. In a precursor ion scan, ions in Q1 are scanned, fragmented in Q2, and a constant m/z ratio is selected for detection in Q3. The MRM signal is monitored over the chromatographic elution time. The mass fragments of each component for the ternary mixture examined in this study are depicted in Figure 6.5. The mass spectra are depicted in the appendix (Chapter 7) for cholesterol, DOPC, and SSM. These were obtained with external standards using isochratic HPLC elution of single constituent solutions reconstituted in solvent A.

MS/MS spectra were collected at a mass to charge ratio (m/z) = 404.4 for cholesterol (corresponding to the addition of water to the molecular ion), m/z = 786.8 for DOPC (corresponding to the molecular ion), and m/z = 731.8 for SSM (corresponding to the molecular ion). Both DOPC and SSM have the same mass fragment at m/z = 184, corresponding to the phosphocholine headgroup. The ion transitions monitored by MRM were m/z = 404.4 to m/z = 369.4 for cholesterol, m/z =

786.8 to m/z = 184.1 for DOPC, and m/z = 731.8 to m/z = 184.1 for SSM. The MS/MS spectra, precursor ion scans, and MRM spectra are depicted in the appendix (Chapter 7). To prepare standard curves using MRM analysis of stock solutions and of control mixtures, 4 data points (dilutions) were collected for each solution, with two replicate runs of each point. Not surprisingly, it was found that gradient elution resulted in lower detection limits due to separation in elution times between SSM and DOPC. These detection limits were 100pg cholesterol (26nM for 10µL injection), 1pg DOPC (1.4nM for 10µL injection), and 2pg SSM (2.8nM for 10µL injection) for isochratic elution with external standards, and 20pg (5.2nM for 10µL injection) cholesterol and 100fg (0.14nM for 10µL injection) DOPC and SSM for gradient elution with external standards. The use of the internal standards described here lowered these limits by approximately half; these were not incorporated into the vesicles samples, however, so external standard curves were used to analyze that data. The detection limit of cholesterol could additionally be improved to picomolar by derivatizing the molecule and its internal standard such that it ionizes with greater efficiency (Sandhoff et al 1999).

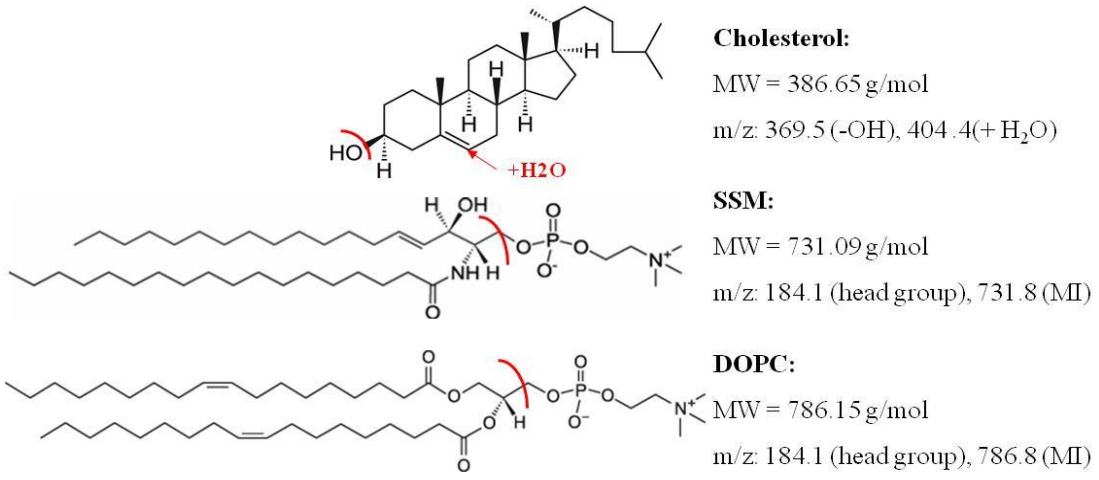

Figure 6.5 Mass fragments. The major mass fragments monitored in these experiments are depicted. MI = molecular ion.

6.3 RESULTS AND DISCUSSION

To determine the relative abundances in the vesicle and excised patch samples, the areas under the curves from MRM analysis were fit to the standard curves for controlled-composition ternary mixtures prepared from stock solutions. The resulting concentrations of each component in the samples were then converted into molar ratios and divided by the percent yield calculated for each component's internal standard: 0.761, 0.824, and 0.852 for cholesterol, SSM, and DOPC, respectively. For most samples, there was a consistent systematic error: the amount of cholesterol detected was erroneously high compared to the amount of combined lipid (DOPC and SSM). This was true for both the excised patch samples and the whole vesicle samples, which means that the error may not have been due to the patching.

However, the ratio of SSM to DOPC in two whole vesicle samples was found to match the expected value of each sample to within a maximum 17% error. This error was then applied to the measured SSM to DOPC ratios in patched samples to give upper and lower bounds on the value of the ratio. The data are shown in Table 6.1. The SSM to DOPC ratio for each phase (L_o or L_d) of the excised patch samples was then used to determine approximate tie lines. This was accomplished by graphing the experimentally determined ratios as lines on the ternary diagram along with the upper and lower bounds; the point where this line intersects the coexistence curve describes the composition of the endpoint of the tie line. The selection of which line was used from the set of three (measured value, lower bound, or upper bound) was determined according to the rules that tie lines do not intersect one another. This method is only accurate if one assumes that the experimentally determined ratios are representative of those originally sampled, i.e., that whatever process responsible for the selective loss of lipid versus cholesterol was equally destructive to SSM and DOPC such that their ratio is preserved in the excision process. Note that the

Table 6.1 Ternary data. The ratio of SSM to DOPC in whole vesicle and patch excised samples determined by mass spectrometry is reported. The upper and lower bounds represent an error of 17% above or below the measured value of the ratio. This was chosen because it is the maximum error of the deviation of the ratio for the whole vesicle samples.

Chol/SSM/DOPC (phase)	SSM: DOPC expected	SSM:DOPC measured	Lower bound SSM:DOPC	Upper bound SSM:DOPC
0.29/0.50/0.21 (whole vesicle)	2.38	2.78	2.31	3.25
0.20/0.56/0.24 (whole vesicle)	2.33	2.80	2.32	3.23
0.40/0.43/0.17 (L_d)	--	0.69	0.57	0.81
0.40/0.25/0.35 (L_d)	--	0.67	0.56	0.78
0.40/0.25/0.35 (L_o)	--	1.29	1.07	1.51

compositional uncertainty in the coexistence boundary provides an additional source of error.

A graphical representation of the measured values and tie line determination is depicted in Figure 6.6. The lines of constant SSM to DOPC ratio and the corresponding 17% error bounds are depicted as vertical lines; the different colors correspond to different samples. The middle line in a set of three corresponds to the measured value of the SSM to DOPC ratio. Note that the lines of constant SSM to DOPC ratio can intersect the coexistence curve at two locations. However, if both the L_o and L_d phases are measured, then the appropriate tie line will contain the composition point describing the overall mixture and the "wrong" direction can be discarded. The appropriate directions match fairly well with that of the tie line determined using an all optical method described in Chapter 5 of this dissertation, which is shown in blue in Figure 6.6. This is encouraging, considering that neither set of measurements was particularly robust or included a substantial population of data.

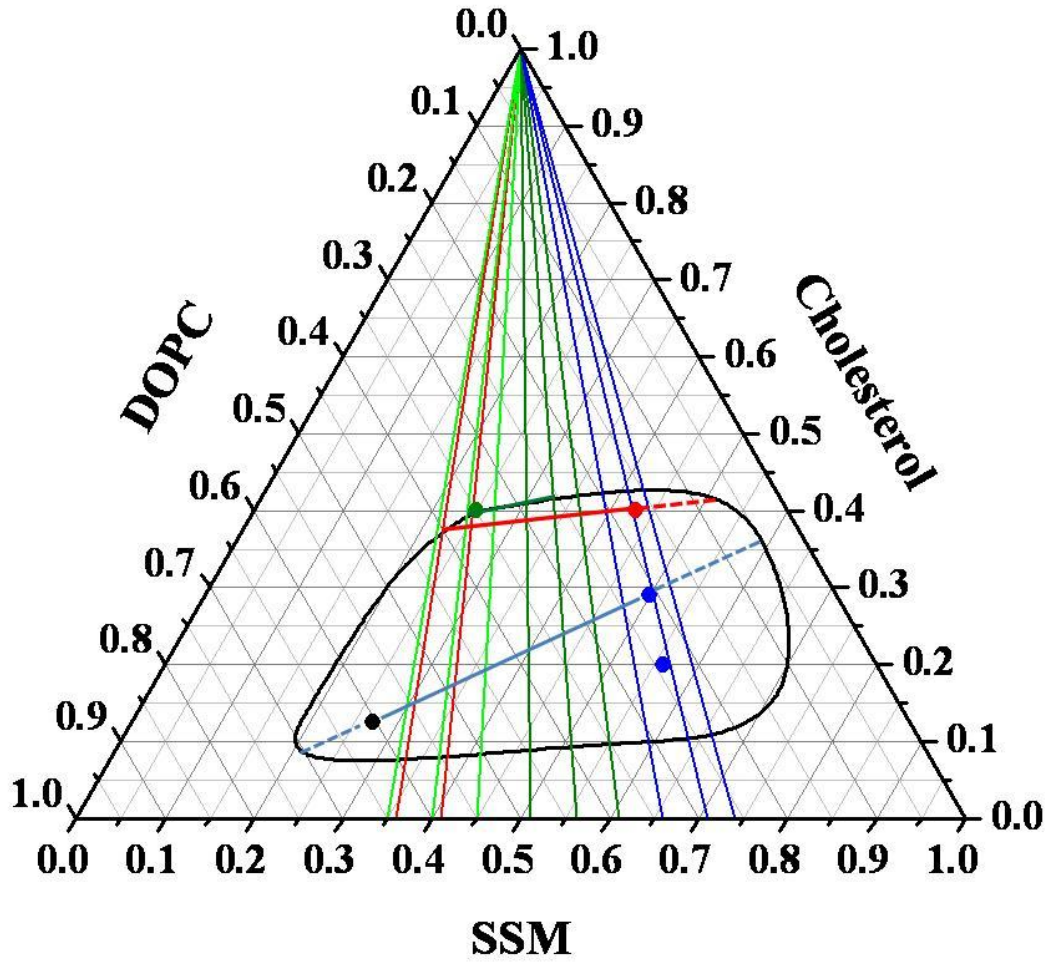

Figure 6.6 Ratiometric method for tie line determination. Vertical light green lines: SSM:DOPC ratio with upper and lower bounds for L_d phase of sample with overall composition cholesterol/SSM/DOPC = 0.40/0.25/0.35 (circular green marker). Vertical dark green lines: SSM:DOPC ratio with upper and lower bounds for L_o phase of sample with overall composition cholesterol/SSM/DOPC = 0.40/0.25/0.35 (circular green marker). Vertical red lines: SSM:DOPC ratio with upper and lower bounds for L_d phase of sample with overall composition cholesterol/SSM/DOPC = 0.40/0.43/0.17 (circular red marker). Vertical blue lines: SSM:DOPC ratio with upper and lower bounds for sample with overall composition of cholesterol/SSM/DOPC = 0.29/0.50/0.21 (circular blue marker, upper). The lines for the other whole vesicle sample (lower blue marker at 0.20/0.56/0.24) are not shown because they fall almost on top of those for composition 0.29/0.50/0.21. The horizontal red and green lines are the tie lines deduced from the ratiometric data. The blue tie line comes from the data in chapter 5 and is shown to emphasize that the results for the tie line directions agree.

6. 4 CONCLUSIONS

The most glaring error of these experiments was the falsely high apparent concentration of cholesterol compared to the lipids in membrane samples analyzed by mass spectrometry: cholesterol concentrations determined by MRM analysis were found to be 10 to 50 times those of each lipid on average, and sometimes exceeded the estimated amount of total material in each sample. However, this was only the case for membrane whole and patched samples, and not for ternary lipid control mixtures prepared directly in solvent. Thus, it is likely not due to the mass spectrometry protocol, a conclusion supported by the fact that cholesterol is known to have a lower ionization efficiency than the lipids in ESI mass spectrometry (Sandhoff et al 1999). The seeming selective loss of lipids over cholesterol is likely at least partially due to the preferential adherence of lipids to the pipette. Lipids are more polar than cholesterol and are larger; thus, they likely form stronger electrostatic and van der Waals interactions with the glass (Opsahl and Webb 1994, Gil et al 1999). Moreover, cholesterol may be preferentially solubilized in methanol during the rinsing of the pipette. Another source of error could be that membrane material is sticking to the pipette as the pipette is moved through the solution, but that areas where this occurs are not in the field of view of the microscope. Preferential interaction of the phospholipid with the glass over cholesterol would then lead to the preferential dissolving of the cholesterol in the methanol bath.

Two other obvious possible sources of error are the fluorescent dyes and the products of phospholipid hydrolysis. The dyes would only be expected to influence the overall concentrations, but cannot account for the erroneously high values for the cholesterol concentration observed in these experiments. For example, consider a dye added at 0.1 mole % that partitioned exclusively into the minority phase. Assume that the minority phase makes up only 10% area fraction vesicle (much less than any

vesicles used in these experiments) and that lipids in both phases had roughly the same surface area. Then the dye would comprise roughly 1 mole % of this phase, which still is not enough to account for the large discrepancies seen in the cholesterol content. Lipid degradation may also be responsible, though it would be very unlikely that the ratios of DOPC and SSM would be recovered for the whole vesicle samples. A more thorough approach to this experiment would have the lipid compositions analyzed by phosphate assay at each step.

Future applications for this kind of hybrid analysis include a more accurate characterization of the composition of each phase and elucidation of tie lines from that information; measurement of the overall compositional variation from vesicle to vesicle within a given sample preparation; and measurement of the relative amounts of peroxidation or other impurity products produced with different electroswelling substrates and different imaging conditions. It would also be interesting to compare impurities formed by the two other main methods of model membrane preparation: gentle hydration (Akashi et al 1996) and rapid solvent exchange (Buboltz and Feigenson 1999). The latter investigation could shed light on the mechanisms for lipid breakdown and help researchers to make better choices for vesicle preparation protocols. Perhaps another variation on the theme of this technique would be to subject each pipette tip loaded with a single patch to thermogravimetric analysis (TGA).

CHAPTER 7: APPENDIX

This chapter contains supplementary material for the research described in the dissertation. Section 7.1 contains the experimental protocol for the determination of lipid stock solution concentrations using the phosphate assay developed by Kingsley and Feigenson (1979). Section 7.2 contains the Labview code in diagram form for gathering the fluorescence intensity as a function of angle as described in Chapter 5 of this dissertation. Section 7.3 contains the Matlab code used to open and edit Biorad ".pic" files in the Matlab workspace. In section 7.4, the method for determining the area fractions of each phase for the L_o-L_d region is described. Section 7.5 is a collection of the mass spectra used for Chapter 6. Finally, section 7.6 describes the three main theoretical frameworks that have been developed to describe the interaction of cholesterol with phospholipids.

7.1 THE PHOSPHATE ASSAY

The microphosophorus determination was modified from the protocol described in Kingsley and Feigenson (1979) used in the Feigenson lab. It is restated here in its entirety.

Gloves should be worn at all times as oils and contaminants from human skin seriously contaminate the assay, and the color reagent is very toxic. If making one's own phosphate stock solution rather than using a commercial source, care should be taken to make sure it is concentrated enough that more than ~100uL will not have to be added for the highest concentration on the standard calibration curve. This is one of the main reasons the Avanti protocol did not work well: it calls for a 0.65mM phosphate standard, as opposed to the ~5mM in the current protocol. A good assay, in terms of accurate concentrations and having the ashing reactions proceed properly, is contingent upon having all of the liquid (phosphate stock, lipid samples, acid, and H_2O_2) evaporated before adding the color reagent, and the more dilute phosphate stocks were observed to result in leftover liquid.

Step 1: Ashing

Materials: 12 13x100mm glass test tubes, phosphate standard stock solution (5.355mM KH_2PO_4), lipid sample solutions in chloroform, cleaned Hamilton syringes, 10% (v/v) sulfuric acid, 30% H_2O_2.

- Thoroughly wash test tubes with hot water and low phosphorous soap, then rinse with Milli-Q deionized water (DI), and blow dry or put into heating block if it is already above 100°C. The DI rinse is important since many commercial soaps may contain phosphates.
- Start the heating block at 220°C in the dry bath and note that the heating block should be high enough to cover almost all of 13x100mm tube to prevent refluxing. The heating apparatus should be inside a chemical (fume) hood.

- Add the following volumes (left column) of phosphate stock solution to the cleaned test tubes using a Hamilton syringe:

uL of 5.355mM stock	nmoles phosphate	absorbance at 820nm[8]
0	0	0.01
2	10.71	0.3
4	21.42	0.66
12	64.26	1.74
16	85.68	2.26
20	107.10	2.8

- Add the appropriate volume of each chloroform lipid stock solution to a test tube to give about 100 nmole phosphate per tube using Hamilton syringes. *Precision in the volume measurement is critical*. For example, if the concentration obtained from weighing out the samples, or from the vendor if the solution comes predissolved, is 25mg lipid/mL chloroform, use 2.5uL per test tube; if it is 10mg lipid/mL, use 5uL per test tube. Note that this assumes one phosphate per lipid, and an average molecular weight of 700g/mole. At least three replicates of each sample should be used.
- Add 200uL 10% (v/v) sulfuric acid (H_2SO_4) solution to each test tube.
- Place samples into the pre-heated aluminum test tube heating block at 200°C-220°C and let sit for 1 hour. All liquid should evaporate in this time. Tweezers or tongs should be used to add and remove the tubes from the high block at this point as contaminants from skin can give erroneous calibration curves (and because the block is really hot).
- Add 20uL 30% H_2O_2 to each tube, while the tubes are still in heat block, and

[8] These numbers refer to absobances (in a.u.) determined on a CARY 300 UV-Vis spectrophotometer (Varian, Inc., Palo Alto, CA). Absolute values will be different depending on the instrument used.

let the tubes heat for 40 additional minutes.

- If any black color (indicative of residual carbon) is present after 40 minutes, add an additional 20uL of peroxide to all tubes and heat the tubes for 40 minutes after the last peroxide addition. Note that one should never need more than 20uL peroxide for phospholipids, and the addition of more than 150uL 30% peroxide will affect the blank absorption in the following colorimetric determination.

Step 2: Preparation of the color reagent

Materials (assuming 12 test tubes): 9mL DI water, a vortexer, 9mL 0.022% (w/v) ascorbic acid solution (4.44g ascorbic acid : 200mL Milli-Q water), 1.0mL 5% (w/v) ammonium molybdenate solution (5g ammonium molybdenate : 95mL Milli-Q water), 12 sample tubes, a large clean test tube or beaker.

- Remove samples from heating block and cool to room temperature (22°C).
- Place an aluminum heat block into a dry bath and set the temperature to 50°C.
- Turn on spectrophotometer to warm up the lamp, and set it to measure absorbance at 820nm for 2s.
- For 1 mL final total volume per test tube, add 0.5mL DI to each test tube, being careful to wash the sides. Vortex each for a few seconds. The bottom of the tube may become slightly warm.
- Combine 9mL ascorbic acid solution and 1mL ammonium molybdenate solution in large clean test tube or beaker and vortex for a few seconds. The solution should be a light “lemon” yellow. Note that this solution should be used immediately once it is made, as it does not have a shelf life.
- Add 0.5mL of the molybdenate and ascorbic acid solution (“color reagent”) to each of the 12 test tubes to which DI was just added and vortex each for a few seconds. The solutions should turn various shades of blue depending on the

phosphate concentration in each. The color gradient will change from light yellow to dark blue as phosphate concentration increases.

- Place the samples into the dry bath at 50°C and let them sit for 25-30 minutes. They may be covered loosely with tinfoil for this step to prevent dust or particulates from contaminating them.
- Dispose of any remaining color reagent into an appropriate waste receptacle as it is very toxic and should not be washed down the sink.

Step 3: Colorimetric absorption assay

- Using the 1mL (or smaller) quartz cuvettes, read the absorbance of DI water. Then zero the absorbance reading with the water in place: this serves as the blank and is thus subtracted from subsequent readings. The absorbance of DI should be around 0.038 absorption units at 820nm.
- Using the 1mL (or smaller) quartz cuvettes, read and record the absorbance of each sample at 820nm. Start with the least concentrated of the phosphate standard samples and work up to the most concentrated. Perform measurements on the lipid samples last. At least two absorption readings per sample should be obtained. Aspirate the cuvette and/or rinse with DI in between samples.

Step 4: Analysis and data plotting

- Convert the *uL* phosphate standard to *nmoles* by multiplying by the *mM* concentration
- Plot “nmoles phosphate” (*x*) vs. “absorbance” (*y*) to obtain the standard calibration curve. Generate the linear equation for the curve.
- If the calibration plot is acceptably linear, calculate the lipid concentration of the lipid samples using the experimental absorbance of the lipid samples using the equation for the line of the standard curve.

7.2 POLARIZATION IMAGING: LABVIEW IMAGE ANALYSIS

The Labview circuit diagram for analyzing and integrating annular regions of intensity is depicted in Figure 7.1. This was used to obtain intensity versus angle data for equatorial GUV sections as described in Chapters 2 and 5. It was written by Dan Dombeck.

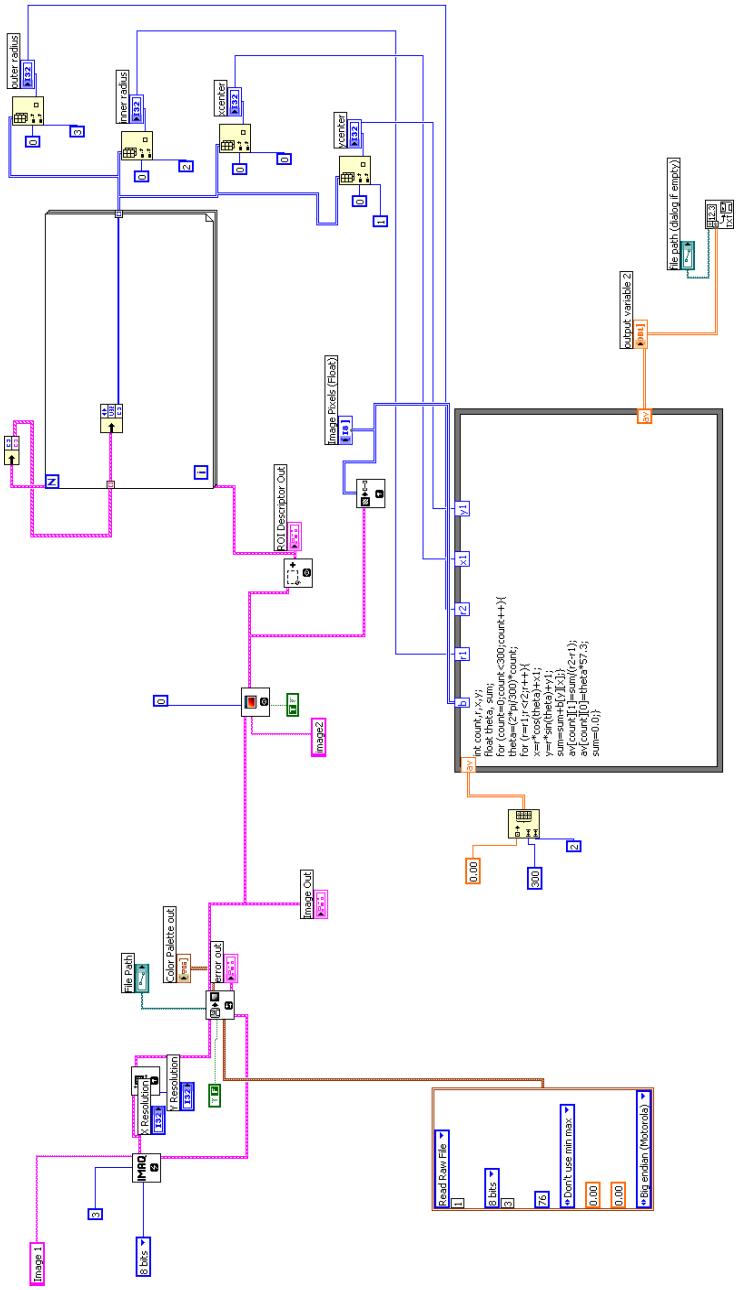

Figure 7.1 Labview code for the intensity versus angle analysis.

7.3 MATLAB CODE

readpic.m: This code was originally devised by Alex Kwan, a former PhD student in the Webb group. It is used to open Biorad 'pic' files in Matlab for image analysis.

```
function y=readpic(myfilename);
fid = fopen(myfilename,'r','n');
nPictureSize = fread(fid,[1,2],'int16');    %reads the first two double-bytes
nX = nPictureSize(1,1);                     %sets nX to the width of the images
nY = nPictureSize(1,2);                     %sets nY to the height of the images
NumberOfImages = fread(fid,1,'int16');      %reads the next double-byte with the total
%number of the slices
junk = fread(fid,6,'int16');                %reads the information about the images it is
%not used for anything, just to jump to the filename
Name = char(fread(fid,[1,32],'uchar'));     %reads the filename in ASCII-code
junk = fread(fid,26,'int8');                %reads the rest of the header, to jump to the first
picture
for i = 1:NumberOfImages,
   pic(:,:,i) = fread(fid,[nX,nY], 'uint8=>uint8')';
end
fclose(fid);                                %closes the file .pic
y=pic;
```

7.4 AREA FRACTION ANALYSIS

For L_o-L_d coexistence where there are only two domains, a very simple image analysis process can be used to obtain the area fractions of the two phases. The area of the minority phase, *SA*, is computed as: $SA = 2\pi Rh = \pi(a^2 + h^2)$, where *R* is the radius of the spherical vesicle and *a* and *h* are the lengths as depicted in Figure 7.2. For most non-spherical vesicles, this will not work. If each domain comprises part of a sphere instead an ellipse or oval, however, a similar technique can be used.

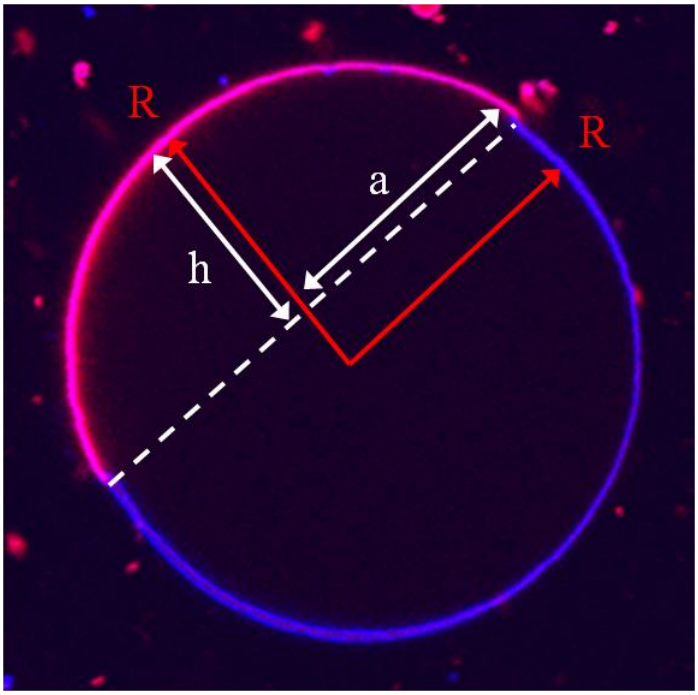

Figure 7.2 Determination of the area fraction of the minority phase for spherical vesicles. R is the vesicle radius. The surface area SA of the L_d phase (red) is given by $SA = 2\pi Rh = \pi(a^2 + h^2)$.

7.5 MASS SPECTRA AND STANDARD CURVES

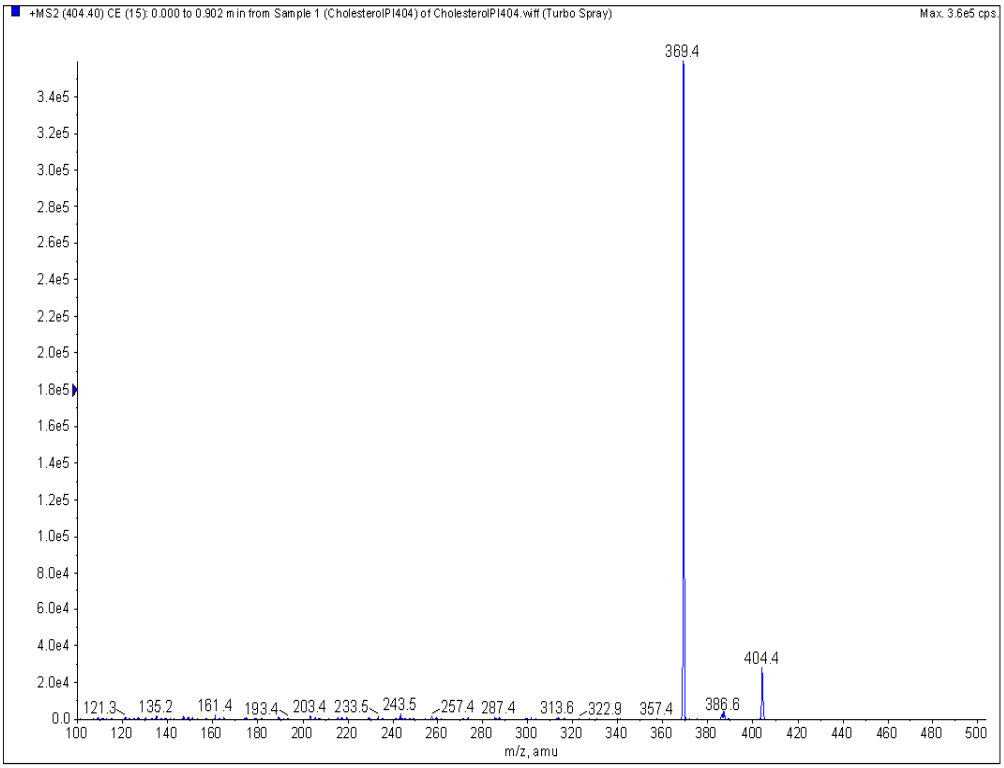

Figure 7.3 MS/MS spectrum for cholesterol at m/z = 404.4.

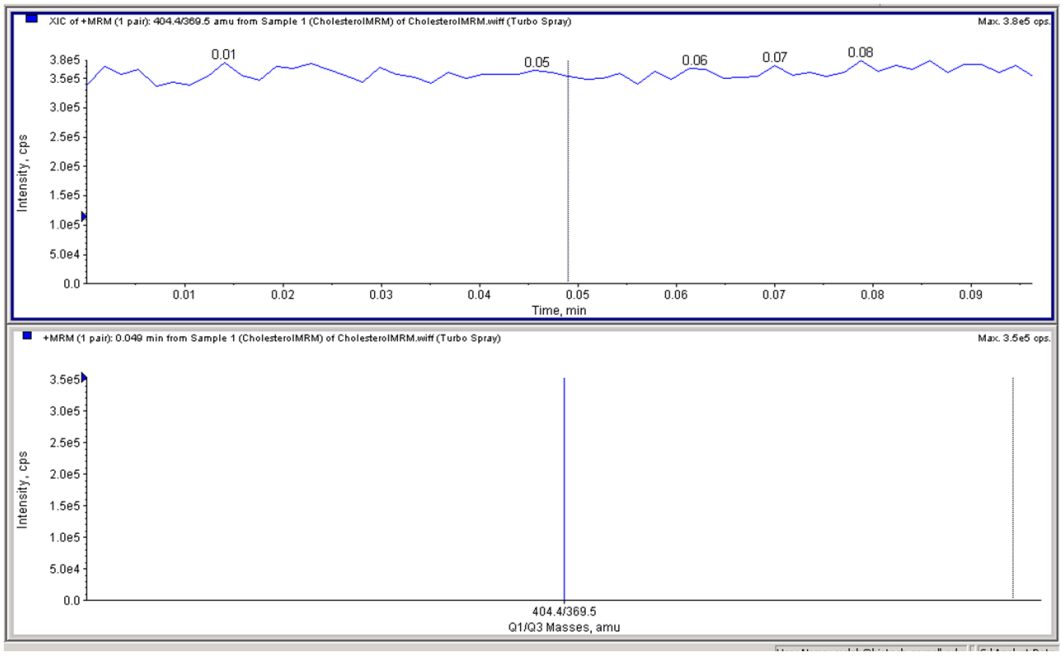

Figure 7.4 MRM for cholesterol transition ions of 404.4 to 369.4.

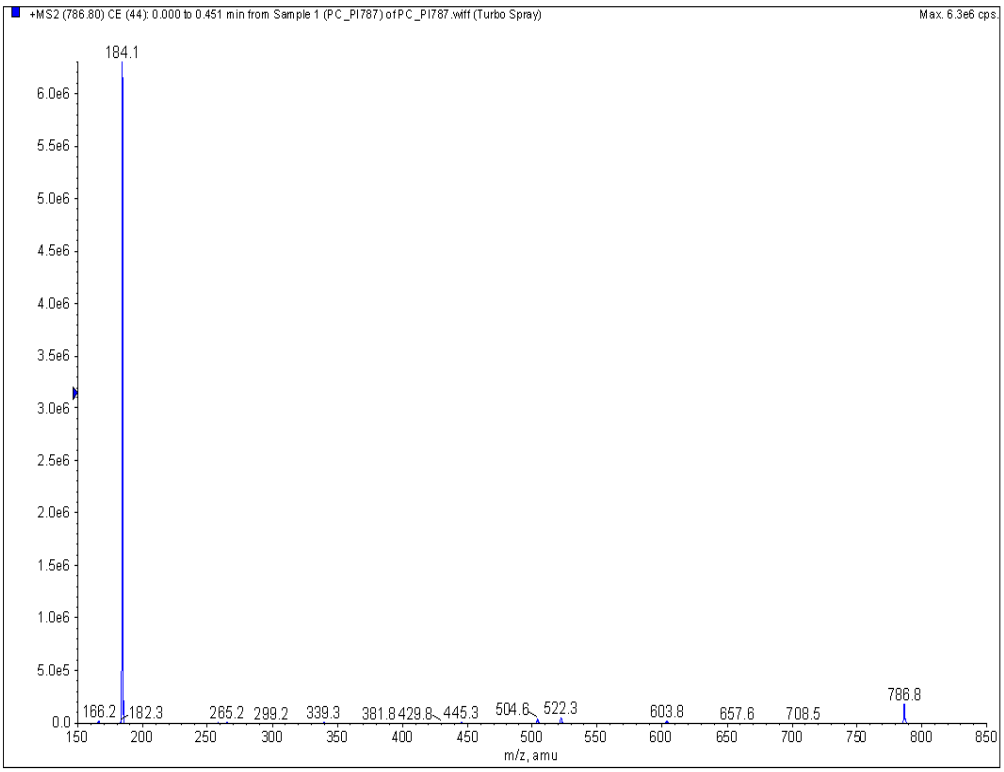

Figure 7.5 MS/MS spectrum for DOPC at m/z = 786.8.

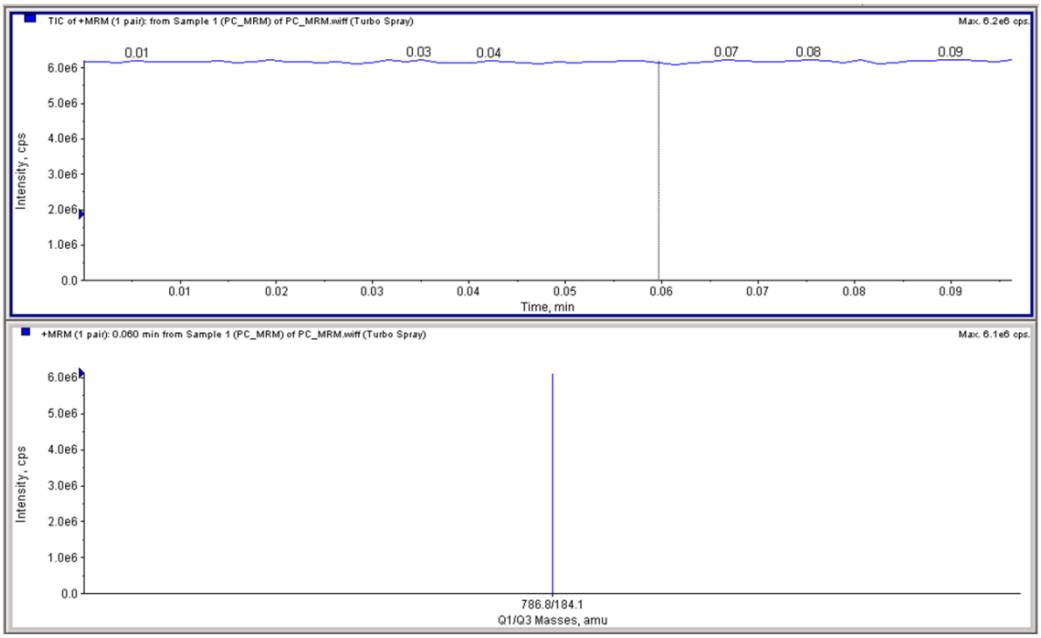

Figure 7.6 MRM for DOPC transition ions of 786.8 to 184.1.

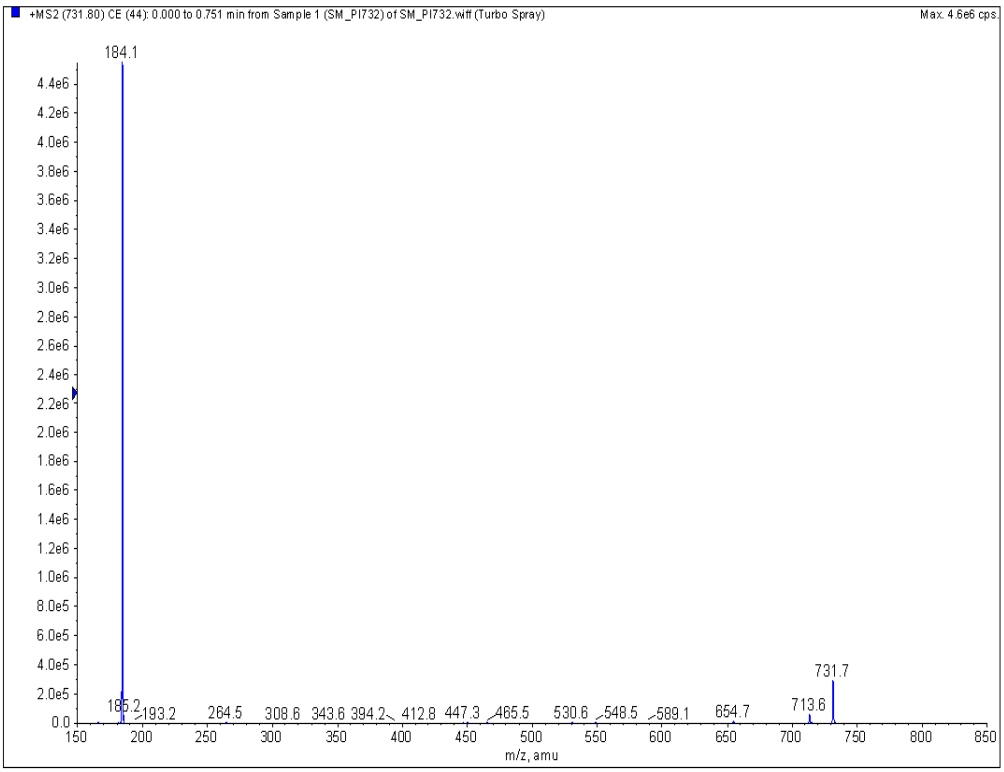

Figure 7.7 MS/MS spectrum for SSM at m/z = 731.8.

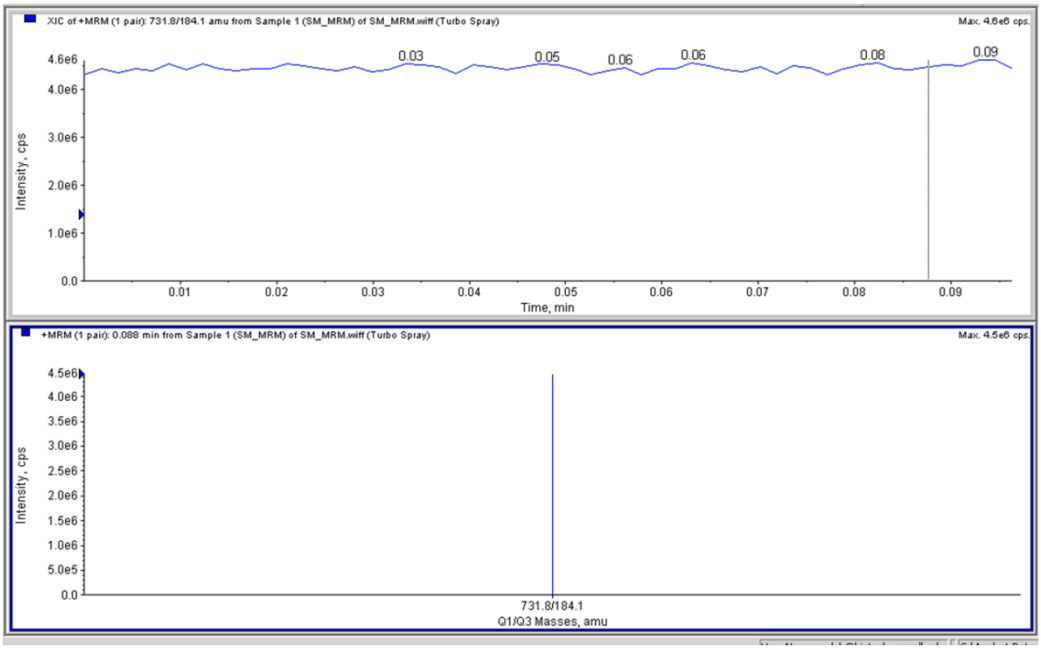

Figure 7.8 MRM for SSM transition ions of 731.8 to 184.1.

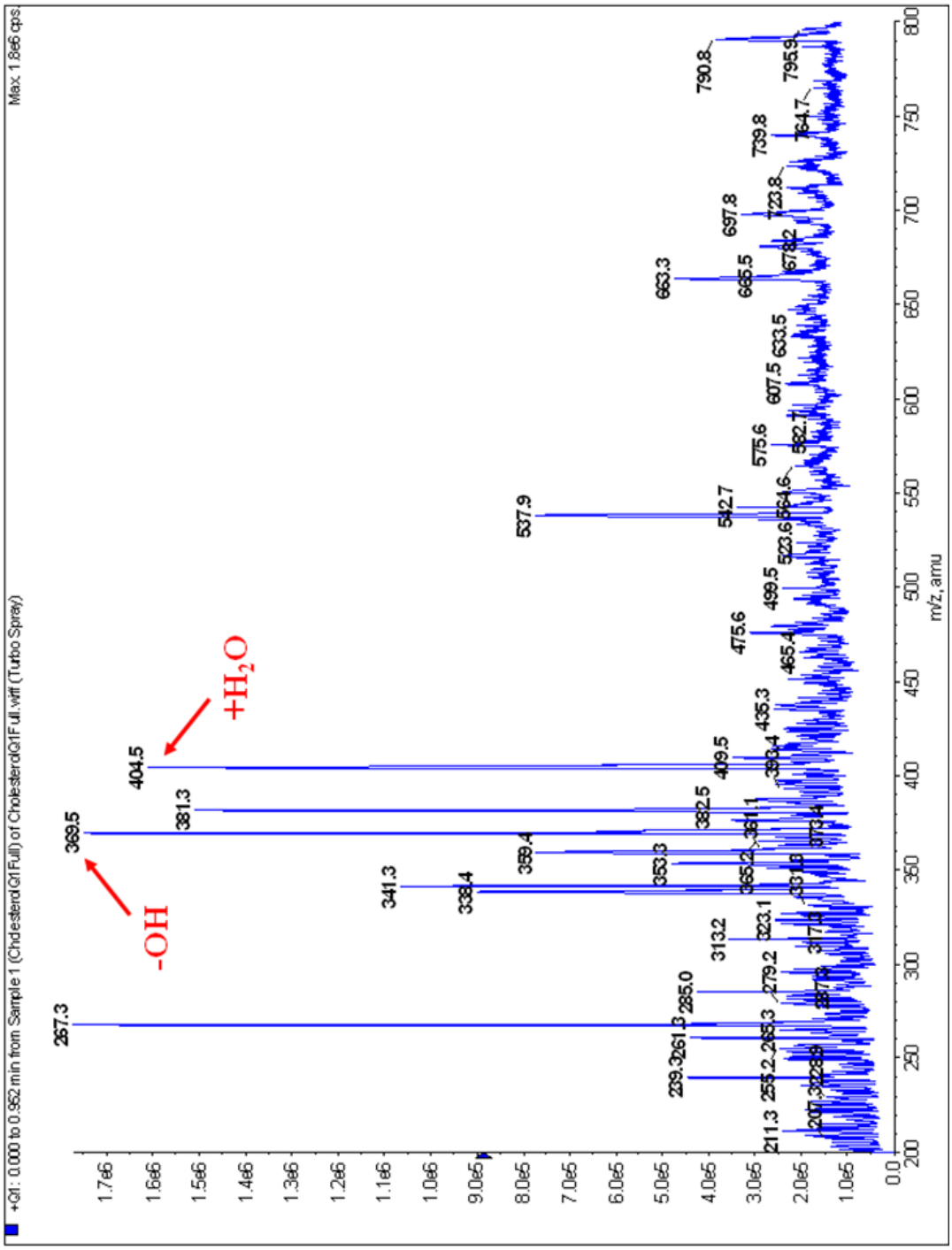

Figure 7.9 Mass spectrum cholesterol.

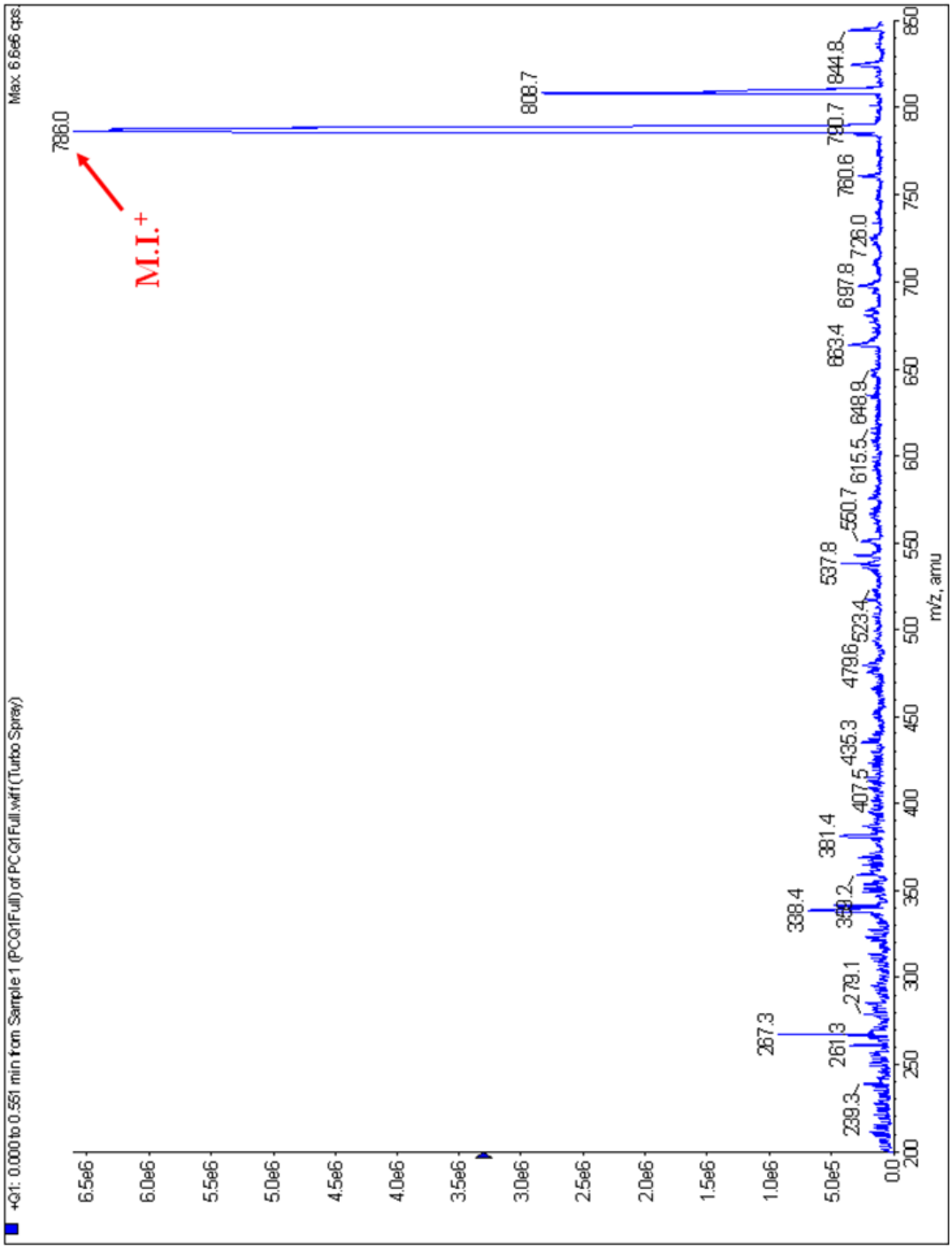

Figure 7.10 Mass spectrum of DOPC.

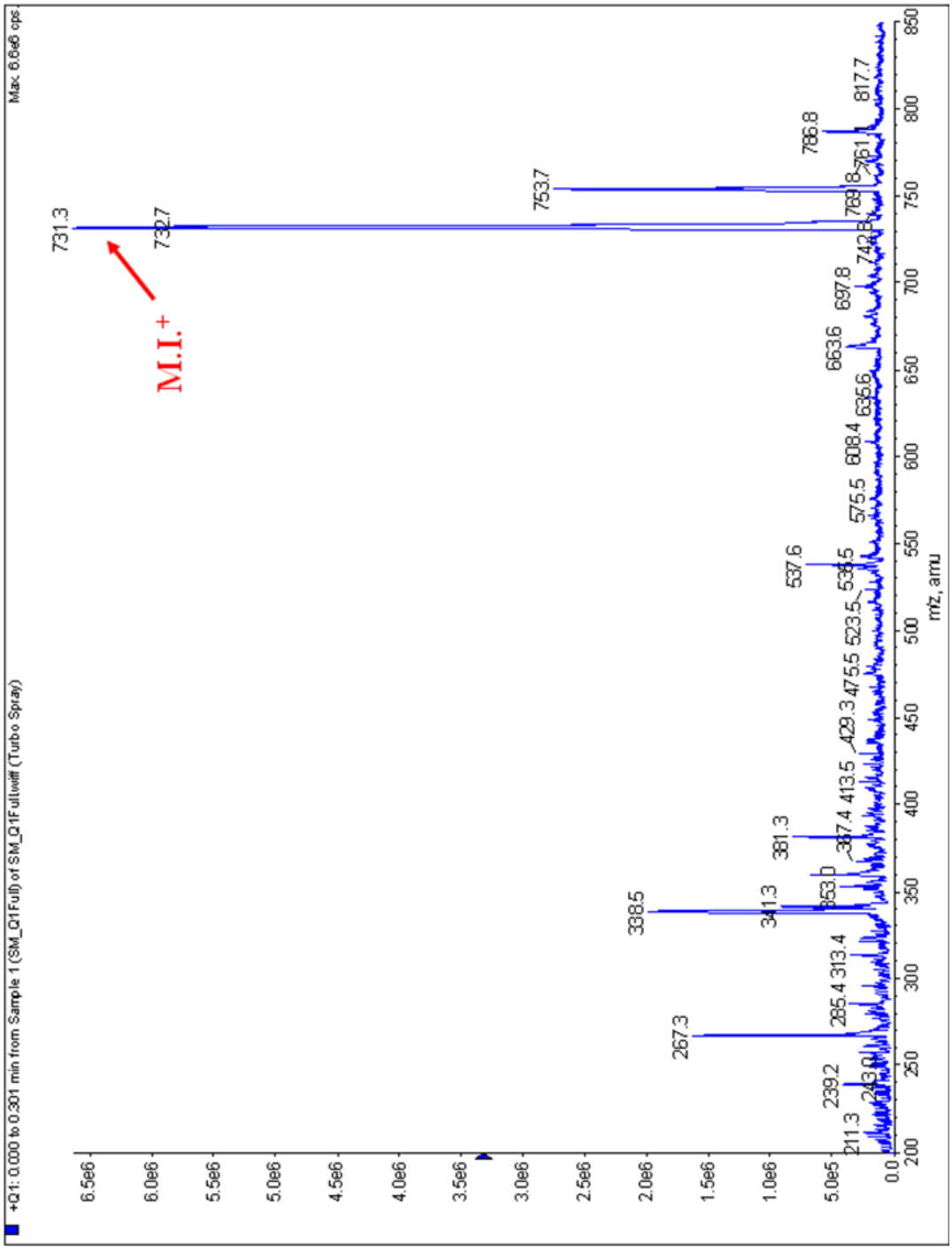

Figure 7.11 Mass spectrum of SSM.

7.6 THEORIES DESCRIBING CHOLESTEROL-LIPID INTERACTIONS

Several theories have been developed to explain these observations and to delineate a driving force for the preferential association of cholesterol with saturated acyl chains. The models of Ipsen et al (1987 and 1989) successfully describe the decoupling of order using a theory first formulated by Pink and Carroll (1978). In this theory, ten conformational states describe the accessible conformations of the gel phase. The lattice model of Ipsen et al (1987) is an extension of the Pink model to include the translational order; it is equivalent to a Potts lattice-gas model with vacancies. Each lipid monolayer is viewed as a triangular lattice. The total energy has two main contributions, that from the chain order, and that from the translational order. Each occupied site on the lattice has an internal degree of freedom (chain conformation) for which two (or ten in subsequent research, Ipsen et al 1989) conformational states are possible, one of which corresponds to the chain disordered state and the other(s) to chain-ordered states. Crystalline ordering, characterized by translation and tilt order parameters, can be accounted for by invoking the Q-state Potts model, which imposes an energetic penalty on dislike grain boundaries for nearest neighbors on a lattice. Each molecule in the ordered state possesses a Potts variable 1…Q, where there are Q possible crystalline orientations. A mixture of ordered and disordered phases will phase separate and the ordered phase will align to minimize the grain boundaries and maximize packing. Thus, the two order parameters are coupled through the occupancy of ordered sites on the lattice.

The phase transition described by this microscopic model is strongly first order and entropically driven, in accordance with the fact that the Q-state Potts model for $q>4$ describes first order transitions. This is also in partial agreement with experimental studies on L_d-gel phase transitions. This model is very relevant in that salient degrees of order, chain and crystalline, are demarcated in a relatively simple

manner. In this model, cholesterol interacts with both the translation and chain order degrees of freedom as an external field. The unfavorable free energy of cholesterol solvation in the gel phase is balanced by a favorable short-ranged interaction of cholesterol with the acyl chains of the unsaturated lipid. At high enough cholesterol concentrations, the two degrees of freedom uncouple. In this work, regular solution and microscopic lattice models were compared, and both reproduced the salient features of the phase diagram shown in Figure 1.6c. This model does not distinguish between the subset of order parameters a polymorphic gel phase may have.

The model described above assumes that a van der Waals interaction between cholesterol and lipid acyl chains is the dominant force driving cholesterol to preferentially interact with saturated chains; this is still the subject of considerable theoretical debate. There are two additional main theoretical descriptions which differ from the Ipsen model in the interpretation of the origin of cholesterol-lipid chain interactions, though none of them deem it intrinsically unfavorable. These driving forces are an energetically unfavorable interaction of cholesterol with water (Huang and Feigenson 1999) and a stable stoichiometric complex formation between cholesterol and saturated lipids (Anderson and McConnell 2001, McConnell 2005, Radhakrishnan and McConnell 2005).

In the model of Feigenson and Huang (Huang and Feigenson 1999), the interaction between cholesterol and lipids extends to a multibody interaction that includes next nearest neighbors on a triangular lattice. The driving force for the interaction of the cholesterol with the acyl chains is dominated by the energetically unfavorable interaction of cholesterol with water. Thus, the lipid headgroups act as umbrellas to shield cholesterol from water. That cholesterol has a preference for saturated acyl chains (Silvius et al 1996, Wang and Silvius 2003) is interpreted in terms of its ability to pack more closely with these chains so it is better shielded from

water; an increase in cholesterol should thus be accompanied by an overall increase in the chain order parameter until the maximum solubility is reached. This model correctly predicts the maximum solubilities of cholesterol in bilayers of various lipids (Huang and Feigenson 1999), and emphasizes the importance of the lipid headgroup in cholesterol-lipid interactions, which other theories ignore. It can also explain the condensing effect of cholesterol (Stockton and Smith 1976), in which the effective surface area of a lipid is decreased upon interaction with cholesterol since its chains become more ordered in the presence of cholesterol.

The condensed-complex model suggests that cholesterol-lipid association is dominated by an interaction more favorable than van der Waals interactions. Here, cholesterol reversibly forms oligomeric complexes with unsaturated lipids with stoichiometric ratios of 3:2 lipid:cholesterol or 2:1 lipid:cholesterol. There can thus be four phases in a binary lipid-cholesterol system if the Lo phase separates into additional complex-rich and complex-depleted phases. This model was formulated in light of the lack of macroscopic phase separation in saturated lipid-cholesterol binary systems and can explain some of the anomalous behaviors observed in monolayers. More recently it has been shown to provide the correct trend in NMR line broadening data for ternary mixtures (McConnell and Radhakrishnan 2007 and 2008).

REFERENCES

Ahmed, S.N., D.A. Brown, and E. London (1997) On the origin of sphingolipid/cholesterol-rich detergent-insoluble cell membranes: physiological concentrations of cholesterol and sphingolipid induce formation of a detergent-insoluble, liquid-ordered lipid phase in model membranes, *Biochemistry*, **36**, 10944-10953.

Akashi, K., H. Miyata, H. Itoh, and K. Kinosita (1996) Preparation of giant liposomes in physiological conditions and their characterization under an optical microscope, *Biophysical Journal*, **71**, 3242–3250.

Albrecht, O., H. Gruler, and E. Sackmann (1978) Polymorphism in phospholipid monolayers, *Le Journal de Physique*, **39**, 301-313.

Almeida, P. F. F., W. L. C. Vaz, and T. E. Thompson (1993) Percolation and diffusion in three-component lipid bilayers: effect of cholesterol on an equimolar mixture of two phosphatidylcholines, *Biophysical Journal*, **64**, 399-412.

Almeida, P.F., W.L. Vaz, and T.E. Thompson (1992) Lateral diffusion in the liquid phases of DMPC/cholesterol lipid bilayers: a free volume analysis, *Biochemistry*, **31**, 6739-6747.

Angelova, M.I. et al (1992) Preparation of giant vesicles by external AC fields: kinetics and applications, *Progress in Colloid and Polymer Science*, **89**, 127-131.

Angelova, M. I. And D. S. Dimitrov (1986) Liposome electroformation, *Faraday Discussions of the Chemical Society*, **81**, 303-311.

Anderson, R.G.W. and K. Jacobsen (2002) A role for lipid shells in targeting proteins to caveolae, rafts, and other lipid domains, *Science*, **296**, 1821-1825.

Anderson, T.G. and H.M. McConnell (2001) Condensed complexes and the calorimetry of cholesterol-phospholipid bilayers, *Biophysical Journal*, **81**, 2774-2785.

Andleman, D., T. Kawakatsu, and K. Kawasaki (1992) Equilibrium shape of two-component unilamellar membranes and vesicles, *Europhysics Letters*, **19**, 57-62.

Anisimov, M. A. (1991) *Critical Phenomena in Liquids and Liquid Crystals*, Gordon and Breach Science Publishers: Philadelphia, PA.

Anisimov, M. A., E. E. Gorodetskii, and V. M. Zaprudskii (1981) Phase transitions with coupled order parameters, *Soviet Physics Uspekhi*, **24**, 57-75.

Anisimov, M. A., E. E. Gorodetskii, and N. G. Shmakov (1973) Experimental verification of the isomorphism hypothesis of critical phenomena, *Soviet Physics JETP*, **36**, 1143-1150.

Anisimov, M. A. (1975) Investigations of critical phenomena in liquids, *Soviet Physics Uspekhi*, **17**, 722-744.

Ariola, F. S., D. J. Mudaliar, R. P. Walvick, and A. A. Heikal (2006) Dynamics imaging of lipid phases and lipid-marker interactions in model biomembranes, *Physical Chemistry Chemical Physics*, **8**, 4517-29.

Arnulphi, C. et al (2007) Triton X-100 partitioning into sphingomyelin bilayers at subsolubilizing detergent concentrations: effect of lipid phase and a comparison with dipalmitoylphosphatidylcholine, *Biophysical Journal*, **93**, 3504–3514.

Axelrod, D. (1979) Carbocyanine dye orientation in red cell membrane studied by microscopic fluorescence polarization, *Biophysical Journal*, **26**, 557-574.

Ayuyan, A. G. and F. S. Cohen (2006) Lipid peroxides promote large rafts: effects of excitation of probes in fluorescence microscopy and electrochemical reactions during vesicle formation, *Biophysical Journal*, **91**, 2172–2183.

Bacia, K., P. Schwille, and T. Kurzchalia (2005) Sterol structure determines the separation of phases and the curvature of the liquid-ordered phase in model membranes, *Proceedings of the National Academy of Sciences (USA)*, **102**, 3272-3277.

Bacia, K., D. Scherfeld, N. Kahya, and P. Schwille (2004) Fluorescence correlation spectroscopy relates rafts in model and native membranes, *Biophysical Journal*, **87**, 1034-1043.

Bagatolli, L. A. and E. Gratton (2000) Two photon fluorescence microscopy of coexisting lipid domains in giant unilamellar vesicles of binary phospholipid mixtures, *Biophysical Journal*, **78**, 290–305.

Bagatolli, L.A. and E. Gratton (1999) Two-photon microscopy observation of shape changes at the phase transition in phospholipid giant unilamellar vesicles, *Biophysical Journal*, **77**, 2090-2101.

Barenholz, Y. et al (1976) A calorimetric study of the thermotropic behavior aqueous dispersions of natural and synthetic sphingomyelins, *Biochemistry*, **15**, 2441-2447.

Baumgart, T., S. Hess, and W.W. Webb (2003) Imaging coexisting fluid domains in biomembrane models coupling curvature and line tension, *Nature*, **425**, 821-824.

Baumgart, T. et al (2005) Membrane elasticity in giant vesicles with fluid phase coexistence, *Biophysical Journal*, **89**, 1067–1080.

Baumgart T. et al (2007a) Large-scale fluid/fluid phase separation of proteins and lipids in giant plasma membrane vesicles, *Proceedings of the National Academy of Sciences (USA)*, **104**, 3165–3170.

Baumgart, T, G. Hunt, E. R. Farkas, W. W. Webb, and G. W. Feigenson (2007b) Fluorescence probe partitioning between Lo/Ld phases in lipid membranes, *Biochimica et Biophysica Acta,* **1768**, 2182-2194.

Benninger, R.K.P. et al. (2005) Fluorescence imaging of two-photon linear dichroism: cholesterol depletion disrupts molecular orientation in cell membranes, *Biophysical Journal*, **88**, 609-622.

Berde, C.B., H.C. Andersen, and B.S. Hudson. (1983) A theory of the effects of headgroup structure and chain unsaturation on the chain melting transition of phospholipid dispersions, *Biochemistry*, **19**, 4279-4293.

Blackman, S. M., C. E. Cobb, A. H. Beth, and D. W. Piston (1996) The orientation of eosin-5-maleimide on human erythrocyte band 3 measured by fluorescence polarization microscopy, *Biophysical Journal*, **71**, 194-208.

Blagoi, Y. P., V. I. Sokhan, and A. A. Pavlichenko (1970) Hydrostatic effect in a binary solution near critical dissolution point, *JETP Letters*, **11**, 190-193.

Bloom, J.A. and W.W. Webb (1984) Photo-damage to intact erythrocyte-membranes at high laser intensities - methods of assay and suppression, *Journal of Histochemistry and Cytochemistry*, **32**, 608-616.

Brewster, R., P. A. Pincus, and S. A. Safran (2009) Hybrid lipids as a biological surface-active component, *Biophysical Journal*, **97**, 1087-1094.

Brown, D.A. and J.K. Rose (1992) Sorting of GPI-anchored proteins to glycolipid-enriched membrane subdomains during transport to the apical cell surface, *Cell*, **68**, 533-544.

Brown, R.E. and E. London. (2000) Structure and function of sphingolipid- and cholesterol-rich membrane rafts, *Journal of Biological Chemistry*, **275**, 17221-17224.

Brown, R.E. and T.E. Thomson. (1987) Spontaneous transfer of ganglioside GM1 between phospholipid vesicles, *Biochemistry*, **26**, 8484-8490.

Bruckner, E., P. Sonntag, and H. Rehage (2001) Light-induced shape transitions of unilamellar vesicles, *Langmuir*, **17**, 2308-2311.

Buboltz, J. T. and G. W. Feigenson (1999) A novel strategy for the preparation of liposomes: rapid solvent exchange, *Biochimica et Biophysica Acta*, **1417**, 232-245.

Burgos, P., C. Yuan, M. L. Viriot, and L. J. Johnston (2003) Two-color near-field microscopy studies of microdomains ("rafts") in model membranes, *Langmuir*, **19**, 8002-8009.

Burke, N. A. D., M. Templin, and J. E. Guillet (1996) The mechanism of perylene photo-oxidation in a water soluble polymeric photocatalyst, *Journal of Photochemistry and Photobiology A*, **100**, 93-100.

Busch, N. A., M. L. Yarmush, and M. Toner (1998) A theoretical formalism for aggregation of peroxidized lipids and plasma membrane stability during photolysis, *Biophysical Journal*, **75**, 2956–2970.

Calhoun, W. and G. G. Shipley (1979) Sphingomyelin-lecithin bilayers and their interaction with cholesterol, *Biochemistry: Cholesterol-phospholipid interactions*, **18**, 1717-1722.

Callis, P. R. (1993) On the theory of two-photon induced fluorescence anisotropy with application to indoles, *Journal of Chemical Physics*, **99**, 27-37.

Cantu, L., M. Corti, E. Del Favero, and A. Raudino (1997) Physical aspects of non-ideal mixing of amphiphilic molecules in solution: the interesting case of gangliosides, *Journal of Physics: Condensed Matter*, **9**, 5033-5055.

Carter, W. G. and S. I. Hakomori (1981) A new cell surface, detergent-insoluble glycoprotein matrix of human and hamster fibroblasts, *Journal of Biological Chemistry*, **256**, 6953-6960.

Celli, A., S. Beretta, and E. Gratton (2008) Phase fluctuations on the micron-submicron scale in GUV's composed of a binary lipid mixture, *Biophysical Journal*, **94**, 104-116.

Chabala, L. D. et al (1985) A microscope stage temperature controller for the study of whole-cell or single-channel currents, *European Journal of Physiology*, **404**, 374-377.

Chaikin, P.M. and T.C. Lubensky (2000) *Principles of Condensed Matter Physics*, Cambridge Press: New York, NY.

Chakrabarti, D. and B. Bagchi (2006) Anisotropic translational diffusion in the nematic phase: Dynamical signature of the coupling between orientational and translational order in the energy landscape, *Physical Review E*, **74**, 041704(4).

Chashkin, Y. R., V. G. Gorbunova, and A. V. Voronel (1966) Influence of impurities on singularity of thermodynamic potential at liquid-vapor critical point, *Soviet Physics JETP*, **22**, 304-306.

Chen, R. F. and R. L. Bowman (1965) Fluorescence polarization: measurement with ultraviolet-polarizing filters in a spectrophotofluorometer, *Science*, **147**, 729-732.

Chen, S. Y. and B. W. Van Der Meer (1993) Theory of two-photon induced fluorescence anisotropy decay in membranes, *Biophysical Journal*, **64**, 1567-1575.

Cheng, W.H. (1980) A theoretical description of phase diagrams for non-ideal lipid mixtures, *Biochimica et Biophysica Acta*, **600**, 358-366.

Chiang, Y.W. et al (2005) New method for determining tie-lines in coexisting membrane phases using spin-label ESR, *Biochimica et Biophysica Acta*, **1668**, 99-105.

Chong, P. L. G., B. W. van der Meer, and T. E. Thompson (1985) The effects of pressure and cholesterol on rotational rates of perylene in lipid bilayers, *Biochimica et Biophysica Acta*, **814**, 253-265.

Christ, T. et al (2001) Watching the photo-oxidation of a single aromatic hydrocarbon molecule, *Angewandte Chemie International Edition*, **40**, 4192-4195.

Clarke, J. A., A. J. Heron, J. M. Seddon, and R. V. Law (2006) The diversity of the liquid ordered (L_o) phase of phosphatidylcholine/cholesterol membranes: a variable temperature multinuclear solid-state NMR and x-ray diffraction study, *Biophysical Journal*, **90**, 2383-2393.

Clayden, N. J. et al. (1999) Dynamics of dioloeoylphosphatidylcholine by muon spin relaxation, *Physical Chemistry Chemical Physics*, **1**, 4379-4382.

Collado, M.I. et al (2005) Domain formation in sphingomyelin/cholesterol mixed membranes studied by spin-label electron spin resonance spectroscopy, *Biochemistry*, **44**, 4911-4918.

Corry, B. et al (2006) Determination of the orientational distribution and orientation factor for transfer between membrane-bound fluorophores using a confocal microscope, *Biophysical Journal*, **91**, 1032-1045.

Crane, J.M. and L.K. Tamm (2004) Role of cholesterol in the formation and nature of lipid rafts in planar and spherical model membranes, *Biophysical Journal*, **86**, 2965-2979.

Dale, R. E. et al (1999) Model-independent analysis of the orientation of fluorescent probes with restricted mobility in muscle fibers, *Biophysical Journal*, **76**, 1606-1618.

Davenport, L. (1997) Fluorescence probes for studying membrane heterogeneity, *Methods in Enzymology*, **278**, 487-512.

Davenport, L. and P. Targowski (1996) Submicrosecond phospholipid dynamics using a long-lived fluorescence emission anisotropy probe, *Biophysical Journal*, **71**, 1837-1852.

de Almeida, R. F. M. et al (2007) Complexity of lipid domains and rafts in giant unilamellar vesicles revealed by combining imaging and microscopic and macroscopic time-resolved fluorescence, *Biophysical Journal*, **93**, 539-553.

de Almeida, R. F. M. et al (2005) Lipid rafts have different sizes depending on membrane composition: a time-resolved fluorescence resonance energy transfer study, *Journal of Molecular Biology*, **346**, 1109-1120.

de Almeida, R. F. M., A. Federov, and M. Prieto (2003) Sphingomyelin/ phosphatidylcholine/ cholesterol phase diagram: Boundaries and composition of lipid rafts, *Biophysical Journal*, **85**, 2406-2416.

de Almeida, R. F. M., L. M. S. Loura, A. Fedorov, and M. Prieto (2002) Nonequilibrium phenomena in the phase separation of a two-component lipid bilayer, *Biophysical Journal*, **82**, 823-834.

Deitrich, C. et al. (2001) Lipid rafts reconstituted in model membranes, *Biophysical Journal*, **80**, 1417-1428.

Denk, W., J. H. Strickler, and W. W. Webb (1990) Two-photon laser scanning fluorescence microscopy, *Science*, **248**, 73-76.

Dibble, A. R. G., M. D. Yeager, and G. W. Feigenson (1993) Partitioning of gramicidin A' between coexisting fluid and gel phospholipid phases, *Biochimica et Biophysica Acta*, **1153**, 155-162.

Dimitrov, D.S. and M.I. Angelova (1987) Electric field mediated lipid swelling and liposome formation, *Studia Biophysica*, **119**, 61-65.

Dix, J. A. and A. S. Verkman (1990) Mapping of fluorescence anisotropy in living cells by ratio imaging: Application to cytoplasmic viscosity, *Biophysical Journal*, **57**, 231-240.

Doniach, S. (1978) Thermodynamic fluctuations in phospholipid bilayers, *Journal of Chemical Physics*, **68**, 4912-4916.

Dorgan, J. R. and D. Yan (1998) Kinetics of spinodal decomposition in liquid crystalline polymers: processing effects on the phase separation morphology, *Macromolecules*, **31**, 193-200.

Drobnies, A. E. et al (1999) CTP:phosphocholine cytidylyltransferase activation by oxidized phosphatidylcholines correlates with a decrease in lipid order: a ^{2}H NMR analysis, *Biochemistry*, **38**, 15606-15614.

Edidin, M. (2003) The state of lipid rafts: from model membranes to cells, *Annual Reviews of Biophysics and Biomolecular Structure*, **32**, 257-283.

Edwards, C., J. A. Lipa, and J. M. Buckinham (1968) Specific heat of xenon near the critical point, *Physical Review Letters*, **20**, 496-499.

Epand, R. M. et al (2001) Protein-induced formation of cholesterol-rich domains, *Biochemistry*, **40**, 10514-10521.

Ernst, H. J., F. Fabre, and J. Lapujoulande (1992) Observation of dynamical scaling in "spinodal decomposition" in two dimensions, *Physical Review Letters*, **69**, 458-461.

Eroglu, C. et al. (2003) Glutamate-binding affinity of Drosphila metatropic glutamate receptor is modulated by association with lipid rafts, *Proceedings of the National Academy of Sciences (USA)*, **100**, 10219-10224.

Esposito, C. et al (2007) Flicker Spectroscopy of thermal lipid bilayer domain boundary fluctuations, *Biophysical Journal*, **93**, 3169–3181.

Estep, T. N., D. B. Mountcastle, R. L. Biltonen, and T. E. Thompson (1978) Studies on the anomalous thermotropic behavior of aqueous dispersions of dipalmitoylphosphatidylcholine cholesterol mixtures, *Biochemistry*, **17**, 1984-1989.

Estep, T.N. et al. (1979) Thermal behavior of sphingomyelin-cholesterol dispersions, *Biochemistry*, **19**, 2112-2117.

Estep, T.N. et al. (1981) Evidence for metastability in stearoylsphingomyelin bilayers, *Biochemistry*, **20**, 7115-7118.

Fahey, P.F. and W.W. Webb. (1978) Lateral diffusion in phospholipid bilayer membranes and multilamellar liquid crystals, *Biochemistry*, **17**, 3046-3053.

Fahsel, S. et al (2002) Modulation of concentration fluctuations in phase-separated lipid membranes by polypeptide insertion, *Biophysical Journal*, **83**, 334-344.

Faraudo, J. (2002) Diffusion equation on curved surfaces. I. Theory and application to biological membranes, *Journal of Chemical Physics*, **116**, 5831-5841.

Feigenson, G.W. and J.T. Buboltz (2001) Ternary phase diagram of dipalmitoyl-PC/dilauryl-PC/cholesterol: nanoscopic domain formation driven by cholesterol, *Biophysical Journal*, **80**, 2775-2788.

Fiałkowski, M. And R. Holyst (2002) Morphological changes during the order-disorder transition in the two- and three-dimensional systems of scalar nonconserved order parameters, *Physical Review E*, **66**, 46121-46134.

Field, K.A., D. Holowka, and B. Baird (1995) FcεRI-mediated recruitment of p53/56(lyn) to detergent-resistant membrane domains accompanies cellular signaling field, *Proceedings of the National Academy of Sciences (USA)*, **92**, 9201–9205.

Filipov, A., G. Oradd, and G. Lindblom (2006) Sphingomyelin structure influences the lateral diffusion and raft formation in lipid bilayers, *Biophysical Journal*, **90**, 2086-2092.

Fisher, M. E. (1967) The theory of equilibrium critical phenomena, *Reports on Progress in Physics*, **30**, 615-730.

Fisher, M. E. and Y. C. Kim (2002) Right and wrong near critical endpoints, *Journal of Chemical Physics*, **117**, 779-787.

Florine-Casteel, K. (1990) Phospholipid order in gel- and fluid-phase cell-size liposomes measured by digitized video fluorescence microscopy, *Biophysicsl Journal*, **57**, 1199-1215.

Florine, K. I. and G. W. Feigenson (1987) Protein redistribution in model membranes: clearing of M 13 coat protein from calcium-induced gel-phase regions in phosphatidylserine/ phosphatidylcholine multilamellar vesicles, *Biochemistry*, **26**, 2978-2983.

Fridriksson, E. K. et al (1999) Quantitative analysis of functionally important membrane domains from RBL-2H3 mast cells using tandem high-resolution mass spectrometry, *Biochemistry*, **38**, 8056-8063.

Frolov, V.A.J., Y. A. Chizmadzhev, F. S. Cohen, and J. Zimmerberg (2006) ‘‘Entropic traps’’ in the kinetics of phase separation in multicomponent membranes stabilize nanodomains, *Biophysical Journal*, **91**, 189-205.

Fukuzawa, K. et al (2006) Measurement of phosphatidylcholine hydroperoxides in solution and in intact membranes by the ferric–xylenol orange assay, *Analytical Biochemistry*, **359**, 18–25.

Fuller, N. and R. P. Rand (2001) The influence of lysolipids on the spontaneous curvature and bending elasticity of phospholipid membranes, *Biophysical Journal*, **81**, 243-254.

Galley, H.U., A. Seeling, and J. Seeling (1976) Cholesterol-induced rod-like motion of fatty-acid acyl chains in lipid bilayers: a deuterium magnetic resonance study, *Hoppe Seylers Zeitschrift fur Physiologische Chem*ie, **357**, 1440-1450.

Geoffroy, M. et al (2000) Role of hydroxyl radicals and singlet oxygen in the formation of primary radicals in unsaturated lipids: A solid state electron paramagnetic resonance study, *Journal of Agricultural and Food Chemistry*, **48**, 974-978.

Gandhavadi, M., D. Allende, A. Vidal, S. A. Simon, and T. J. McIntosh (2002) Structure, composition, and peptide binding properties of detergent soluble bilayers and detergent resistant rafts, *Biophysical Journal*, **82**, 1469-1482.

Gidwani, A., D. Holowka, and B. Baird (2001) Fluorescence anisotropy measurements of lipid order in plasma membranes and lipid rafts from RBL-2H3 mast cells, *Biochemistry*, **40**, 12422–12429.

Gil, Z., K. L. Magleby, and S. D. Silerberg (1999) Membrane-pipette interactions underlie delayed voltage activation of mechanosensitive channels in *xenopus* oocytes, *Biophysical Journal*, **76**, 3118-3127.

Girard, P., J. Prost, and P. Bassereau (2005) Passive or active fluctuations in membranes containing proteins, *Physical Review Letters*, **94**, 88102-88105.

Goncalves, S., G. Martinez, and J. R. Iglesias (1997) Non-universality of phase separation in two-dimensional critical binary-fluid mixtures, *Europhysics Letters*, **39**, 281-286.

Griffiths, R.B. and B. Widom (1973) Multicomponent fluid tricritical points, *Physical Review A*, **8**, 2173-2175.

Grit, M. et al (1993) Hydrolysis of partially saturated egg phosphatidylcholine in aqueous liposome dispersions and the effect of cholesterol incorporation on hydrolysis kinetics, *Journal of Pharmaceutics and Pharmacology*, **45**, 490-495.

Guo, W. et al (2002) A solid-state NMR study of phospholipid-cholesterol interactions: sphingomyelin-cholesterol binary systems, *Biophysical Journal*, **83**, 1465-1478.

Gu, M. et al (1997) Ceramide profiling of complex lipid mixtures by electrospray ionization mass spectrometry, *Analytical Biochemistry*, **244**, 347–356.

Haas, C. and J. M. Torkelson (1995) 2D coarsening in phase-separated polymer solutions: dependence on distance from criticality, *Physical Review Letters*, **75**, 3134-3137.

Haines, G. V. (1985) Spherical cap harmonic analysis, *Journal of Geophysical Research*, **90**, 2583-2591.

Halstenberg, S., W. Schrader, P. Das, J. K. Bhattacharjee, and U. Kaatze (2003) Critical fluctuations in the domain structure of lipid membranes, *Journal of Chemical Physics*, **118**, 5683-5691.

Haluska, C. K. et al (2008) Combining fluorescence lifetime and polarization microscopy to discriminate phase separated domains in giant unilamellar vesicles, *Biophysical Journal*, **95**, 5737-5747.

Hancock, J. F. (2006) Lipid rafts: contentious only from simplistic standpoints, *Nature Reviews: Molecular and Cellular Biology*, **7**, 456- 462.

Hankey, A., T.S. Chang, and H.E. Stanley (1974) Tricritical points in multicomponent fluid mixtures, *Physical Review A*, **9**, 2573-2578.

Hao, M. M., S. Mukherjee, and F.R. Maxfield (2001) Cholesterol depletion induces large scale domain segregation in living cell membranes, *Proceedings of the National Academy of Sciences (USA)*, **98**,13072–13077.

Harder, T. and M. Kuhn (2000) Selective accumulation of raft-associated membrane protein LAT in T-cell receptor signaling assemblies, *Journal of Cell Biology*, **151**, 199-207.

Hare, F. (1983) Simplified derivation of angular order and dynamics of rodlike fluorophores in models and membranes: simultaneous estimation of the order and

fluidity parameters for diphenylhexatriene by only coupling steady-state illumination polarization and lifetime of fluorescence, *Biophysical Journal*, **42**, 205-218.

Haataj, M. (2009) Critical dynamics in multicomponent lipid membranes, *Physical Review E*, **80**, 020902 (4).

Heerklotz, H. (2002) Triton promotes domain formation in lipid raft mixtures, *Biophysical Journal*, **83**, 2693-2701.

Heimberg, T. (2000) A model for the lipid pretransition: coupling of ripple formation with the chain-melting transition, *Biophysical Journal*, **78**, 1154-1165.

Heimberg, T. (1998) Mechanical aspects of membrane thermodynamics. Estimation of the mechanical properties of lipid membranes close to the chain melting transition from calorimetry, *Biochimica et Biophysica Acta*, **1415**, 147-162.

Heinrich, M. C., I. Levental, H. Gelman, P. A. Janmey, and T. Baumgart (2008) Critical exponents for line tension and dipole density difference from lipid monolayer domain boundary fluctuations, *Journal of Physical Chemistry B.*, **112**, 8063-8068.

Heyn, M. P. (1979) Determination of lipid order parameters and rotational correlation times from fluorescence depolarization experiments, *FEBS Letters*, **108**, 359-364.

Hoff, B., E. Strandberg, A. S. Ulrich, D. P. Tieleman, and C. Posten (2005) ^{2}H NMR study and molecular dynamics simulation of the location, alignment, and mobility of pyrene in POPC bilayers, *Biophysical Journal*, **88**, 1818–1827.

Holyst, R., D. Plewczynski, and A. Aksimentiev (1999) Diffusion on curved periodic sufaces, *Physical Review E*, **60**, 302-307.

Honerkamp-Smith, A. et al (2008) Line tensions, correlation lengths, and critical exponents in lipid membranes near critical points, *Biophysical Journal*, **95**, 236-246.

Hopkins, B. C. et al (1998) Fluorescence polarization transients from rhodamine isomers on the myosin regulatory light chain in skeletal muscle fibers, *Biophysical Journal*, **74**, 3093-3110.

Huang, J. and G.W. Feigenson (1999) A microscopic model of maximum solubility of cholesterol in lipid bilayers, *Biophysical Journal*, **76**, 2142-2157.

Huang, T. H., C. W. B. Lee, S. K. Das Gupta, and R. G. Griffin (1993) A ^{13}C and ^{2}H nuclear magnetic resonance study of phosphatidylcholine/cholesterol interactions: characterization of liquid– gel phases, *Biochemistry*, **32**, 13277–13287.

Hung, W. C., F.Y. Chen, H. W. Huang (2000) Order-disorder transition in bilayers of diphytanoyl phosphatidylcholine, *Biochimica et Biophysica Acta*, **1467**, 198-206.

Hwang, J. et al (1998) Domains in cell plasma membranes investigated by near-field scanning optical microscopy, *Biophysical Journal*, **74**, 2184–2190.

Ipsen, J. H., O. G. Mouritsen, and M. Bloom (1990) Relationships between lipid membrane area, hydrophobic thickness, and acyl-chain orientational order, *Biophysical Journal*, **57**, 405-412.

Ipsen, J.H. et al. (1987) Phase equilibria in the phosphatidylcholine-cholesterol system, *Biochimica et Biophysica Acta*, **905**, 162-172.

Ipsen, J.H., O.G. Mourtisen, and M.J. Zuckermann. (1989) Theory of thermal anomalies in the specific heat of lipid bilayers containg cholesterol, *Biophysical Journal*, **56**, 661-667.

Ivanova, P.T. et al (2001) Electrospray ionization mass spectrometry analysis of changes in phospholipids in RBL-2H3 mastocytoma cells during degranulation, *Proceedings of the National Academy of Sciences (USA)*, **98**, 7152-7157.

Jahnig, F. (1981b) Critical effects from lipid-protein interaction in membranes II. Interpretation of experimental results, *Biophysical Journal*, **36**, 347-357.

Jahnig, F. (1981a) Critical effects from lipid-protein interaction in membranes I. Theoretical description, *Biophysical Journal*, **36**, 329-345.

Jahnig, F. (1979) Molecular theory of lipid membrane order, *Journal of Chemical Physics*, **70**, 3279-3290.

Jahnig, F. (1979) Structural order of lipids and proteins in membranes: evaluation of fluorescence anisotropy data, *Proceedings of the National Academy of Sciences (USA)*, **76**, 6361-6365.

Jensen, M. O. and O. G. Mouritsen (2004) Lipids do influence protein function—the hydrophobic matching hypothesis revisited, *Biochimica et Biophysica Acta*, **1666**, 205-226.

Jin, L. et al (2005) Cholesterol-enriched lipid domains can be visualized by di-4-ANEPPDHQ with linear and nonlinear optics, *Biophysical Journal*, **89**, L04-L06.

Jin, A.J., M. Edinin, R. Nossal, and N.L Gershfeld (1999) A singular state of membrane lipids at cell-growth temperatures, *Biochemistry*, **38**, 13275-13278.

Jorgenson, K. and O. G. Mouritsen (1995) Phase separation dynamics and lateral organization of two-component lipid membranes, *Biophysical Journal*, **95**, 942-954.

Kaiser, J. H. et al (2009) Order of lipid phases in model and plasma membranes, *Proceedings of the National Academy of Sciences (USA)*, **39**, 16645-16650.

Kamat, R. K. and G. M. Naik (2002) Thermistors-In search of new applications, manufacturers cultivate advanced NTC techniques, *Sensor Review*, **22**, 334-340.

Kingsley, P. B. and G. W. Feigenson (1979) The synthesis of a perdeuterated phospholipid: 1,2-dimyristoyl-sn-glycero-3-phosphocholine-d71, *Chemistry and Physics of Lipids*, **24**, 135-147.

Kinosita, K., S. Kawato, and A. Ikegami (1977) A theory of fluorescence depolarization in membranes, *Biophysical Journal*, **20**, 289-305.

Kinosita, K., A. Ikegami, and S. Kawato (1982) On the wobbling-on-a-cone analysis of fluorescence anisotropy decay, *Biophysical Journal*, **37**, 461-464.

Knoll, W., K. Ibdel, and E. Sackmann (1981) Small angle neutron scattering study of lipid phase diagrams by the contrast variation method, *Biochemistry*, **20**, 6379-6383.

Knoll, W. et al. (1983) Critical demixing in fluid bilayers of phospholipid mixtures: a neutron diffraction study, *Journal of Chemical Physics*, **79**, 3439-3442.

Knutson, J. R., L. Davenport, and L. Brand (1986) Anisotropy decay associated fluorescence-spectra and analysis of rotational heterogeneity .1. Theory and applications, *Biochemistry*, **25**, 1805–1810.

Kodati, V. R., and M. Lafleur (1993). Comparison between orientational and conformational orders in fluid lipid bilayers, *Biophysical Journal*, **64**,163-170.

Koivusalo, M. et al (2004) Partitioning of pyrene-labeled phospho- and sphingolipids between ordered and disordered bilayer domains, *Biophysical Journal*, **86**, 923-935.

Komura, S. et al. (2004) Lateral phase separation in mixtures of lipids and cholesterol, *Europhysics Letters*, **67**, 321-327.

Korlach, J., T. Baumgart, W. W. Webb, and G. W. Feigenson (2005) Detection of motional heterogeneities in lipid bilayer membranes by dual probe fluorescence correlation spectroscopy, *Biochimica et Biophysica Acta*, **1668**, 158-163.

Korlach, J et al. (1999) Characterization of lipid bilayer phases by confocal microscopy and fluorescence correlation spectroscopy, *Proceedings of the National Academy of Sciences (USA)*, **96**, 8461-8466.

Korolev, K. S. and D. R. Nelson (2008) Defect-mediated emulsification in two dimensions, *Physical Review E*, **77**, 051702 (11).

Kraft, M. L. et al (2006) Phase separation of lipid membranes analyzed with high-resolution secondary ion mass spectrometry, *Science*, **313**, 1948-1951.

Kumar, P. B. S., G. Gomper, and R. Lipowski (1999) Modulated phases in multicomponent fluid membranes, *Physical Review E*, **60**, 4610-4618.

Kuo, A.L. and C.G. Wade (1979) Lipid lateral diffusion by pulsed nuclear magnetic resonance, *Biochemistry*, **18**, 2300-2308.

Kusumi, A. et al (2005) Paradigm shift of the plasma membrane concept from the two-dimensional continuum fluid to the partitioned fluid: high-speed single molecule tracking of membrane molecules, *Annual Review of Biophysics and Biomolecular Structure*, **34**, 351-378.

Laggner, P. (1993) Nonequilibrium phenomena in lipid membrane phase transitions, *Journal de Physique IV*, **3**, 259-269.

Lakowicz, J. R. et al (1992) Two photon-induced fluorescence intensity anisotropy decays of diphenylhexatriene in and lipid bilayers, *Journal of Fluorescence*, **2**, 247-258.

Lakowicz, J. R. et al (1980) Hindered depolarizing rotations of perylene in lipid bilayers—Detection by lifetime-resolved fluorescence anisotropy measurements, *Biochemistry*, **19**, 905–911.

Laradji, M., O. G. Mouritsen, and S. Toxvaerd (1994) Dynamics of phase separation in ternary-fluid mixtures, *Europhysics Letters*, **28**, 157-162.

Larmer, J. et al (1997) Imaging excised apical plasma membrane patches of MDCK cells in physiological conditions with atomic force microscopy, *European Journal of Physiology*, **434**, 254–260.

Lasch, J. et al (1998) Photooxydative damage of skin lipids in liposomes (hSCLLs)—interference of sterols with the lipid peroxidation chain, *International Journal of Pharmaceutics*, **162**, 129-136.

Lee, A. G. (1977) Lipid phase transitions and phase diagrams. I. Lipid phase transitions, *Biochimica et Biophysica Acta*, **472**, 237-281.

Leibler, S. and D. Andelman (1987) Ordered and curved meso-structures in membranes and amphiphilic films, *Journal de Physique*, **48**, 2013-2018.

Lentz, B. R., D.A. Barrow, and M. Hoechli. (1980) Cholesterol-phosphtidylcholine interactions in multilamellar vesicles, *Biochemistry*, **19**, 1943-1954.

Lentz, B. R., M. Hoechli, and Y. Barenholz (1981) Acyl chain order and lateral domain formation in mixed phosphatidylcholine-sphingomyelin multilamellar and unilamellar vesicles, *Biochemistry*, **20**, 6803-6808.

Lentz, B.R., Y. Barenholz, and T.E. Thompson (1976) Fluorescence depolarization studies of phase transitions and fluidity in phospholipid bilayers 2: two-component phosphatidylcholine liposomes, *Biochemistry*, **15**, 4529-4537.

Levitas, V. I., D. L. Preston, and D. W. Lee (2006) Ginzburg-Landau theory of microstructures: Stability, transient dynamics, and functionally graded nanophases, *Europhysics Letters*, **75**, 84-90.

Lipari, G. and A. Szabo (1980) Effect of librational motion on fluorescence depolarization and nuclear magnetic resonance relaxation in macromolecules and membranes, *Biophysical Journal*, **30**, 489-506.

Lipowski, J. (1992) Budding of membranes induced by intramembrane domains, *Journal de Physique II*, **2**, 1825-1840.

Lis L.J.,M. McAlister, N. Fuller, R. P. Rand, V. A. Parsegian (1982) Interactions between neutral phospholipid bilayer membranes, *Biophysical Journal*, **37**, 657–665.

Lodish et al (2004) *Molecular Cell Biology* (5th Edition), W. H. Freeman and Company: New York, NY.

Loura, L. M. S., A. Federov, and M. Prieto (2001) Fluid-fluid membrane microheterogeniety: a fluorescence resonance energy transfer study, *Biophysical Journal*, **80**, 776-788.

Mabrey, S. and J.M. Sturtevant (1976) Investigation of phase transitions of lipids and lipid mixtures by high sensitivity differential scanning calorimetry, *Proceedings of the National Academy of Sciences (USA)*, **73**, 3862-3866.

Magee, A. I., J. Adler, and I. Parmryd (2005) Cold-induced coalescence of T-cell plasma membrane microdomains activates signalling pathways, *Journal of Cell Science*, **118**, 3141-3151.

Mahammad, S. and I. Parmryd (2008) Cholesterol homeostasis in T-cells: Methyl-β-cyclodextrin treatment results in equal loss of cholesterol from Triton X-100 soluble and insoluble fractions, *Biochimica et Biophysica Acta*, **1778**, 1251-1258.

Maier, W. and A. Saupe (1958) A simple molecular theory of the nematic crystalline-liquid state, *Zeitschrift fur Naturforschung Teil A*, **13**, 564-566.

Maloney, K.M. et al (1996) Membrane microstructural templates for enzyme domain formation, *Journal of Molecular Recognition*, **9**, 368-374.

Mathivet, L., S. Cribier, P.F. Devaux (1996) Shape change and physical properties of giant phospholipid vesicles prepared in the presence of an AC electric field, *Biophysical Journal*, **70**, 1112–1121.

Maulik, P.M. and G.G. Shipley (1996) N-palmitoylshingomyelin bilayers: structure and interaction with cholesterol and dipalmitoylphosphatidylcholine, *Biochemistry*, **35**, 8025-8034.

Maulik, P. R., P. K. Sripada, and G. G. Shipley (1991) Structure and thermotropic properties of hydrated N-stearoyl sphingomyelin bilayer-membranes, *Biochimica et Biophysica Acta*, **1062**, 211-219.

McClain, W.M. (1971) Excited state symmetry assignment through polarized two-photon absorption studies of fluids, *Journal of Chemical Physics*, **55**, 2789-2796.

McConnell, H. (2009) Nuclear relaxation and critical fluctuations in membranes containing cholesterol, *Journal of Chemical Physics*, **130**, 165103-165110.

McConnell, H. and A. Radhakrishnan (2008) Molecular motion at the critical point in lipid membranes, *Biophysical Journal*, **95**, L22-L24.

McConnell, H. and A. Radhakrishnan (2007) Composition fluctuations, chemical exchange, and nuclear relaxation in membranes containing cholesterol, *Journal of Chemical Physics*, **126**, 185101-185111.

McConnell, H. and A. Radhakrishnan (2006) Theory of deuterium NMR of sterol-phospholipid membranes, *Proceedings of the National Academy of Sciences (USA)*, **103**, 1184-1189.

McConnell, H. (2005) Complexes in ternary cholesterol-phospholipid mixtures, *Biophysical Journal: Biophysics Letters*, L23-L25.

McIntosh, T. (1978) The effect of cholesterol on phosphatidylcholine bilyers, *Biochimica et Biophysica Acta*, **513**, 43-58.

McQuaw, C. et al (2007) Localization of sphingomyelin in cholesterol domains by imaging mass spectrometry, *Langmuir*, **23**, 5645–5650.

Mecke, K. R. and V. Sofonea (1997) Morphology of spinodal decomposition, *Physical Review E*, **56**, R3761-R3764.

Mills, T. T., G. E. S. Toombes, S. Tristram-Nagle, D.-M. Smielgies, G. W. Feigenson and J. F. Nagle (2008) Order parameters and areas in fluid-phase oriented lipid membranes using wide angle X-ray scattering, *Biophysical Journal*, **95**, 669-681.

Mills, J. K. and D. Needham (2005) Lysolipid incorporation in pipalmitoylphasphatidylcholine bilayer membranes enhances the ion permeability and drug release rates at the membrane phase transition, *Biochimica et Biophysica Acta*, **1716**, 77-96.

Mitaku, S., T. Jippo, and R. Kataoka (1983) Thermodynamic properties of the lipid bilayer transition. Pseudocritical phenomena, *Biophysical Journal*, **42**, 137-144.

Mitchell, D. C. and B. J. Litman (1998) Effect of cholesterol on molecular order and dynamics in highly unsaturated phospholipid bilayers, *Biophysical Journal*, **75**, 896-908.

Mitchell, A. G., and W. F. K. Wynne-Jones (1953) Thermodynamic and other properties of solutions involving hydrogen bonding, *Discussions of the Faraday Society*, **15**, 161-168.

Mozuraityte, R. et al (2008) The role of iron in peroxidation of polyunsaturated fatty acids in liposomes, *Journal of Agricultural and Food Chemistry*, **56**, 537–543.

Mukherjee, S. et al (1998) Cholesterol distribution in living cells: fluorescence imaging using dehydroergosterol as a fluorescent cholesterol analog, *Biophysical Journal*, **75**, 1915-1925.

Murase, K. et al (2004) Ultrafine membrane compartments for molecular diffusion as revealed by single molecule techniques, *Biophysical Journal*, **86**, 4075-4093.

Nagano, H., H. Yao, and K. Ema (1995) Dynamic heat capacity at the gel to liquid-crystalline phase transition in large unilamellar vesicles of dimyristoylphosphtidylcholine in the ultralow frequency region, *Physical Review E*, **51**, 3363-3367.

Nagle, J. F. (1980) Theory of the main lipid bilayer phase transition, *Annual Review of Physical Chemistry*, **31**, 157-195.

Nagle, J. F. and D. A. Wilkinson (1978) Lecithin bilayers. Density measurement and molecular interactions, *Biophysical Journal*, **23**, 159–175.

Nagle, J. F. and J. C. Bonner (1976) Phase transitions: beyond the simple Ising model, *Annual Review of Physical Chemistry*, **27**, 291-317.

Nagle, J. F. (1973) Theory of biomembrane phase transitions, *Journal of Chemical Physics*, **58**, 252-264.

Nail, S.L, L. M. Her, C. P. B. Proffitt, and L. L. Nail (1994) An improved microscope stage for direct observation of freezing and freeze drying, *Pharmaceutical Research*, **11**, 1098-1100.

Narayanasamy, J. and J.D. Kubicki (2005) Mechanism of hydroxyl radical generation from a silica surface: molecular orbital calculations, *Journal of Physical Chemistry B*, **109**, 21796-21807.

Neilson, M. et al (1996) Random lattice models and simulation algorithms for the phase equilibria in two-dimensional condensed systems of particles with coupled internal and translational degrees of freedom, *Physical Review E*, **54**, 6889-6905.

Nelson, D.R. and L. Peliti (1987) Fluctuations in membranes with crystalline hexatic order, *Journal de Physique*, **48**, 1085-1092

Nuchi et al (2002) Ability of lipid hydroperoxides to partition into surfactant micelles and alter lipid oxidation rates in emulsions, *Journal of Agricultural and Food Chemistry*, **50**, 5445-5449.

Okada, Y., G. Mugnai, E. G. Bremer, and S. I. Hakomori (1984) Glycosphingolipids in detergent-insoluble substrate attachment matrix (DIAM) prepared from substrate attachment material (SAM): Their possible role in regulating cell adhesion, *Experimental Cell Research*, **155**, 448-456.

Opanasyuk, O. et al (2009) Two-photon excited fluorescence depolarization and electronic energy migration within donor-donor pairs, *Physical Chemistry Chemical Physics*, **11**, 7152-7160.

Opsahl, L.R. and W.W. Webb (1994) Lipid-glass adhesion in giga-sealed patch-clamped membranes, *Biophysical Journal*, **66**, 75-79.

Oreopoulos, J. and C. M. Yip (2009) Probing membrane order and topography in supported lipid bilayers by combined polarized total internal reflection fluorescence-atomic force microscopy, *Biophysical Journal*, **96**, 1970–1984.

Pal, B. (1919) On the numerical calculation of the roots of the equations $P_n^m(\mu) = 0$ and $d/d\mu\ (P_n^m(\mu)) = 0$ regarded as equations in *n*, *Bulletin of the Calcutta mathematical Society*, **9** (2), 85-95.

Pan, J., T. T. Mills, S. Tristam-Nagle, and J. F. Nagle (2008) Cholesterol perturbs lipid bilayers nonuniversally, *Physical Review Letters*, **100**, 189103 (3).

Pauls, S. W., J. F.Hedstrom, and C. K. Johnson (1998) Rotational relaxation of perylene in n-alcohols and n-alkanes studied by two-photon induced anisotropy decay, *Chemical Physics*, **237**, 205-222.

Pastor, R., R. M. Venable, and M. Karplus (1991) Model for the structure of the lipid bilayer, *Proceedings of the National Academy of Sciences (USA)*, **88**, 892-896.

Pei, B. and J. W. Chen (2003) More ordered, convex ganglioside-enriched membrane domains: The effects of GM1 on sphingomyelin bilayers containing a low level of cholesterol, *Journal of Biochemistry*, **134**, 575–581.

Peterson, N. O. and S. I. Chan (1977) More on the motional state of lipid bilayer membranes: interpretation of order parameters obtained from nuclear magnetic resonance experiments, *Biochemistry*, **16**, 2657-2667.

Peticolas, W. L., R. Norris, and K. E. Reickhoff (1965) Polarization effects in the two-photon excitation of anthracene fluorescence, *Journal of Chemical Physics*, **42**, 416-4169.

Pink, D. A. and C. E. Carroll (1978) A model of cholesterol in lipid bilayers, *Physical Review Letters*, **66A**, 157-160.

Polozov, I. V. and K. Gawrisch (2006) Characterization of the liquid-ordered state by photon MAS NMR, *Biophysical Journal*, **90**, 2051-2061.

Potoma, E. O. and X. S. Xie (2003) Detection of single lipid bilayers with coherent anti-Stokes Raman scattering (CARS) microscopy, *Journal of Raman Spectroscopy*, **34**, 642-650.

Pott, T., H. Bouvrais, and P. Meleard (2008) Giant unilamellar vesicle formation under physiologically relevant conditions, *Physics and Chemistry of Lipids*, **154**, 115-119.

Prost, J., J.B. Manneville, and R. Bruinsma (1998) Fluctuation-magnification of non-equilibrium membranes near a wall, *European Physics Journal B*, **1**, 465-480.

Rademacher, A., S. Maerkle, H. Langhals (1982) Loesliche perylen-fluoreszenzfarbstoffe mit hoher photostabilitaet, *Chemische Berichte*, **115**, 2927–2934.

Radhakrishnan, A. and H. McConnell (2005) Condensed complexes in vesicles containing cholesterol and phospholipids, *Proceedings of the National Academy of Sciences (USA)*, **102**, 12662-12666.

Raudino, A. (1998) A model for the enzyme activity in systems with large composition fluctuations. An application to the unusual kinetics of phospholipase A2, *European Physics Journal B*, **2**, 197-210.

Reinl, H., T. Brumm, and T. M. Bayer (1992) Changes of the physical properties of the liquid-ordered phase with temperature in binary mixtures of DPPC with cholesterol: A 2H-NMR, FT-IR, DSC, and neutron scattering study, *Biophysical Journal*, **61**, 1025-1035.

Rectenwald, D.J. and H.M. McConnell (1981) Phase equilibria in binary mixtures of phosphatidylcholine and cholesterol, *Biochemistry*, **20**, 4505-4510.

Rinia, H. A., M. M. E. Snel, J. P. J. M. van der Eerden, and B. deKruijff (2001) Visualizing detergent resistant domains in model membranes with atomic force microscopy, *FEBS Letters*, **501**, 92–96.

Ruggiero, A. and B. Hudson (1989) Critical density fluctuations in lipid bilayers detected by fluorescence lifetime, *Biophysical Journal*, **55**, 1111-1124.

Sacconi, L. D. A Dombeck and W. W. Webb (2006) Overcoming photodamage in second-harmonic generation microscopy: Real-time optical recording of neuronal action potentials, *Proceedings of the National Academy of Sciences (USA)*, **103**, 3124-3129.

Sackmann, E. (1995) *Handbook of Biological Physics* (Chapter 5), **1**, Elsevier Science B.V.: St. Louis, MO.

Salamon, Z. and G. Tollin (2001) Optical anisotropy in lipid bilayer membranes: couples plasmon-waveguide resonance measurements of molecular orientation, polarizability, and shape, *Biophysical Journal*, **80**, 1557-1567.

Samsonov, A.V., I. Mikhalov, and F.S. Cohen (2001) Characterization of cholesterol-sphingomyelin domains and their dynamics in bilayer membranes, *Biophysical Journal*, **81**, 1486-1500.

Sandhoff, R. et al (1999) Determination of cholesterol at the low picomole level by nano-electrospray ionization tandem mass spectrometry, *Journal of Lipid Research*, **40**, 126-132.

Sankaram, M. B. and T. E. Thompson (1990a) Interaction of cholesterol with various glycerophospholipids and sphingomyelin, *Biochemistry*, **29**, 10670-10675.

Sankaram, M. B. and T. E. Thompson (1990b) Modulation of phospholipid acyl chain order by cholesterol. A solid-state ^{2}H nuclear magnetic resonance study, *Biochemistry*, **29**, 10676–10684.

Schroeder, R., E. London, and D. Brown (1994) Interactions between saturated acyl chains confer detergent resistance on lipids and glycosylphosphatidylinositol (GPI)-anchored proteins: GPI-anchored proteins in cells and liposomes show similar behavior, *Proceedings of the National Academy of Sciences (USA)*, **91**, 12130-12134.

Seelig, J., and W. Niederberger (1974) Deuterium-labeled lipids as structural probes in liquid crystalline bilayers. A deuterium magnetic resonance study, *Journal of the American Chemical Society*, **96**, 2069-2072.

Seelig, A., and J. Seelig (1974) The dynamic structure of fatty acyl chains in a phospholipid bilayer measured by deuterium magnetic resonance, *Biochemistry*, **13**, 4839-4845.

Seifert, U. (1993) Curvature-induced lateral phase segregation in two-component vesicles, *Physical Review Letters*, **70**, 1335-1338.

Sepiol, J. et al (1997) Single molecules observed by immersion mirror objective. The orientation of terrylene molecules via the direction of its transition dipole moment, *Chemical Physics Letters*, **273**, 444-448.

Seul, M. and D. Andelman (1995) Domain shapes and patterns: the phenomenology of modulated phases, *Science*, **267**, 476-483.

Sharma, P. et al (2004) Nanoscale organization of multiple GPI-anchored proteins in living cell membranes, *Cell*, **116**, 577-589.

Sheets, E. D., D. Holowka, and B. Baird (1999a) Membrane organization in immunoglobin E receptor signaling, *Current Opinion in Chemical Biology*, **3**, 95-99.

Sheets, E. D., D. Holowka, and B. Baird (1999b) Critical role for cholesterol in Lyn-mediated tyrosine phosphorylation of FcεRI and their association with detergent-resistant membranes, *The Journal of Cell Biology*, **145**, 877-887.

Shimshick, E. J. and H.M. McConnell (1973) Lateral phase separation in phospholipid membranes, *Biochemistry*, **12**, 2351-2360.

Shipley, G., L. S. Avecilla, and D.M. Small (1974) Phase behavior and structure of aqueous dispersions of sphingomyelin, *Journal of Lipid Research*, **15**, 124-131.

Siggia, E. D. (1979) Late stages of spinodal decomposition in binary mixtures, *Physical Review A*, **20**, 595-607.

Silver, B. L. (1985) The physical chemistry of membranes, The Solomon Press: New York, NY.

Silvius, J. R., D. del Giudice, and M. Lafluer (1996) Cholesterol at different bilayer concentrations can promote or antagonize lateral segregation of phospholipids of differing acyl chain length, *Biochemistry*, **35**, 15198-15208.

Simons, K. and E. Ikonen (1997) Functional rafts in cell membranes, *Nature*, **387**, 569-572.

Simons, K. and G. van Meer (1988) Lipid sorting in epithelial cells. *Biochemistry*, **27**, 6197-6202.

Singer, S. J. and G. L. Nicolson (1972) The fluid-mosiac model of the structure of cell membranes, *Science*, **175**, 720-731.

Smith, A. K. and J. H. Freed (2009) Determination of tie-line fields for coexisting lipid phases: an ESR study, *Journal of Physical Chemistry B*, **113**, 3957-3971.

Snyder, B. and E. Freire (1980) Compositional domain structure in phosphatidylcholine-cholesterol and sphingomyelin-cholesterol bilayers, *Proceedings of the National Academy of Sciences (USA)*, **77**, 4055-4059.

Soubias, O., S. L. Niu, D. C. Mitchell, and K. Gawrisch (2008) Lipid-rhodopsin hydrophobic mismatch alters rhodopsin helical content, *Journal of the American Chemical Society*, **130**, 12465-12471.

Spickett, C. M. and G. Dever (2005) Studies of phospholipid oxidation by electrospray mass spectrometry: from analysis in cells to biological effects, *BioFactors*, **24**, 17-31.

Stockton, G. W., and I. C. Smith (1976) A deuterium nuclear magnetic resonance study of the condensing effect of cholesterol on egg phosphatidylcholine bilayer membranes. I. Perdeuterated fatty acid probes, *Chemistry and Physics of Lipids*, **17**, 251-263.

Stratton, S. P. and D. C. Leibler (1997) Determination of singlet oxygen-specific versus radical-mediated lipid peroxidation in photosensitized oxidation of lipid bilayers: effect of β-carotene and α-tocopherol, *Biochemistry*, **36**, 12911-12920.

Sun, W., R. M. Suter, M. A. Knewtson, C. R. Worthington, S. Tristram-Nagle, R. Zhang, and J. F. Nagle (1994) Order and disorder in fully hydrated unoriented bilayers of gel-phase dipalmitoylphosphatidylcholine, *Physical Review E*, **49**, 4665–4676.

Surviladze, Z. et al (2007) FcεRI and Thy-1 domains have unique protein and lipid compositions, *Journal of Lipid Research*, **48**, 1325-1335.

Surviladze, Z., L. Draberova, L. Kubinova, and P. Draber, (1998) Functional heterogeneity of Thy-1 membrane microdomains in rat basophilic leukemia cells, *European Journal of Immunololgy*, **28**, 1847–1858.

Swamy, M. J. et al (2006) Coexisting domains in the plasma membranes of live cells characterized by spin-label ESR spectroscopy, *Biophysical Journal*, **90**, 4452-4465.

Takamori, S. et al (2006) Molecular anatomy of a trafficking organelle, *Cell*, **127**, 831–846.

Tanaka, H. and T. Nishi (1984) Direct determination of the probability distribution function of concentration in polymer mixtures undergoing phase separation, *Physical Review Letters*, **59**, 692-696.

Taniguchi, T. (1996) Shape deformation and phase separation dynamics of two-component vesicles, *PRL*, **76**, 4444-4447.

Tejero, I., A. G. Lafont, J. M. Lluch, and L. A. Eriksson (2007) Theoretical modeling of hydroxyl-radical-induced lipid peroxidation reactions, *Journal Physical Chemistry B*, **111**, 5684-5693.

Thomas, J.L. et al (1994) Large-scale co-aggregation of fluorescent lipid probes with cell surface proteins, *Journal of Cell Biology*, **125**, 795-802.

Tokamasu, F. et al (2003) Nanoscopic lipid domains revealed by atomic force microscopy, *Biophysical Journal*, **84**, 2609-2618.

Tong, A. (2001) Improving the accuracy of temperature measurements, *Sensor Review*, **21**, 193-198.

Tserkovnyak, Y. and D. R. Nelson (2006) Conditions for extreme sensitivity of protein diffusion in membranes to cell environments, *Proceedings of the National Academy of Sciences (USA)*, **103**, 15002–15007.

Turkyilmaz, S. et al (2009) Loosening and reorganization of fluid phospholipid bilayers by chloroform, *Journal of the American Chemical Society*, **131**, 5068-5069.

Van Blitterswik, W.J., R.P Van Hoven, and B.W. Van der Meer (1981) Lipid structural order parameters (reciprocal of fluidity) in biomembranes derived from steady-state fluorescence polarization measurements, *Biochimica et Biophysica Acta*, **644**, 323-332.

Van der Meer, W. et al (1984) Effect of orientational order on the decay of the fluorescence anisotropy in membrane suspensions. A new approximate solution of the rotational diffusion equation, *Biophysical Journal*, **46**, 515-523.

Van Ginkle, G. and A. Sevanian (1994) Lipid peroxidation-induced membrane structural alterations, *Methods in Enzymology*, **233**, 273-288.

Van Meer, G. and K. Simons (1988) Lipid polarity and sorting in epithelial cells, *Journal of Cell Biochemistry*, **144**, 459-462.

Varma, R. and S. Mayor (1998) GPI-anchored proteins are organized in submicron domains at the cell surface, *Nature*, **394**, 798-801.

Veatch, S. et al (2007) Critical fluctuations in domain-forming lipid mixtures, *Proceedings of the National Academy of Sciences (USA)*, **104**, 17650–17655.

Veatch, S. and S.L. Keller (2005) Miscibility phase diagrams of giant vesicles containing sphingomyelin, *Physical Review Letters*, **94**, 148101-148104.

Veatch, S. et al. (2004) Liquid domains in vesicles investigated by NMR and fluorescence microscopy, *Biophysical Journal*, **86**, 2910-2922.

Veatch, S. and S. Keller (2003) Separation of liquid phases in giant vesicles of ternary mixtures of phospholipids and cholesterol, *Biophysical Journal*, **85**, 3074-3083.

Veatch, S. L. and S. L. Keller (2002) Organization in lipid membranes containing cholesterol, *Physical Review Letters*, **89**, 268101-268104.

Vist, M.R. and J.H. Davis (1990) Phase behavior of cholesterol/DPPC mixtures, *Biochemistry*, **29**, 451-464.

Vladimirova, N., A. Malagoli, and R. Mauri (1999) Two-dimensional model of phase segregation in liquid binary mixtures, *Physical Review E*, **60**, 6968-6977.

Voronel, A. V. (1976) Thermal measurements and critical phenomena in liquids, *Phase Transitions and Critical Phenomena*, **5B**, Editors C. Domb and M. S. Green, Academic Press: New York, NY, 343-391.

Wack, D.C. and W.W. Webb (1989) Synchrotron X-ray study of the modulated lamellar phase $P_{\beta'}$ in the lecithin-water system, *Physical Review A*, **40**, 2712-2730.

Wang, C. C. and R. Pecora (1980) Time-correlated functions for rotational diffusion, *Journal of Chemical Physics*, **72**, 5333-5340.

Wang, T.Y. and J.R. Silvius (2003) Sphingolipid partitioning into ordered domains in cholesterol-free and cholesterol-containing lipid bilayers, *Biophysical Journal*, **84**, 367-378.

Warachawski, D. E. and P. F. Devaux (2005) 1H-13C polarization transfer in membranes: a tool for probing lipid dynamics and the effect of cholesterol, *Journal of Magnetic Resonance*, **177**, 166-171.

Watanabe, S. and T. Usui (1985) Phase transition in coupled order parameter system, *Progress of Theoretical Physics*, **73**, 1305-1319.

Wenk, M. R. et al (2003) Phosphoinositide profiling in complex lipid mixtures using electrospray ionization mass spectrometry, *Nature Biotechnology*, **21**, 813-817.

Widom, B. (1967) Plait points in two- and three- component liquid mixtures, *The Journal of Chemical Physics*, **46**, 3324-3333.

Widom, B. (1964) Degree of the critical isotherm, *The Journal of Chemical Physics*, 41, 1633-1634.

Wilson, B. S. et al (2004) Markers for detergent-resistant lipid rafts occupy distinct and dynamic domains in native membranes, *Molecular Biology of the Cell*, **15**, 2580-2592.

Wolff, S. (1994) Ferrous ion oxidation in presence of ferric ion indicator xylenol orange for measurement of hydroperoxides, *Methods in Enzymology*, **233**, 182-189.

Wu, F. Y. (1973) Phase diagram of a decorated Ising system, *Physical Review B*, **8**, 4219-4222.

Wu, Y. et al (1995) Effects of hydrodynamics on phase transition kinetics in two-dimensional binary fluids, *Physical Review Letters*, **74**, 3852-3855.

Wulfsberg, G. (2000) *Inorganic Chemistry*, University Science Books: Sausalito, CA.

Yan, Y. and G. Marriott (2003) Fluorescence resonance energy transfer imaging microscopy and fluorescence polarization imaging microscopy, *Methods in Enzymology*, **360**, 561-580.

Yeagle, P. L. (1985) Cholesterol and the cell membrane, *Biochimica et Biophysica Acta*, **822**, 267-287.

Yethiraj, A. and J. C. Weisshaar (2007) Why are lipid rafts not observed *in vivo*?, *Biophysical Journal*, **93**, 3113-3119.

Yoshigaki, T. (2007) Theoretically predicted effects of Gaussian curvature on lateral diffusion of membrane molecules, *Physical Review E*, **75**, 41901-41917.

Yu, W., P. T. So, T. French, and E. Gratton (1996) Fluorescence generalized polarization of cell membranes: a two-photon scanning microscopy approach, *Biophysical Journal*, **70**, 626-636.

Yu, J. A., D. G. Nocera, and G. E. Leroi (1990) Two-photon excitation of perylene in solution, *Chemical Physics Letters*, **167**, 85-89.

Yuan, C. et al (2002) The size of lipid rafts: An atomic force microscopy study of ganglioside GM1 domains in sphingomyelin/DOPC/cholesterol membranes, *Biophysical Journal*, **82**, 2520-2535.

Zandvoort, M. A. M. J., H. C. Gerritsen, G. Van Ginkel, Y. K. Levine, R. Tarroni, C. Zannoni, (1997) Distribution of hydrophobic probe molecules in lipid bilayers. 2. Time-resolved fluorescence anisotropy study of perylene in vesicles, *Journal of Physical Chemistry B*, **101**, 4149-4154.

Zannoni, C., A. Arcioni, and P. Cavatorta (1983) Fluorescence depolarization in liquid crystals and membrane bilayers, *Chemistry and Physics of Lipids*, **32**, 197-250.

Zhang, Z., M. M. Sperotto, M. J. Zuckermann, and O. G. Mouritsen (1993) A microscopic model for lipid/protein bilayers with critical mixing, *Biochimica et Biophysica Acta*, **1147**, 154-160.

Zhao, J., J. Wu, H. Shao, F. Kong, N. Jain, G. Hunt, and G. W. Feigenson (2007) Phase studies of model biomembranes: Macroscopic coexistence of $L_\alpha + L_\beta$, with light-induced coexistence of $L_\alpha + L_o$ phases, *Biochimica et Biophysica Acta*, **1768**, 2777-2786.